



**HAL**  
open science

# Magnetic and transport properties of single and double perpendicular magnetic tunnel junctions

Léa Cuchet

► **To cite this version:**

Léa Cuchet. Magnetic and transport properties of single and double perpendicular magnetic tunnel junctions. Condensed Matter [cond-mat]. Université Grenoble Alpes, 2015. English. NNT : 2015GREAY060 . tel-01312194

**HAL Id: tel-01312194**

**<https://theses.hal.science/tel-01312194>**

Submitted on 4 May 2016

**HAL** is a multi-disciplinary open access archive for the deposit and dissemination of scientific research documents, whether they are published or not. The documents may come from teaching and research institutions in France or abroad, or from public or private research centers.

L'archive ouverte pluridisciplinaire **HAL**, est destinée au dépôt et à la diffusion de documents scientifiques de niveau recherche, publiés ou non, émanant des établissements d'enseignement et de recherche français ou étrangers, des laboratoires publics ou privés.

## THÈSE

Pour obtenir le grade de

### DOCTEUR DE L'UNIVERSITÉ GRENOBLE ALPES

Spécialité : **Physique des Matériaux**

Arrêté ministériel : 7 août 2006

Présentée par

**Léa CUCHET**

Thèse dirigée par **Bernard RODMACQ**  
et codirigée par **Ricardo SOUSA**

préparée au sein du **Laboratoire SPINTEC**  
dans l'**École Doctorale de Physique**

## Propriétés de transport et d'anisotropie de jonctions tunnel magnétiques perpendiculaires avec simple ou double barrière

*Magnetic and transport properties of single and double  
perpendicular magnetic tunnel junctions*

Thèse soutenue publiquement le **10 novembre 2015**,  
devant le jury composé de :

**M. Olivier FRUCHART**

D.R. au CNRS, Institut Néel, Grenoble (Président)

**M. Stéphane MANGIN**

Professeur, Institut Jean Lamour, Nancy (Rapporteur)

**M. Dafiné RAVELOSONA**

D.R. au CNRS, Institut d'Electronique Fondamentale, Orsay (Rapporteur)

**M. Paulo FREITAS**

Professeur, Iberian Nanotechnology Laboratory, Braga (Examinateur)

**M. Bernard RODMACQ**

Ingénieur chercheur CEA, SPINTEC, Grenoble (Directeur de thèse)

**M. Ricardo SOUSA**

Ingénieur chercheur CEA, SPINTEC, Grenoble (Co-Directeur de thèse)



# REMERCIEMENTS

La soutenance étant terminée, il est temps de passer à la dernière mais non moins importante étape de la thèse : les remerciements. Car ces trois années de thèse n'auraient pas été aussi fructueuses sans les belles rencontres qui les ont ponctuées.

Je commencerai en remerciant chaleureusement mon directeur de thèse Bernard Rodmacq pour m'avoir énormément appris pendant ces trois ans. J'ai beaucoup apprécié notre travail ensemble au quotidien et nos nombreux échanges qui m'ont permis d'acquérir la rigueur nécessaire au travail de développement de matériaux. Merci également à Ricardo Sousa pour m'avoir intégrée à l'équipe MRAM et m'avoir permis d'aller plus loin vers l'application en m'apprenant le processus de nanofabrication. C'est grâce à vous que j'ai pu participer à de nombreuses conférences et je vous remercie tous les deux pour la confiance que vous m'avez accordée dès mes débuts à Spintec.

Je voudrais aussi remercier tous les membres de mon jury de thèse pour avoir accepté d'évaluer ce travail de thèse. Merci à Dafiné Ravelosona et Stéphane Mangin, mes deux rapporteurs, pour le temps qu'ils ont consacré à la lecture de ce manuscrit et leurs commentaires. Merci à Olivier Fruchart d'avoir accepté de présider mon jury et à Paulo Freitas pour ses questions et remarques.

Merci à Stéphane Auffret pour m'avoir tout appris de la machine de dépôt. J'ai énormément appris sur le fonctionnement d'un tel outil à tes côtés. Notre Actemium est une bête capricieuse et qui je crois n'aura jamais qu'un seul véritable maître ! Merci encore Stéphane pour ta sympathie, ça aura été un plaisir de travailler/discuter avec toi de matériaux (ou autre !).

Je remercie également Clarisse Ducruet de m'avoir formée à l'outil de caractérisation Capres et d'avoir toujours suivi avec intérêt mes travaux de thèse. Merci pour toutes les mesures et recuits que tu as effectué pour moi et ton éternelle bonne humeur. J'en profite pour remercier également ici Céline Portemont et Claire Creuzet de Crocus pour m'avoir fourni tous les substrats de CuN et pour les coups de main à la salle blanche du BHT.

Je tenais à remercier tout particulièrement Bernard Dieny et Lucian Prejbeanu qui ont toujours suivi de près mes travaux. Merci pour votre aide sur les différentes publications mais également lors de la préparation à la soutenance.

Du côté du process de nanofabrication, je voudrais remercier Laurent Vila qui a réalisé pour nous toutes les lithographies électroniques ainsi que Guillaume Lavaitte pour s'être occupé de mes plaques en fin de thèse lorsque j'étais en période de rédaction. C'était toujours un plaisir de vous croiser à la salle blanche. Je remercie également l'ensemble du personnel de la PTA pour son accueil et son aide sur les

différents équipements : Thierry Chevolleau, Christophe Lemonias, Marlène Terrier, Frédéric Gustavo et Jean-Luc Thomassin.

Pour leurs aides plus ponctuelles, je remercie Lavinia Nistor et Sébastien Bandiera, mes prédécesseurs aux études matériaux sur l'anisotropie perpendiculaire. Merci Lavinia notamment pour les mesures à Applied Materials. Merci à Isabelle Joumard pour les petits coups de main au VSM, avec les fours, etc. Je tiens également à remercier Stéphanie Pouget pour son aide sur les mesures de réflectivité des rayons X pour les étalonnages de la machine de dépôt. Un grand merci aussi à Gilles Gaudin et Jan Vogel (ainsi que Lavinia) pour leur aide pour les premiers tests d'Effet Kerr focalisé sur les structures SAF sans Pt.

Je voudrais remercier également tous les membres permanents du laboratoire pour leur accueil et leur sympathie : Vincent, Stéphane, Gilles, Hélène, Clarisse, Claire, Isabelle, Mair, Olivier, Mihai, Daria, Ursula, Grégory, Guillaume, Liliana, etc... Une petite mention spéciale à nos trois secrétaires Cat, Rachel et Sandra pour leur aide précieuse pour toutes les questions administratives. Je sais que beaucoup de changements sont à venir en 2016 mais j'espère que « l'esprit de Spintec » perdurera car j'ai passé trois merveilleuses années dans ce laboratoire où il fait si bon vivre !

Il est maintenant temps de remercier les non-permanents de Spintec en commençant par le petit groupe de post-docs hispanophones (mais pas que !) avec qui j'ai eu le plaisir de manger de temps en temps : Karla, Alex, Lara, Miguel, Marina, Pablo, Nikolai, Jannier, Ana, Thomas, Andrey, Eldar. Aquí me gustaría agradecer especialmente a mi compañera de tandem franco-español : Karla. Te convertiste en una verdadera amiga y te deseo lo mejor para tus próximas aventuras al otro lado del mundo !

Vous avez été aussi nombreux les autres thésards et post-docs avec qui j'ai partagé ces trois années d'aventures. Sans vous la vie à Spintec et en dehors n'aurait pas été la même alors je vous remercie pour tout : Magali (qui m'a accompagnée du début à la fin !), Mélissa, Cécile, Claire et Alex (les meilleur(e)s co-bureau, vive le chocolat et les dessins au tableau !), P-Y, Marc, Alex, Selma, Christophe, Kamil, Giovanni, Tulio, Karol, Emilie, Safeer, Antoine, Alexu, Mathieu, Paulo, Lamprini, Kékile. Je souhaite aussi bonne chance aux autres membres de l'équipe MRAM : Tan et Jyotirmoy.

Je tiens à ajouter ici une petite mention spéciale à l'attention de mes amis insaliens : Jérem, Mamie, Fux, Flo, Nico (c'est grâce à toi que j'ai trouvé mon stage et donc ma thèse !), Edgar et Romain. Ca a toujours été un grand plaisir de vous retrouver à la cantine ou en dehors pour raconter des bêtises !

Je terminerai en remerciant mes proches en commençant par Yvan. Merci de m'avoir soutenue pendant cette thèse et de m'avoir donné un peu plus confiance en moi. Je remercie du fond du cœur ma famille et je voudrais dédier ce manuscrit à mes parents, car sans votre soutien inconditionnel à toutes les étapes de ma vie, je ne serai jamais arrivée là.

*A mes parents.*



<b>REMERCIEMENTS.....</b>	<b>1</b>
<b>INTRODUCTION .....</b>	<b>7</b>
References .....	10
<b>CHAPTER I: Introduction to the concepts and the experimental techniques.....</b>	<b>11</b>
I-1. Origin of perpendicular magnetic anisotropy.....	14
I-2. Tunnel magnetoresistance and perpendicular magnetic tunnel junctions.....	20
I-3. Perpendicular magnetic tunnel junctions for Spin Transfer Torque MRAM applications.....	26
I-4. Thin films deposition .....	32
I-5. Characterisation techniques .....	35
I-6. Annealing procedure .....	42
I-7. Conclusions.....	45
I-8. References.....	46
<b>CHAPTER II: Development of magnetic tunnel junctions with a bottom reference.....</b>	<b>53</b>
II-1. Optimization of the Ta insertion .....	56
II-2. Development of bottom synthetic antiferromagnetic references .....	67
II-3. Optimization of magnetic electrode thicknesses .....	82
II-4. Conclusions.....	91
II-5. References.....	92
<b>CHAPTER III: Towards double junctions with perpendicular anisotropy .....</b>	<b>95</b>
III-1. Influence of a MgO capping.....	98
III-2. Development of magnetic tunnel junctions with a top reference.....	108
III-3. Double junctions with perpendicular anisotropy .....	117
III-4. Conclusions.....	123
III-5. References.....	124
<b>CHAPTER IV: Pt- and Pd-free synthetic antiferromagnetic structures .....</b>	<b>127</b>
IV-1. Variation of the coupling strength as a function of the nature and thickness of the insertion layer.....	130
IV-2. Magnetic properties of FeCoB-based SAF .....	137
IV-3. Use of an FeCoB-based SAF in double junctions .....	143
IV-4. FeCoB-based SAF as reference layers in single magnetic tunnel junctions.....	149
IV-5. Stability of the SAF configuration in small pillars .....	152

IV-6.	Conclusions.....	154
IV-7.	References.....	155

**CHAPTER V: Electrical testing of patterned perpendicular magnetic tunnel junctions ..... 157**

V-1.	Nanofabrication process .....	160
V-2.	Testing of standard magnetic tunnel junctions with a bottom SAF reference and a top Ta-capped FeCoB storage layer .....	166
V-3.	Conclusions.....	175
V-4.	References.....	176

**CONCLUSION ..... 177**

References .....	181
------------------	-----

**FRENCH SUMMARY .....184**

Introduction .....	185
Chapitre I.....	188
Chapitre II.....	191
Chapitre III.....	193
Chapitre IV.....	195
Chapitre V.....	197
Conclusion.....	198
Références .....	202

# INTRODUCTION

For millennia, storing and transmitting information have played a great role in Man's life. After ages of oral transmission, the appearance of Writing gave us the ability to store some of the information in a more reliable way on an external support such as a book. In the last century, the advent of the electronics era has seen the quantity of the stored information exploding.

Magnetism is a phenomenon that has always fascinated men. It is difficult to date precisely the first use of magnetism but some documents seem to place the discovery of the compass in the 11<sup>th</sup> century, in China. It is however only in the 19<sup>th</sup> century that a better understanding and mastering of magnetism appeared thanks to the numerous advances made in the field of the electromagnetism.

One of the first ways to store information thanks to magnetism was the creation the magnetic tape in 1928. The data were stored in iron oxide particles deposited on a flexible substrate. This technology enabled to record audio and video data but was also used in the first computers. It was quickly replaced a few years later in the 1950s by the Hard Disk Drive technology that provides faster reading of the information. A lot of research has been performed on these devices, in particular to increase the storage capacities. Nowadays, the hard disk drives can reach densities of a few Tbit/in<sup>2</sup>.

More recently, the discoveries in terms of spin transport in ferromagnetic materials gave rise to a new kind of discipline: the spintronics (also known as spin-electronics). The main idea is to add the spin information of the electron to the conventional charge displacement used in standard electronics so as to create new functionalities. This field was particularly boosted by the discovery of the Giant MagnetoResistance (GMR) in the late 1980s by A. Fert [[Bai-88](#)] and P. Grünberg [[Bin-89](#)] who received the Nobel Prize of Physics in 2007 for their work. This effect was quickly used to advantageously enhance the performances of the read heads in the Hard Disk Drives [[Die-91](#)]. A few years later, another spin-related phenomenon started to appear interesting in the field of memory applications: the Tunnel MagnetoResistance (TMR). It relies on the relative orientation of the magnetizations of two magnetic layers separated by an insulating layer. Such a stack is known as a Magnetic Tunnel Junction and constitutes the basic component of Magnetic Random Access Memories (MRAM). This technology further developed with the discovery of Spin Transfer Torque (STT) switching thanks to the theories developed by J. C. Slonczewski [[Slo-96](#)] and L. Berger [[Ber-96](#)].

As predicted by the Moore's law, the number of components on a chip has been increasing exponentially in the last decades. Even if this tendency is starting to slow down recently, there are still a lot of developments towards downsize scalability. In

that matter, MRAM and in particular STT-MRAM that have been proved to be particularly competitive among the emerging non-volatile memory technologies. It was indeed identified, along with redox RRAM, by the International Technology Roadmap for Semiconductors (ITRS, [Itr-10]) as the emerging technologies that could scale down to the 16 nm node and beyond. Besides, MRAM is also seen as a possible candidate to build a new universal memory that would have the ability of replacing DRAM (known for its high speed, low power, good endurance and reliability) and Flash memory with its large capacity and non-volatility. A comparison between the Flash, Ferroelectric RAM (another emerging technology), MRAM and STT-RAM is given in Table 1.

	Flash-NAND	FeRAM	MRAM	STT-MRAM
Storage capacity	> 1 Gb	> 10 Mb	16 Mb	1 Gb
Write time	1 ms	10 ns	20 ns	3-10 ns
Read time	50 ns	45 ns	10 ns	10 ns
Write energy (pJ/bit)	> 0.01	0.03	70	0.1

Table 1: Comparison between different non-volatile memory technologies [Hu-11].

In this context, SPINTEC was founded in 2002 to combine both fundamental and applied research in the field of spintronics. This thesis has been realized in the MRAM team, with the idea of continuing the materials developments of magnetic tunnel junctions with perpendicular anisotropy. Indeed, this property of the magnetic materials that is characterized by an out-of-plane orientation of the magnetization has been found to be particularly interesting for practical applications. Compared to the previously in-plane magnetized structures, perpendicular anisotropy gives the possibility to reduce the size of the devices, which improves the storage density. Besides, this type of anisotropy should provide larger thermal stability to the memory elements. Moreover, the STT efficiency of such structures is known to be particularly good with perpendicularly magnetized materials.

The objective of this thesis is to enhance the magnetic and transport properties of perpendicular magnetic tunnel junctions by carefully adapting the different parts of the magnetic stack to the required functionality. This can only be achieved through a good mastering of the deposition tool and of the different materials involved. In a first Chapter, we will recall the origin of perpendicular anisotropy and the different concepts that have accompanied the developments of MRAM, in particular in the case of perpendicular systems. We will also present the different experimental procedures that have been used during this thesis regarding samples preparation and characterization. In the second Chapter, we will see how a standard magnetic tunnel junction with a bottom Co/Pt-based reference can be optimized by tuning the different thicknesses that compose the structure. We will show that both magnetic and transport properties are related and that some compromises have to be done.

## *Introduction*

The third Chapter will show that even more complex structures can be build such as double magnetic tunnel junctions with perpendicular anisotropy. We will start by inserting a second MgO layer as a capping and after developing a top reference layer, we will show the realization of full double structures. In the fourth Chapter, we will focus on the development of FeCoB-based synthetic antiferromagnetic layers comprising various spacers. We will see that these systems can play different roles in a double junction but can also be made stable enough to be used as reference layers in single Pt- or Pd-free junctions. Finally, the fifth Chapter will present the nanofabrication process and some of the results obtained by electrical testing of patterned junctions.

## References

[Bai-88] M. N. Baibich, J.-M. Broto, A. Fert, F. Nguyen Van Dau, F. Petroff, P. Etienne, G. Creuzet, A. Friederich, and J. Chazelas, *Giant magnetoresistance of (001)Fe/(001)Cr magnetic superlattices*, [\*Phys. Rev. Lett.\* \*\*61\*\*, 2472-2475 \(1988\)](#).

[Ber-96] L. Berger, *Emission of spin waves by a magnetic multilayer traversed by a current*, [\*Phys. Rev. B\* \*\*54\*\*, 9353-9358 \(1996\)](#).

[Bin-89] G. Binasch, P. Grünberg, F. Saurenbach, and W. Zinn, *Enhanced magnetoresistance in layered magnetic structures with antiferromagnetic interlayer exchange*, [\*Phys. Rev. B\* \*\*39\*\*, 4828-4830 \(1989\)](#).

[Die-91] B. Dieny, V. S. Speriosu, S. S. P. Parkin, B. A. Gurney, D. R. Wilhoit, and D. Mauri, *Giant magnetoresistive effect in soft ferromagnetic multilayers*, [\*Phys. Rev. B\* \*\*43\*\*, 1297-1300 \(1991\)](#).

[Hu-11] J.-M. Hu, Z. Li, L.-Q. Chen, and C.-W. Nan, *High-density magnetoresistive random access memory operating at ultralow voltage at room temperature*, [\*Nat. Commun.\* \*\*2\*\*, 553 \(2011\)](#).

[Itr-10]

[http://www.itrs.net/Links/2010ITRS/2010Update/ToPost/ERD\\_ERM\\_2010FINAL\\_ReportMemory\\_Assessment\\_ITRS.pdf](http://www.itrs.net/Links/2010ITRS/2010Update/ToPost/ERD_ERM_2010FINAL_ReportMemory_Assessment_ITRS.pdf)

[Slo-96] J.C. Slonczewski, *Current-driven excitation of magnetic multilayers*, [\*J. Magn. Magn. Mater.\* \*\*159\*\*, L1-L7 \(1996\)](#).

# CHAPTER I

## Introduction to the concepts and the experimental techniques

<b>I-1. Origin of perpendicular magnetic anisotropy .....</b>	<b>14</b>
I-1.1 Definition of the magnetic anisotropy .....	14
I-1.2 Perpendicular anisotropy originating from spin-orbit interactions.....	15
I-1.3 Perpendicular anisotropy at metal/oxide interface.....	15
I-1.4 Experimental determination of the anisotropy constant.....	17
<b>I-2. Tunnel magnetoresistance and perpendicular magnetic tunnel junctions.....</b>	<b>20</b>
I-2.1 What is tunnel magnetoresistance? .....	20
I-2.2 First developments of planar magnetic tunnel junctions .....	22
I-2.3 Materials developments for magnetic tunnel junctions with perpendicular anisotropy.....	24
<b>I-3. Perpendicular magnetic tunnel junctions for Spin Transfer Torque MRAM applications.....</b>	<b>26</b>
I-3.1 The different families of MRAM.....	26
I-3.2 What is Spin Transfer Torque? .....	28
I-3.3 Interest of perpendicular anisotropy for STT-MRAM applications.....	29
<b>I-4. Thin films deposition .....</b>	<b>32</b>
<b>I-5. Characterisation techniques .....</b>	<b>35</b>
I-5.1 Magnetic characterization.....	35
I-5.2 Characterization of the transport properties (Current In-Plane Tunneling) .....	39
<b>I-6. Annealing procedure .....</b>	<b>42</b>
I-6.1 Effect of the presence of a magnetic field during annealing on the magnetic properties .....	42
I-6.2 Set-up equivalence.....	43
<b>I-7. Conclusions .....</b>	<b>45</b>
<b>I-8. References .....</b>	<b>46</b>



Perpendicular magnetic anisotropy is a phenomenon that has been known for many years, in particular in the field of Hard Disk Drive. However, the interest for such a property has been growing dramatically recently due to the development of the MagnetoResistive Random Access Memories (MRAM).

As we will see, this effect can have several origins that are mostly material dependent. A large breakthrough was made with the discovery of perpendicular anisotropy at metal/oxide interface as it enables building magnetic tunnel junctions (MTJs) with perpendicularly magnetized electrodes.

In this Chapter, we will see how perpendicular magnetic anisotropy is defined and where it originates from. We will describe how the developments of MRAM followed the advances of spintronics and which materials developments have been necessary to achieve perpendicular magnetic tunnel junctions. This type of junctions was found particularly promising for Spin Transfer Torque MRAM applications and we will explain what compromises must be made to ensure low power consumption as well as long lasting data retention. Finally we will describe our experimental procedures regarding materials deposition, properties characterization and annealing conditions.

## I-1. Origin of perpendicular magnetic anisotropy

Magnetic materials may present preferential orientations for their magnetization. This effect is defined as the magnetic anisotropy. The preferred axis is known as easy axis of magnetization. The effective magnetic anisotropy is characterized by a constant  $K_{\text{eff}}$ , which accounts for a volume energy. The total energy of a system then is given by  $E = -K_{\text{eff}} \cos^2(\theta)$ , where  $\theta$  is the angle between the magnetization and the anisotropy axis.

### I-1.1 Definition of the magnetic anisotropy

The magnetic anisotropy consists of different contributions:

- The magnetocrystalline anisotropy: it originates from the organization of the atoms in the crystal lattice and induces a favored crystallographic direction for the magnetization. This effect is due to the electrostatic interactions between atoms by spin-orbit coupling.
- The magnetoelastic anisotropy: stresses in the material may modify the easy axis of magnetization by changing the magnetocrystalline anisotropy. In thin films, such stresses can appear because of lattice mismatch or a difference in thermal expansion coefficients.
- The shape anisotropy: it is due to the existence of a demagnetizing field originating from dipolar interactions. This contribution tends to align the magnetization along the largest dimension of the sample, that is to say in-plane in the case of magnetic thin films.
- The surface anisotropy: it appears because of the change of environment encountered by the atoms at the interfaces and may induce interactions between different materials. Surface roughness is particularly important as it can generate local demagnetizing fields that reduce shape anisotropy. This contribution is essential for perpendicular anisotropy, as we will see in the following.

The effective anisotropy is described by the anisotropy constant  $K_{\text{eff}}$  which is defined as follows:  $K_{\text{eff}} = K_v - 2\pi M_s^2 + \frac{2K_s}{t}$ , where  $K_v$  is the volume contribution (magnetocrystalline and magnetoelastic anisotropies),  $-2\pi M_s^2$  is the demagnetizing field,  $K_s$  the surface contribution and  $t$  the magnetic thickness.

As we will see in the following, perpendicular anisotropy can have bulk and interfacial contributions.

### **I-1.2 Perpendicular anisotropy originating from spin-orbit interactions**

One of the prevailing effects in magnetic anisotropy is the spin-orbit interaction. This interaction links the spin of an electron with its orbital motion and is then particularly influenced by the lattice arrangement in the material. Commonly, large spin-orbit coupling is observed in heavy materials such as Pt, Au, Ta, rare earths...

This is why, during the development of perpendicularly magnetized media for Hard Disk Drive (HDD), alloys such as CoPtCr or L<sub>10</sub> ordered FePd [Geh-97] were found particularly interesting. In those cases, perpendicular anisotropy originates from the large spin-orbit coupling of Pt or Pd associated with reduced crystal symmetry, both resulting in a strong magnetocrystalline anisotropy. Perpendicular anisotropy has in that case a bulk origin.

As magnetic films get thinner, interfacial properties become more and more important and reinforce the part played by surface anisotropy. This effect has already been predicted in 1954 by L. Néel [Née-54] and was attributed to a change in the symmetry at the interfaces. This is particularly the case in multilayers such as (Co/Pt) or (Co/Pd). These systems take benefit both from the large spin-orbit coupling of the Pt or Pd elements and the interfacial effects at the ferromagnetic material/heavy metal interfaces. The anisotropy can have several sources. Indeed, strains due to lattice mismatch between neighboring elements may introduce magnetostriction effects [Joh-95]. Besides, perpendicular anisotropy can also arise from electron hybridization at the interface [Daa-94].

### **I-1.3 Perpendicular anisotropy at metal/oxide interface**

More recently, another form of interfacial anisotropy was found to appear at the interface between transition metals and oxides. It was relatively surprising as spin-orbit coupling is rather weak in those materials but the anisotropy can reach values as large as those obtained in Co/Pt multilayers ( $\sim 1.4 \text{ erg.cm}^{-2}$ ).

This type of anisotropy was first observed in 2002 in Pt<sub>3</sub>/CoFe<sub>0.6</sub>/AlO<sub>x</sub> stacks [Mon-02] and found to be extremely dependent on the oxidation state at the interface. Indeed, as shown in Figure I-1 (a), for samples that were naturally oxidized in air for 24h, the anisotropy depends a lot on the deposited Al thickness. Without any Al layer, the magnetization is in-plane whereas for thicknesses between 0.2 and 0.4 nm the signal is characteristic of a perpendicularly magnetized layer. For Al thicknesses larger than 0.6 nm the magnetization falls back in-plane. This suggests that, as the interface goes from over-oxidized to under-oxidized, there exists an

optimal oxidation condition that brings strong perpendicular anisotropy to the system. This is confirmed in Figure I-1 (b), where the same behavior is observed for Pt<sub>3</sub>/Co<sub>6</sub>/AlO<sub>x</sub> samples in which the AlO<sub>x</sub> barrier is obtained by plasma oxidation of metallic Al with different oxidation times [Rod-03]. Similarly, an optimal oxidation time between 2-3 min allows getting perpendicular anisotropy.

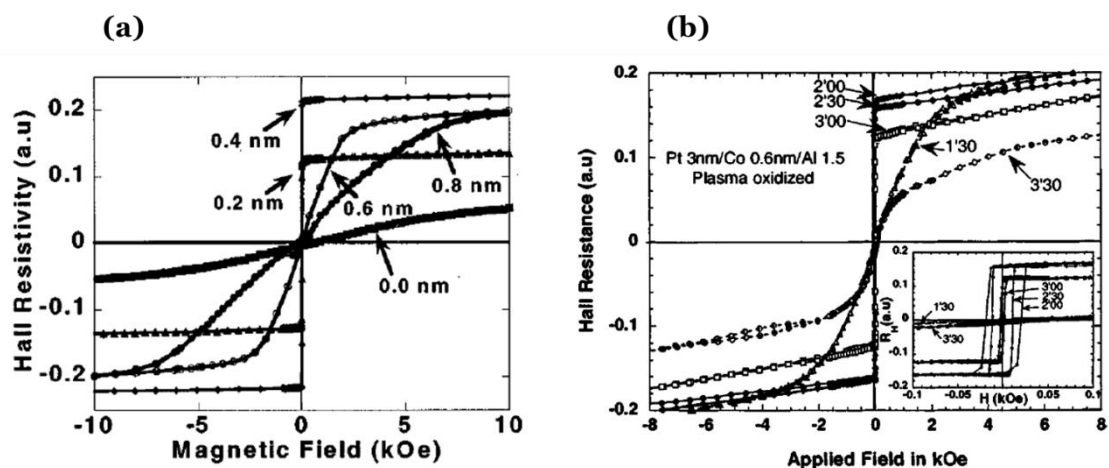


Figure I-1: Hall resistance as a function of perpendicular applied field for (a) Pt<sub>3</sub>/CoFe<sub>0.6</sub>/AlO<sub>x</sub> samples naturally oxidized in air with varying thicknesses of Al [Mon-02] (b) Pt<sub>3</sub>/Co<sub>0.6</sub>/AlO<sub>x</sub> samples plasma oxidized with different oxidation times [Rod-03].

This phenomenon was found to be relatively general and could be observed for a large range of oxides, either crystalline or amorphous (CrO<sub>x</sub>, AlO<sub>x</sub>, TaO<sub>x</sub>, MgO, RuO). It also does not depend on the type of oxidation (natural, plasma or RF sputtered) [Man-08].

In this study, it was found that the loss of remanence observed for over-oxidized samples can be attributed to the creation of up and down domains due to the oxygen diffusion at the Co grain boundaries. Further chemical analyses (X-ray absorption and photoemission) revealed that as the oxidation time is increased, the interface goes from pure Co to pure CoO. The maximum perpendicular anisotropy is obtained when Co-O bonds have appeared at the interface but when Co remains unoxidized in the rest of the layer. This indicates that the origin of the anisotropy in these systems can be explained by the hybridization of the transition metal atomic orbitals with those of oxygen. This type of mechanism had been predicted since 1989 [Bru-89] and was later confirmed by ab-initio calculations [Yan-11]. These calculations showed that perpendicular anisotropy arises at the metal/oxide interface because of the hybridization of the 3d orbitals of the metal with the 2p orbitals of oxygen. They also confirmed that perpendicular anisotropy is reduced for over-oxidized or under-oxidized interfaces due to the modification of hybridized states in the case of an additional (or missing) oxygen atom at the interface.

Furthermore, the key role played by the oxidation state at the metal/oxide interface was also evidenced in studies on the effect of annealing [Rod-09]. It

appeared for example that the range of oxidation time enabling to obtain perpendicular anisotropy gets larger as the annealing temperature is increased. It was shown that this annealing step leads to the migration of oxygen atoms towards the interface where they are more stable, which improves perpendicular anisotropy.

As we will see in the following, this perpendicular anisotropy at metal/oxide interface is particularly interesting for devices. It indeed gives the possibility to prepare magnetic tunnel junctions with perpendicular anisotropy, thanks to the properties of the magnetic electrode/oxide barrier interface.

### **I-1.4 Experimental determination of the anisotropy constant**

As seen previously, the effective anisotropy may be defined by the following formula:

$$K_{eff} = -2\pi M_s^2 + K_v + \frac{2K_s}{t}$$

where  $2\pi M_s^2$  stands for the demagnetizing field energy,  $K_v$  is the volume contribution (magnetocrystalline and magnetoelastic anisotropies),  $K_s$  is the surface contribution and  $t$  the magnetic thickness. As the layer gets thinner, the surface contribution becomes more and more important. Note that  $2K_s$  might be developed as  $K_{s1}+K_{s2}$  to discriminate between the top and bottom interfaces. Indeed, if the two interfaces differ, their respective contributions to the anisotropy might be different.

By convention,  $K_{eff}$  is positive when the easy axis of magnetization is perpendicular to the layer plane. If  $K_{eff}$  is negative, the easy axis lies in the film plane.

One can determine the volume and surface contributions by plotting the evolution of the  $K_{eff}.t$  product as a function of magnetic material thickness  $t$ . An example of the obtained curve is given in Figure I-2. With such graphs, the critical thickness at which the transition between perpendicular and planar orientation occurs, as well as the volume (slope) and surface (zero intercept) anisotropy energies, can be estimated.

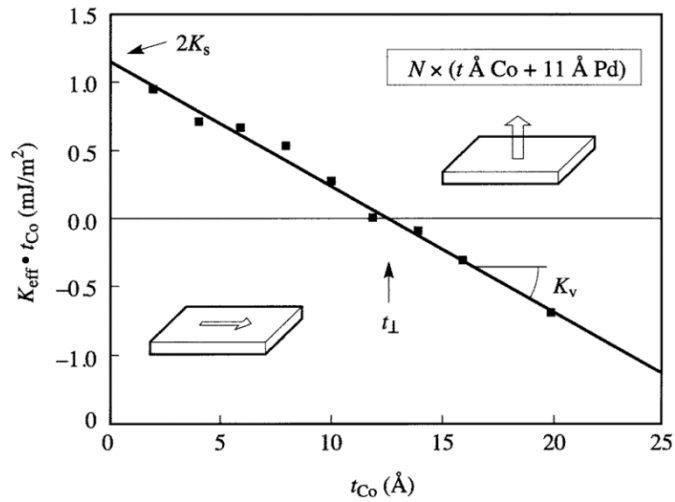


Figure I-2: Example of a plot of  $K_{\text{eff}} \cdot t$  as a function of  $t$  for Co/Pd multilayers [Joh-96].

$K_{\text{eff}}$  corresponds to the energy that is necessary to switch the direction of the magnetization from the easy axis to the hard axis. It can be extracted from easy and hard axis magnetic measurements.

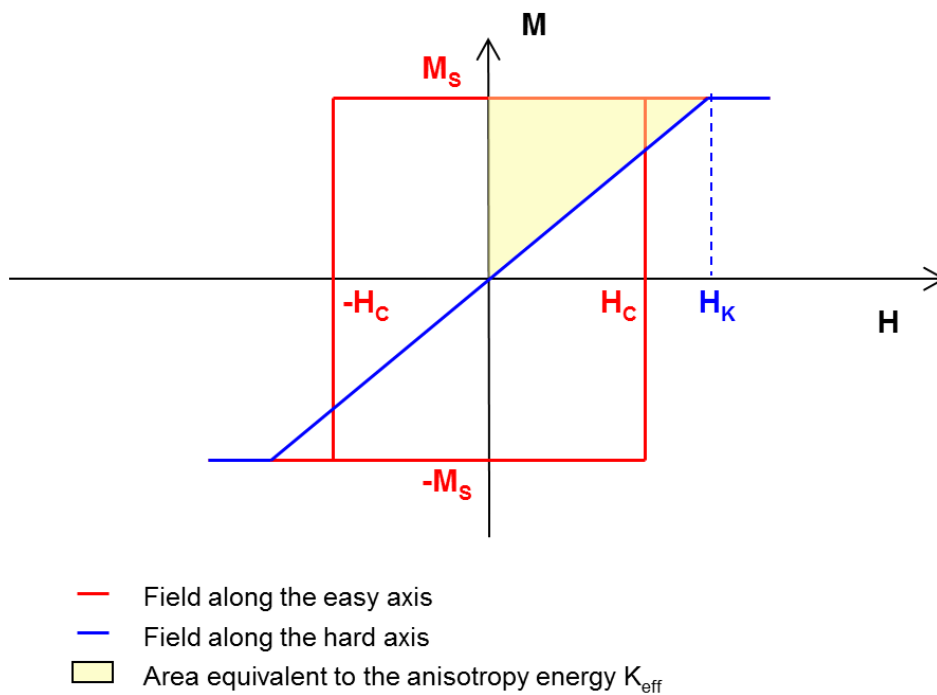


Figure I-3: Schematic magnetic cycles for a field applied parallel (red) or perpendicularly (blue) to the anisotropy axis.

$H_c$  corresponds to the coercive field (that is to say the field that must be applied to change the magnetization orientation),  $M_s$  the saturation magnetization and  $H_K$  the anisotropy field.

$K_{eff}$  may be then calculated as the difference between the areas above the curves measured along the hard and easy axis.

$$K_{eff} = \int_{hard\ axis} M dH - \int_{easy\ axis} M dH$$

Most of the time the easy axis contribution is negligible, but it might not be the case near the critical thickness, when the anisotropy is switching from perpendicular to planar. In the simplest cases,  $K_{eff}$  can then be expressed this way:

$$K_{eff} = \frac{H_K M_s}{2}$$

If the variation of magnetization as a function of applied field is linear in the hard axis curve,  $H_K$  will be equivalent to the saturation field  $H_s$ . If it is not the case, only the difference of areas will allow estimating  $K_{eff}$ . Note that obtaining the absolute value of  $M_s$  is not straightforward. Indeed many measurement techniques give signals that are solely proportional to the magnetization (Extraordinary Hall Effect, magneto-optic Kerr effect). In the case of Vibrating Sample Magnetometry (VSM), the size of the sample and position on the sample holder introduce uncertainties that prevent from achieving a precise estimation of  $M_s$  on a unique sample. This is why we will use dedicated studies that combine a series of samples with varying thicknesses as well as the use of an internal reference. This method will be detailed later in this manuscript.

## I-2. Tunnel magnetoresistance and perpendicular magnetic tunnel junctions

The discovery of the tunnel magnetoresistance has been a major breakthrough for the development of Magnetic Random Access Memories. It gave the possibility to build a new type of non-volatile memories which characteristics are particularly promising. More interestingly, systems with perpendicular anisotropy have been found to be particularly relevant in the race towards downsize scalability. As we will see in the following, this step could only be achieved through a good mastering of the deposited materials.

### I-2.1 What is tunnel magnetoresistance?

At the early stages of the Hard Disk Drive (HDD) industry, the read heads were based on the Anisotropic MagnetoResistance (AMR) effect, in which the resistance varies as a function of the angle between the current and the magnetization direction [Gui-75]. However this signal amounts only to a few percent. A major breakthrough was then achieved thanks to the Giant MagnetoResistance (GMR) effect that allowed a large increase of the signal. It was discovered in (Fe/Cr) multilayers and Fe/Cr/Fe trilayers by A. Fert [Bai-88] and P. Grünberg [Bin-89] in the late 80s, both of them being granted the Nobel Prize of Physics in 2007 for this research work. This discovery followed earlier work on transport in ferromagnetic materials that suggested electrons are separated into two channels: one for the majority electrons (with spins parallel to the magnetization) and one for minority electrons (with spins antiparallel to the magnetization) [Mot-36]. In the structures studied by A. Fert and P. Grünberg, it appeared that two resistance states could be measured depending on the relative orientation of the magnetizations in the magnetic layers: when they are antiparallel a high resistance state is measured whereas a lower resistance is obtained when they are parallel. This can be explained by the conduction model with two channels. In the case of an antiparallel configuration, both minority and majority electrons are diffused the same way as their spin is parallel to the magnetization of one layer and antiparallel to the other one. On the contrary, in the case of a parallel configuration, the minority electrons are more diffused than the majority ones, leading to a difference of resistance between the two channels that results in an overall lower resistance level.

The giant magnetoresistance is defined by the ratio:  $GMR = \frac{R_{AP}-R_P}{R_P}$ , where  $R_{AP}$  and  $R_P$  stand for the resistances in the antiparallel and parallel states of the magnetizations, respectively. The difference in resistances is normalized to  $R_P$ , so that

the maximum of GMR tends towards infinity. It is usually known as the “optimistic definition”.

In terms of applications, this phenomenon has been particularly important for the development of read heads for HDD [Die-91]. Generally, they employed spin valves that consist of NiFe layers separated by a Cu spacer. One of the layers is pinned thanks to exchange bias with an antiferromagnet while the other one is free to align its magnetization to the one of the memory element. Reading the resistance state of the spin-valve allows retrieving the information stored in the probed byte.

The Tunnel MagnetoResistance (TMR) effet is slightly similar and happens when two ferromagnetic layers are separated by an insulating spacer, instead of a metallic one. This type of stack is known as Magnetic Tunnel Junction (MTJ). The insulating layer is called tunnel barrier and is generally characterized by its Resistance-Area product (RA). It was firstly evidenced by M. Jullière in 1975 in a Fe/GeO/Co junction which exhibited a TMR signal of 14 % at 4.2 K [Jul-75]. In the model developed to explain this phenomenon, the first hypothesis is that the spin of the electron is conserved during tunneling. The second one states that the tunneling probability is proportional to the densities of states at the Fermi level in both transmitting and receiving electrodes. The conductance of the structure can then be viewed as  $G \propto D_1^\uparrow D_2^\uparrow + D_1^\downarrow D_2^\downarrow$ , where  $D_1$  and  $D_2$  are the densities of states in the two electrodes for either spin up or spin down electrons.

If the magnetizations are parallel  $D_1^\uparrow > D_1^\downarrow$  and  $D_2^\uparrow > D_2^\downarrow$  whereas if they are antiparallel  $D_1^\uparrow > D_1^\downarrow$  and  $D_2^\downarrow > D_2^\uparrow$  (see the schematic representation of Figure I-4). Therefore, when changing the magnetic configuration, one modifies the amount of current crossing the barrier. In Jullière’s model, the polarization of the electrode  $i$  is defined as  $P_i = \frac{D_i^\uparrow - D_i^\downarrow}{D_i^\uparrow + D_i^\downarrow}$ . For non-magnetic materials  $P$  is then zero while for fully polarized materials  $|P|=1$ .

Similarly to the GMR effect, the resistance level is higher in the case of the antiparallel configuration of the electrodes than in the parallel one. The TMR ratio can be defined as:  $TMR = \frac{G_P - G_{AP}}{G_{AP}} = \frac{R_{AP} - R_P}{R_P} = \frac{2P_1 P_2}{1 - P_1 P_2}$ .

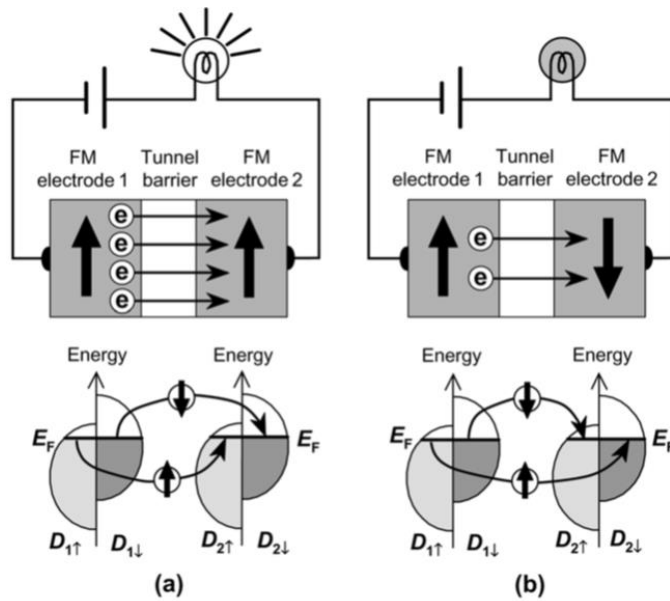


Figure I-4: Schematic representation of the tunnel magnetoresistance effect for (a) parallel configuration of the magnetizations (b) antiparallel configuration of the magnetizations [Yua-07].

### I-2.2 First developments of planar magnetic tunnel junctions

At the early stages of magnetic tunnel junction development, the barriers were mostly made of amorphous alumina. This is thanks to the use of this type of barrier that TMR ratios around 18 % could be achieved at room temperature in 1995 [Miy-95, Moo-95]. Even though further research on AlO<sub>x</sub> barriers enabled to reach TMR levels as large as 70 % at room temperature [Wan-04], those signals are still too low to satisfy the requirements of the memory industry. Indeed, TMR ratios above 150 % should be preferred to guaranty a good readability of the stored information.

In 2001, theoretical studies predicted that epitaxial systems with crystalline tunnel barriers could exhibit TMR of the order of several 1000 % [But-01, Mat-01]. This can be explained by the nature of the tunneling that becomes coherent instead of incoherent with amorphous barriers. Due to the crystallographic symmetries, the tunneling effect appears to be more efficient as illustrated in Figure I-5.

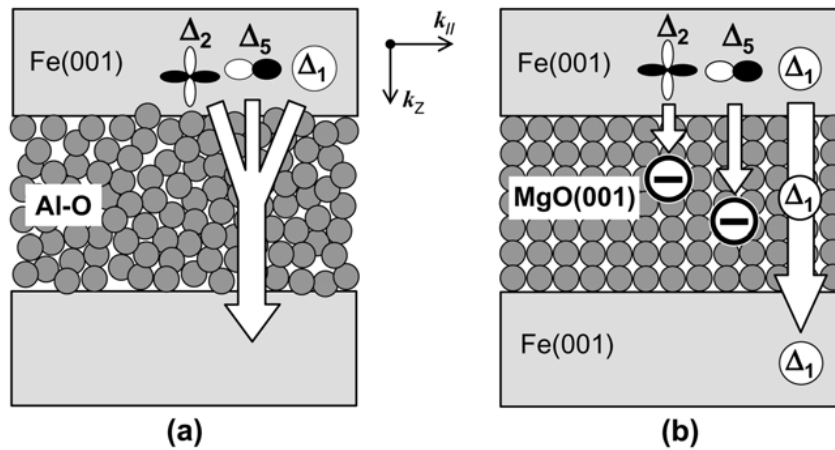


Figure I-5: Schematic representation of electron tunneling through (a) an amorphous AlO<sub>x</sub> barrier (b) a crystalline MgO barrier [Yua-07].

These theoretical predictions led to a rapidly growing interest for magnetic tunnel junctions with a crystalline MgO tunnel barrier. The same year, a room temperature TMR of 30 % could be achieved in an epitaxial Fe/MgO/FeCo structure [Bow-01]. This is however only when the quality of the materials growth got much better and the interfaces got cleaner that TMR ratios of the order of 200 % could be reached [Yua-04, Par-04].

Despite the good results obtained in epitaxial junctions, the deposition technique (Molecular Beam Epitaxy, MBE) is not compatible with the development of these structures at the industry level due to its high cost. Junctions prepared by sputtering techniques have been thus favored in the more recent developments that focused mainly on CoFeB/MgO/CoFeB stacks. One of the advantages of CoFeB alloys is that they are amorphous in the as-deposited state. It was observed that when the MgO barrier is deposited on top of amorphous CoFeB it grows with its naturally oriented polycrystalline (001) structure, which is required for a good tunneling effect [Dja-05]. As illustrated in Figure I-6, TEM images revealed the good crystallinity of the MgO barrier, even in the as-deposited state. Such a structure could yield a TMR of 230 % at room temperature but much higher levels of the order of 500 % are achievable by properly tuning the thickness and composition of the CoFeB electrodes [Lee-07].

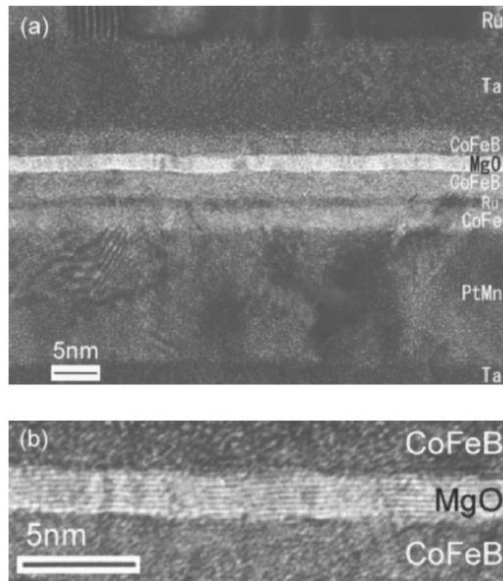


Figure I-6: (a) TEM cross section of a planar magnetic tunnel junction with CoFeB electrodes and MgO crystalline barrier (b) zoom on the same junction on the barrier region [Dja-05].

As already pointed out in [Lee-07], the crystallization of the CoFeB electrodes plays a crucial role in the tunnel magnetoresistance effect. It was indeed observed that upon annealing the CoFeB electrodes crystallize, using as a template the crystalline MgO barrier. This provides them a bcc (001) texture that ensures a coherent tunneling effect thanks to an “epitaxial-like” behavior [Yua-05, Cho-07].

### I-2.3 Materials developments for magnetic tunnel junctions with perpendicular anisotropy

In the early stages of the magnetic tunnel junction developments, research was mostly done on in-plane magnetized systems. The progresses made in the field of perpendicular magnetic anisotropy gave way to even more promising devices in terms of MRAM applications.

The first report on perpendicularly magnetized tunnel junctions was released in 2002 and was presenting AlO<sub>x</sub>-based junctions that exhibited TMR values of around 50 % [Nis-02]. But a major breakthrough was achieved in 2010 when Ikeda *et al.* presented results on Ta/CoFeB/MgO-based perpendicular tunnel junctions. Taking advantage of the perpendicular anisotropy arising at the CoFeB/MgO interface, they were able to build structures stable at small dimensions and with high TMR of 120 % [Ike-10].

If in this first approach, junctions were composed of Ta/CoFeB electrodes solely, another type of structure became rapidly standard. It comprises a Synthetic

AntiFerromagnetic (SAF) reference made with Co/Pt or Co/Pd multilayers coupled to a CoFeB layer at the interface with MgO and a CoFeB storage layer [Wor-11, Miz-11]. As we have seen previously, the Pt (Pd)-based multilayers provide strong perpendicular anisotropy and are thus used to harden the reference layer, making it particularly stable. We will come back with more details on the advantages of these SAF structures in the next Chapter.

A lot of effort has followed to optimize the anisotropy and transport properties of perpendicular magnetic tunnel junctions focusing in particular on the materials aspect. Indeed, these properties are extremely sensitive to the stack composition.

There have been then various studies on the influence of buffer layers on the perpendicular anisotropy of the CoFeB magnetic electrodes. Standard materials such as Cr, Ru, Ta, Al were investigated and it appeared that the best results were obtained for Ta buffer layers [Wor-11]. This can be explained by the getter properties of Ta that has indeed the ability to attract boron away from the CoFeB/MgO interface which is beneficial both to the perpendicular anisotropy and the TMR [Koz-10]. Further studies showed that Hf could be a good candidate to replace Ta as it increases the anisotropy by 35 % [Liu-12]. This material was also found to be amorphous at small thickness, providing good growth conditions to the CoFeB and MgO layers. In another research group, Ta has been doped with nitrogen and it resulted in an increase in perpendicular anisotropy [Sin-13]. This was interpreted as TaN acting as a diffusion barrier that prevents intermixing between CoFeB and Ta. This is an interesting property as limiting Ta diffusion has been shown to enhance the TMR signal of planar junctions [Ike-08]. More recently, promising results have been obtained with Mo underlayers in terms of anisotropy and thermal endurance, with however no information on the transport properties with such Mo/CoFeB electrodes [Liu-14].

At the same time, similar work was performed on the capping layers. If Ta gives relatively satisfying results, some studies drew the attention on MgO and V capping layers [Nat-12, Kub-12, Yam-12]. Focus on MgO capping will be developed in Chapter III of this manuscript.

Another important factor playing a role on the perpendicular anisotropy of the CoFeB magnetic layer is the alloy composition. Indeed, as seen in ab-initio calculations, larger interfacial anisotropy is obtained for Fe/MgO interfaces than for Co/MgO ones [Yan-11]. This was experimentally confirmed: as the Fe content increases, the anisotropy field increases as well [Dev-13, Lam-13].

Note that to be able to rigorously compare the anisotropies of different systems, it is necessary to know the magnetic dead layer thicknesses that appear at the interfaces. This way, only the effective magnetic thicknesses are taken into account.

### **I-3. Perpendicular magnetic tunnel junctions for Spin Transfer Torque MRAM applications**

Magnetic Random Access Memories (MRAM) are a new type of non-volatile memories that rely on the tunnel magnetoresistance effect to code binary information. As we have seen, depending on the relative orientation of the magnetizations of the electrodes in a magnetic tunnel junction, two resistance states can be measured: a high resistance one when they are antiparallel and a low resistance one when they are parallel. This allows coding a “1” and a “0”, respectively. The higher the TMR of the junction is, the easier the reading of the information will be. This type of memories is particularly promising as, in addition to providing non-volatility, MRAM can be made extremely dense and reach high write speed of a few nanoseconds, as well as possibly infinite endurance ( $>10^{16}$  write cycles). They are also considered very interesting for aerospace applications due to their radiation hardness.

In 2010, the International Technology Roadmap for Semiconductors identified Spin Transfer Torque MRAM and redox RRAM as the two emerging technologies capable of scaling to and beyond the 16 nm generation. This led to a lot of effort in research on STT-RAM, both in laboratories and in the industry.

#### **I-3.1 The different families of MRAM**

The progresses made in the field of MRAM closely followed the discoveries of spintronics. Figure I-7 schematically represents the different generations of MRAM. In the first generation, field-induced switching was employed. In Stoner-Wolfarth MRAM, two perpendicular field lines are used to switch the magnetization of the storage layer. One drawback of this structure is that even though only the junction located at the intersection of the two field lines should be written, as the lines are shared by several junctions, an unwanted writing of another junction may happen. The selectivity of the junction has been improved in 2003 by Motorola [\[Sav-03\]](#), using a new kind of design named toggle-MRAM. In that case, a Synthetic Antiferromagnetic storage layer is used and writing is done by applying two orthogonal fields in a 4-steps sequence. This type of MRAM has been commercialized for the first time in 2006 by Everspin. Both methods are however not scalable enough due to both the presence of field lines and the relatively large currents needed to generate the magnetic fields.

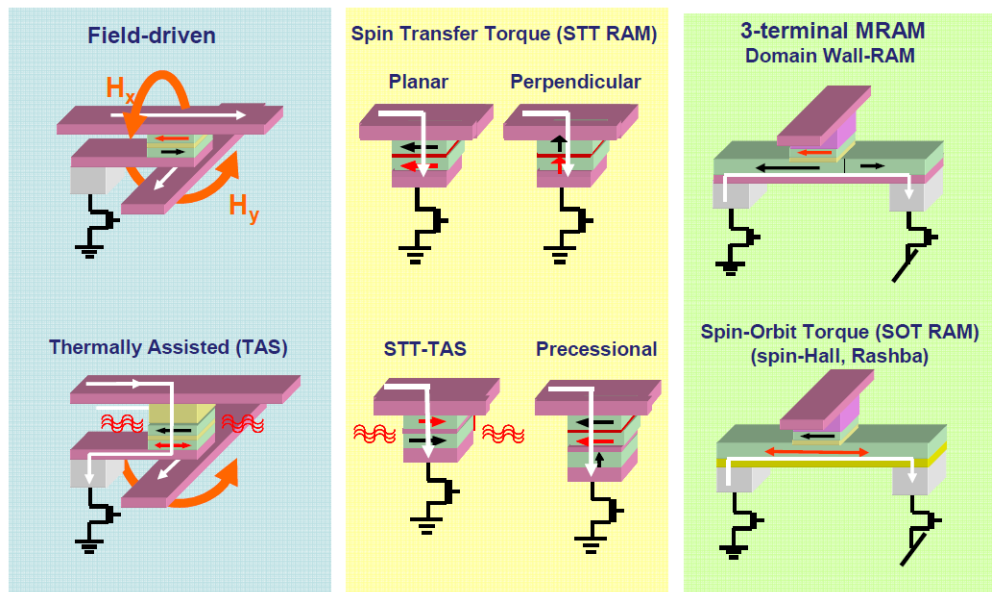


Figure I-7: Schematic representation of the different generation of MRAMs [Die-15].

To enhance writability of the memory dot, a new method was proposed using thermal assistance [Die-01, Pre-07]. The idea is that heating allows reducing the energy barrier for switching which decreases the power consumption of the device. The selectivity is also improved as the current path for heating is specific to each junction. This new design is at the origin of the creation of the start-up Crocus Technology in Grenoble.

However, the performances of MRAM really started to become competitive in the field of memory applications when Spin Transfer Torque switching was introduced, and even more in perpendicularly magnetized systems. As we will see in more details in the following, this approach uses a spin-polarized current to switch the magnetization. This allows the creation of new designs that are particularly compact as no field lines are needed anymore.

More recently a new type of structure has emerged: called 3-terminal MRAM, the memory is composed of a magnetic tunnel junction in which the storage layer is switched thanks to an in-plane current flowing through a metallic stripe. Different phenomena can be used for switching such as domain wall propagation or spin-orbit torques [Mir-10, Cub-14]. Even though this type of MRAM cannot be scaled down to very small dimensions, such a structure, with separated write and read paths, can be interesting in terms of circuit design, in particular in the field of ultrafast switching.

### I-3.2 What is Spin Transfer Torque?

The main idea behind the phenomenon of Spin Transfer Torque (STT) is that if the magnetization of a layer has the ability to polarize a current flowing through it, the reverse effect also exists. Thus, as a polarized current is injected in a magnetic layer, the spin of the electrons can act on the magnetization thanks to a torque and induce a precession that may be large enough to reverse its direction. The theory of spin transfer torque was developed in 1996 by J. C. Slonczewski [Slo-96] and L. Berger [Ber-96]. It relies on the idea that angular momentum should be conserved. If the spin polarization  $\vec{P}$  of the electrons that flow through the magnetic layer is not collinear to the magnetization  $\vec{M}$ , the electrons will start to be polarized along the magnetization direction. To conserve the angular momentum, a torque will appear as the electrons precess around the magnetization axis and tend to orient the magnetization along the initial polarization direction. This can be seen as a transfer of angular momentum between the electrons and the magnetization. The torque is expressed as:

$$\overrightarrow{\Gamma}_{STT} = a_j \vec{M} \times (\vec{M} \times \vec{P}) + b_j \vec{M} \times \vec{P}$$

where  $\vec{P}$  is the spin polarization of the current,  $\vec{M}$  the magnetization and  $a_j$  and  $b_j$  two coefficients.  $a_j$  depends on the current amplitude and its sign. The first term corresponds to the longitudinal component of the torque and is known as Slonczewski torque while the second term is orthogonal to the first one and is named field-like torque. This torque can then be injected in the Landau-Lifshitz-Gilbert (LLG) equation that describes the magnetization dynamics:

$$\frac{d\vec{M}}{dt} = -\gamma_0 \vec{M} \times \overrightarrow{H}_{eff} + \frac{\alpha}{M_s} \vec{M} \times \frac{d\vec{M}}{dt} + \overrightarrow{\Gamma}_{STT}$$

with  $H_{eff}$  the effective field (comprising the external applied field, the dipolar field and the anisotropy field),  $\gamma$  the gyromagnetic ratio,  $\alpha$  the Gilbert damping parameter and  $M_s$  the saturation magnetization.

The first term represents the precession of the magnetization around the effective field  $H_{eff}$ . The second one corresponds to the damping term that tends to put back the magnetization along the effective field direction. As the sign of  $a_j$  depends on the current direction, the STT component can then either strengthen the damping or act against it. If the STT has the same sign as the damping, the magnetization will be stabilized in its initial orientation. On the contrary, if they have opposite signs and the STT becomes greater than the damping term, then the magnetization will switch in the other direction. There is then a critical current density allowing the reversal of the magnetization:

$$j_c = \frac{2e}{\hbar} \frac{\alpha t M_s}{\eta(\theta)} H_{eff}$$

where  $e$  is the electron charge,  $\hbar$  the reduced Planck constant,  $\alpha$  the Gilbert damping parameter,  $M_s$  the saturation magnetization,  $t$  the magnetic thickness,  $\eta(\theta)$  a function that depends on the angle between the two magnetizations and the polarization, and  $H_{\text{eff}}$  the effective field.

The first experimental observations of STT switching were done with Co/Cu/Co spin-valves [Tso-98, Mye-99, Kat-00], only a few years after the theoretical predictions of J. C. Slonczewski and L. Berger. It could also be observed in magnetic tunnel junctions with low RA (Resistance-Area product) AlO<sub>x</sub> barrier [Hua-04]. In that study, a critical current density of  $8.10^6$  A/cm<sup>2</sup> was measured, with however low TMR between 1 and 20 %. More interestingly, spin torque-induced magnetization switching had been observed in MgO-based planar tunnel junctions [Kub-05, Kub-06, Hay-05, Dia-05]. Such devices exhibit critical current densities of a few MA/cm<sup>2</sup> and much larger TMR signals over 100 %.

### I-3.3 Interest of perpendicular anisotropy for STT-MRAM applications

In the first developments of STT-MRAM, work was essentially done on in-plane magnetized tunnel junctions as they were the most mastered devices at that time. Memory cells had then to be patterned into elliptical pillars in order to provide shape anisotropy to the system. This was used to increase the stability of the stored information but this anisotropy cannot be large enough to provide long lasting data retention. The thermal stability of a memory dot is characterized by a constant  $\Delta$  defined as  $\Delta = \frac{K_{\text{eff}}V}{k_B T}$ , where  $K_{\text{eff}}$  is the effective anisotropy constant, as defined previously,  $V$  the magnetic volume and  $T$  the temperature. To guaranty a data retention of 10 years, which is one of the requirements of the memory industry,  $\Delta$  must be greater than 50-60. It appears then that due to their large anisotropy constant, perpendicular MTJs are particularly promising compared to their in-plane counterparts.

Besides, in the case of out-of-plane magnetization, no elliptical shape is needed to stabilize the direction of the magnetization. This gives the opportunity to pattern the junctions in circular pillars which allows scaling down even further the memory elements. Larger storage capacities are then expected.

#### a) In-plane systems with reduced demagnetizing field

One first idea to improve the STT performances of planar magnetic tunnel junctions was to introduce some contribution of perpendicular anisotropy in the storage layer. As a matter of fact, in the case of in-plane magnetized layers, the energy barrier to overcome for STT switching is mostly related to the demagnetizing energy. To switch, the magnetization has to precess in the out-of-plane direction which is

facilitated when the perpendicular anisotropy component of the “still planar storage layer” is increased. Indeed, the additional perpendicular anisotropy counterbalances the demagnetizing field which leads to a decrease of its switching current density. This concept gave rise to several patents [[Ngu-04](#), [Rod-06](#)]. To increase the perpendicular anisotropy component, one can for example play with the thickness of the storage layer: as it gets thinner, the interfacial anisotropy component arising at the CoFeB/MgO interface becomes more and more important [[San-14](#)].

This design has been proved to be functional as it was used by Everspin in their 64 Mb STT-RAM product [[Riz-13](#)].

#### b) Fully perpendicular magnetic tunnel junctions

As the stacks of perpendicularly magnetized junctions were becoming more and more known and mastered, their properties regarding STT switching started to be tested. It appeared their advantages over planar systems are significant, in particular in terms of switching current density [[Wol-10](#), [Yod-10](#), [Hei-10](#)].

In the case of perpendicular structures, when introducing the thermal stability constant in the formula of the critical switching current density, one finds:

$$I_c = \frac{4e}{\hbar} \frac{\alpha k_B T}{\eta} \Delta$$

As we have seen previously, large stability factors are required to ensure a long data retention. However, at the same time,  $\Delta$  should be reduced if ones want to obtain low switching currents. A compromise must then be found.

It has been observed that the type of magnetization reversal depends on pillar diameter. Indeed for pillar sizes greater than 40 nm, the stability factor appears to remain almost constant as the magnetic volume increases [[Sat-11](#)]. This suggests that nucleation-propagation type of switching occurs, because in that case the dot size is larger than the domain wall width. At the same time, the intrinsic critical current  $I_{c0}$  (i.e. the current necessary to switch in 1 ns) was found to increase linearly with the cell area. It can seem then interesting to work at small dimensions. However, to maintain the stability against thermal fluctuations, the volume reduction has to be compensated by a larger perpendicular anisotropy  $K_{\text{eff}}$ .

Similarly, another important parameter playing a role in the STT efficiency is the Gilbert damping parameter  $\alpha$ . If one could consider materials such as Co/Pt (Pd) multilayers to bring large perpendicular anisotropy, their strong spin-orbit coupling leads to a large damping parameter. Besides, as we have shown in the previous part, this type of materials cannot yield large TMR signal if used as storage layers in MgO-based tunnel junctions due to bad growth conditions for the barrier. Some materials such as Co/Ni multilayers or some Heusler alloys have been found to exhibit perpendicular anisotropy and weak Gilbert damping. They do not provide however sufficiently high TMR signals to fulfill the requirements in terms of readability.

Luckily, the Ta/CoFeB/MgO systems present a relatively low damping parameter in addition to their good anisotropy properties. Nevertheless, the dependence of the damping parameter  $\alpha$  as a function of magnetic thickness works against STT efficiency. Indeed, as was shown by Ikeda *et al.* in 2010 on their Ta/CoFeB/MgO/CoFeB/Ta perpendicular MTJs (see Figure I-8), the damping parameter  $\alpha$  increases sharply as the electrode thickness decreases [Ike-10]. Thin layers are however needed to ensure a strong perpendicular anisotropy. Once again a compromise has to be made here.

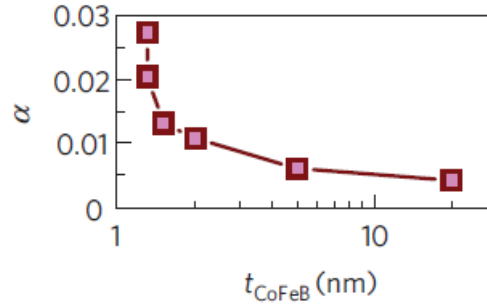


Figure I-8: Variation of damping parameter  $\alpha$  as a function of CoFeB thickness [Ike-10].

Some ferromagnetic resonance measurements showed that the damping parameter of perpendicularly magnetized CoFeB layers depends on the composition of the alloy. Lower values of  $\alpha$  are obtained for Fe-rich alloys than for Co-rich ones [Dev-13]. Along with a lower perpendicular anisotropy, the Co-rich alloys are then less interesting for STT applications.

Fully perpendicular magnetic tunnel junctions are thus particularly promising devices for STT-MRAM. They allow good data retention thanks to their large anisotropy and they provide lower switching current densities which make them competitive in the field of low power consumption. However, there exist some compromises to make between thermal stability and switching current, mostly adapting materials parameters and size of the nanopillars. For example, in 2010, IBM demonstrated the feasibility of a 4-kbit memory array with perpendicular MTJs exhibiting TMR of about 100 % (on full sheet samples, the signal dropping down to 70 % after patterning due to etching defects) and RA around  $10 \Omega\mu\text{m}^2$ . Structures were patterned into 80 nm circular pillars. Perpendicular anisotropy was found large enough to guaranty a stability factor  $\Delta > 50$  and a 0.008 damping parameter was measured. These good parameters allowed achieving a critical current density of about  $3 \text{ MA}\cdot\text{cm}^{-2}$ . Narrow switching distributions were measured which indicate a good reproducibility from junction to junction. No information was however given on the nature of the materials deposited in that study [Wor-10].

## I-4. Thin films deposition

All samples we used in this project were deposited by magnetron sputtering. This is a technique of physical vapor deposition that uses a plasma to accelerate ions towards a target made of the material one wants to deposit. Deposition is performed in a chamber under vacuum in order to ensure a good purity of the deposited materials (typically in the range of  $10^{-6}$  to  $10^{-9}$  mbar, depending on the performance of the tool). To create the plasma, an inert gas is employed, in our case argon. The target material is positioned at the cathode while the substrate is at the anode. By applying an electrical potential, a discharge appears and ionizes the argon atoms. The  $\text{Ar}^+$  ions are then accelerated towards the target. If their kinetic energy overcomes the binding energy of the target atoms, those atoms will be ejected and start to deposit themselves on the substrate.

In the case of magnetron sputtering, a magnet is installed at the cathode. The magnetic field modifies the trajectory of the electrons above the cathode leading to an increase in the number of collisions with the Ar atoms and then the number of  $\text{Ar}^+$  ions. This effect allows increasing the deposition rate. The principle of magnetron sputtering is illustrated in the schematic representation of Figure I-9.

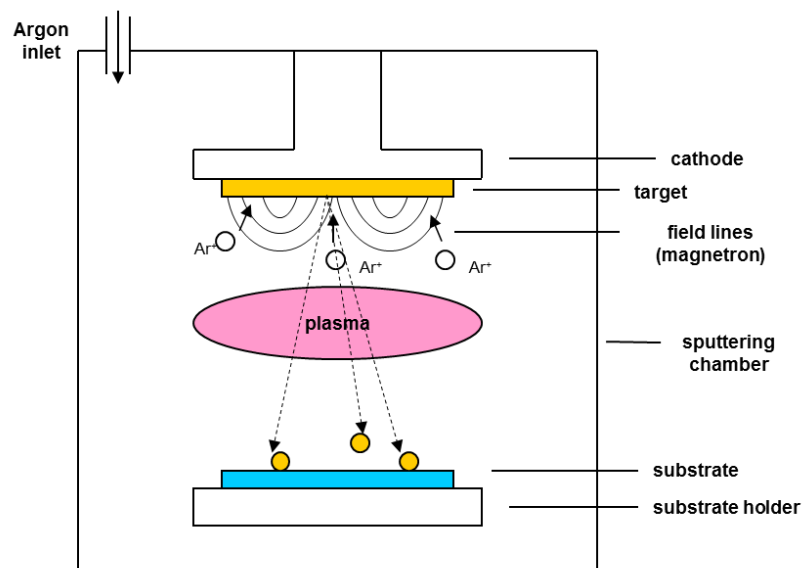


Figure I-9: Schematic representation of a sputtering chamber.

Our tool is an Actemium machine which possesses 12 targets that give us the opportunity to develop complex stacks involving a wide range of materials. Targets diameter is 125 mm which leads to a good homogeneity of the depositions on 100 mm wafers. This is also ensured by the rotation of the sample holder at  $600^\circ/\text{s}$  upon deposition. The whole deposition process is automated. Indeed, as shown in Figure I-10, our tool is equipped with a treatment chamber in which oxidation and etching

steps are taking place and a robot allows transferring the substrate from one chamber to the other as well as moving the substrate to place it in front of the chosen target. The deposited thicknesses are determined by the opening time of the shutter that covers the target. Deposition rates can be modulated by adjusting the current set point (typically between 60 and 350 mA), that is to say the power applied to the cathode. The Ar pressure in the chamber will also influence the deposition rate. In our system, it is set to  $2 \cdot 10^{-3}$  mbar. The rates are basically ranging between 0.03 nm/s and 0.2 nm/s, making it possible to deposit layers as thin as a few tenths of nanometer. In order to calibrate them properly, X-rays reflectivity is used. Regular calibrations are performed as aging of the targets will tend to reduce the deposition rates.

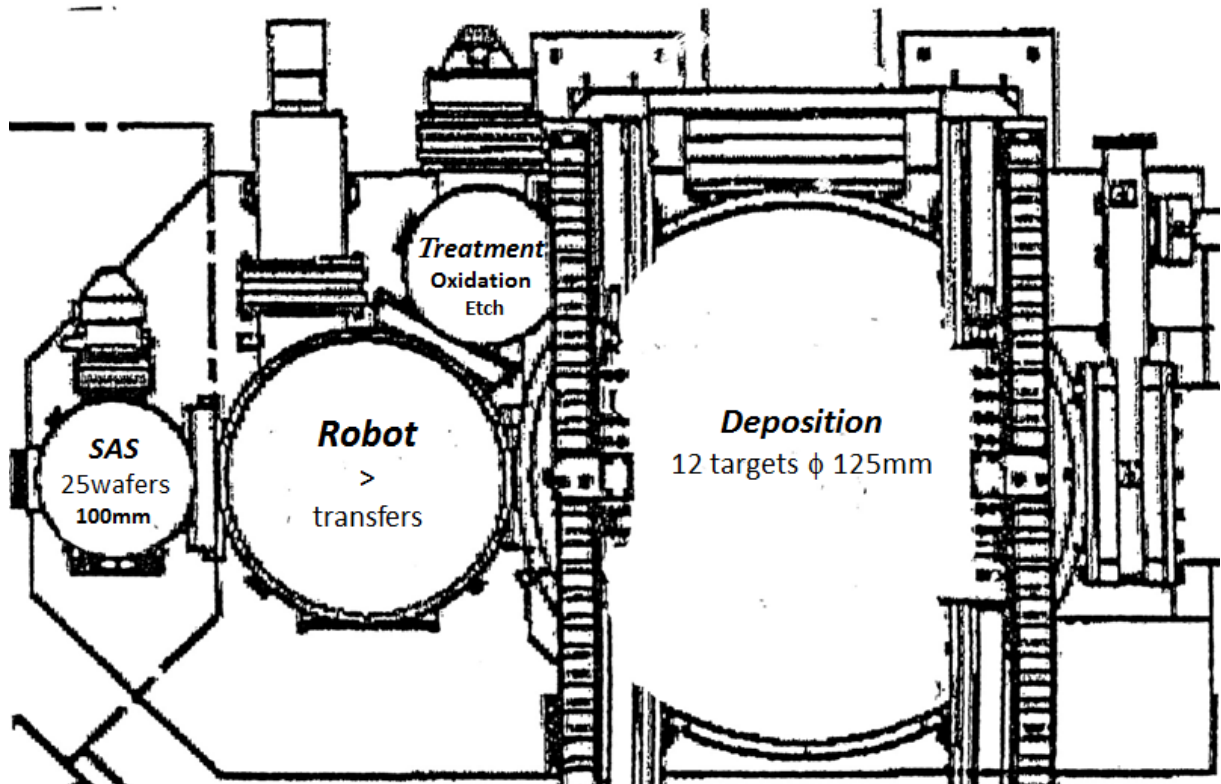


Figure I-10: Plan of the Actemium deposition tool showing the organization of the different chambers.

One interesting feature of our deposition machine is that we have the ability to create thickness gradients by shifting the substrate from the on-axis position. The two configurations are represented in Figure I-11. When the substrate is in the off-axis position and the sample holder is not rotated, a gradient of thickness appears in the deposited material. This wedge depends on the distance between the sample and the target. In the standard configuration, the distance amounts to 100 mm and allows a variation of about a factor 2 along the 100 mm wafer surface. The gradients are calibrated for each material, either by X-rays reflectivity or resistivity measurements.

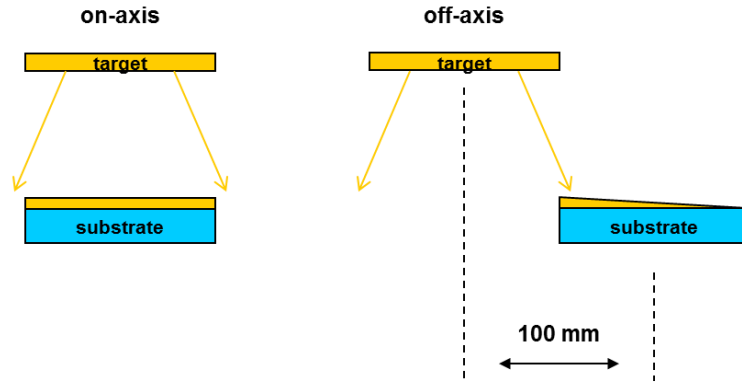


Figure I-11: Schematic representation of the two possible geometries in our deposition tool.

As we said earlier, our deposition tool is equipped with a treatment chamber in which oxidation steps can be performed. This is one way to create the oxide barriers of the tunnel junctions. In our studies, we used mostly MgO barriers obtained by natural oxidation of metallic Mg. A thin layer of Mg is deposited in the sputtering chamber and is then exposed to an oxygen atmosphere for a given time in the treatment chamber. Two procedures are employed depending on the RA levels that are targeted. For low RA (typically  $5-10 \Omega\mu\text{m}^2$ ), a dynamic oxidation is performed at a low oxygen pressure of  $3 \cdot 10^{-2}$  mbar, with a 100 sccm flow, for 360 s. For higher RA (typically  $25-50 \Omega\mu\text{m}^2$ ), a static oxidation is used in which the sample is exposed to a high oxygen pressure of 150 mbar for 10s. The tool is also able to perform plasma oxidations that utilize an oxygen plasma to oxidize a metallic element. This technique is more commonly applied to alumina barriers. Besides, we also have the possibility to deposit the oxide directly from a ceramic MgO target. In that case, a radiofrequency power supply is needed. A current of alternative polarity is applied to the target, avoiding the accumulation of charges that would otherwise strongly decrease the deposition rate of the material.

## I-5. Characterisation techniques

### I-5.1 Magnetic characterization

#### a) Vibrating Sample Magnetometry

Vibrating Sample Magnetometry is a tool used to characterize the magnetic properties of a sample. It allows measuring the variation of the magnetic moment as a function of applied field, thus enabling to plot its hysteresis loop. To do this, the sample is fixed to a sample holder located in the gap of an electromagnet. It is then translated vertically at a given frequency. This vibration induces a change of magnetic flux related to the magnetic moment of the sample that is transformed into a current in the detection coils. A schematic representation is given in Figure I-12.

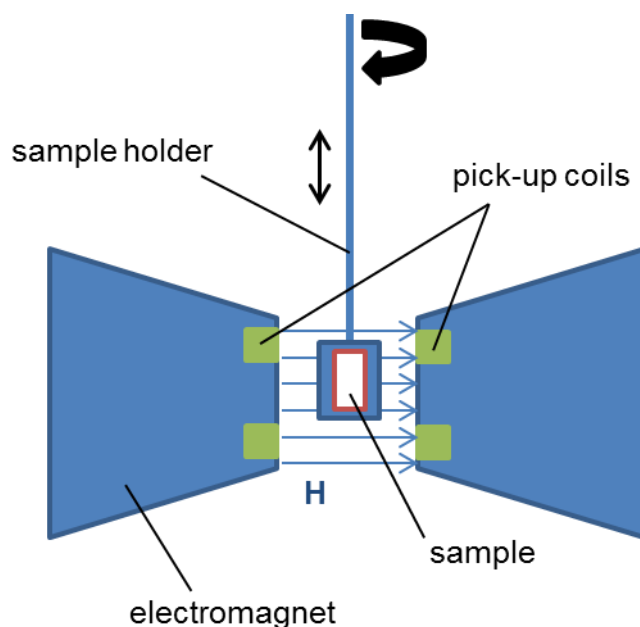


Figure I-12: Working principle of a VSM.

The advantage of this technique is that it is rather accurate (around  $10^{-5}$  emu) and that magnetic field can be applied along any direction of the sample by setting the measurement angle. This is a convenient and rapid way to evaluate the anisotropy of a sample as both easy and hard axis loops can be performed. With our tool, magnetic fields as high as 17 kOe may be reached. One should note that the sample holder adds a contribution to the measured signal. Most of the time, it can be easily removed as it varies linearly with field (diamagnetic or paramagnetic holder). However, in the case of a sample presenting a very large saturation field, the slope might be difficult to determine.

In order to show the limitations of a VSM tool and establish the samples preparation procedure we deposited a 50 nm thick NiFe layer on a 3x10 mm substrate previously cut. This implies that the edges of the substrate are perfectly flat. The edges along the smallest dimension are covered with Kapton in order to fix the substrate on the sample holder which means that only the top surface and the longest edges are exposed during deposition. The sample is then measured in the VSM in two different configurations: planar field along the largest dimension (longitudinal measurement) and planar field along the smallest dimension (transverse measurement). The results are gathered in Figure I-13, where only half loops coming from positive fields saturation are presented.

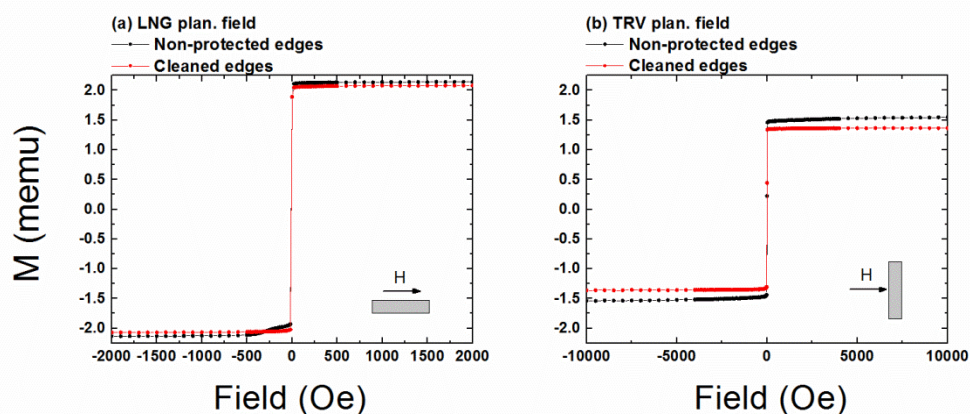


Figure I-13: Magnetic loops of a 50 nm NiFe sample measured by VSM in different configurations (a) longitudinal planar field (b) transverse planar field, before and after cleaning of the edges.

It appears that there is a difference in signal amplitude depending on the orientation of the sample in the gap of the electromagnet. The total signal is much smaller in the transverse measurement as the sample is in this case further away from the pick-up coils compared to the longitudinal configuration. Note that the tool calibration, both in sensitivity and sample holder position, is generally done with a Ni test sample which exhibits a magnetization of a few emu, much larger than the expected value on our samples. However, precise centering of the sample holder cannot be performed with the calibration menu using our samples as the holder signal is too large in comparison. Thus, all these effects prevent us from getting any absolute value of the magnetization of our samples, even though their size is reduced to limit the influence of the geometry. This is the reason why, when trying to extract any numerical value from VSM measurements, we will use an internal reference (that is to say a layer with known magnetization included in the stack). More detailed information on this data treatment technique will be given in Chapter II.

Another part of the experiment consisted in cleaning the edges of the sample to see the effect of removing the magnetic materials located there. As can be seen in Figure I-13 (a), when the field is applied along the long dimension of the sample, cleaning the edges allows removing the magnetic signal present between 0 and -500

Oe. In the case of a transverse configuration, a hard signal that saturates at about 5000 Oe is present in the sample with unprotected edges and it disappears after the cleaning step (see Figure I-13 (b)). These two parasitic signals can be then attributed to a magnetic contribution from the edges. Indeed, the longitudinal configuration corresponds to applying a magnetic field in the plane of the edges whereas in the transverse configuration, the field is applied perpendicularly to the edges which now corresponds to a hard axis configuration. In both cases, the amplitude of this extra signal represents about 5 % of the total signal. Knowing that the ratio of surfaces between the edges and the front face is 33 %, we can estimate the thickness deposited on the edges to represent about 15 % of the total deposited thickness, that is to say about 7 nm. Note that this estimation would not be possible in the case of cleaved samples as the edges geometry is unpredictable.

The case of a 3x10 mm substrate is obviously one of the most unfavorable situations as the surface of the edges is particularly large compared to the total surface. However, we also observed this effect in a standard perpendicular junction with a bottom SAF reference and a top 1.4 nm thick FeCoB storage layer. The deposition was made on 2 square substrates, one with non-protected edges and the other one with edges covered with Kapton. The corresponding magnetic curves measured by VSM with perpendicular applied field are shown in Figure I-14, with focus on the minor loop on the storage layer. Similarly a parasitic signal that saturates around 500 Oe appears when the edges are not covered. It is not present in the case of protected edges.

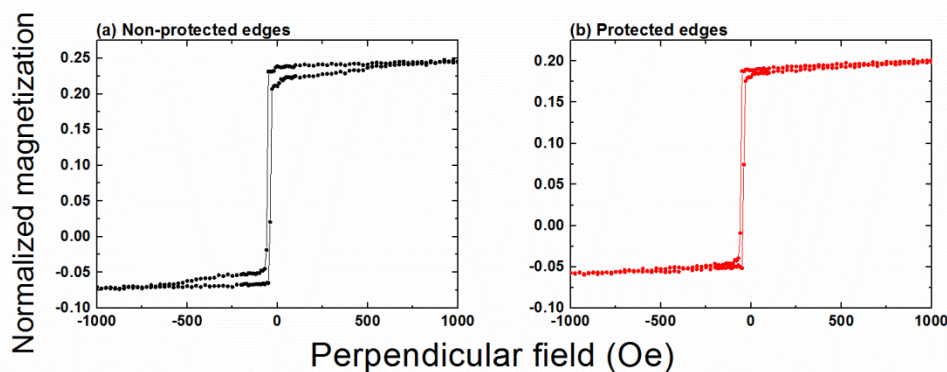


Figure I-14: Magnetic loops measured by VSM with perpendicular applied field on standard magnetic tunnel junctions with (a) non-protected or (b) protected edges.

An ideal solution to get clean measurements could be to deposit the stack on full 100 mm wafers and then cut small pieces of determined size after putting a protective resist. Circular shapes would be the best to reduce the geometry effects. However, this procedure would be extremely time-consuming and would considerably slow down the developments. For this reason, we decided to work with about 12x12 mm cleaved squares which edges are covered with Kapton before deposition.

## b) Extraordinary (or anomalous) Hall Effect

Another way to characterize the magnetic properties of a sample is to take advantage of the extraordinary Hall Effect that arises in magnetic materials.

The Hall Effect is due to the Lorentz force that affects the electrons when an electrical current passes through a material submitted to a magnetic field that is perpendicular to the current direction. This force deflects the electrons and a voltage, known as Hall voltage, appears in the direction perpendicular to both current and magnetic field.

In the case of ferromagnetic materials, an additional component, which is proportional to the magnetization, exists and is called extraordinary or anomalous Hall Effect. The Hall resistance that will be then measured by the set-up can be expressed as:

$$R_H = R_o B + R_E M_z$$

where  $R_o$  is the ordinary Hall Effect coefficient,  $R_E$  the extraordinary Hall Effect coefficient,  $B$  the magnetic induction and  $M_z$  the out-of-plane component of the magnetization. This technique is particularly well adapted to study samples with perpendicular anisotropy as it is only sensitive to the out-of-plane component of the magnetization. It is also possible to perform planar measurements where magnetic field is applied in the film plane. The in-plane component of magnetization is then deduced from its perpendicular projection ( $M_x^2=1-M_z^2$ ).

In general, the ordinary Hall Effect is negligible in magnetic materials compared to the extraordinary one. The factor between the respective coefficients can be as high as 100. Thus, the ordinary contribution appears as a linear slope that can be easily subtracted from the total signal.

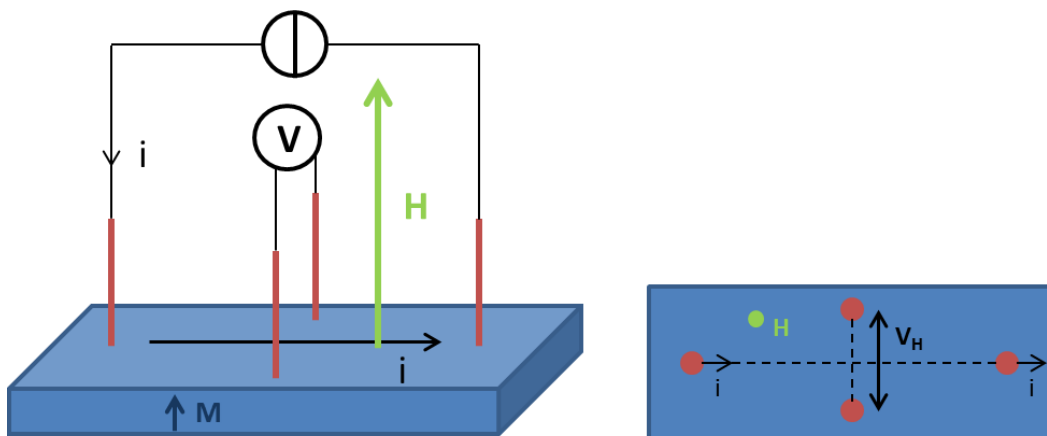


Figure I-15: Schematic representation of the configuration of the probes in an Extraordinary Hall Effect measurement set-up.

As shown in Figure I-15, the measurement is done using a Van der Pauw configuration, in which the current is injected through probes that are perpendicularly oriented to those employed to determine the Hall voltage.

It is worth noting that a Hall Effect measurement does not allow getting the numerical value of magnetization. The Hall signal is only proportional to it and depends a lot on the thicknesses of the other layers involved in the stack. Indeed, a variable part of the current will be derived in the metallic buffer and capping layers, reducing the final Hall amplitude. This method is however practical to compare similar samples and gives precise values of the transition fields.

In our laboratory set-up, magnetic fields as large as 17.5 kOe may be applied.

### **I-5.2 Characterization of the transport properties (Current In-Plane Tunneling)**

When studying magnetic tunnel junctions, the tunnel magnetoresistance (TMR) and Resistance.Area (RA) product are particularly important parameters to control. One procedure to evaluate them consists in fabricating pillars with nanometric size, in which a current is applied perpendicularly to the plane of the tunnel barrier. To do this, many steps such as etching, lithography, metallic contact depositions, etc. are necessary, as we will see in Chapter V. These techniques are time-consuming and may modify the magnetic properties of the tunnel junctions by introducing defects.

This is the reason why a measurement technique that is directly applicable to non-patterned tunnel junctions has been developed in 2003 by D. C. Worledge and P. L. Trouilloud at IBM laboratories [[Wor-03](#)]. Named Current In-Plane Tunneling (CIPT), this method allows working with macroscopic samples.

The method relies on a 4-point resistance measurement with aligned probes and different spacings. Current is injected in the external probes while the voltage is measured with the internal ones. Spacing  $x$  between contacts is varied, using multiprobes heads. Resistance measurements are performed for increasing values of probe spacing in both parallel and antiparallel configuration of the magnetizations. For very small values of  $x$ , current flows only in the top electrode, enabling to get the value of its sheet resistance  $R_T$  as shown in Figure I-16. For large values of  $x$ , the barrier resistance becomes negligible and one can extract the resistance of the combination of the bottom and top electrodes resistances in parallel. For each spacing the magnetoresistance  $MR_{cip}$  is calculated using the values of resistance in the parallel ( $R_{low}$ ) and antiparallel ( $R_{high}$ ) configuration:  $MR_{cip}=(R_{high}-R_{low})/R_{low}$ .

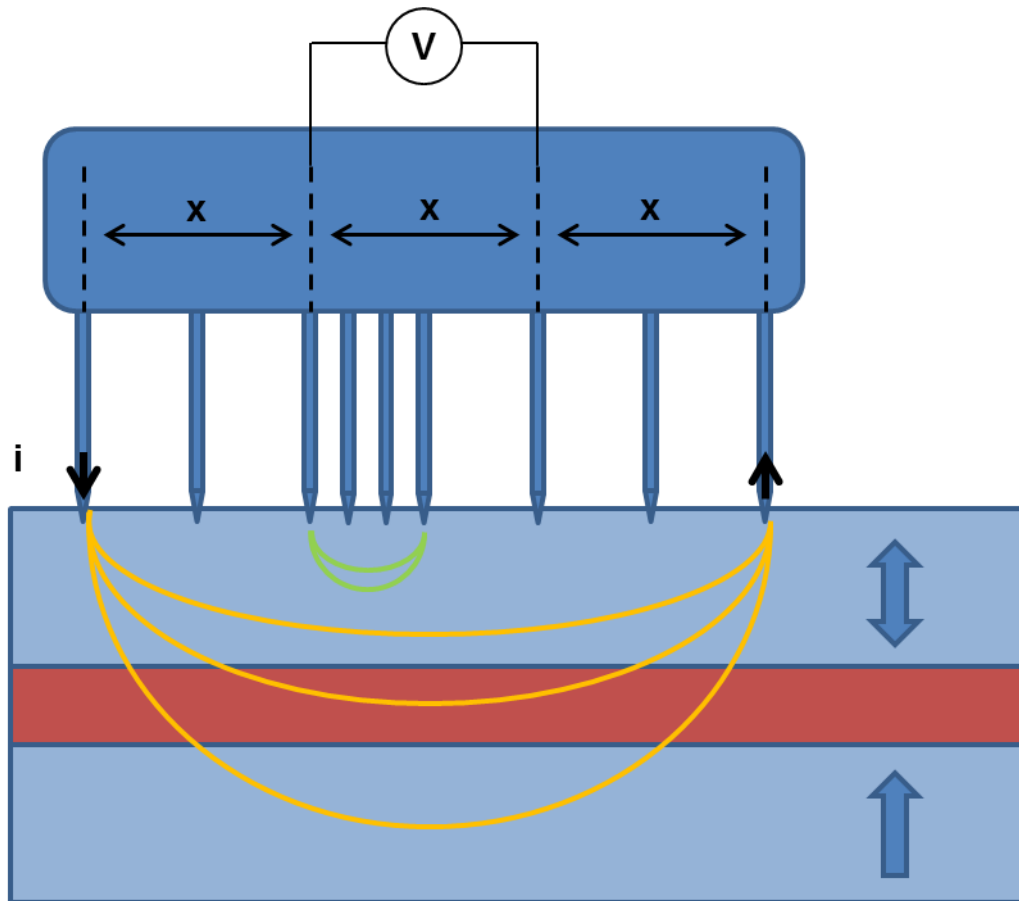


Figure I-16: Schematic representation of the CIPT technique.

The RA and TMR, as well as  $R_T$  and  $R_B$ , are then estimated using a model that realizes fitting of the resistance vs probe distance and  $MR_{cip}$  vs probe distance curves. The ideal fitting conditions have been found to be obtained when the probe distance ranges between  $\lambda$  and  $5\lambda$ , where  $\lambda$  is a length scale that depends on the sample parameters,  $\lambda = \sqrt{\frac{RA}{R_T + R_B}}$ . Thus depending on the RA of the sample, one should select among the different measurement heads with varying probe configurations the one that suits the best. This is not necessarily straightforward as the RA of the measured sample might not be known before the measurement. It is only when the parameters  $R_T$ ,  $R_B$  and  $x$  are well adapted to the barrier properties that a maximum will clearly appear in the  $MR_{cip}$  vs probe distance curve, as shown in the example of Figure I-17. This guaranties a good reliability of the fitted RA and TMR parameters.

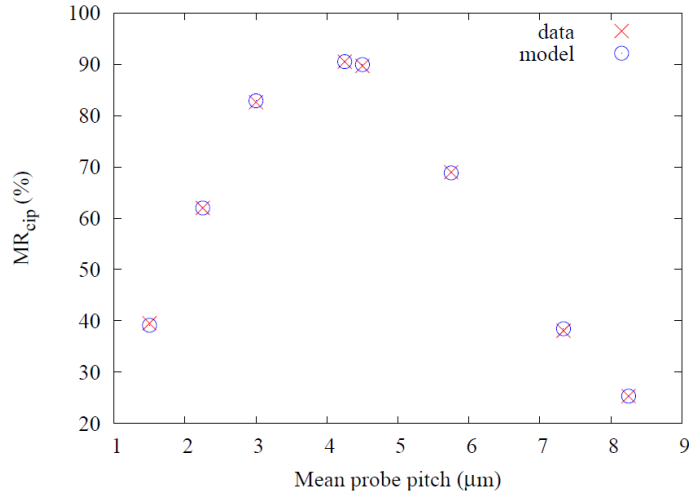


Figure I-17: Example of the evolution of the  $MR_{cip}$  as a function of the probe distance for a standard planar junction. The curve includes both the experimental data points and the fit of the CIPT tool.

Similarly, there exist some conditions on  $R_T$  and  $R_B$  to get a good fit. Indeed,  $R_T$  has to be higher than  $R_B$  in order to force the current to flow in the entire structure through the barrier. A ratio of 5 is sufficient to ensure good results. To obtain a low  $R_B$ , our samples are deposited on 60 nm thick CuN buffer layers. The advantage of CuN, apart from its good electrical conductivity, is that compared to Cu, it exhibits a lower surface roughness. The value of  $R_T$  is adjusted by depositing a ruthenium capping layer on top of the magnetic stack. This Ru layer provides a hard surface for the mechanic contacts of the probes (preventing them to go through the barrier) and good electrical contact is guaranteed as Ru oxide is a conductive material. In order to avoid chemical contamination of the surface, the Ru deposition is performed after the annealing step and is preceded by a surface etching.

During this thesis, CIPT measurements have been performed on a Capres tool at Crocus Technology, Grenoble. This tool gives us the possibility to characterize both planar and perpendicular systems. In the planar configuration, resistance vs field loops can be measured, enabling the user to determine the fields to apply to switch between the parallel and antiparallel states. The maximum field available is in that case 250 Oe. In the perpendicular configuration resistance vs field loops cannot be measured. Transition fields have then to be checked before the measurement, either by VSM or Extraordinary Hall Effect. Note that the presence of a CuN buffer prevents from doing Hall measurements as this layer would derive too much current. If necessary, depositions can be performed on two types of substrate: CuN and  $SiO_2$ . The perpendicular Capres set-up allows applying perpendicular fields as high as 1500 Oe.

## **I-6. Annealing procedure**

As we have seen previously, the TMR signal of a magnetic tunnel junction depends greatly on the crystallization state of the CoFeB electrodes [Yua-05, Cho-07]. In the case of perpendicularly-magnetized systems, perpendicular anisotropy as well as TMR amplitude have been found to show relatively the same trends as a function of annealing temperature [Gan-11, Men-11, Wan-11, Nat-13]. They present first an improvement with increasing the annealing temperature followed by a decay due to a degradation of the magnetic properties. The optimal temperature is generally found around 300-350 °C. Note that the choice of the annealing temperature of our samples will be described in more details in Chapter II.

In our laboratory, two furnaces can be used to anneal samples under vacuum (typically at a pressure around  $10^{-6}$  mbar). A larger one exhibits a 200 mm capacity while the small one can only hold samples with sizes up to 15x60 mm. However, due to its reduced volume, the small set-up allows reaching annealing cycles of about 2 h in total (including heating and cooling ramps) instead of a full day in the large structure. The latter one will be thus chosen only when large surfaces are needed (wafers for the nanofabrication for example), while the small furnace will be favored for “every day” materials development. The large furnace possesses a permanent magnet with a 2.3 kOe planar field that cannot be removed. In the case of the small one, the permanent magnet can be removed or put in perpendicular or planar configurations. It is known that, for planar magnetic tunnel junctions that comprise an exchange bias pinned reference layer, a magnetic field is required during annealing in order to set the exchange direction. As this is not the case in perpendicular junctions, we will first check the effect of applying a field during annealing on the magnetic properties of samples with perpendicular anisotropy.

### **I-6.1 Effect of the presence of a magnetic field during annealing**

In the case of perpendicularly magnetized materials, there are usually two types of situations encountered in the literature: either a perpendicular magnetic field is applied during annealing or no magnetic field at all is present. To check the effect of putting a magnetic field during the annealing step we deposited a top electrode with the following composition: MgO/CoFeB<sub>1.5</sub>/Ta<sub>0.3</sub>/Co<sub>0.3</sub>/(Pd<sub>1.2</sub>/Co<sub>0.3</sub>)<sub>4</sub>/Pd<sub>2</sub>. Three different field configurations for the annealing have been used:

- No field
- In-plane field of 2.3 kOe
- Perpendicular field of 2.3 kOe

The annealing was performed in the small furnace at a temperature of 300°C, with a duration of 1 h, which is the standard time used in the laboratory with this set-up. The time given here corresponds to the duration at which the set temperature is maintained and does not include the heating and cooling ramps (60 °C/min and about 10 °C/min, respectively). The magnetic properties of the electrode measured by Extraordinary Hall Effect are shown in Figure I-18.

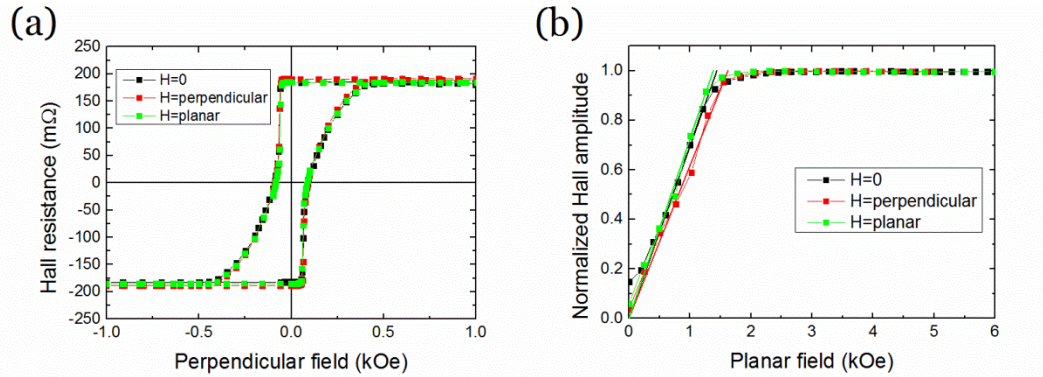


Figure I-18: Extraordinary Hall Effect loops measured on a top electrode with (a) perpendicular applied field and (b) in-plane field for varying configurations of the magnetic field during annealing. In (b), only half of the loop is shown and the signal is normalized to its maximal amplitude.

It appears that the presence of a magnetic field during annealing has a negligible effect on the magnetic properties of perpendicular electrodes. Whatever the configuration, the magnetic curves are almost identical. For the following studies done during this thesis, no field will be applied when using the small furnace.

This study also confirms that the presence of a planar field in the larger set-up will not be detrimental to the properties of our samples.

## I-6.2 Set-up equivalence

As we have said at the beginning, we have access to two different furnaces and using the largest one is necessary if we want to work with large samples such as full wafers. We have seen that the permanent in-plane field that is present in this furnace will not modify the properties of the perpendicularly magnetized layers.

The equivalence between the two apparatus has been then determined using magnetic and transport properties. It appeared that annealing conditions of 300 °C for 1 hour in the small furnace give equivalent properties as 250 °C for 1h30 in the large furnace.

Note that in the large set-up, the set time is longer. This is to minimize the parts played by the heating and mostly the cooling ramps that take much more time with this furnace compared to the small one (around 10 °C/min and 0.5 °C/min, respectively with the large set-up).

## **I-7. Conclusions**

We have seen that mastering the magnetic and transport properties of perpendicular magnetic tunnel junctions is not straightforward and requires a good knowledge of the deposited materials. There exists however a strong interest for those structures as they give the opportunity to create particularly efficient memories. This is what motivated the works of this thesis.

In the following of this manuscript, we will see that starting from a relatively standard structure, with a Co/Pt-based reference and a top storage layer, we can enhance its properties by tuning the stack parameters and that we can also go towards even more complex designs.

## I-8. References

[Bai-88] M. N. Baibich, J.-M. Broto, A. Fert, F. Nguyen Van Dau, F. Petroff, P. Etienne, G. Creuzet, A. Friederich, and J. Chazelas, *Giant magnetoresistance of (001)Fe/(001)Cr magnetic superlattices*, [Phys. Rev. Lett.](#) **61**, 2472-2475 (1988).

[Ber-96] L. Berger, *Emission of spin waves by a magnetic multilayer traversed by a current*, [Phys. Rev. B](#) **54**, 9353-9358 (1996).

[Bin-89] G. Binasch, P. Grünberg, F. Saurenbach, and W. Zinn, *Enhanced magnetoresistance in layered magnetic structures with antiferromagnetic interlayer exchange*, [Phys. Rev. B](#) **39**, 4828-4830 (1989).

[Bow-01] M. Bowen, V. Cros, F. Petroff, A. Fert, C. Martinez Boubeta, J. L. Costa-Kramer, J. V. Anguita, A. Cebollada, F. Briones, J. M. de Teresa, L. Morellon, M. R. Ibarra, F. Guell, F. Peiro, and A. Cornet, *Large magnetoresistance in Fe/MgO/FeCo(001) epitaxial tunnel junctions on GaAs(001)*, [Appl. Phys. Lett.](#) **79**, 1655-1657 (2001).

[Bru-89] P. Bruno, *Tight-binding approach to the orbital magnetic moment and magnetocrystalline anisotropy of transition-metal monolayers*, [Phys. Rev. B](#) **39**, 865-868 (1989).

[But-01] W. H. Butler, X. -G. Zhang, T. C. Schulthess, and J. M. MacLaren, *Spin-dependent tunneling conductance of Fe|MgO|Fe sandwiches*, [Phys. Rev. B](#) **63**, 092402 (2001).

[Cho-07] Y. S. Choi, K. Tsunekawa, Y. Nagamine, and D. Djayaprawira, *Transmission electron microscopy study on the polycrystalline CoFeBMgOCoFeB based magnetic tunnel junction showing a high tunneling magnetoresistance, predicted in single crystal magnetic tunnel junction*, [J. Appl. Phys.](#) **101**, 013907 (2007).

[Cub-14] M. Cubukcu, O. Boule, M. Drouard, K. Garello, C. O. Avci, I. M. Miron, J. Langer, B. Ocker, P. Gambardella, and G. Gaudin, *Spin-orbit torque magnetization switching of a three-terminal perpendicular magnetic tunnel junction*, [Appl. Phys. Lett.](#) **104**, 042406 (2014).

[Daa-94] G. H. O. Daalderop, P. J. Kelly, and M. F. H. Schuurmans, *Magnetic anisotropy of a free-standing Co monolayer and of multilayers which contain Co monolayers*, [Phys. Rev. B](#) **50**, 9989-10003 (1994).

[Dev-13] T. Devolder, P.-H. Ducrot, J.-P. Adam, I. Barisic, N. Vernier, Joo-Von Kim, B. Ockert, and D. Ravelosona, *Damping of  $Co_x Fe_{80-x}B_{20}$  ultrathin films with perpendicular magnetic anisotropy*, [Appl. Phys. Lett.](#) **102**, 022407 (2013).

[Dia-05] Z. Diao, D. Apalkov, M. Pakala, Y. Ding, A. Panchula, and Y. Huaia, *Spin transfer switching and spin polarization in magnetic tunnel junctions with MgO and AlO<sub>x</sub> barriers*, [Appl. Phys. Lett.](#) **87**, 232502 (2005).

[Die-91] B. Dieny, V. S. Speriosu, S. S. P. Parkin, B. A. Gurney, D. R. Wilhoit, and D. Mauri, *Giant magnetoresistive effect in soft ferromagnetic multilayers*, [Phys. Rev. B](#) **43**, 1297-1300 (1991).

[Die-01] B. Dieny, and O. Redon, *Magnetic device with magnetic tunnel junction, memory array and read/write methods using same*, [U. S. Patent 6950335 \(B2\)](#), Jan. 06 2001.

[Die-15] B. Dieny, and M. Chshiev, *Perpendicular-to-plane magnetic anisotropy at magnetic transition metal/oxide interfaces and its applications*, submitted to Rev. Mod. Phys. (2015).

[Dja-05] D. D. Djayaprawira, K. Tsunekawa, M. Nagai, H. Maehara, S. Magamata, N. Watanabe, S. Yuasa, Y. Suzuki, and K. Ando, *230% room-temperature magnetoresistance in CoFeB/MgO/CoFeB magnetic tunnel junctions*, [Appl. Phys. Lett.](#) **86**, 092502 (2005).

[Gan-11] H. D. Gan, H. Sato, M. Yamanouchi, S. Ikeda, K. Miura, R. Koizumi, F. Matsukura, and H. Ohno, *Origin of the collapse of tunnel magnetoresistance at high annealing temperature in CoFeB/MgO perpendicular magnetic tunnel junctions*, [Appl. Phys. Lett.](#) **99**, 252507 (2011).

[Geh-97] V. Gehanno, A. Marty, B. Gilles, and Y. Samson, *Magnetic domains in epitaxial ordered FePd(001) thin films with perpendicular magnetic anisotropy*, [Phys. Rev. B](#) **55**, 12552-12555 (1997).

[Gui-75] T. R. McGuire, and R. I. Potter, *Anisotropic magnetoresistance in ferromagnetic 3d alloys*, [IEEE Trans. Magn.](#) **11**, 1018-1038 (1975).

[Hay-05] J. Hayakawa, S. Ikeda, Y. M. Lee, R. Sasaki, T. Meguro, F. Matsukura, H. Takahashi, and H. Ohno, *Current-driven magnetization switching in CoFeB/MgO/CoFeB magnetic tunnel junctions*, [Jpn. J. Appl. Phys.](#) **44**, L 1267-L 1270 (2005).

[Hei-10] O. G. Heinonen, and D. V. Dimitrov, *Switching-current reduction in perpendicular anisotropy spin torque magnetic tunnel junctions*, [J. Appl. Phys.](#) **108**, 014305 (2010).

[Hua-04] Y. Huai, F. Albert, P. Nguyen, M. Pakala, and T. Valet, *Observation of spin-transfer switching in deep submicron-sized and low-resistance magnetic tunnel junctions*, [Appl. Phys. Lett.](#) **84**, 3118 (2004).

[Ike-08] S. Ikeda, J. Hayakawa, Y. Ashizawa, Y. M. Lee, K. Miura, H. Hasegawa, M. Tsunoda, F. Matsukura, and H. Ohno, *Tunnel magnetoresistance of 604% at 300*

*K* by suppression of Ta diffusion in CoFeB/MgO/CoFeB pseudo-spin-valves annealed at high temperature, [Appl. Phys. Lett.](#) **93**, 082508 (2008).

[Ike-10] S. Ikeda, K. Miura, H. Yamamoto, K. Mizunuma, H. D. Gan, M. Endo, S. Kanai, J. Hayakawa, F. Matsukura, and H. Ohno, *A perpendicular-anisotropy CoFeB–MgO magnetic tunnel junction*, [Nature Mater.](#) **9**, 721-724 (2010).

[Joh-95] M. T. Johnson, R. Jungblut, P. J. Kelly, and F. J. A. den Broeder, *Perpendicular magnetic anisotropy of multilayers: recent insights*, [J. Magn. Magn. Mater.](#) **148**, 118-124 (1995).

[Joh-96] M. T. Johnson, P. J. H. Bloemen, F. J. A. den Broeder, and J. J. de Vries, *Magnetic anisotropy in metallic multilayers*, [Rep. Prog. Phys.](#) **59**, 1409-1458 (1996).

[Jul-75] M. Jullière, *Tunneling between ferromagnetic films*, [Phys. Lett.](#) **54A**, 225-226 (1975).

[Kat-00] J. A. Katine, F. J. Albert, R. A. Buhrman, E. B. Myers, and D. C. Ralph, *Current-driven magnetization reversal and spin-wave excitations in Co/Cu/Co pillars*, [Phys. Rev. Lett.](#) **84**, 3149 (2000).

[Koz-10] X. Kozina, S. Ouardi, B. Balke, G. Stryganyuk, G. H. Fecher, C. Felser, S. Ikeda, H. Ohno, and E. Ikenaga, *A nondestructive analysis of the B diffusion in Ta–CoFeB–MgO–CoFeB–Ta magnetic tunnel junctions by hard X-ray photoemission*, [Appl. Phys. Lett.](#) **96**, 072105 (2010).

[Kub-05] H. Kubota, A. Fukushima, Y. Ootani, S. Yuasa, K. Ando, H. Maehara, K. Tsunekawa, D. D. Djayaprawira, N. Watanabe, and Y. Suzuki, *Magnetization switching by spin-polarized current in low-resistance magnetic tunnel junction with MgO (001) barrier*, [IEEE Trans. Magn.](#) **41**, 2633-2635 (2005).

[Kub-06] H. Kubota, A. Fukushima, Y. Ootani, S. Yuasa, K. Ando, H. Maehara, K. Tsunekawa, D. D. Djayaprawira, N. Watanabe, and Y. Suzuki, *Dependence of spin-transfer switching current on free layer thickness in Co–Fe–BMgO/Co–Fe–B magnetic tunnel junctions*, [Appl. Phys. Lett.](#) **89**, 032505 (2006).

[Kub-12] H. Kubota, S. Ishibashi, T. Saruya, T. Nozaki, A. Fukushima, K. Yakushiji, K. Ando, Y. Suzuki, and S. Yuasa, *Enhancement of perpendicular magnetic anisotropy in FeB free layers using a thin MgO cap layer*, [J. Appl. Phys.](#) **111**, 07C723 (2012).

[Lam-13] D. D. Lam, F. Bonell, S. Miwa, Y. Shiota, K. Yakushiji, H. Kubota, T. Nozaki, A. Fukushima, S. Yuasa, and Y. Suzuki, *Composition dependence of perpendicular magnetic anisotropy in Ta/Co<sub>x</sub>Fe<sub>80-x</sub>B<sub>20</sub>/MgO/Ta ( $x=0, 10, 60$ ) multilayers*, [J. Magn.](#) **18**, 5-8 (2013).

[Lee-07] Y. M. Lee, J. Hayakawa, S. Ikeda, F. Matsukura, and H. Ohno, *Effect of electrode composition on the tunnel magnetoresistance of pseudo-spin-valve*

magnetic tunnel junction with a MgO tunnel barrier, [Appl. Phys. Lett.](#) **90**, 212507 (2007).

[Liu-12] T. Liu, J. W. Cai, and L. Sun, *Large enhanced perpendicular magnetic anisotropy in CoFeB/MgO system with the typical Ta buffer replaced by an Hf layer*, [AIP Advances](#) **2**, 032151 (2012).

[Liu-14] T. Liu, Y. Zhang, J. W. Cai, and H. Y. Pan, *Thermally robust Mo/CoFeB/MgO trilayers with strong perpendicular magnetic anisotropy*, [Sci. Rep.](#) **4**, 5895 (2014).

[Man-08] A. Manchon, C. Ducruet, L. Lombard, S. Auffret, B. Rodmacq, B. Dieny, S. Pizzini, J. Vogel, V. Uhlir, M. Hochstrasser, and G. Panaccione, *Analysis of oxygen-induced anisotropy crossover in Pt/Co/MO<sub>x</sub> trilayers*, [J. Appl. Phys.](#) **104**, 043914 (2008).

[Mat-01] J. Mathon, and A. Umerski, *Theory of tunneling magnetoresistance of an epitaxial Fe/MgO/Fe(001) junction*, [Phys. Rev. B](#) **63**, 220403(R) (2001).

[Men-11] H. Meng, R. Sbiaa, C. C. Wang, S. Y. H. Lua, and M. A. K. Akhtar, *Annealing temperature window for tunneling magnetoresistance and spin torque switching in CoFeB/MgO/CoFeB perpendicular magnetic tunnel junctions*, [J. Appl. Phys.](#) **110**, 103915 (2011).

[Mir-10] I. M. Miron, G. Gaudin, S. Auffret, B. Rodmacq, A. Schuhl, S. Pizzini, J. Vogel, and P. Gambardella, *Current-driven spin torque induced by the Rashba effect in a ferromagnetic metal layer*, [Nature Mater.](#) **9**, 230-234 (2010).

[Miy-95] T. Miyazaki., and N. Tezuka, *Giant magnetic tunneling effect in Fe/Al<sub>2</sub>O<sub>3</sub>/Fe junction*, [J. Magn. Magn. Mater.](#) **139**, L231-L234 (1995).

[Miz-11] K. Mizunuma, M. Yamanouchi, S. Ikeda, H. Sato, H. Yamamoto, H.-D. Gan, K. Miura, J. Hayakawa, F. Matsukura, and H. Ohno, *Pd layer thickness dependence of tunnel magnetoresistance properties in CoFeB/MgO-based magnetic tunnel junctions with perpendicular anisotropy CoFe/Pd multilayers*, [Appl. Phys. Expr.](#) **4**, 023002 (2011).

[Mon-02] S. Monso, B. Rodmacq, S. Auffret, G. Casali, F. Fettar, B. Gilles, B. Dieny, and P. Boyer, *Crossover from in-plane to perpendicular anisotropy in Pt/CoFe/AlO<sub>x</sub> sandwiches as a function of Al oxidation: A very accurate control of the oxidation of tunnel barriers*, [Appl. Phys. Lett.](#) **80**, 4157-4159 (2002).

[Moo-95] J.S. Moodera, L. R. Kinder, T. M. Wong, and R. Meservey, *Large magnetoresistance at room temperature in ferromagnetic thin film tunnel junctions*, [Phys. Rev. Lett.](#) **74**, 3273 (1995).

[Mot-36] N. F. Mott, *The resistance and thermoelectric properties of the Transition Metals*, [Proc. Roy. Soc. London](#) **156**, 368-382 (1936).

[Mye-99] E. B. Myers, D. C. Ralph, J. A. Katine, R. N. Louie, and R. A. Buhrman, *Current-induced switching of domains in magnetic multilayer devices*, [\*Science\* \*\*285\*\*](#), 867-870 (1999).

[Nat-12] A. Natarajarathinam, Z. R. Tadisina, T. Mewes, S. Watts, E. Chen, and S. Gupta, *Influence of capping layers on CoFeB anisotropy and damping*, [\*J. Appl. Phys.\* \*\*112\*\*](#), 053909 (2012).

[Nat-13] A. Natarajarathinam, B. D. Clark, A. Singh, and S. Gupta, *Influence of annealing on tunnelling magnetoresistance of perpendicular magnetic tunnel junctions*, [\*J. Phys. D: Appl. Phys.\* \*\*46\*\*](#), 095002 (2013).

[Née-54] L. Néel, *Anisotropie magnétique superficielle et surstructures d'orientation*, [\*J. Phys. Radium\* \*\*15\*\*](#), 225-239 (1954).

[Ngu-04] P. P. Nguyen, and Y. Huai, *Spin transfer magnetic element with free layers having high perpendicular anisotropy and in-plane equilibrium magnetization*, [\*U. S. Patent 7531882 \(B2\)\*](#), Feb. 26 2004.

[Nis-02] N. Nishimura, T. Hirai, A. Koganei, T. Ikeda, K. Okano, Y. Sekiguchi, and Y. Osada, *Magnetic tunnel junction device with perpendicular magnetization films for high-density magnetic random access memory*, [\*J. Appl. Phys.\* \*\*91\*\*](#), 5246 (2002).

[Par-04] S. S. P. Parkin, C. Kaiser, A. Panchula, P. M. Rice, B. Hughes, M. Samant, and S.-H. Yang, *Giant tunnelling magnetoresistance at room temperature with MgO (100) tunnel barriers*, [\*Nature Mater.\* \*\*3\*\*](#), 862-867 (2004).

[Pre-07] I. L. Prejbeanu, M. Kerekes, R. C. Sousa, H. Sibuet, O. Redon, B. Dieny, and J.-P. Nozières, *Thermally-assisted MRAM*, [\*J. Phys. Condens. Matter\* \*\*19\*\*](#), 165218 (2007).

[Riz-13] N. D. Rizzo, D. Houssameddine, J. Janesky, R. Whig, F. B. Mancoff, M. L. Schneider, M. DeHerrera, J. J. Sun, K. Nagel, S. Deshpande, H.-J. Chia, S. M. Alam, T. Andre, S. Aggarwal, and J. M. Slaughter, *A fully functional 64 Mb DDR3 ST-MRAM built on 90 nm CMOS technology*, [\*IEEE Trans. Magn.\* \*\*49\*\*](#), 4441-4446 (2013).

[Rod-03] B. Rodmacq, S. Auffret, B. Dieny, S. Monso, and P. Boyer, *Crossovers from in-plane to perpendicular anisotropy in magnetic tunnel junctions as a function of the barrier degree of oxidation*, [\*J. Appl. Phys.\* \*\*93\*\*](#), 7513-7515 (2003).

[Rod-06] B. Rodmacq, and B. Dieny, *Thin-layered magnetic device with high spin polarization perpendicular to the plane of the layers, and magnetic tunnel junction and spin valve using such a device*, [\*U. S. Patent 7813202 \(B2\)\*](#), Aug. 3 2006.

[Rod-09] B. Rodmacq, A. Manchon, C. Ducruet, S. Auffret, and B. Dieny, *Influence of thermal annealing on the perpendicular magnetic anisotropy of Pt/Co/AlO<sub>x</sub> trilayers*, [\*Phys. Rev. B\* \*\*79\*\*](#), 024423 (2009).

- [San-14] L. San Emeterio Alvarez, B. Lacoste, B. Rodmacq, L. E. Nistor, M. Pakala, R. C. Sousa, and B. Dieny, *Field-current phase diagrams of in-plane STT-RAM cells with low effective magnetization storage layers*, [\*J. Appl. Phys.\* \*\*115\*\*, 17C713 \(2014\)](#).
- [Sat-11] H. Sato, M. Yamanouchi, K. Miura, S. Ikeda, H. D. Gan, K. Mizunuma, R. Koizumi, F. Matsukura, and H. Ohno, *Junction size effect on switching current and thermal stability in CoFeB/MgO perpendicular magnetic tunnel junctions*, [\*Appl. Phys. Lett.\* \*\*99\*\*, 042501 \(2011\)](#).
- [Sav-03] L. Savtchenko, B. N. Engel, N. D. Rizzo, M. F. DeHerrera, and J. A. Janesky, *Method of writing to scalable magnetoresistance random access memory element*, [\*U. S. Patent 6545906 \(B1\)\*](#), Apr. 08 2003.
- [Sin-13] J. Sinha, M. Hayashi, A. J. Kellock, S. Fukami, M. Yamanouchi, H. Sato, S. Ikeda, S. Mitani, S. -H. Yang, S. S. P. Parkin, and H. Ohno, *Enhanced interface perpendicular magnetic anisotropy in Ta|CoFeB|MgO using nitrogen doped Ta underlayers*, [\*Appl. Phys. Lett.\* \*\*102\*\*, 242405 \(2013\)](#).
- [Slo-96] J.C. Slonczewski, *Current-driven excitation of magnetic multilayers*, [\*J. Magn. Magn. Mater.\* \*\*159\*\*, L1-L7 \(1996\)](#).
- [Tso-98] M. Tsoi, A. G. M. Jansen, J. Bass, W.-C. Chiang, M. Seck, V. Tsoi, and P. Wyder, *Excitation of a magnetic multilayer by an electric current*, [\*Phys. Rev. Lett.\* \*\*80\*\*, 4281 \(1998\)](#).
- [Wan-04] D. Wang, C. Nordman, J. M. Daughton, Z. Qian, and J. Fink, *70% TMR at room temperature for SDT sandwich junctions with CoFeB as free and reference layers*, [\*IEEE Trans. Magn.\* \*\*40\*\*, 2269-2271 \(2004\)](#).
- [Wan-11] W. -G. Wang, S. Hageman, M. Li, S. Huang, X. Kou, X. Fan, J. Q. Xiao, and C. L. Chien, *Rapid thermal annealing study of magnetoresistance and perpendicular anisotropy in magnetic tunnel junctions based on MgO and CoFeB*, [\*Appl. Phys. Lett.\* \*\*99\*\*, 102502 \(2011\)](#).
- [Wol-10] S. A. Wolf, J. Lu, M. R. Stan, E. Chen, and D. M. Treger, *The promise of nanomagnetism and spintronics for future logic and universal memory*, [\*Proc. IEEE\* \*\*98\*\*, 2155-2168 \(2010\)](#).
- [Wor-03] D. C. Worledge, and P. L. Trouilloud, *Magnetoresistance measurement of unpatterned magnetic tunnel junction wafers by current-in-plane tunneling*, [\*Appl. Phys. Lett.\* \*\*83\*\*, 84-86 \(2003\)](#).
- [Wor-10] D. C. Worledge, G. Hu, P. L. Trouilloud, D. W. Abraham, S. Brown, M. C. Gaidis, J. Nowak, E. J. O'Sullivan, R. P. Robertazzi, J. Z. Sun, and W. J. Gallagher, *Switching distributions and write reliability of perpendicular spin torque MRAM*, [\*Int. Electron Devices Meeting Tech. Digest\*](#), 12.5.1-12.5.4 (2010).

[Wor-11] D. C. Worledge, G. Hu, D. W. Abraham, J. Z. Sun, P. L. Trouilloud, J. Nowak, S. Brown, M. C. Gaidis, E. J. O'Sullivan, and R. P. Robertazzi, *Spin torque switching of perpendicular Ta/CoFeB/MgO-based magnetic tunnel junctions*, [\*Appl. Phys. Lett.\* \*\*98\*\*, 022501 \(2011\)](#).

[Yam-12] H. Yamamoto, J. Hayakawa, K. Miura, K. Ito, H. Matsuoka, S. Ikeda, and H. Ohno, *Dependence of magnetic anisotropy in  $Co_{20}Fe_{60}B_{20}$  free layers on capping layers in MgO-based magnetic tunnel junctions with in-plane easy axis*, [\*Appl. Phys. Expr.\* \*\*5\*\*, 053002 \(2012\)](#).

[Yan-11] H. X. Yang, M. Chshiev, B. Dieny, J. H. Lee, A. Manchon, and K. H. Shin, *First-principles investigation of the very large perpendicular magnetic anisotropy at Fe/MgO and Co/MgO interfaces*, [\*Phys. Rev. B\* \*\*84\*\*, 054401 \(2011\)](#).

[Yod-10] H. Yoda, T. Kishi, T. Nagase, M. Yoshikawa, K. Nishiyama, E. Kitagawa, T. Daibou, M. Amano, N. Shimomura, S. Takahashi, T. Kai, M. Nakayama, H. Aikawa, S. Ikegawa, M. Nagamine, J. Ozeki, S. Mizukami, M. Oogane, Y. Ando, S. Yuasa, K. Yakushiji, H. Kubota, Y. Suzuki, Y. Nakatani, T. Miyazaki, and K. Ando, *High efficient spin transfer torque writing on perpendicular magnetic tunnel junctions for high density MRAMs*, [\*Curr. Appl. Phys.\* \*\*10\*\*, e87-e89 \(2010\)](#).

[Yua-04] S. Yuasa, T. Nagahama, A. Fukushima, Y. Suzuki, and K. Ando, *Giant room-temperature magnetoresistance in single-crystal Fe/MgO/Fe magnetic tunnel junctions*, [\*Nature Mater.\* \*\*3\*\*, 868-871 \(2004\)](#).

[Yua-05] S. Yuasa, Y. Suzuki, T. Katayama, and K. Ando, *Characterization of growth and crystallization processes in CoFeB/MgO/CoFeB magnetic tunnel junction structure by reflective high-energy electron diffraction*, [\*Appl. Phys. Lett.\* \*\*87\*\*, 242503 \(2005\)](#).

[Yua-07] S. Yuasa, and D. D. Djayaprawira, *Giant tunnel magnetoresistance in magnetic tunnel junctions with a crystalline MgO(001) barrier*, [\*J. Phys. D: Appl. Phys.\* \*\*40\*\*, R337-R354 \(2007\)](#).

## CHAPTER II

# Development of magnetic tunnel junctions with a bottom reference

<b>II-1. Optimization of the Ta insertion .....</b>	<b>56</b>
II-1.1 Role of the Ta insertion .....	56
II-1.2 Magnetic coupling between the multilayer and the CoFeB layer through the Ta spacer .....	57
II-1.3 Effect of the Ta insertion thickness on transport properties.....	64
II-1.4 Conclusions .....	65
<b>II-2. Development of bottom synthetic antiferromagnetic references .....</b>	<b>67</b>
II-2.1 Origin of the antiferromagnetic coupling: RKKY interactions.....	67
II-2.2 What is a synthetic antiferromagnet? .....	68
II-2.3 Magnetic behavior of a synthetic antiferromagnet .....	70
II-2.4 Optimization of layers thicknesses in the bottom SAF electrode .....	71
II-2.5 Choice of the optimal annealing temperature .....	78
II-2.6 Conclusions.....	80
<b>II-3. Optimization of magnetic electrode thicknesses .....</b>	<b>82</b>
II-3.1 Determination of the critical thicknesses .....	82
II-3.2 Determination of saturation magnetization and magnetic dead layer thickness .....	84
II-3.3 Anisotropy measurements on the top electrode.....	87
II-3.4 Correlation between magnetic and transport properties.....	88
<b>II-4. Conclusions .....</b>	<b>91</b>
<b>II-5. References .....</b>	<b>92</b>



From the review of Chapter I on the recent developments of magnetic tunnel junctions with perpendicular anisotropy, it appears that getting functional structures is not easy and that a lot of materials parameters are involved. Indeed, mastering the growth conditions of the different layers is extremely important, in particular because perpendicular magnetic anisotropy has mostly interfacial origins.

Both seed and cap layers play a role in the magnetic properties of the stacks, as well as the chemical composition of the electrodes of the magnetic tunnel junction. To create functional devices it is necessary to have a good knowledge of the working window of each parameter, in particular the thicknesses. As we will see, varying the composition of the stack will influence both the magnetic and the transport properties.

In this Chapter, we will first show how the thickness of the Ta insertion separating the Co/Pt multilayer from the CoFeB layer in the reference layer can be optimized to enhance the properties of the whole junction [\[Cuc-13\]](#). We will then describe the development of the bottom Synthetic AntiFerromagnetic (SAF) reference, in particular the choice of the thicknesses of each material. Finally, we will see that optimizing both the bottom and top CoFeB thicknesses allows improving the magnetic and transport properties of the junctions [\[Cuc-14\]](#).

## II-1. Optimization of the Ta insertion

### II-1.1 Role of the Ta insertion

As we have seen in the first Chapter, CoFeB alloys are good candidates to get large tunnel magnetoresistance effects since they allow coherent tunneling when used with MgO barriers. However, the stability of the reference layer in Ta/CoFeB/MgO/CoFeB/Ta magnetic tunnel junctions is much lower than what can be obtained with Co/Pt or Co/Pd multilayers. That is why both systems were combined to create composite layers in which the CoFeB layer in contact with the MgO barrier is coupled to the multilayers.

It has been shown that the texture of the CoFeB layer plays a dominant role to get high TMR signal. Thus, it is necessary to introduce a spacer between the multilayers and the CoFeB. Indeed, the bcc (100) texture that guaranties a good tunneling effect cannot be obtained in the CoFeB electrodes if they grow directly in contact with a Co hcp (0001) or a Pt (Pd) fcc (111) layer. In 2011, Worledge *et al.* introduced a thin Ta layer between the bottom Co/Pt multilayer and the CoFeB film [[Wor-11](#)]. This technique has also been employed by other groups with Co/Pd multilayers [[Nat-12](#)]. As thin Ta is amorphous, it allows the CoFeB alloy, which is also amorphous after deposition, to crystallize from the MgO side into the right bcc (100) structure upon annealing.

Using a Ta insertion has also another advantage: it attracts boron away from the interface with MgO during annealing. This effect has been observed and proved to be beneficial for TMR. As the annealing temperature increases, the boron content of the CoFeB electrode decreases at the MgO interface and the crystalline structure is improved [[Koz-10](#)].

We decided to investigate the effect of this Ta spacer in perpendicular magnetic tunnel junctions both on their magnetic and transport properties.

## II-1.2 Magnetic coupling between the multilayer and the CoFeB layer through the Ta spacer

### a) Case of a “thick” bottom CoFeB layer

To study the impact of varying the thickness of the Ta spacer on the magnetic properties of our magnetic tunnel junctions, we deposited samples composed of a bottom Co/Pt multilayer coupled through Ta to a Co-rich CoFeB layer. The top electrode is a single layer of Fe-rich CoFeB composition and represents the free layer in this case. The stack is the following Ta<sub>3</sub>/Pt<sub>5</sub>/(Co<sub>0.5</sub>/Pt<sub>0.4</sub>)<sub>5</sub>/Co<sub>0.5</sub>/Ta<sub>x</sub>Ta/CoFeB<sub>1.2</sub>/MgO/FeCoB<sub>1.2</sub>/Ta<sub>1</sub>/Pt<sub>2</sub>, where thicknesses are given in nanometers. The Ta insertion thickness is varied between 0 and 0.9 nm. The depositions are done on CuN buffer layers to allow performing transport measurements by CIPT (see Chapter I). Samples are vacuum-annealed at 300°C for 1 h.

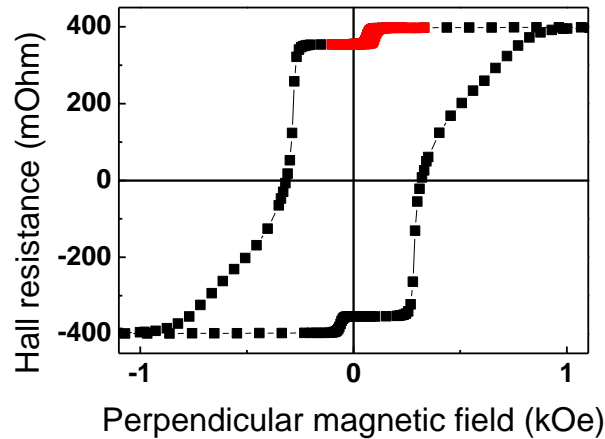


Figure II-1: Typical EHE loop obtained for  $x_{Ta}=0$  nm with a perpendicular field. The red curve corresponds to the minor loop on the top free layer.

We show in Figure II-1 an example of the magnetic loop we measure for a sample with no Ta insertion ( $x_{Ta}=0$  nm) using our Extraordinary Hall Effect (EHE) set-up, with perpendicular applied field. Transitions of both the top soft layer and the bottom hard electrode are visible. A minor loop is performed on the free layer and is included in red in the Figure. It can be seen that this cycle is not centered on zero field but is slightly shifted towards positive fields. As the measurement is performed coming from positive saturation, this shift corresponds to the typical antiferromagnetic coupling that exists through the MgO barrier. For this sample, it amounts to about -80 Oe. This type of indirect exchange coupling has been theorized using spin torque mediated effects through the MgO barrier [Slo-89, Bru-95]. One cannot however exclude the possibility of magnetostatic coupling due to surface roughness. L. Néel

proposed such an explanation defining what is known as orange peel coupling [Née-62]. This theory can indeed be adapted to perpendicular systems and leads to the existence of an antiferromagnetic coupling in the case of strong perpendicular anisotropy [Mor-04]. It was firstly observed in epitaxial systems for which the coupling goes from antiferromagnetic to ferromagnetic as the barrier thickness increases [Fau-02]. The amplitude of the coupling is found to decrease as the barrier thickness increases, as shown in Figure II-2. In the case of sputtered systems the antiferromagnetic coupling persists up to larger barrier thicknesses, probably due to a greater surface roughness associated with this deposition technique. This indirect exchange coupling was also found to oscillate in amplitude as a function of magnetic thickness and to be dependent on annealing temperature [Nis-10b], in agreement with theoretical predictions [Bru-93].

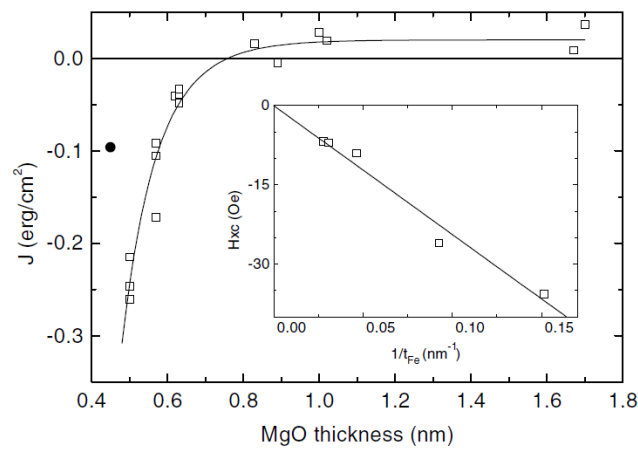


Figure II-2: Evolution of the indirect coupling energy as a function of MgO barrier thickness for Fe/MgO/Fe/Co epitaxial structures [Fau-02].

Similar measurements to the one shown in Figure II-1 were then done for samples with increasing Ta thickness and we present in Figure II-3 the results for Ta thicknesses of 0.4, 0.5 and 0.6 nm. All curves have been normalized to their maximum Hall resistance in order to facilitate the comparison between samples. Only the part comprised between -1 and 4 kOe is shown here. One can observe that a hard axis component abruptly appears in the signal for  $x_{\text{Ta}}=0.5$  and 0.6 nm. This planar signal is attributed to the bottom CoFeB layer. As its magnetization decouples from that of the underlying Co/Pt multilayer, it abruptly falls in-plane. This means that the thickness of 1.2 nm of CoFeB we are working with cannot retain perpendicular anisotropy on its own. As can be seen in Figure II-3, a field of about 3 kOe is necessary to pull the magnetization out-of-plane, once it is magnetically decoupled from the Co/Pt multilayer.

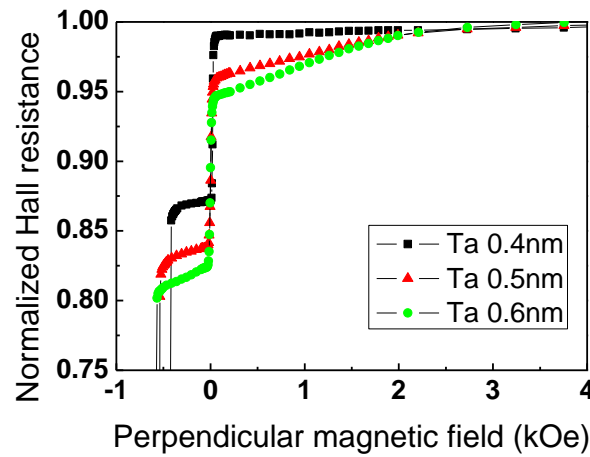


Figure II-3: Partial EHE loop performed on samples with  $x_{\text{Ta}}=0.4, 0.5,$  and  $0.6$  nm.

The amplitude of the planar signal has been evaluated for all Ta thicknesses and normalized to the bottom electrode contribution. Results are given as a function of the Ta spacer thickness in Figure II-4. It comes out that for Ta thicknesses up to 0.45 nm, no in-plane component is visible in the magnetic loop, meaning that the CoFeB layer is still strongly coupled to the Co/Pt multilayer. Above 0.55 nm of Ta, the amplitude of the planar signal remains constant at a value of about 4.5 % of the bottom multilayer contribution. Note that this amplitude is a lot smaller than what we would expect from the magnetizations of both layers. This is due to the fact that the Hall coefficient of CoFeB is much lower than the one of Co/Pt layers. For the 0.5 nm thick Ta insertion, the planar signal has not reached yet its maximum value. We assume that, at this thickness, the system is in an intermediate state in which the magnetization of the CoFeB layer is not homogeneous and some parts have kept perpendicular anisotropy (probably because of the roughness).

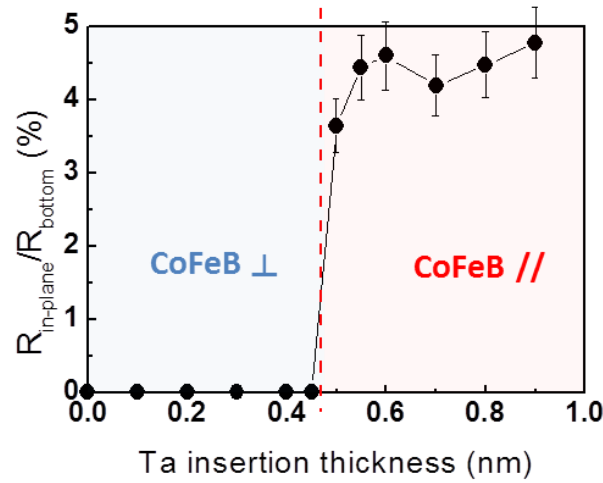


Figure II-4: Relative Hall contribution of the in-plane component of the bottom electrode as a function of Ta insertion thickness.

The antiferromagnetic coupling that exists through the MgO is also a representative parameter of the effect of the Ta layer thickness. The evolution of this coupling field as a function of spacer thickness is plotted in Figure II-5. We remind that due to the sign convention, negative field values correspond to antiferromagnetic coupling. As the Ta insertion gets thicker, the coupling field amplitude decreases from -80 Oe without Ta to about -20 Oe for  $x_{\text{Ta}}=0.5$  nm. This is explained by a reduction of the MgO barrier roughness thanks to the beneficial effect of the underlying Ta layer, as it becomes thicker. When the Ta spacer thickness is larger than 0.5 nm, the coupling field remains constant as the CoFeB magnetization is now in-plane. This non zero asymptotic value might probably originate from a remaining interfacial roughness. It leads to the existence of stray fields that prevent the magnetizations on both sides of the MgO from being fully orthogonal to each other. Note that as the coupling energy can be expressed as  $J = H_{\text{cpl}}M_s t$ , with  $M_s$  and  $t$  the saturation magnetization and the thickness of the top FeCoB layer that switches, any variation of the coupling field  $H_{\text{cpl}}$  can only be attributed to a change in coupling energy.

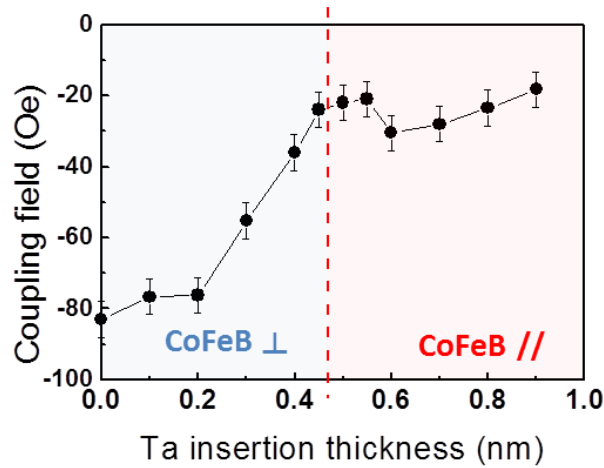


Figure II-5: Variation of the coupling field between the bottom and top magnetic layers through the MgO barrier as a function of Ta thickness.

The anisotropy field of the planar contribution has been evaluated for the different values of Ta insertion thickness. Results are presented in Figure II-6. This field corresponds to the field needed to orient perpendicularly the magnetization of the CoFeB layer and is taken with a negative value, following the usual convention to state that the anisotropy is planar. Note that we cannot extract the anisotropy of the CoFeB layer when it is coupled to the underlying Co/Pt multilayer as its contribution cannot be estimated separately. At the appearance of the planar signal for  $x_{\text{Ta}}=0.5$  nm, the anisotropy field amounts to about -3 kOe. It then decreases in amplitude upon increasing the Ta insertion thickness to reach -1 kOe for  $x_{\text{Ta}}=0.9$  nm. This can be explained by an increase of the perpendicular anisotropy of the in-plane magnetized CoFeB for increasing Ta thicknesses. The effect of Ta on perpendicular anisotropy is not easily interpreted. Indeed, if some studies attribute a contribution of the interface with Ta to PMA [Wor-11, Yam-12], others state that it solely originates from the CoFeB/MgO interface, Ta ensuring only a better growth to the layers [Liu-12]. As already pointed out, Ta plays a role in the enhancement of TMR by attracting boron away from the interface with MgO during annealing [Koz-10]. This diffusion of boron atoms that improves TMR might also have a beneficial impact on PMA [Nis-10a]. One could also think that as the Ta spacer gets thicker a possible alloying between Ta and CoFeB might lead to a reduction of effective CoFeB thickness and then to a decrease of the anisotropy field. However, the fact that the amplitude of the planar signal stays constant for  $x_{\text{Ta}}>0.55$  nm (as seen in Figure II-4) seems to exclude the possibility of a change of magnetic dead layer with Ta thickness in that case.

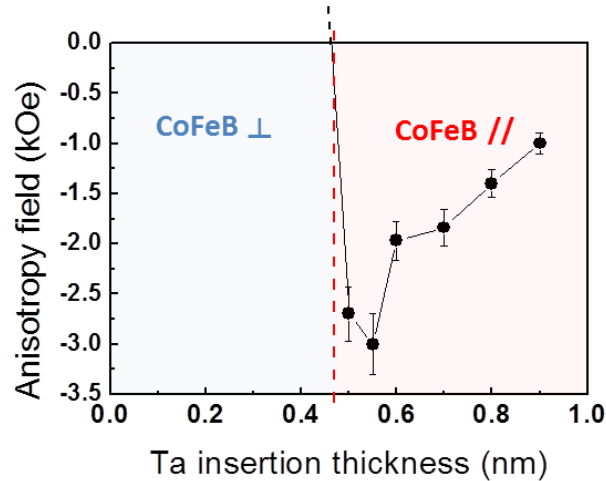


Figure II-6: Perpendicular anisotropy field of the in-plane magnetized CoFeB layer as a function of Ta insertion thickness.

b) Case of a fully perpendicular system (“thin” bottom FeCoB)

After seeing this effect of decoupling between the bottom Co/Pt multilayer and a CoFeB layer that loses its perpendicular magnetization, we wanted to investigate the case of a fully perpendicular system, that is to say a structure in which the CoFeB layer keeps perpendicular anisotropy even when it is decoupled from the Co/Pt multilayer. To do this, we deposited bottom electrodes with the following stack: Ta<sub>5</sub>/Pt<sub>5</sub>/(Co<sub>0.5</sub>/Pt<sub>0.25</sub>)<sub>5</sub>/Co<sub>0.5</sub>/Ru<sub>0.9</sub>/(Co<sub>0.5</sub>/Pt<sub>0.25</sub>)<sub>3</sub>/Co<sub>0.5</sub>/Ta<sub>x</sub>Ta/FeCoB<sub>1</sub>/MgO/FeCoB<sub>0.5</sub>/Ta<sub>1</sub>/Pt<sub>2</sub>, with thicknesses given in nm. Note that in this study we used a bottom FeCoB layer as the Co-rich composition target had been removed from our deposition tool at that time. The structure is in that case a synthetic antiferromagnet in which one bottom Co/Pt multilayer is antiferromagnetically coupled through a Ru spacer to a top Co/Pt multilayer plus a 1 nm thick FeCoB layer. Details on the optimization of the SAF layer will be given later. In those stacks, we put a 0.5 nm thick FeCoB on top of the barrier, which we know is non-magnetic due to dead layer formation. This allows having the same interfaces without getting a magnetic contribution of the free layer that might be mixed with the signal of the bottom FeCoB layer.

Typical hysteresis loops obtained by VSM are shown in Figure II-7 for  $x_{Ta}=0.3$ , 0.5 and 0.8 nm. Magnetic loops are measured coming from positive fields saturation and a minor loop is performed on the top part of the SAF (red curves in Figure II-7). Curves are normalized to their total amplitude in order to make comparison easier. Note that the edges of the substrates were not protected for this series of samples so a parasitic signal appears at small fields between  $\pm 500$  Oe, as explained in Chapter I. This signal will not be taken into account in the discussion. For  $x_{Ta}=0.3$  nm the bottom FeCoB layer is still strongly coupled to the Co/Pt multilayer so we only see

two transitions in the magnetic loop, corresponding to the bottom and top part of the SAF respectively. For  $x_{Ta}=0.5$  nm, new transitions are visible in the hysteresis loop. Around a positive field of 1300 Oe, an abrupt transition appears. It corresponds to the switching of the bottom FeCoB magnetization which starts to decouple from the underlying Co/Pt multilayer. Contrary to the case of a 0.8 nm thick Ta insertion, this signal is not centered on zero field. This means that the system is in an intermediate state in which the multilayer and the FeCoB layer are still partly coupled, probably because of some interfacial roughness.

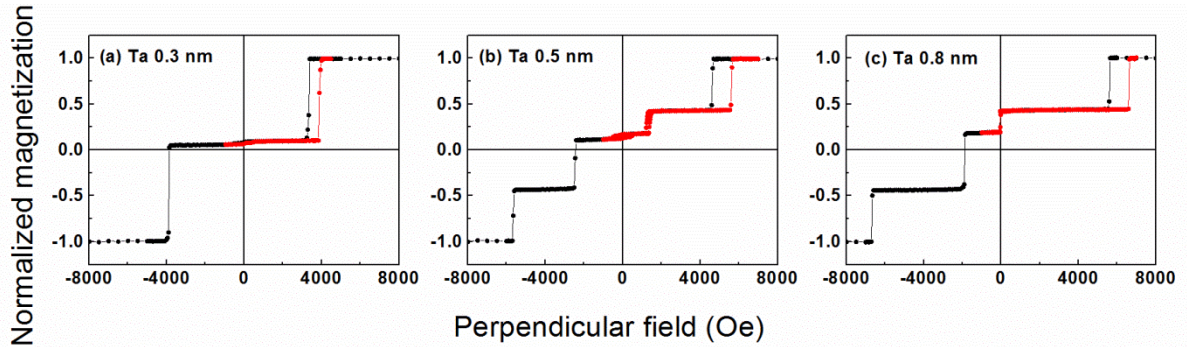


Figure II-7: Magnetic loops measured with perpendicular field for bottom SAF with increasing thicknesses of Ta insertion ( $x_{Ta}=0.3$  (a), 0.5 (b) or 0.8 nm (c)). Minor loops on the top part of the SAF are included in red.

The value of the shift of the bottom FeCoB transition has been evaluated for all samples of this study and is presented as a function of Ta thickness in Figure II-8 (a). In the case of strong ferromagnetic coupling between the FeCoB and the multilayer, that is to say when they switch together, we cannot extract any value of the coupling field. Thus, no data points are presented for  $x_{Ta}<0.5$  nm.

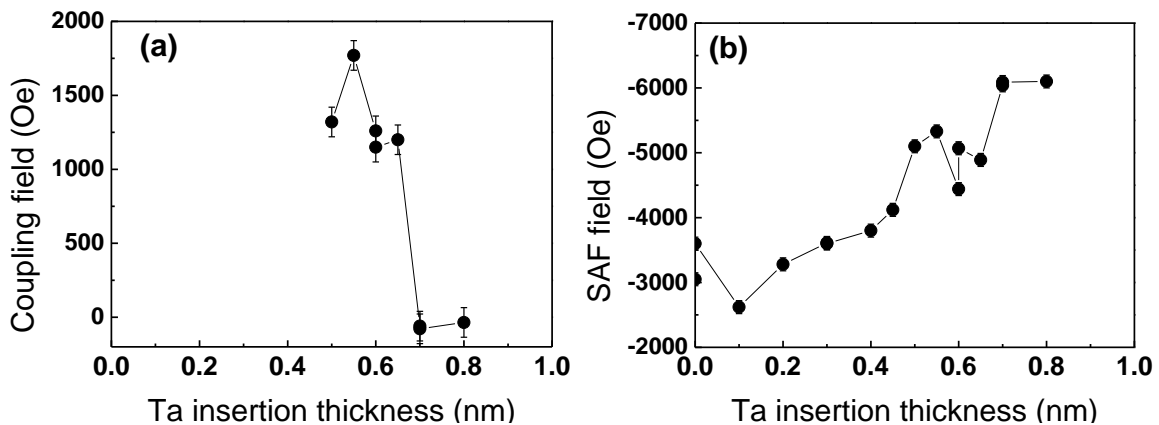


Figure II-8: Evolution of (a) the coupling field of the FeCoB layer and (b) the SAF field as a function of Ta insertion thickness.

As we have seen in the magnetic loop of Figure II-7, the signal of the FeCoB layer starts to appear for  $x_{Ta}=0.5$  nm. This thickness is equivalent to the one we had previously observed in the case of a thick CoFeB layer. The coupling field reaches about 1800 Oe for  $x_{Ta}=0.55$  nm and then decreases to become null as soon as  $x_{Ta}$  is greater than 0.7 nm, when the FeCoB magnetization is fully decoupled from the rest of the SAF. This curve shows that the transition between a strongly coupled system and two decoupled layers is not sharp and happens between 0.45 and 0.7 nm.

When the FeCoB layer starts decoupling from the Co/Pt multilayer, a supplementary transition appears for negative fields around -2000 Oe (see Figure II-7 (b)). This is due to the fact that the RKKY coupling energy through the Ru spacer now predominates over the anisotropy energy leading to an additional reversal of the net moment of the SAF, still keeping an antiferromagnetic coupling. This effect will be described in more details in the following part. In the meantime, as the FeCoB magnetization is no longer coupled to the top Co/Pt multilayer, the total thickness of the layers involved in the SAF is reduced. This leads to a decrease in the amplitude of the first transition (coming from positive fields) as it now corresponds to the top multilayer only. Besides, its reversal happens at larger fields as the coupling field through the Ru spacer is increased for thinner layers, for a constant coupling energy. The evolution of the SAF coupling field as a function of Ta thickness is given in Figure II-8 (b). Note that due to the sign convention, the coupling field values are taken with a negative sign to account for the antiferromagnetic nature of the coupling. It roughly exhibits the same behavior as the coupling field on the FeCoB layer. The SAF field is more or less constant around 3500 Oe for  $x_{Ta}<0.45$  nm and then, as the FeCoB layer decouples itself from the Co/Pt multilayer, its value increases to reach a constant value of about 6000 Oe for  $x_{Ta}>0.7$  nm.

### **II-1.3 Effect of the Ta insertion thickness on transport properties**

To study the impact of varying the Ta insertion thickness on the transport properties of magnetic tunnel junctions, we used the series of samples described in the previous part, in the case of a thick bottom CoFeB layer. Transport measurements were performed using a CIPT set-up, after applying a field of 1.5 kOe to saturate the samples. Magnetic fields of +/-150 Oe are applied in order to switch the top FeCoB free layer and resistance is measured in each case. The TMR ratio as a function of Ta thickness is given in Figure II-9.

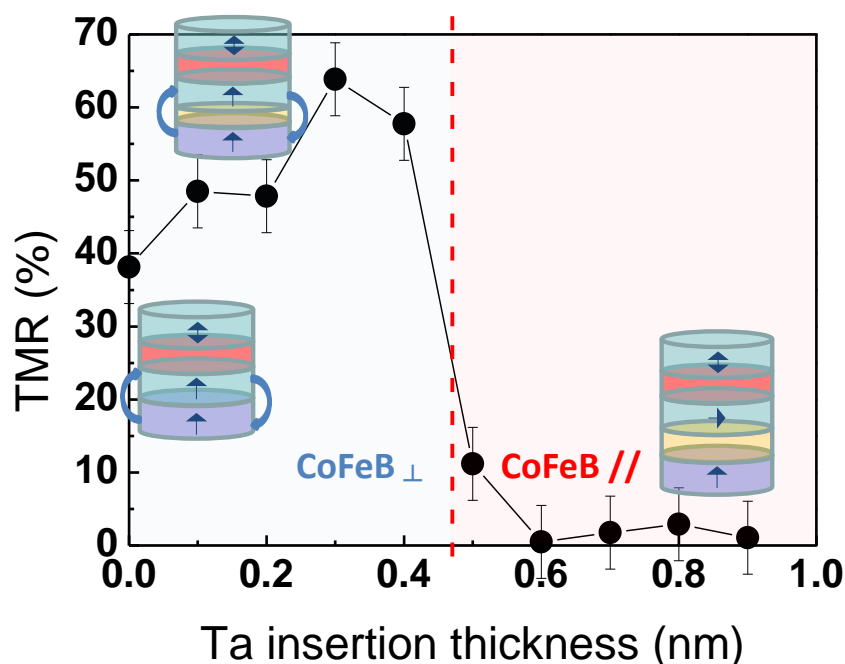


Figure II-9: TMR evolution as a function of Ta insertion thickness.

Without any Ta insertion, the TMR is around 40% and it increases up to almost 70 % when the Ta spacer thickness is increased to 0.4 nm. This reflects the improvement of the texture of the CoFeB layer thanks to a thin Ta layer. Above 0.45 nm, the TMR signal drops which is consistent with the reorientation of the CoFeB magnetization in the plane of the magnetic film. Indeed, once the CoFeB magnetization is in-plane, no matter which direction the free layer takes (up or down), the level of resistance will always be the same, which translates into zero magnetoresistance. We have thus a clear correlation between the magnetic and the transport properties of our magnetic tunnel junctions as a function of Ta insertion thickness.

#### II-1.4 Conclusions

In this part, we have seen that the Ta insertion that is introduced in the hard magnetic electrode of a magnetic tunnel junction to decouple the growth of the CoFeB layer from the adjacent Co/Pt(Pd) multilayer has to be chosen carefully. Indeed, the Ta insertion enhances significantly the TMR signal of the magnetic tunnel junctions by improving the crystalline structure of the CoFeB alloy. However, it is

necessary to keep this spacer thin enough in order to maintain a strong magnetic coupling between the layers. As we have shown, any decoupling between the CoFeB and the multilayer translates into a decrease of TMR.

From the magnetic and transport measurements that have been performed on different types of structures, it appears that a good compromise would be to choose a thickness of Ta around 0.3 nm. This gives us the largest TMR signals while remaining in the coupled zone. For the following studies, this thickness will be kept as the standard value to use for Ta spacers between a Co/Pt(Pd) multilayer and a CoFeB layer.

## II-2. Development of bottom synthetic antiferromagnetic references

### II-2.1 Origin of the antiferromagnetic coupling: RKKY interactions

In a stack comprising two ferromagnetic layers separated by a non-magnetic spacer, it has been observed that an indirect exchange coupling could appear between the magnetic layers. In the case of interfacial roughness, a ferromagnetic coupling may exist due to the existence of magnetostatic charges. This dipolar coupling is known as Neel type or orange peel coupling [Née-62]. However, even when the interfaces are smooth, some coupling can arise from the polarization of the electrons of the non-magnetic material in contact with the magnetic layers. Indeed, a magnetic impurity present in a non-magnetic material can polarize the conduction electrons leading to a disequilibrium between the densities of spin up and spin down electrons. This polarization oscillates with a period of  $2k_F$ , where  $k_F$  is the Fermi wave vector, and decreases in amplitude with a  $1/r^3$  behavior,  $r$  being the distance from the impurity. In the presence of two impurities, both polarization waves will interact to couple indirectly the two magnetic moments, either ferromagnetically or antiferromagnetically depending on the distance between them. This phenomenon is called RKKY interaction and is named after the researchers who worked on it: Ruderman and Kittel [Rud-54], Kasuya [Kas-56] and Yosida [Yos-57]. The same kind of behavior exists between two ferromagnetic layers separated by a non-magnetic spacer. The sign of the coupling oscillates as a function of spacer thickness and decreases in amplitude as the spacer gets thicker.

In 1991, S. S. P. Parkin showed that this oscillatory behavior is a general phenomenon for almost all transition metals [Par-91]. He worked on numerous spacer materials sandwiched between different magnetic layers (Co or Fe) and found that the coupling field oscillates as a function of spacer thickness with a period of approximately 1.0 nm for all transition metals (with the exception of Cr, which presents a larger period). An example of the obtained oscillations for Co/V, Co/Mo and Co/Rh multilayers is given in Figure II-10. In our studies, we will mostly work with ruthenium spacers which had also been found to exhibit RKKY coupling [Par-91].

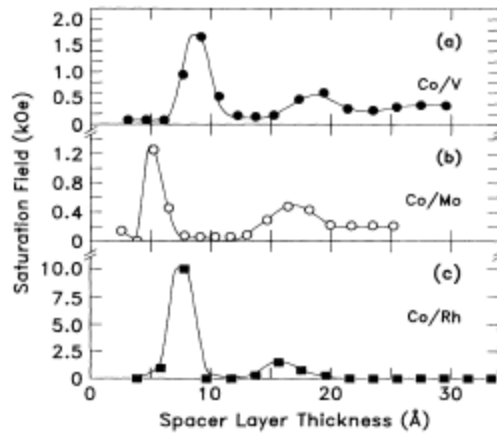


Figure II-10: Oscillations of the coupling as a function of spacer thickness for different materials (Co/V, Mo or Rh). Data extracted from [Par-91].

### II-2.2 What is a synthetic antiferromagnet?

Being able to couple antiferromagnetically two magnetic layers is particularly interesting for spintronic devices. Indeed, as the lateral sizes of the pillars are reduced to enhance storage density, strong dipolar couplings appear between the reference and storage electrodes. This coupling is increasing as the pillar diameter decreases and adds to the existing indirect couplings through the tunnel barrier to become even predominant at small sizes. This effect translates into a shift of the hysteresis loop of the storage layer and might lead to a loss of a bistable state in zero field as illustrated in Figure II-11.

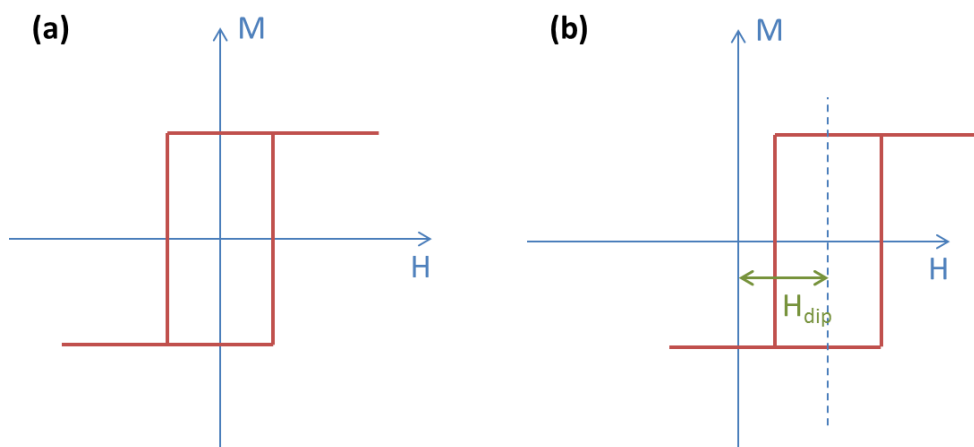


Figure II-11: Schematic representation of the magnetic loop of the storage layer in the case of (a) no dipolar coupling and (b) a dipolar coupling.  $H_{dip}$  corresponds to the amplitude of the shift of the hysteresis loop.

This is the reason why Synthetic AntiFerromagnetic (or SAF) structures have been developed in which two ferromagnetic layers are antiferromagnetically coupled through a metallic spacer. They are mostly used as reference layers and have been observed to be strongly effective to reduce dipolar coupling in small size pillars. The first SAFs were inserted in magnetic tunnel junctions with planar anisotropy. In that case, magnetic compensation on both sides of the spacer allows suppressing the coupling field that act on the storage layer. Figure II-12 schematically shows how the field lines are locked in a compensated planar SAF.

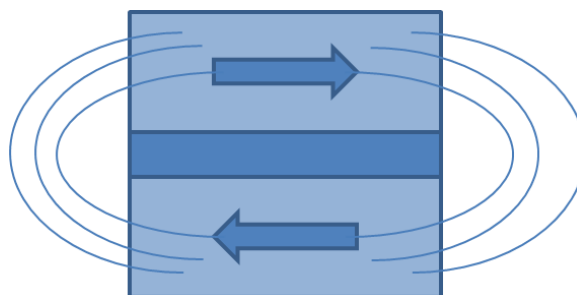


Figure II-12: Schematic representation of a planar SAF.

In the case of perpendicular anisotropy, RKKY coupling also exists and it is possible to create SAF reference layers. Similarly to the planar systems, the coupling field can be strongly reduced. However, the compensation is not straightforward and varies significantly with pillar diameters. S. Bandiera *et al.* compared magnetic tunnel junctions with either a single layer or a SAF reference [Ban-10]. Calculations revealed that the stray fields mostly come for the edges of the nanopillars and are much lower in amplitude for the SAF systems. To minimize the loop shift of the free layer, the ratio of magnetizations in the SAF has to be adjusted and depends on the pillar diameter. In Figure II-13, the coupling field is represented as a function of the ratio  $\alpha = M_1/M_2$ , where  $M_2$  is the magnetization of the layer the closest to the barrier and  $M_1$  the farthest one. It appears that the optimal ratio to suppress any loop shift depends on the size of the pillar and is increasing rapidly for diameters smaller than 200 nm. Note that in any case, the magnetization of the layer that is farther from the free layer has to be larger due to a distance effect.

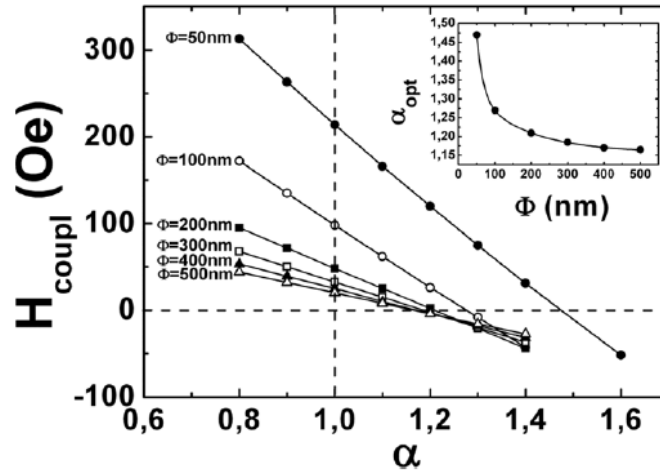


Figure II-13: Calculated coupling field on the free layer as a function of magnetizations ratio  $\alpha$  in the SAF (from [Ban-10]).

### II-2.3 Magnetic behavior of a synthetic antiferromagnet

Using a SAF stack gives the possibility to stabilize an antiparallel configuration of the magnetizations of the ferromagnetic layers at zero field. In a SAF system  $F_1/\text{Ru}/F_2$  under applied field, different energy terms have to be taken into account: the Zeeman energy, the anisotropy energy and the RKKY coupling energy. Depending on their relative contributions, two different magnetic behaviors are possible. They are schematically represented in Figure II-14.

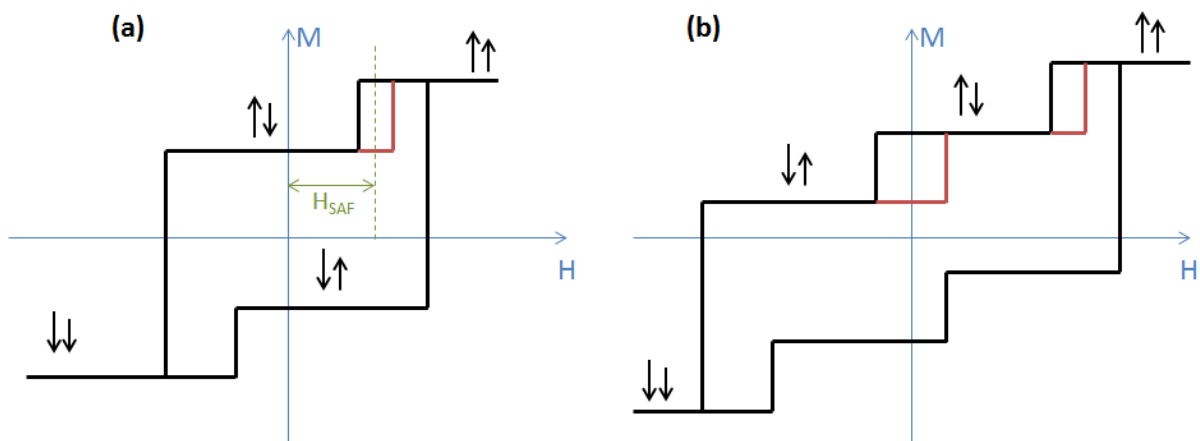


Figure II-14: Schematic hysteresis loops of a SAF in the case where (a) the RKKY coupling energy is smaller than the Zeeman and anisotropy contributions (b) the opposite situation. We add in red minor loops.

In both cases, coming from positive field saturation, where the two magnetizations are aligned in the field direction, a first transition is observed and corresponds to the switching of the softest layer of the SAF. A minor loop can be performed on this layer, by increasing again the amplitude of the magnetic field, as shown in red. The shift of this minor loop gives the coupling field  $H_{\text{SAF}}$ , that can be used to calculate the coupling energy  $J_{\text{Ru}} = H_{\text{SAF}} M_2 t_2$ , with layer 2 being the softest one. If one continues to decrease the field to go towards negative saturation, the switching of the hardest layer  $F_1$  occurs. In the case where the Zeeman and anisotropy energies of  $F_2$  are larger than the coupling energy (Figure II-14 (a)), only one transition is visible and  $F_1$  switches while  $F_2$  stays parallel to the field direction. In the opposite case (Figure II-14 (b)), when the RKKY coupling through Ru is strong, the switching of  $F_1$  translates into a back-switching of  $F_2$ , as the layers are preferably in antiparallel configuration. This corresponds to the alignment of the net magnetization of the system in the field direction. As the field keeps decreasing,  $F_2$  finally switches so that both layers are parallel to the field. In both cases, two antiparallel configurations can be stabilized in zero field.

## II-2.4 Optimization of layers thicknesses in the bottom SAF electrode

In order to develop reference layers for perpendicular magnetic tunnel junctions, we decided to work on SAF systems with Co/Pt multilayers coupled to a CoFeB layer through a thin Ta spacer. Due to their large perpendicular anisotropy, Co/Pt multilayers are particularly good candidates to create magnetically hard layers that can be used as references. In the meantime, as we have seen previously, this kind of structure will have the advantage of reducing stray fields in the future patterned samples. This strategy had already been adopted by Worledge *et al.* in 2011 in the case of a top reference stack with Co/Pd multilayers [Wor-11]. Here we focus on the development of a bottom reference layer, in which the different layers have to be tuned properly so as to get the optimal magnetic behavior.

The typical stacks we will study in this part are the following: Ta<sub>3</sub>/Pt<sub>5</sub>/(Co/Pt)<sub>5</sub>/Co/Ru/(Co/Pt)<sub>3</sub>/Co/Ta<sub>0.3</sub>/CoFeB<sub>1.2</sub>/MgO/FeCoB<sub>1.4</sub>/Ta<sub>1</sub>/Pt<sub>2</sub>, with thicknesses in nm.

### a) Choice of the Ru spacer thickness

The oscillatory nature of RKKY coupling implies that the strength of this coupling will depend on spacer thickness. To enhance the reference stability, one needs to achieve the largest antiparallel plateau as possible. To that aim, we deposited a series

of samples with varying Ru thickness in which the thicknesses of Co and Pt in the multilayers were fixed at 0.5 and 0.25 nm respectively. Some examples of the hysteresis loops we obtain by VSM with perpendicular applied field are shown in Figure II-15. We only present half loops, measured from positive saturation (in black) and minor loops are performed both on the free layer and the softest part of the SAF (in red). Coming from positive fields, the first transition corresponds to the top part of the SAF, which is the magnetically softest one. Then, the top FeCoB layer switches, with its minor loop almost centered on zero field. Finally, for negative applied fields, the hard bottom multilayer is reversed. It appears that the magnetic behavior of the magnetic tunnel junctions varies a lot as a function of Ru thickness. In Figure II-15 (a), for a Ru spacer of 0.45 nm, the RKKY coupling is large with an antiparallel plateau that extends between about -5500 and 5000 Oe. This strong coupling gives rise to rounded shapes of the transitions and the appearance of a third transition in the SAF, as we have shown in Figure II-14 (b). For Ru thicknesses of 0.55 and 0.9 nm (Figure II-15 (b) and (c)), the magnetic loops are very similar with however distinct coupling fields that amount to 2300 and 3300 Oe, respectively. For a thicker Ru layer of 1.1 nm, the coupling strength is drastically reduced. As we can observe in Figure II-15 (d), the coupling field is very low (around 700 Oe) and the antiparallel plateau is almost lost at this thickness. Note that for strong RKKY coupling, the stability of the SAF reference layer appears to be much larger than in the case of the single ferromagnetic reference seen in the previous part. Indeed, as observed in Figure II-1, the coercive field of the ferromagnetic reference is only around 350 Oe whereas SAF structures give antiferromagnetic plateaus as large as a few kOe.

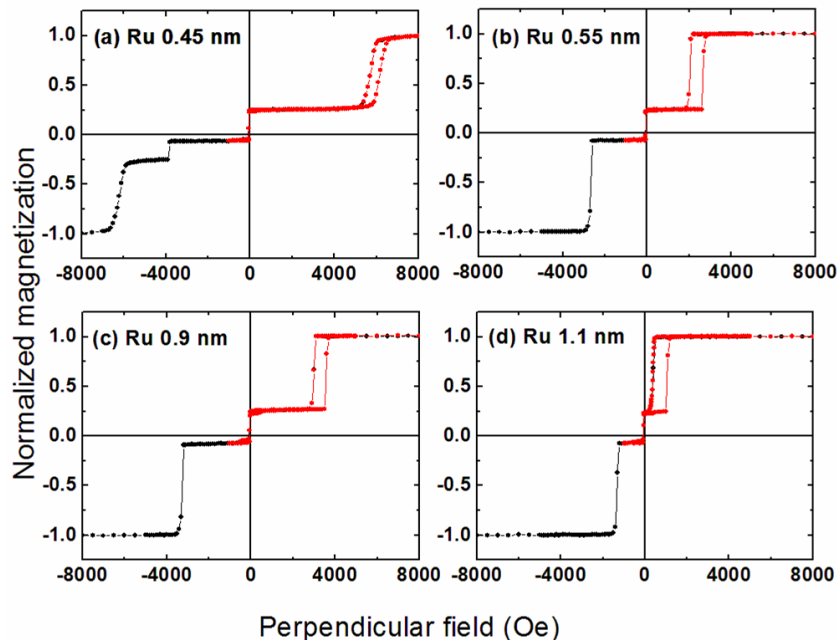


Figure II-15: Magnetic cycles measured by VSM with perpendicular field for samples composed of a bottom SAF reference with varying Ru spacer thickness and a top free layer. Minor loops are included in red.

The value of the RKKY coupling field  $H_{\text{SAF}}$  has been measured for Ru thicknesses varying between 0.3 and 1.1 nm. As shown in Figure II-16, the expected oscillatory behavior is observed.

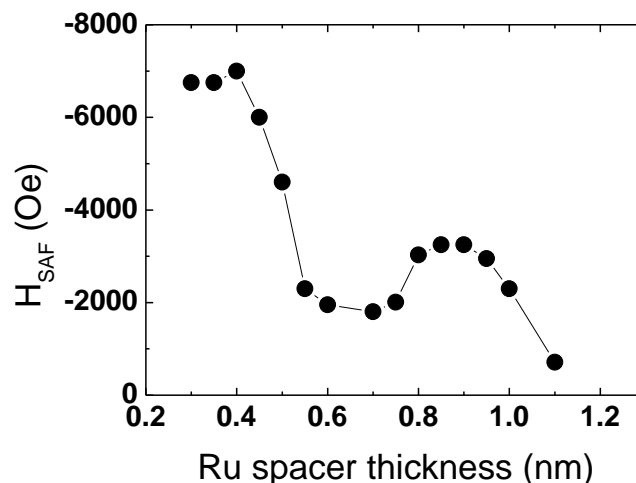


Figure II-16: RKKY coupling field as a function of Ru spacer thickness.

For a Ru thickness of 0.4 nm, the amplitude of the coupling field is very high around -7000 Oe. Upon increasing the Ru thickness, the coupling field decreases quickly to reach a minimum of 2000 Oe between 0.5 and 0.7 nm. A peak is obtained around 0.9 nm, with an amplitude of about -3200 Oe. For thicker spacers, the coupling strength decreases again. Note that for Ru insertions thinner than 0.3 nm it is not possible to measure coupling fields as both layers start to be ferromagnetically coupled, probably due to direct coupling through pinholes. We cannot then consider the first “peak” at small thicknesses as a real maximum since the coupling turns abruptly from an indirect antiferromagnetic to a direct ferromagnetic one at small Ru thicknesses.

According to this study, the best option seems to be using a thickness of Ru spacer around 0.9 nm. Indeed, even though larger RKKY coupling amplitudes can be reached for thinner spacers, they vary really quickly in the range between 0.4 and 0.6 nm. This might induce reproducibility issues as the deposited thickness of Ru may fluctuate a little. Besides, as we have seen in Figure II-15 (a) for a Ru spacer of 0.45 nm, tilted transitions appear for systems with thin insertion layers. On the contrary, for a 0.9 nm thick layer of Ru, perpendicular anisotropy is sufficiently high and we have a relatively large range of thicknesses for which the coupling energy is stable (typically between 0.8 and 1.0 nm). This makes these structures more stable against possible fluctuations of the deposition rates.

## b) Optimization of the Co thickness in the (Co/Pt) multilayers

After setting the Ru insertion thickness to 0.9 nm, we now try to optimize the Co thickness in the multilayers. In the previous series with varying Ru thickness, Co had been fixed at 0.5 nm in the Co/Pt multilayers and as shown in Figure II-15 (c), already good SAF references were obtained. However, to check if the anisotropy and coupling properties could be further enhanced, we investigated the effect of modifying the Co thickness, in a small range around 0.5 nm. For this study, Pt thickness is fixed at 0.25 nm in the multilayers and the thickness of Co is varied between 0.4 and 0.6 nm. In Figure II-17, VSM loops are plotted for three different Co thicknesses. All curves are relatively similar and all SAF structures are working in those cases. Nevertheless, there are slight modifications in the coupling strength and the anisotropy. Indeed, as the Co thickness increases, coercive fields of the bottom and top parts of the SAF decrease. In Figure II-17 (c), for 0.6 nm thick layers of Co, the transitions are clearly less sharp than those of the thinner cases, indicating that perpendicular anisotropy is weaker. This behavior is expected as thicker the magnetic layer is, the smaller the perpendicular anisotropy energy gets.

The coupling field  $H_{\text{SAF}}$ , extracted as presented in Figure II-14, as well as the coercive field  $H_{\text{C1}}$  of the bottom Co/Pt multilayer are shown for all Co thicknesses in Figure II-18. We observe that the coercive field of the bottom Co/Pt multilayer is monotonously decreasing as the thickness of Co is increased. The coupling field does not vary so much between 0.4 and 0.5 nm and then starts decreasing rapidly above 0.5 nm. It thus seems that in order to enhance the width of the antiparallel plateau and perpendicular anisotropy, the Co thickness has to be chosen around 0.4-0.5 nm.

This study allows confirming the order of switching since, as can be observed in Figure II-17, as the thickness of Co increases, the amplitude of the transition at negative fields gets larger. Knowing that the amount of Co is increasing faster in the bottom multilayer, we can then attribute the transition at large positive fields to the top part of the SAF that is in contact with the MgO barrier.

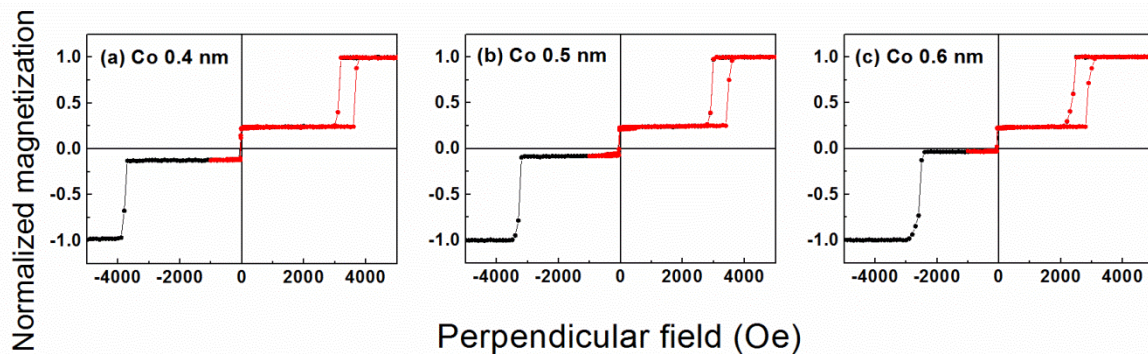


Figure II-17: Magnetic loops measured by VSM with perpendicular applied field for magnetic tunnel junctions with varying Co thickness in the Co/Pt multilayers.

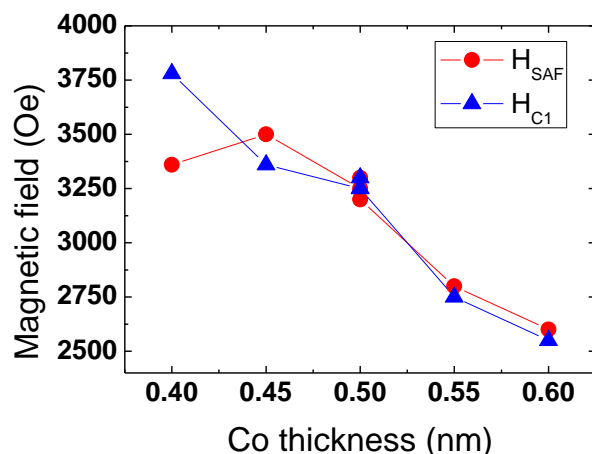


Figure II-18: Variation of the coupling field  $H_{SAF}$  and the coercive field  $H_{C1}$  of the bottom multilayer as a function of Co thickness in the Co/Pt multilayers.

### c) Optimization of the Pt thickness in the (Co/Pt) multilayers

Similarly, the thickness of Pt in the multilayers was tested. In this study, Co was set to 0.5 nm and magnetic tunnel junctions with varying thicknesses of Pt were deposited. We present in Figure II-19 the magnetic loops obtained for three different thicknesses: (a) 0.2 nm, (b) 0.25 nm and (c) 0.4 nm.

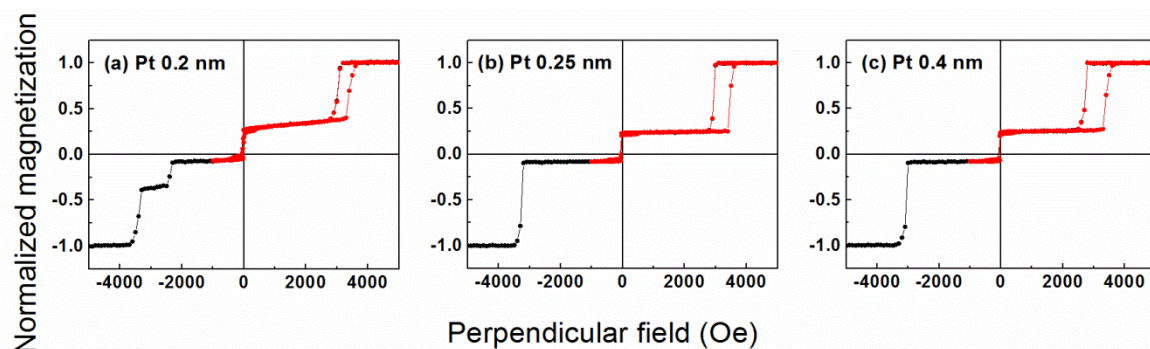


Figure II-19: Magnetic loops measured by VSM with perpendicular applied field for magnetic tunnel junctions with varying Pt thickness in the Co/Pt multilayers.

For 0.2 nm of Pt, we observe that the SAF exhibits tilted transitions and the 3 steps behavior that we presented in Figure II-14 (b), which is not the case for the two other thicknesses. This suggests that a Pt layer as thin as 0.2 nm does not allow keeping a high perpendicular anisotropy. For 0.25 and 0.4 nm thick Pt layers, the

anisotropy is much larger and the transitions appear sharper. Both thicknesses seem to give roughly the same results.

In the same way we did for the Co layer optimization, we plotted the value of the coupling field  $H_{\text{SAF}}$  and the coercive field  $H_{\text{C1}}$  of the bottom multilayer as a function of the Pt thickness. In that case, the coupling field appears to be independent of the Pt thickness and amounts to about 3200 Oe. The coercive field of the bottom part of the SAF however decreases upon increasing the Pt thickness. We did not put a value for 0.2nm thick Pt layers as the SAF switching mechanism is different. It thus seems that to enlarge the antiferromagnetic plateau, thin Pt layers are necessary but they have to be kept thick enough to keep perpendicular anisotropy. A good compromise would be to set the thickness of Pt in the multilayers at 0.25 nm.

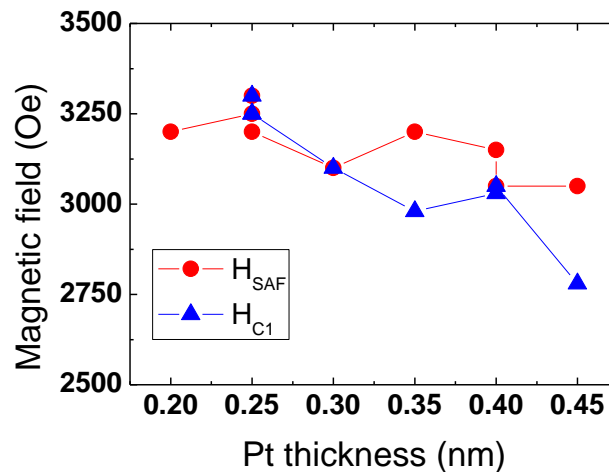


Figure II-20: Variation of the coupling field  $H_{\text{SAF}}$  and the coercive field  $H_{\text{C1}}$  of the bottom multilayer as a function of Pt thickness in the Co/Pt multilayers.

#### d) Optimization of the Pt buffer layer

Finally, we studied the influence of the thickness of the Pt buffer layer. This layer is used to enhance the perpendicular anisotropy of the Co/Pt multilayers that grow upon it. Throughout the beginning of this study on bottom SAF reference optimization, it has been kept at 5 nm. However we wanted to check the influence of the Pt buffer on the magnetic properties of the SAF. As previously, a series of samples has been deposited with Co 0.5 nm and Pt 0.25 nm in the multilayers and various Pt buffer thicknesses. As observed in Figure II-21 (a), for a buffer thickness of 0.25 nm, which is equivalent to the thickness of Pt in the multilayers, the perpendicular anisotropy is very low and there is almost no antiferromagnetic plateau. Increasing

the thickness of the Pt buffer improves the anisotropy as the transitions become sharper for thicker buffers of 1 and 5 nm (Figure II-21 (b) and (c)).

Similarly, the coupling field  $H_{SAF}$  and the coercive field  $H_{C1}$  of the bottom multilayer have been evaluated for all samples and are shown in Figure II-22.  $H_{SAF}$  increases sharply between 0.25 and 2 nm of Pt from 1500 to 3300 Oe. The increase is then much smaller for thicker buffer layers. The coercive field  $H_{C1}$  on the other hand keeps increasing as we increase the Pt thickness. It is relatively stable around 3200 Oe for Pt buffer thicknesses between 1 and 5 nm but it can reach values as high as 3600 Oe for 20 nm thick layers. Even though such large coercive fields can be achieved with very thick Pt buffer layers, it seems reasonable to set it at 5 nm to have a functional structure.

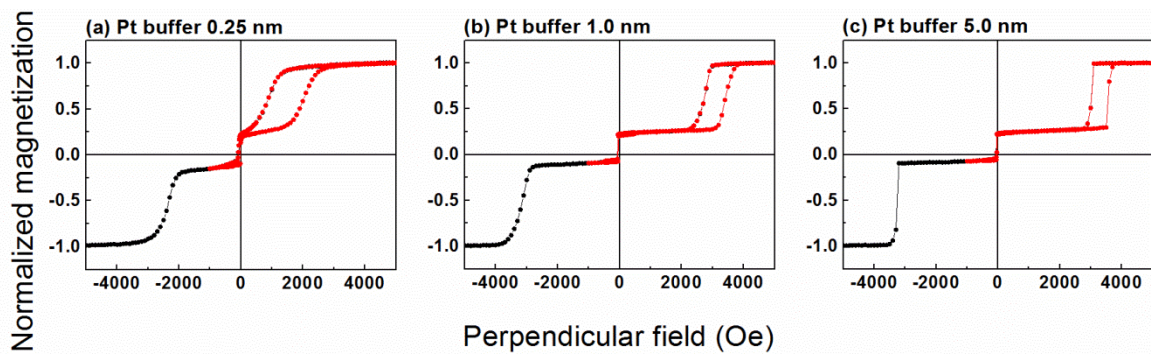


Figure II-21: Magnetic loops measured by VSM with perpendicular applied field for magnetic tunnel junctions with varying Pt buffer thickness.

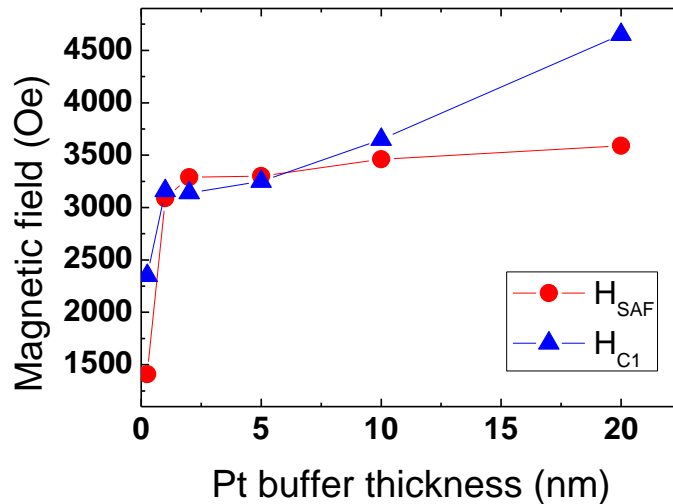


Figure II-22: Variation of the coupling field  $H_{SAF}$  and the coercive field  $H_{C1}$  of the bottom multilayer as a function of Pt buffer thickness.

## II-2.5 Choice of the optimal annealing temperature

In order to determine the best temperature to use for the annealing of our perpendicularly magnetized samples, a series of annealing temperatures was tested in the small furnace on a standard perpendicular MTJ stack. The following stack has been chosen: Ta<sub>3</sub>/Pt<sub>5</sub>/(Co<sub>0.5</sub>/Pt<sub>x</sub>)<sub>5</sub>/Co<sub>0.5</sub>/Ru<sub>0.9</sub>/(Co<sub>0.5</sub>/Pt<sub>x</sub>)<sub>3</sub>/Co<sub>0.5</sub>/Ta<sub>0.3</sub>/CoFeB<sub>1.2</sub>/MgO/FeCoB<sub>1.4</sub>/Ta<sub>1</sub>/Pt<sub>2</sub>. It corresponds to a structure with a bottom SAF reference layer and a top free layer. The Pt thickness is either 0.4 nm which was the former standard value in the structures developed by S. Bandiera [Ban-11] during his thesis in Spintec or 0.25 nm which is the newly chosen thickness.

The annealing temperature has been varied between 260 and 400 °C, 300 °C being the historical standard temperature in the laboratory. Figure II-23 presents the magnetic curves obtained by VSM in the case of the junction with 0.25 nm thick layers of Pt for four different temperatures: 260, 300, 340 and 400 °C.

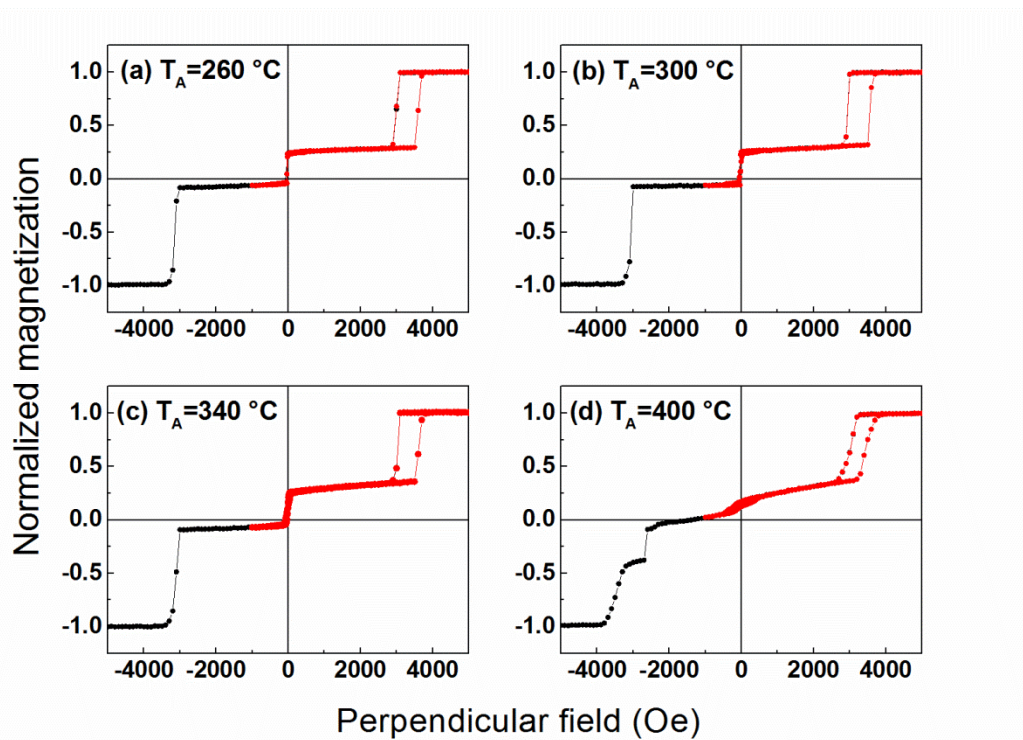


Figure II-23: Magnetic loops measured by VSM with perpendicular applied field for standard perpendicular junctions with Co<sub>0.5</sub>/Pt<sub>0.25</sub> multilayers in the bottom SAF. Three different annealing temperatures are presented: (a) 260 °C (b) 300 °C (c) 340 °C and (d) 400 °C.

As can be seen in the curves, for the first two temperatures, the magnetic cycles are almost identical whereas for a large temperature like 400 °C, the magnetic anisotropy appears really reduced, with strongly tilted transitions. For the intermediate temperature of 340 °C, we still observe abrupt transitions in the SAF but the loop on the top FeCoB layer seems to be more tilted. Zooms on the minor

loops performed on the top storage layer are shown in Figure II-24. From this graph, we see that for an annealing temperature of 300 °C, we have a rather good perpendicular anisotropy, with the possibility to stabilize two magnetic states as the cycle is fully remanent (note that due to the antiferromagnetic coupling through MgO, the cycle is shifted towards negative fields with an off-set of about -30 Oe). As the annealing temperature increases, a progressive decrease of the perpendicular anisotropy is observed: there is a loss of the remanence and at 360 °C a typical planar signal is visible.

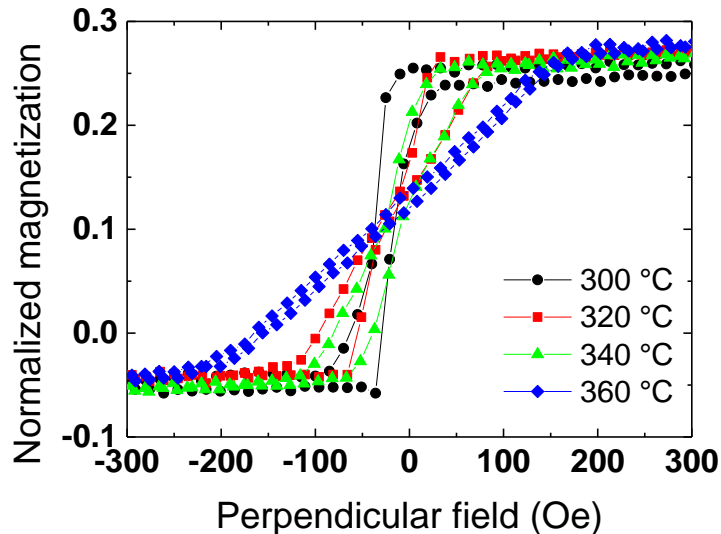


Figure II-24: Minor loops on the top FeCoB storage layer measured by VSM with perpendicular applied field for different annealing temperatures.

The transport properties have been evaluated, using the CIPT technique. In Figure II-25, we show the evolution of the TMR signal as a function of annealing temperature for the junctions with two values of Pt thickness in the multilayers of the SAF. In both cases the trend is the same and looks like the results quoted in the literature. There is first an increase in TMR as the crystallization process occurs. TMR is only 7 % in the case of a non-annealed sample (the data point is not shown on the scale of Figure II-25, as putting it will strongly affect the legibility of the figure). The signal reaches a maximum of about 100 % at the annealing temperature of 340 °C. It decreases then down to about 35 % at 400 °C. The loss of TMR for high annealing temperatures seems then to be due to the reduction in perpendicular anisotropy. However, the signal appears to be maintained for temperatures as high as 380 °C whereas from the magnetic characterizations we have seen that the anisotropy starts decreasing from 320 °C. This is due to the fact that for those temperatures, we are still able to fully saturate the storage layer perpendicularly in both orientations with the maximum field of the CIPT tool. Our results thus agree with other studies that show a link between perpendicular anisotropy and magnetoresistance [Wan-11, Nat-13, Nis-10a].

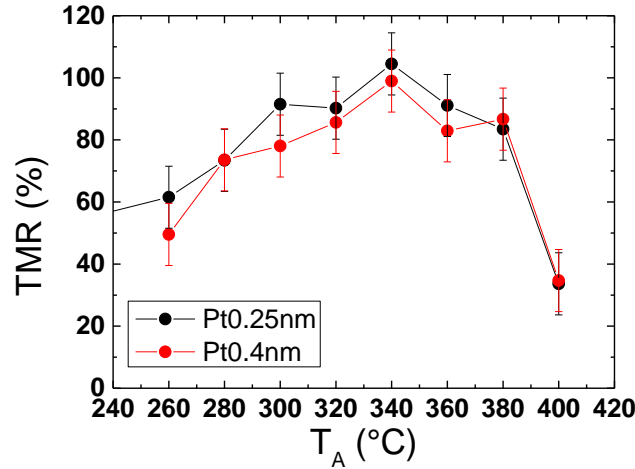


Figure II-25: Variation of the TMR signal as a function of annealing temperature for standard magnetic tunnel junctions with bottom SAF reference and varying thicknesses of Pt in the multilayers.

The similarity in the curves obtained for the two thicknesses of Pt suggests that the diffusion of Pt should not play an important part in this range of annealing temperature. From this curve, the optimal temperature seems then to be 340 °C with this set-up, but a good thermal endurance can be maintained for temperatures as high as 380 °C, if we only take into account the transport properties. However, knowing that the best magnetic properties are obtained at 300 °C for the present magnetic thickness and that the TMR signal appears almost constant between 300 and 380 °C, we will then choose 300 °C as the standard annealing temperature for our perpendicular samples.

## II-2.6 Conclusions

The use of RKKY coupling is particularly interesting to create synthetic antiferromagnetic reference layers that will have the advantage of exhibiting reduced stray fields once patterned into small size devices. However, in the case of magnetic tunnel junctions with perpendicular anisotropy, there are several parameters to master in order to get an optimal magnetic behavior.

In this part, we have shown that the thicknesses of the different layers composing the SAF must be adapted to get large perpendicular anisotropy and a good stability of the antiparallel plateau at the same time. According to the different series of samples that have been made the final stack we will be choosing as the bottom reference of

our magnetic junctions is the following: substrate/Ta<sub>3</sub>/Pt<sub>5</sub>/(Co<sub>0.5</sub>/Pt<sub>0.25</sub>)<sub>n</sub>/Co<sub>0.5</sub>/Ru<sub>0.9</sub>/(Co<sub>0.5</sub>/Pt<sub>0.25</sub>)<sub>m</sub>/Co<sub>0.5</sub>/Ta<sub>0.3</sub>/CoFeB<sub>x</sub>, where thicknesses are given in nm. The choice of the thickness  $x$  of CoFeB will be detailed in the following part. The numbers of repeats  $n$  and  $m$  of the Co/Pt multilayers will be adapted to the magnetization of the CoFeB layer used in the bottom electrode so as to optimize the ratio  $M_1/M_2$ , in order to minimize stray fields at small pillar sizes.

These structures were found to exhibit a rather large thermal endurance as annealing temperatures up to 380 °C can be applied without any deterioration of the transport properties. However, to maintain a good enough perpendicular anisotropy, the annealing temperature will be limited to 300 °C. Note that we could probably maintain the anisotropy properties at higher temperatures by choosing a thinner storage layer.

## II-3. Optimization of magnetic electrode thicknesses

Having optimized the composition of Co/Pt multilayers of the bottom SAF reference, one now has to adjust the thicknesses of the bottom and top CoFeB electrodes and find windows for which the magnetizations of the electrodes is perpendicular-to-plane, with a thickness large enough to maximize tunnel magnetoresistance. Knowing the influence of these thicknesses on the transport properties is essential to be able to design a device exhibiting the best performances as possible.

In this study, we will work on samples with the following stack: substrate/Ta<sub>3</sub>/Pt<sub>5</sub>/(Co<sub>0.5</sub>/Pt<sub>0.25</sub>)<sub>5</sub>/Co<sub>0.5</sub>/Ru<sub>0.9</sub>/(Co<sub>0.5</sub>/Pt<sub>0.25</sub>)<sub>3</sub>/Co<sub>0.5</sub>/Ta<sub>0.3</sub>/CoFeB/MgO/FeCoB/Ta<sub>1</sub>/Pt<sub>2</sub>, with thicknesses in nm. They comprise the optimal Co/Pt SAF structure we have developed previously and can be schematically represented as M<sub>1</sub>/Ru/M<sub>2</sub>/MgO/M<sub>3</sub>. For the bottom electrode we use our Co-rich Co<sub>60</sub>Fe<sub>20</sub>B<sub>20</sub> alloy and for the top electrode the Fe-rich Fe<sub>72</sub>Co<sub>8</sub>B<sub>20</sub> one is employed. They are deposited on standard 60 nm thick CuN buffers to allow CIPT measurements and annealed at 300 °C for 1 hour.

### II-3.1 Determination of the critical thicknesses

Two series of samples were deposited in which the thicknesses of CoFeB and FeCoB are varied independently. For varying thickness of bottom CoFeB, the top FeCoB layer is kept at 1.4 nm while in the case of varying top FeCoB, the bottom CoFeB remains at 1.2 nm. Examples of the magnetic loops that are obtained by VSM with perpendicular applied field are shown in Figure II-26. As observed before, coming from positive field saturation, the first transition around 2800 Oe corresponds to the reversal of the top part of the bottom SAF M<sub>2</sub>. This can be verified by the increase of its relative contribution as the bottom CoFeB thickness increases (left part of Figure II-26). It can be seen rather easily as the amplitude of the signal at zero field keeps decreasing. The central transition corresponds to the top free FeCoB layer M<sub>3</sub> and the last transition at negative applied fields represents the switching of the bottom hardest part of the SAF which has the largest coercive field, M<sub>1</sub>.

For the samples with bottom CoFeB thicknesses of 0.8, 1.0 and 1.2 nm (Figure II-26, left), perfectly horizontal magnetic signals are measured between sharp transitions. This indicates that the anisotropy is fully perpendicular in the whole structure. In the case of a 1.6 nm thick CoFeB layer, a slope appears in the loop, characteristic of a hard magnetic signal. It is not symmetrical with respect to the applied field, reflecting that it comes from the SAF electrode. The magnetization of the top part of the SAF starts to tilt away from the perpendicular direction and as the

field is decreased it stabilizes  $M_2$  in the perpendicular negative direction, explaining why no slope is observed for negative applied field. In the case of varying top FeCoB thickness (Figure II-26, right), we see the magnetization of the FeCoB layer going from fully perpendicular to planar, a hard axis behavior being clearly recognizable for a thickness of 1.7 nm.

An important parameter to know is the critical thickness, that is to say the thickness at which the out-of-plane to in-plane reorientation of the magnetization occurs. This will allow knowing the upper limit with which we can work. Even though it is not possible to accurately determine the critical thickness in the case of the bottom CoFeB electrode, we can estimate it to be around 1.6 nm. For the top FeCoB layer, a critical thickness of 1.7 nm is estimated from the magnetic loops.

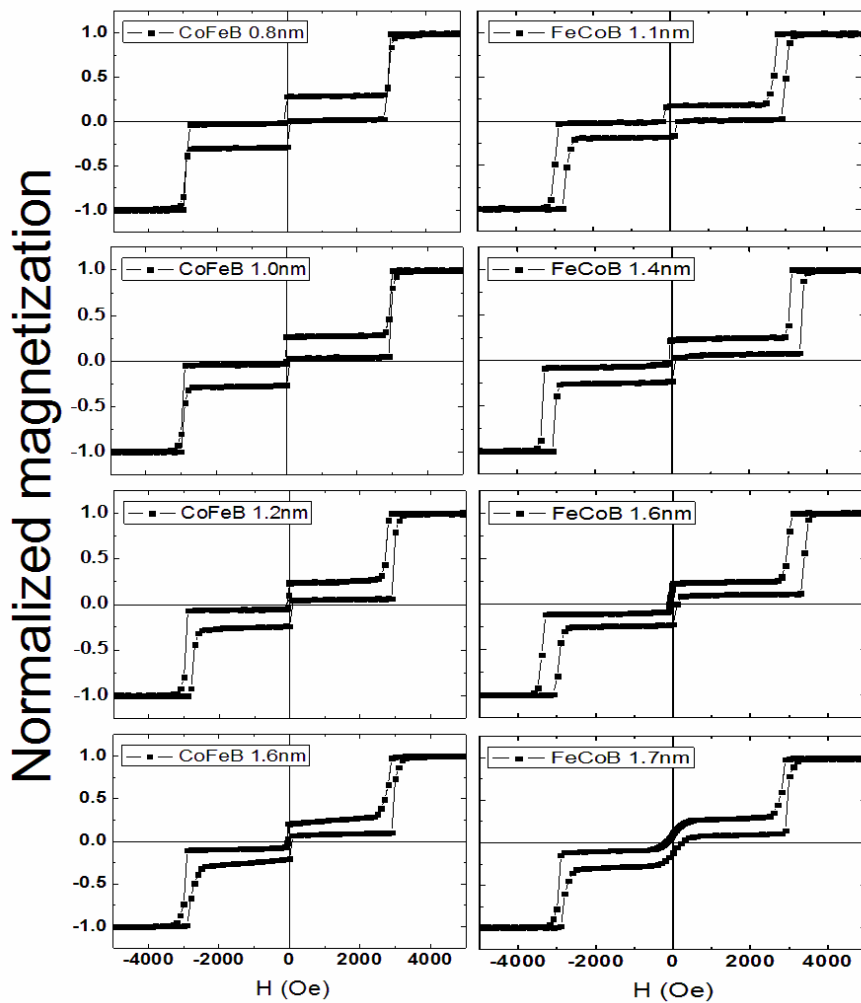


Figure II-26: Magnetic cycles measured by VSM with a perpendicular field for varying thicknesses of bottom CoFeB (left) and top FeCoB (right) electrodes, keeping thicknesses of 1.4 nm for the top FeCoB layer and 1.2 for the bottom CoFeB layer, respectively.

## II-3.2 Determination of saturation magnetization and magnetic dead layer thickness

Series of samples with varying CoFeB or FeCoB enable us to extract materials parameters such as saturation magnetization  $M_s$  and magnetic dead layer thickness  $t_d$ . In a very simple model, the magnetic dead layer corresponds to the non-magnetic layer that forms at the interfaces due to the intermixing of the different materials. It is supposed to preferentially arise at the interface with Ta.

Reminding that our structures can be schematically represented as  $M_1/\text{Ru}/M_2/\text{MgO}/M_3$ , there are always two contributions that stay constant when varying the thickness of CoFeB or FeCoB. They can be used for normalization, enabling us to get rid of any calibration uncertainty of our VSM tool. In Figure II-27, we present the variations of  $M_2/M_1$  for varying bottom CoFeB thickness and  $M_3/M_1$  for varying top FeCoB.

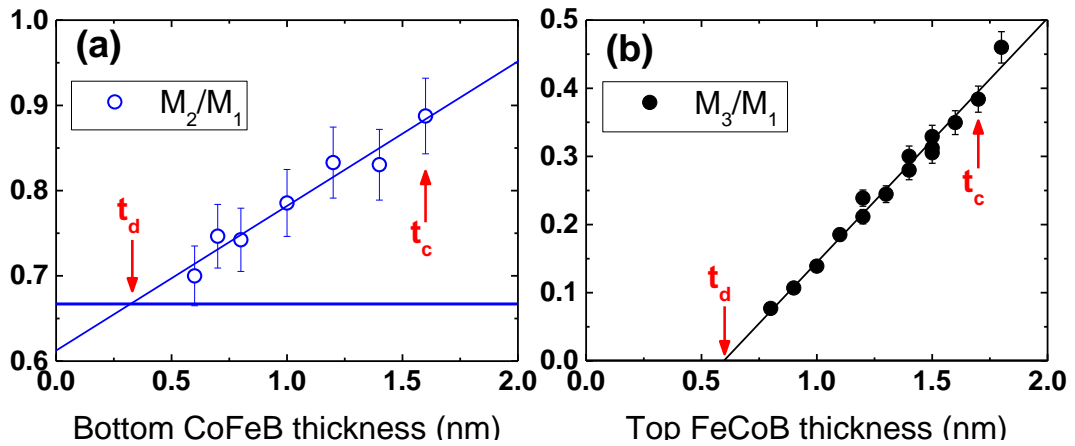


Figure II-27: Magnetization ratio  $M_2/M_1$  as a function of bottom CoFeB thickness (a) and  $M_3/M_1$  as a function of top FeCoB thickness (b). The horizontal line on the left graph corresponds to the ratio  $M_2/M_1$  for zero CoFeB thickness, that is to say  $2/3$ .

The  $M_2/M_1$  ratio can be expressed as

$$\frac{M_2}{M_1} = \frac{4t_{Co}M_{sCo} + (t_{CoFeB} - t_d)M_{sCoFeB}}{6t_{Co}M_{sCo}}$$

where  $t_{Co}$  is the Co thickness in the Co/Pt multilayers,  $t_d$  the magnetic dead layer thickness and  $M_s$  the Co and CoFeB saturation magnetizations.

From Figure II-27 (a) the magnetic dead layer thickness of the bottom CoFeB layer can be extracted at the intercept between the linear fit of the experimental data and the theoretical ratio  $M_2/M_1$  without any CoFeB which is  $2/3$ . A magnetic dead layer  $t_d$  of  $0.33 \pm 0.02$  nm is obtained. This treatment assumes all the layers of Co in

the Co/Pt multilayers have the same contribution, that is to say the same saturation magnetization, despite different interfaces (Co/Ru, Ru/Co or Co/Ta). This also supposes that there is no extra dead layer forming at the Co/Ta interface.

Knowing that  $M_1$  is composed of 6 Co layers of 0.5 nm each, which saturation magnetization  $M_{sCo}$  has been estimated in a previous study around  $1200 \text{ emu.cm}^{-3}$  (about 15% smaller than bulk Co due to Co-Pt interdiffusion) [Ban-10], the fitted slope enables calculating the saturation magnetization of the bottom CoFeB layer,  $M_{sCoFeB} = 600 \pm 30 \text{ emu.cm}^{-3}$ .

A similar treatment can be performed for the top FeCoB layer, using this time the  $M_3/M_1$  ratio.

$$\frac{M_3}{M_1} = \frac{(t_{FeCoB} - t_d)M_{sFeCoB}}{6t_{Co}M_{sCo}}$$

From the fitted data of Figure II-27 (b), we can extract a magnetic dead layer for the top FeCoB electrode of  $0.60 \pm 0.04 \text{ nm}$  and a saturation magnetization  $M_{sFeCoB} = 1300 \pm 60 \text{ emu.cm}^{-3}$ .

One notices that the magnetically dead layer in the case of the top FeCoB layer is almost twice thicker than the one measured for the bottom CoFeB layer. This can be explained by the difference in thickness of the Ta layers that are in contact with the CoFeB and FeCoB electrodes, respectively. Indeed, it has been shown that the dead layer formation mostly comes from the interface with Ta. In the case of the top FeCoB layer, the 1 nm thick Ta cap that is deposited on top of it is much thicker than the 0.3 nm Ta insertion onto which the bottom CoFeB grows. One can then assume more intermixing will happen if the Ta thickness is larger. To rule out any influence of the composition of the CoFeB alloy, a series of samples with bottom Fe-rich FeCoB layer has been deposited. The same data treatment is performed as shown in Figure II-28. From this plot a dead layer  $t_d = 0.24 \text{ nm}$  and a saturation  $M_{sFeCoBbottom} = 1030 \text{ emu.cm}^{-3}$  are extracted. This indicates that we have roughly the same magnetic dead layer thickness whatever the composition we use in the bottom electrode.

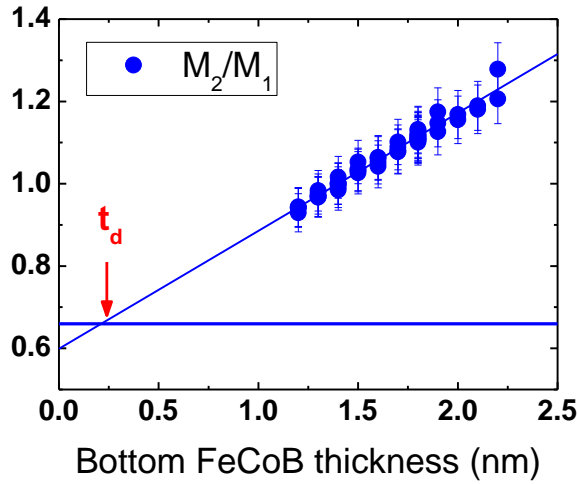


Figure II-28: Magnetization ratio  $M_2/M_1$  as a function of bottom Fe-rich FeCoB thickness. The horizontal line corresponds to the ratio  $M_2/M_1$  for zero FeCoB thickness, that is to say  $2/3$ .

Note that the values we obtained for the saturation magnetizations of both compositions, CoFeB and FeCoB, are in good qualitative agreement with those quoted in the literature [Wor-11, Ike-12]. However, the values reported in the various publications exhibit a rather large scatter. This can be attributed to the strong dependence of  $M_s$  on annealing conditions due to the variations of residual boron concentration [Nat-12].

In order to check the validity of our treatment, we can calculate the theoretical ratios that are supposed to be constant in both cases:  $M_3/M_1$  for varying bottom CoFeB thickness and  $M_2/M_1$  for varying top FeCoB thickness. To do this we used the values of  $M_s$  and  $t_d$  extracted from Figure II-27 and found  $M_3/M_1 = 0.32 \pm 0.03$  and  $M_2/M_1 = 0.81 \pm 0.08$ . In Figure II-29, we compare these theoretical ratios with those extracted from the VSM loops measured on both series of samples. They are found reasonably constant and in good agreement with theoretical calculated values.

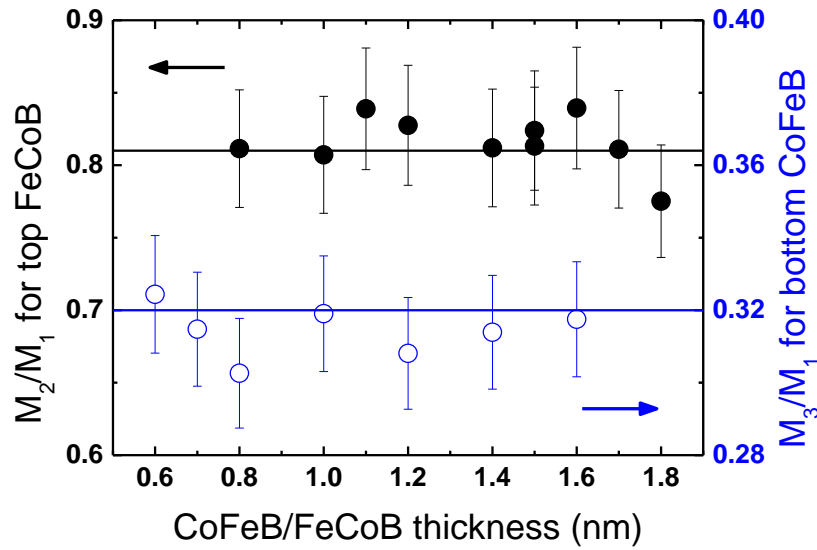


Figure II-29: Magnetization ratio of the constant magnetic contributions  $M_2/M_1$  as a function of top FeCoB thickness, filled black circles, left-hand scale, and  $M_3/M_1$  as a function of bottom CoFeB thickness, open blue circles, right-hand scale. Horizontal lines correspond to the theoretical values, 0.81 and 0.32, respectively.

### II-3.3 Anisotropy measurements on the top electrode

In order to study the variation of the anisotropy constant for the top FeCoB layer, a series of top electrodes with varying thicknesses of FeCoB was deposited. The stack is the following: Ta<sub>3</sub>/FeCoB<sub>0.3</sub>/MgO/FeCoB<sub>x</sub>/Ta<sub>1</sub>/Pt<sub>2</sub>, with thicknesses given in nm.  $x$  varies between 1 and 2.4 nm. The thin bottom FeCoB layer is non-magnetic (as it is thinner than the expected dead layer thickness) and is used to try keeping the same environment for the MgO tunnel barrier as in full junctions.

The anisotropy constant is evaluated using the method presented in Chapter I. Magnetic loops are measured with VSM both with perpendicular and planar configurations of the magnetic field. Only top electrodes are needed since, in the case of full junction, the signal coming from the bottom reference layer would make it difficult to extract the contribution of the top electrode alone, in particular with planar applied field. In Figure II-30, we present the variation of  $K_{eff,t}$  as a function of effective magnetic thickness, that is to say taking into account the magnetic dead layer. This treatment is then complementary to the previous study as it is necessary to know the magnetic dead layer thickness at that stage.

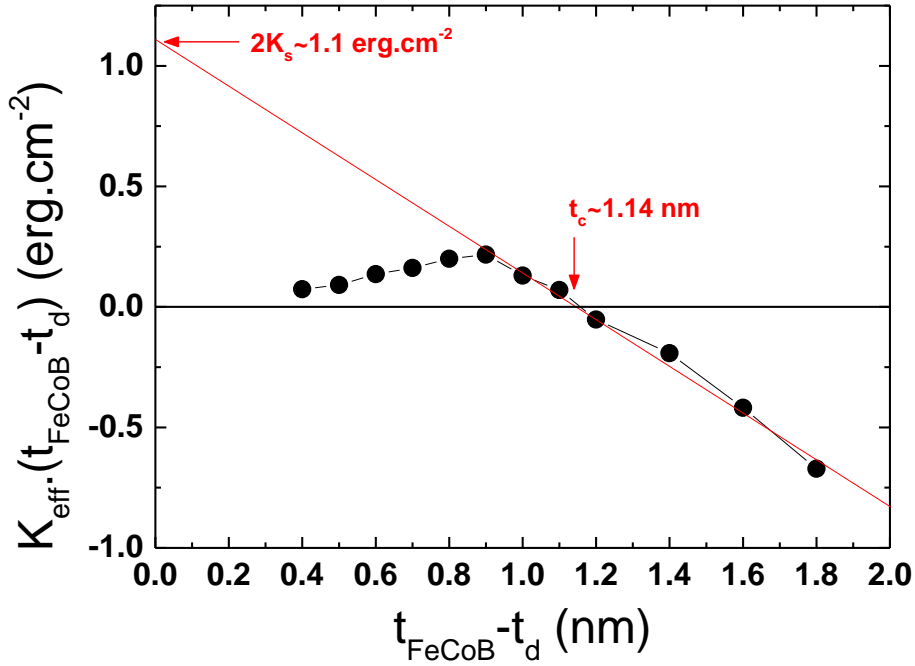


Figure II-30: Variation of  $K_{\text{eff}} \cdot t$  as a function of effective thickness for top FeCoB electrodes capped with Ta.

Recalling that the effective anisotropy constant is expressed as  $K_{\text{eff}} = K_v - 2\pi M_s^2 + \frac{2K_s}{t}$ , we can extrapolate the linear trend to estimate the value of  $2K_s$ . We find here about 1.1 erg.cm<sup>-2</sup>. Assuming a negligible volume anisotropy [Ike-10, Liu-12], the slope gives a saturation magnetization  $M_s = 1240$  emu.cm<sup>-3</sup>, which is in good agreement with the value extracted from the analysis of the full junctions in the previous part. This also confirms that the assumption made on  $K_v$  is not far from reality. At the zero intercept, we find the value of the critical thickness which is in that case around 1.14 nm. This agrees as well with the previously extracted value that is  $1.7 - 0.6 = 1.1$  nm.

Note that for small thicknesses the evolution of  $K_{\text{eff}} \cdot t$  deviates from the linear behavior. This is commonly observed and might be explained by a variation of the  $M_s$  value for very thin layers.

### II-3.4 Correlation between magnetic and transport properties

In order to study the transport properties of our magnetic tunnel junctions as a function of bottom CoFeB and top FeCoB thicknesses, the same series of samples were measured using the CIPT set-up. Figure II-31 (a) shows that as the thickness of

CoFeB increases, the TMR ratio increases as well to reach about 90% for thicknesses between 1.0 and 1.6 nm. It is followed by a decrease in the TMR signal when the low-field slope appears in the magnetic cycles (as seen Figure II-26). As explained earlier, this slope is attributed to a tilt in the magnetization of the top part of the SAF  $M_2$  away from the perpendicular direction. Perfect parallel and antiparallel states cannot be reached anymore with the available maximum field of the Capres tool, which leads to an artificial decrease in TMR. In the case of varying top FeCoB thickness the same increase of TMR with thickness is observed with a similar asymptotic value of 90% for thicknesses between 1.2 and 1.7 nm. Note that even if the magnetization gets planar for the thickest layers, as long as their saturation field is smaller than the maximum field of the CIPT tool (1500 Oe), we are still able to get the full TMR signal.

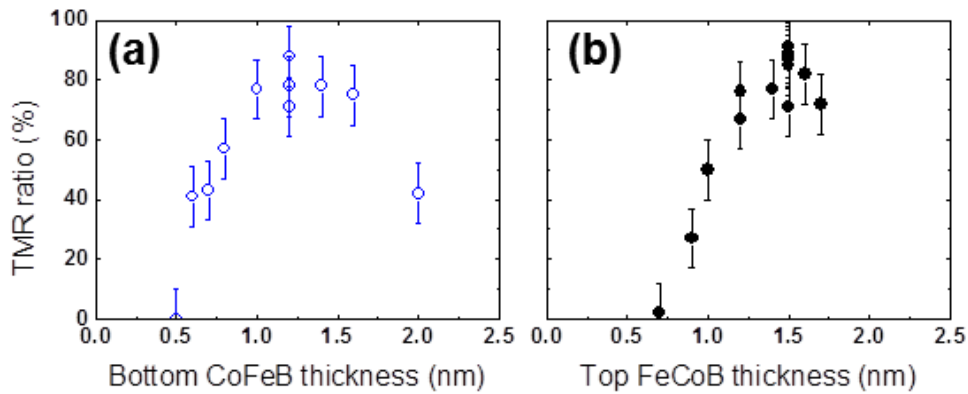


Figure II-31: TMR ratio as a function of bottom CoFeB (a) and top FeCoB (b) nominal thicknesses

One can note that the maximum TMR value is not obtained for the same nominal thicknesses of bottom CoFeB and top FeCoB. This can be explained by different magnetic dead layer thicknesses in both cases: 0.33 nm in the bottom CoFeB layer and 0.6 nm in the top FeCoB layer. A plot of the TMR ratio as a function of effective thickness, i.e. correcting the nominal values from their respective dead layer contributions, is given in Figure II-32. Identical thickness dependences are now obtained: the TMR ratio starts increasing as soon as the effective thickness is larger than 0.3 nm and the maximum signal is reached when it is greater than 0.6 nm. Note that the RA product for these two series of samples is essentially constant around  $30 \Omega\mu\text{m}^2$ , showing that the decrease in TMR for small thicknesses is not related to a deterioration of the quality of the MgO barrier but rather to a progressive decrease of the spin polarization through thinner magnetic electrodes.

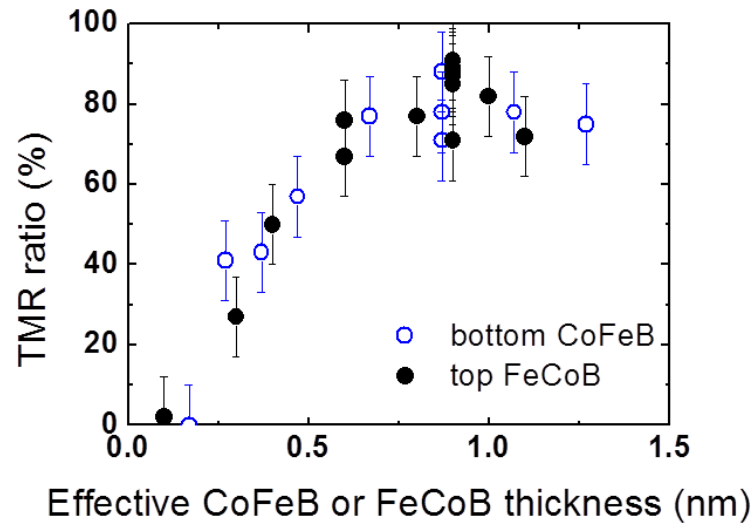


Figure II-32: TMR ratio as a function of bottom CoFeB (blue open circles) and top FeCoB (black filled circles) thicknesses, respectively, after subtraction of their corresponding dead layer thicknesses.

## **II-4. Conclusions**

In this Chapter, we have seen that by carefully adjusting the thickness of the Ta insertion that structurally decouples the CoFeB layer from the adjacent Co/Pt multilayer in the reference layer enables optimizing the transport properties of the magnetic tunnel junctions. The optimal Ta thickness is found around 0.3-0.4 nm.

To harden the reference layer Co/Pt or Co/Pd multilayers may be used. They can advantageously be put in a synthetic antiferromagnetic configuration, which is known to reduce the stray fields acting on the storage in patterned devices. In these systems, all magnetic layers thicknesses have to be chosen carefully to obtain the best magnetic properties as possible. The annealing temperature has also to be adjusted if one wants to enhance simultaneously the anisotropy and the transport properties. We found that with our laboratory furnace, a good compromise is obtained at 300 °C.

Finally, we saw that optimization of the thicknesses of the bottom CoFeB and top FeCoB layers allows maximizing the TMR signal. To determine the operating window of our structures, it is necessary to know the magnetic dead layer thicknesses that depend on the growth conditions, in particular on the nature of the seed or buffer layer in contact with the CoFeB alloy. The upper limit is defined by the critical thickness that is when out-of-plane to in-plane reorientation of the magnetization occurs. A maximal TMR value is found as soon as the effective magnetic thicknesses are greater than 0.6 nm.

## II-5. References

- [Ban-10] S. Bandiera, R. C. Sousa, Y. Dahmane, C. Ducruet, C. Portemont, V. Baltz, S. Auffret, I. L. Prejbeanu, and B. Dieny, *Comparison between synthetic antiferromagnets and single hard layers as reference layer in perpendicular magnetic tunnel junctions*, [IEEE Magn. Lett.](#) **1**, 3000204 (2010).
- [Ban-11] S. Bandiera, *Jonctions tunnel magnétiques à anisotropie perpendiculaire et écriture assistée thermiquement*, [PhD Thesis](#), Grenoble University (2011).
- [Bru-93] P. Bruno, *Oscillations of interlayer exchange coupling vs. ferromagnetic-layers thickness*, [Europhys. Lett.](#) **23**, 615-620 (1993).
- [Bru-95] P. Bruno, *Theory of interlayer magnetic coupling*, [Phys. Rev. B](#) **52**, 411-436 (1995).
- [Cuc-13] L. Cuchet, B. Rodmacq, S. Auffret, R. C. Sousa, C. Ducruet, and B. Dieny, *Influence of a Ta spacer on the magnetic and transport properties of perpendicular magnetic tunnel junctions*, [Appl. Phys. Lett.](#) **103**, 052402 (2013).
- [Cuc-14] L. Cuchet, B. Rodmacq, S. Auffret, R. C. Sousa, and B. Dieny, *Influence of magnetic electrodes thicknesses on the transport properties of magnetic tunnel junctions with perpendicular anisotropy*, [Appl. Phys. Lett.](#) **105**, 052408 (2014).
- [Fau-02] J. Faure-Vincent, C. Tiusan, C. Bellouard, E. Popova, M. Hehn, F. Montaigne, and A. Schuhl, *Interlayer magnetic coupling interactions of two ferromagnetic layers by spin polarized tunnelling*, [Phys. Rev. Lett.](#) **89**, 107206 (2002).
- [Ike-10] S. Ikeda, K. Miura, H. Yamamoto, K. Mizunuma, H. D. Gan, M. Endo, S. Kanai, J. Hayakawa, F. Matsukura, and H. Ohno, *A perpendicular-anisotropy CoFeB–MgO magnetic tunnel junction*, [Nature Mater.](#) **9**, 721-724 (2010).
- [Ike-12] S. Ikeda, R. Koizumi, H. Sato, M. Yamanouchi, K. Miura, K. Mizunuma, H. -D. Gan, F. Matsukura, and H. Ohno, *Boron composition dependence of magnetic anisotropy and tunnel magnetoresistance in MgO/CoFe(B) based stack structures*, [IEEE Trans. Magn.](#) **48**, 3829-3832 (2012).
- [Kas-56] T. Kasuya, *A theory of metallic ferro- and antiferromagnetism on Zener's model*, [Prog. Theor. Phys.](#) **16**, 45-57 (1956).
- [Koz-10] X. Kozina, S. Ouardi, B. Balke, G. Stryganyuk, G. H. Fecher, C. Felser, S. Ikeda, H. Ohno and E. Ikenaga, *A nondestructive analysis of the B diffusion in Ta–CoFeB–MgO–CoFeB–Ta magnetic tunnel junctions by hard X-ray photoemission*, [Appl. Phys. Lett.](#) **96**, 072105 (2010).

[Liu-12] T. Liu, J. W. Cai, and Li Sun, *Large enhanced perpendicular magnetic anisotropy in CoFeB/MgO system with the typical Ta buffer replaced by an Hf layer*, [AIP Advances](#) **2**, 032151 (2012).

[Mor-04] J. Moritz, F. Garcia, J.-C. Toussaint, B. Dieny, and J.-P. Nozières, *Orange peel coupling in multilayers with perpendicular magnetic anisotropy: Application to (Co/Pt)-based exchange-biased spin valves*, [Europhys. Lett.](#) **65**, 123-129 (2004).

[Nat-12] A. Natarajarathinam, Z. R. Tadisina, T. Mewes, S. Watts, E. Chen, and S. Gupta, *Influence of capping layers on CoFeB anisotropy and damping*, [J. Appl. Phys.](#) **112**, 053909 (2012).

[Nat-13] A. Natarajarathinam, B. D. Clark, A. Singh, and S. Gupta, *Influence of annealing on tunnelling magnetoresistance of perpendicular magnetic tunnel junctions*, [J. Phys. D: Appl. Phys.](#) **46**, 095002 (2013).

[Née-62] L. Néel, *Sur un nouveau mode de couplage entre les aimantations de deux couches minces ferromagnétiques*, [C. R. Hebd. Séances Acad. Sci.](#) **255**, 1976 (1962).

[Nis-10a] L. E. Nistor, B. Rodmacq, C. Ducruet, C. Portemont, I. L. Prejbeanu, and B. Dieny, *Correlation between perpendicular anisotropy and magnetoresistance in magnetic tunnel junctions*, [IEEE Trans. Magn.](#) **46**, 1412 (2010).

[Nis-10b] L. E. Nistor, B. Rodmacq, S. Auffret, A. Schuhl, M. Chshiev, and B. Dieny, *Oscillatory interlayer exchange coupling in MgO tunnel junctions with perpendicular magnetic anisotropy*, [Phys. Rev. B](#) **81**, 220407(R) (2010).

[Par-91] S. S. P. Parkin, *Systematic variation of the strength and oscillation period of indirect magnetic exchange coupling through the 3d, 4d, and 5d transition metals*, [Phys. Rev. Lett.](#) **67**, 3598 (1991).

[Rud-54] M. A. Ruderman, and C. Kittel, *Indirect exchange coupling of nuclear magnetic moments by conduction electrons*, [Phys. Rev.](#) **96**, 99-102 (1954).

[Slo-89] J. C. Slonczewski, *Conductance and exchange coupling of 2 ferromagnets separated by a tunnelling barrier*, [Phys. Rev. B](#) **39**, 6995 (1989).

[Wan-11] W.-G. Wang, S. Hageman, M. Li, S. Huang, X. Kou, X. Fan, J. Q. Xiao, and C. L. Chien, *Rapid thermal annealing study of magnetoresistance and perpendicular anisotropy in magnetic tunnel junctions based on MgO and CoFeB*, [Appl. Phys. Lett.](#) **99**, 102502 (2011).

[Wor-11] D. C. Worledge, G. Hu, D. W. Abraham, J. Z. Sun, P. L. Trouilloud, J. Nowak, S. Brown, M. C. Gaidis, E. J. O'Sullivan, and R. P. Robertazzi, *Spin torque switching of perpendicular Ta/CoFeB/MgO-based magnetic tunnel junctions*, [Appl. Phys. Lett.](#) **98**, 022501 (2011).

[Yam-12] H. Yamamoto, J. Hayakawa, K. Miura, K. Ito, H. Matsuoka, S. Ikeda, and H. Ohno, *Dependence of magnetic anisotropy in  $\text{Co}_{20}\text{Fe}_{60}\text{B}_{20}$  free layers on capping layers in MgO-based magnetic tunnel junctions with in-plane easy axis*, [Appl. Phys. Express](#) **5**, 053002 (2012).

[Yos-57] K. Yosida, *Magnetic properties of Cu-Mn alloys*, [Phys. Rev.](#) **106**, 893-898 (1957).

# CHAPTER III

## Towards double junctions with perpendicular anisotropy

<b>III-1. Influence of a MgO capping.....</b>	<b>98</b>
III-1.1 Effect on the magnetic properties.....	98
III-1.2 Anisotropy of top electrodes with Ta or MgO capping.....	101
III-1.3 Effect of changing the nature of the insertion .....	103
III-1.4 Nature of the two MgO barriers .....	106
<b>III-2. Development of magnetic tunnel junctions with a top reference.....</b>	<b>108</b>
III-2.1 Metallic synthetic antiferromagnetic layers .....	108
III-2.2 Optimization of single junctions with SAF top references .....	109
III-2.3 Thermal endurance of the junctions with a top reference.....	114
III-2.4 Compatibility with the bottom SAF references .....	115
<b>III-3. Double junctions with perpendicular anisotropy .....</b>	<b>117</b>
III-3.1 Advantages of double junctions.....	117
III-3.2 Magnetic properties of perpendicular double magnetic tunnel junctions .....	118
III-3.3 Transport properties of perpendicular double magnetic tunnel junctions .....	120
<b>III-4. Conclusions .....</b>	<b>123</b>
<b>III-5. References .....</b>	<b>124</b>



As we have seen in Chapter I, a large perpendicular anisotropy has been found to arise at the metal/oxide interfaces. If in the first developments of perpendicular magnetic tunnel junctions the capping layers were mostly metallic materials such as Ru or Ta (see Chapter II), some research groups started recently to study structures with a second MgO layer used as a capping. This was indeed proved to enhance significantly the magnetic anisotropy of the system.

In parallel, there have been several works on dual magnetic tunnel junctions with planar anisotropy. They comprise two tunnel barriers and two polarizing layers on both sides of a storage layer. The advantages of such structures are mostly seen for a use in STT-MRAM applications. They can indeed reduce drastically the critical current density as well as the bias voltage dependence of TMR.

We propose then to combine the advantages of both perpendicular anisotropy and double magnetic tunnel junctions by building perpendicularly magnetized structures with a double barrier configuration and two synthetic antiferromagnetic reference layers. To do so, we will study in a first part the beneficial effect on the anisotropy of introducing an MgO capping layer in our standard magnetic tunnel junctions with a bottom Co/Pt SAF reference. We will then show how Co/Pd top reference layers can be developed so as to present transition fields compatible with those of the bottom reference. Finally, we will combine all the different magnetic blocks to create a complete double junction with perpendicular anisotropy [\[Cuc-15\]](#).

### III-1. Influence of a MgO capping

As already pointed out in the introduction, perpendicular magnetic anisotropy arises at the metal/oxide interface [Mon-02, Rod-09]. Although the standard Ta capping layer used in our previous samples gave relatively good results in terms of transport and anisotropy, one could imagine replacing it by a second oxide interface to see if perpendicular anisotropy can be further enhanced.

#### III-1.1 Effect on the magnetic properties

In order to investigate the effect of introducing a MgO capping above the top free layer, we deposited a series of junctions composed of our standard bottom reference and a top free layer with varying FeCoB thicknesses : Ta<sub>3</sub>/Pt<sub>5</sub>/(Co<sub>0.5</sub>/Pt<sub>0.25</sub>)<sub>5</sub>/Co<sub>0.5</sub>/Ru<sub>0.9</sub>/(Co<sub>0.5</sub>/Pt<sub>0.25</sub>)<sub>3</sub>/Co<sub>0.5</sub>/Ta<sub>0.3</sub>/FeCoB<sub>1.2</sub>/MgO/FeCoB<sub>x</sub>/Ta<sub>0.3</sub>/FeCoB<sub>x</sub>/MgO/Pt<sub>2</sub>. A thin Ta layer is introduced in the middle of the FeCoB top storage layer. Its role is to attract boron away from the interfaces with MgO upon annealing so that a good crystalline structure is ensured as well as a high TMR signal [Koz-10]. Figure III-1 presents typical loops obtained by VSM for six samples with increasing FeCoB thickness.

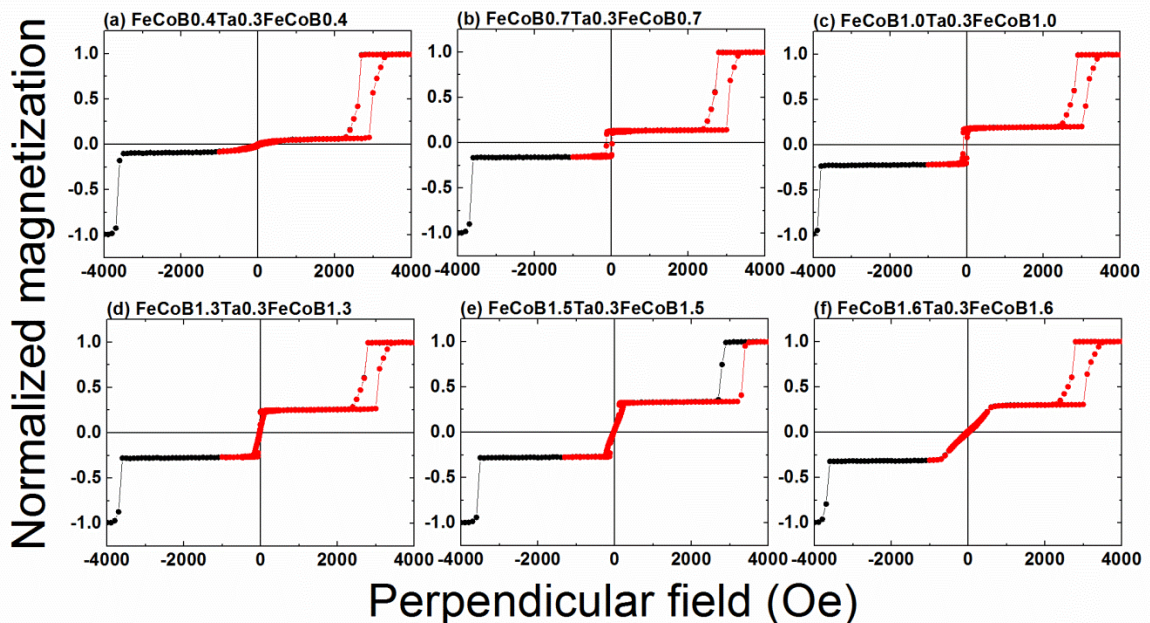


Figure III-1: Magnetic loops measured by VSM with perpendicular applied field for samples with a bottom SAF reference and varying thickness of FeCoB in the top electrode capped with MgO. The total FeCoB thickness goes from 0.8 (a) to 3.2 nm (f).

As expected, the signal of the free layer goes from a fully perpendicular response to a typical hard axis behavior as its thickness increases. Figure III-2 shows a zoom on the minor loop performed on the top free layer for a sample with a FeCoB1.5/Ta0.3/FeCoB1.5 stack. One observes that for this total nominal thickness of 3.0 nm, we are very close to the transition between perpendicular and planar anisotropy. The anisotropy is still perpendicular but magnetization is in a multi-domain state at zero field.

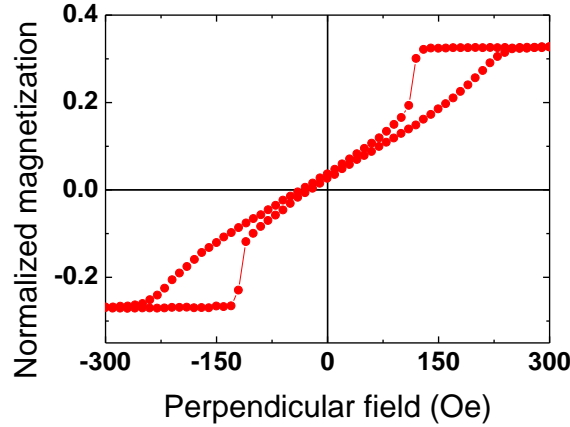


Figure III-2: Minor loop performed on the free layer by VSM with a perpendicular applied field for a sample with a FeCoB1.5/Ta0.3/FeCoB1.5/MgO storage layer.

Compared to the nominal critical thickness of 1.7 nm obtained with a 1 nm thick Ta capping in Chapter II, the MgO capping seems to be a particularly efficient way to improve perpendicular anisotropy. However, to be able to compare rigorously MgO and Ta cappings, the magnetically dead layers present at the interfaces must be taken into account. In order to extract this parameter, we used the same data treatment presented in the previous Chapter for a Ta capping. Note that in the case of a composite free layer, the standard dead layer model might not be really accurate, as in total there will be four interfaces instead of two. The amplitude of the free layer transition  $M_3$  is normalized to the amplitude of the bottom Co/Pt multilayer  $M_1$  and plotted as a function of its total nominal thickness in Figure III-3.

Recalling that the ratio of magnetizations can be expressed as  $\frac{M_3}{M_1} = \frac{(t_{FeCoB} - t_d)M_{sFeCoB}}{6t_{Co}M_{sCo}}$ , the slope enables extracting a saturation magnetization  $M_s = 1100 \text{ emu.cm}^{-3}$  and the extrapolation to zero magnetization gives a magnetically dead layer thickness  $t_d = 0.3 \text{ nm}$ . This value is about half that measured for similar junctions with a 1 nm Ta capping. This might be explained by the difference in Ta content between a thick capping and a thin Ta insertion, as was already the case in Chapter II for the bottom FeCoB layer growing on a 0.3 nm thick Ta insertion.

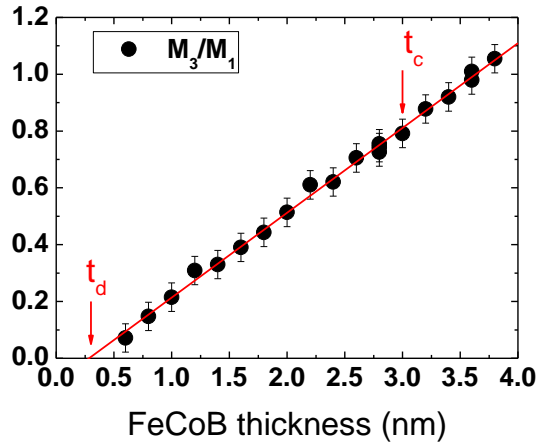


Figure III-3: Magnetization of the FeCoB storage layer with a 0.3 nm Ta insertion as a function of its nominal thickness for junctions with a bottom SAF reference and an MgO capping.  $t_c$  and  $t_d$  stand for dead layer and critical thicknesses, respectively. The magnetization  $M_3$  of the storage layer is normalized to the magnetization  $M_1$  of the bottom part of the SAF (internal reference).

A magnetic dead layer of 0.6 nm had been found in the FeCoB top electrodes with a Ta capping and the critical thickness was in that case 1.7 nm (see Chapter II). The use of an MgO cap layer allows thus increasing the effective critical thickness from 1.1 to 2.7 nm. This effect has already been noted in other studies but with little consideration about a possible modification of dead layer thicknesses between Ta and MgO-capped junctions [Kub-12, Sat-12].

The effective anisotropy constant can be expressed as  $K_{eff} = K_v - 2\pi M_s^2 + \frac{K_{s1} + K_{s2}}{t}$ , where  $K_v$  stands for the volume anisotropy,  $M_s$  the saturation magnetization,  $K_{s1,2}$  the interfacial anisotropy at the bottom and top interfaces and  $t$  the effective magnetic thickness. Assuming a negligible volume anisotropy energy [Liu-12, Ike-10], the critical effective magnetic thicknesses  $t_c$  and the calculated  $M_s$  values can be used to estimate  $K_{s1} + K_{s2}$  knowing that  $K_{eff}=0$  when  $t=t_c$ . This calculation leads to interfacial anisotropy energies of 1.2 and 2.1 erg.cm<sup>-2</sup> for the Ta-capped and MgO-capped junctions, respectively. We can use these values to calculate the thermal stability factor  $\Delta$ , for a given pillar diameter as  $\Delta = \frac{K_{eff}V}{k_B T}$ . An example is given in Figure III-4 for a pillar diameter of 30 nm. It appears clearly that for a given effective magnetic thickness, the MgO capping provides larger thermal stability. Besides, the range of usable thicknesses is much wider with an MgO capping than with a Ta one. In the example of Figure III-4, to maintain a stability factor  $\Delta$  above 70 (horizontal line in the figure), the effective magnetic thickness must be thinner than 0.7 nm with Ta whereas it can reach 2.2 nm in the case of MgO.

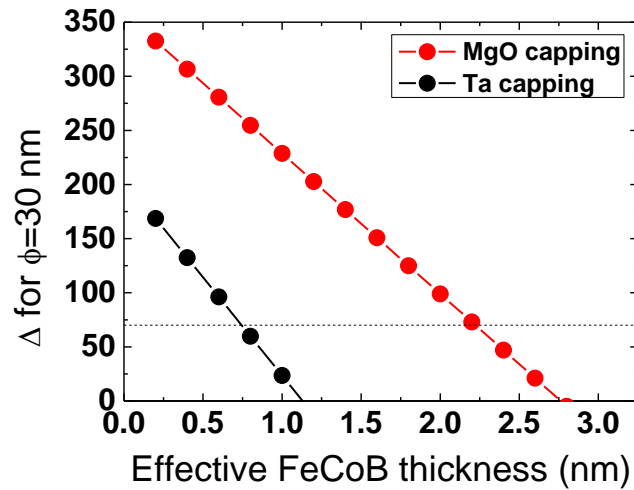


Figure III-4: Calculated thermal stability factor as a function of FeCoB storage layer effective thickness for a pillar diameter of 30 nm. The capping layer is either Ta (black curve) or MgO (red curve).

### III-1.2 Anisotropy of top electrodes with Ta or MgO capping

To estimate more precisely the enhancement of perpendicular anisotropy brought by the MgO capping, series of top electrodes with varying thicknesses of FeCoB have been fabricated. They are capped with either a Ta or an MgO layer. The MgO-capped electrodes are FeCoB bilayers with a 0.3 nm thick Ta insertion in the middle, as in the full junctions. This allows measuring the samples with both a planar and a perpendicular field so as to determine the anisotropy as explained in Chapter I. It is necessary to work with top electrodes only as it is not possible to discriminate between the different contributions when measuring a full junction with a bottom (Co/Pt) SAF reference under an in-plane field. The results for the Ta-capped electrodes have already been presented in Chapter II. They are recalled here to make a direct comparison with the systems capped with MgO, as shown in Figure III-5.

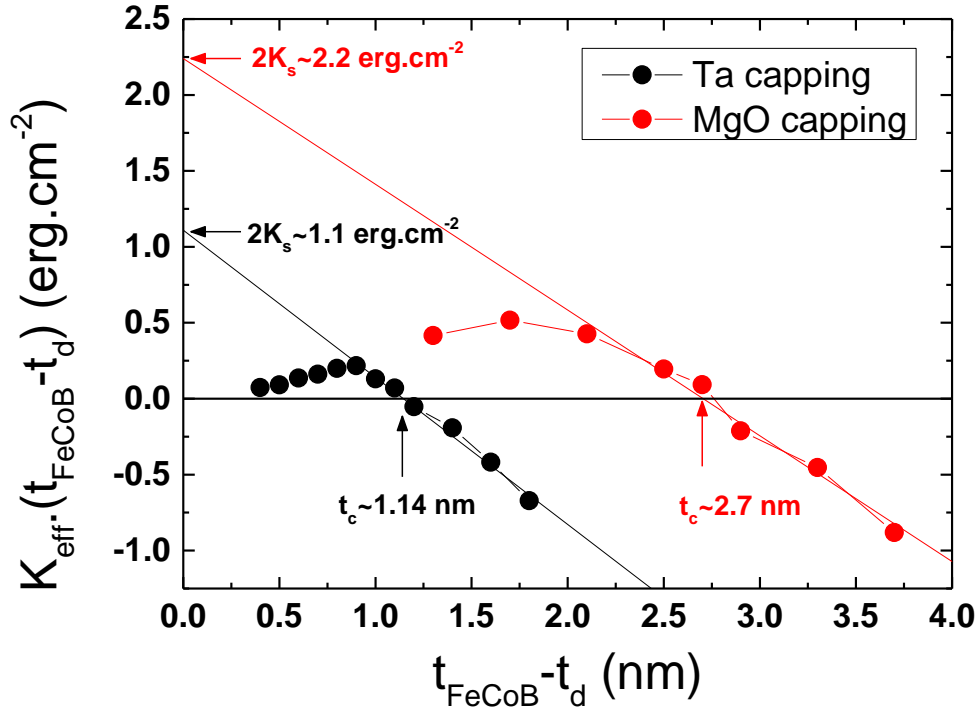


Figure III-5: Variation of  $K_{\text{eff}} \cdot t$  as a function of effective thickness for top FeCoB electrodes capped with Ta or MgO.

As expected, a larger critical thickness is obtained with the MgO capping. The value is here identical to the one we had previously estimated with the data treatment performed on the full junctions. Similarly to what had been done with the Ta-capped electrodes, the extrapolation to zero thickness gives the total surface anisotropy. For MgO-capped electrodes, we find  $2K_s = 2.2 \text{ erg.cm}^{-2}$ , which is twice the value estimated for a Ta capping. This confirms that a large increase of the interfacial anisotropy is observed when a second MgO interface is added to the storage layer. Note that the extracted  $K_s$  are in very good agreement with the previously calculated values using the critical thicknesses.

From the slope of the linear trend, we can estimate the  $M_s$  value to be approximately  $1150 \text{ emu.cm}^{-3}$ , which is also in good agreement with the estimation made with the series of full junctions. We can clearly see that this slope is smaller than in the case of a Ta capping for which a saturation magnetization around  $1300 \text{ emu.cm}^{-3}$  had been found.

### III-1.3 Effect of changing the nature of the insertion

Another series of samples in which the standard Ta insertion layer is replaced by a Ru one has been deposited. The stack is the following: Ta<sub>3</sub>/Pt<sub>5</sub>/(Co<sub>0.5</sub>/Pt<sub>0.25</sub>)<sub>5</sub>/Co<sub>0.5</sub>/Ru<sub>0.9</sub>/(Co<sub>0.5</sub>/Pt<sub>0.25</sub>)<sub>3</sub>/Co<sub>0.5</sub>/Ta<sub>0.3</sub>/FeCoB<sub>1.2</sub>/MgO/FeCoB<sub>x</sub>/Ru<sub>0.3</sub>/FeCoB<sub>x</sub>/MgO/Pt<sub>2</sub>. The Ru thickness is fixed at 0.3 nm to be equivalent to the former Ta one.

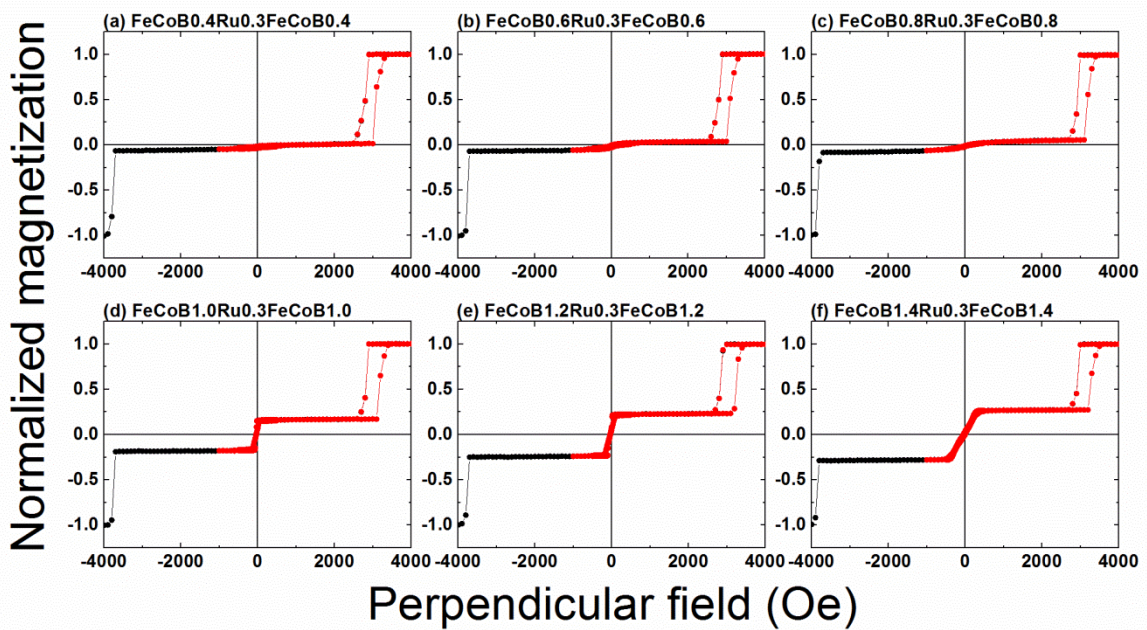


Figure III-6: Magnetic loops measured by VSM with perpendicular applied field for samples with a bottom SAF reference and varying thickness of FeCoB in the top electrode capped with MgO. The total FeCoB thickness goes from 0.8 (a) to 2.8 nm (f).

Figure III-6 shows the magnetic cycles measured by VSM with perpendicular applied field for six different thicknesses of FeCoB. Similarly to what had been observed in the case of a Ta insertion in Figure III-1, the amplitude of the transition of the free layer increases with FeCoB thickness and undergoes the transition between perpendicular and planar anisotropy. The nominal critical thickness is in that case just below 2.8 nm, as a planar signal can be observed for this thickness in Figure III-6 (f). It seems that the perpendicular anisotropy is slightly reduced when using a Ru insertion instead of a Ta one. However, we cannot compare directly the two systems as it has not been possible to extract precisely the magnetic dead layer in the Ru case. Indeed, if we plot  $M_3/M_1$  a clear slope cannot be found easily, as illustrated in Figure III-7. Previous data on junctions with Ta insertion are recalled with black dots (equivalent to Figure III-3). It seems that for the thinner FeCoB layers the magnetic dead layer is much larger with a Ru insertion as the ratio  $M_3/M_1$  is smaller. However, for thicker FeCoB layers, the ratios appear to be relatively similar. This could be the result of a variation of magnetically dead layer thickness with

magnetic thickness in the case of Ru. Globally, we can probably assume a thicker dead layer with Ru compared with Ta.

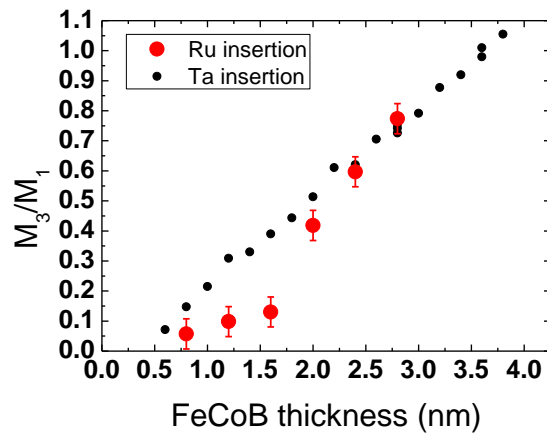


Figure III-7: Magnetization of the FeCoB storage layer with a 0.3 nm Ru insertion as a function of its nominal thickness for junctions with a bottom SAF reference and an MgO capping (red dots). The magnetization  $M_3$  of the storage layer is normalized to the magnetization  $M_1$  of the bottom part of the SAF (internal reference). Results for samples with a Ta insertion are recalled with black dots.

We also tried removing entirely the insertion to see the effect on perpendicular anisotropy. This leads to the following stacks: Ta<sub>3</sub>/Pt<sub>5</sub>/(Co<sub>0.5</sub>/Pt<sub>0.25</sub>)<sub>5</sub>/Co<sub>0.5</sub>/Ru<sub>0.9</sub>/(Co<sub>0.5</sub>/Pt<sub>0.25</sub>)<sub>3</sub>/Co<sub>0.5</sub>/Ta<sub>0.3</sub>/FeCoB<sub>1.2</sub>/MgO/FeCoB<sub>x</sub>/MgO/Pt<sub>2</sub>. Figure III-8 shows four examples of the magnetic loops obtained for such samples.

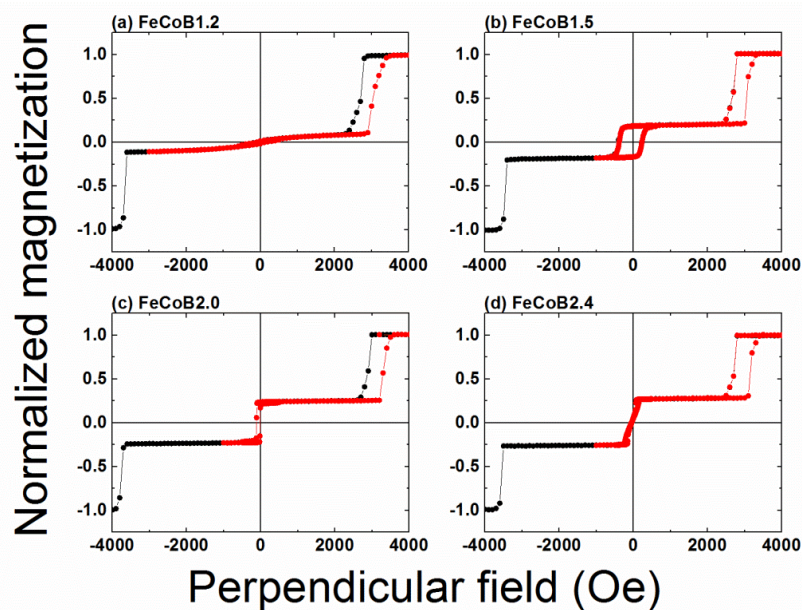


Figure III-8: Magnetic loops measured by VSM with perpendicular applied field for samples with a bottom SAF reference and varying thickness of FeCoB in the top electrode capped with MgO. (a) FeCoB<sub>1.2</sub> (b) FeCoB<sub>1.5</sub> (c) FeCoB<sub>2.0</sub> (d) FeCoB<sub>2.4</sub>.

Surprisingly a very small signal is observed for the 1.2 nm thick FeCoB free layer, indicating that the layer is almost non-magnetic. This is quite unexpected as magnetic dead layers are commonly said to originate from the Ta (or Ru) interface rather than from the MgO one. As the thickness of FeCoB increases, the transition of the free layer becomes more abrupt and a large coercive field appears for a thickness of 1.5 nm. If the thickness is further increased, the coercive field starts decreasing and as seen previously the magnetization gets planar. The values of the coercive fields obtained for these samples without insertion are very large compared to those of the previous series. The variation of the coercive field as a function of FeCoB thickness is given in Figure III-9 (a). It reaches a maximum of about 360 Oe for a thickness of 1.6 nm whereas in systems with Ta or Ru insertion the coercive field rarely exceeds 100 Oe. It might be explained by the fact that putting insertion materials in the FeCoB layer favors the nucleation phenomenon and reduces the coercive field. Besides, when removing the insertion we suppress the possible getter effect of this layer and boron atoms might be differently distributed in the magnetic layer, thus modifying the chemical composition in the bulk and at the interfaces, with unknown consequences on the magnetic properties.

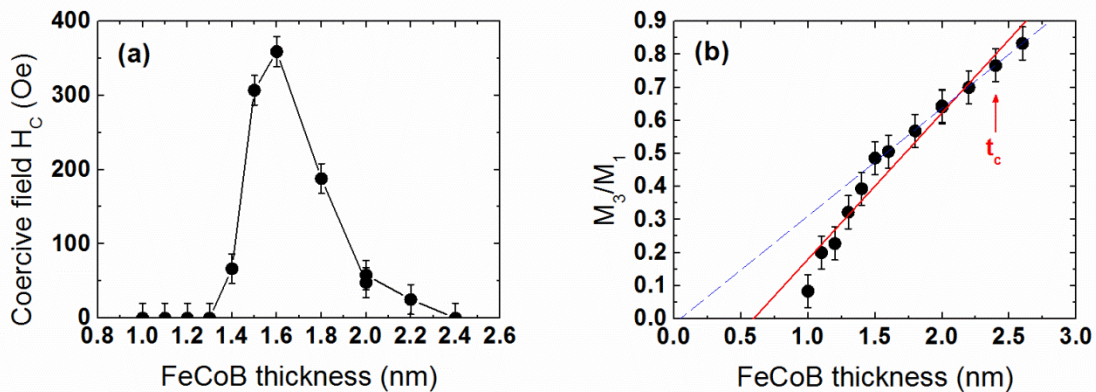


Figure III-9: (a) Coercive field and (b) normalized magnetization of the top FeCoB free layer for magnetic tunnel junctions with MgO capping and without insertion.

In Figure III-9 (b) the standard plot of  $M_3/M_1$  as a function of FeCoB thickness shows that the extraction of the magnetically dead layer is not that simple. Two slopes seem to appear: one for thicknesses between 1 and 1.5 nm and another one for thicker layers. This could mean that, similarly to the case of a Ru insertion, the dead layer thickness depends on the total amount of FeCoB that has been deposited. If we consider the entire range of thicknesses, one can extract a mean dead layer thickness of 0.59 nm and a saturation magnetization of 1600 emu.cm<sup>-3</sup>. However, if we only consider the data points for thicknesses greater than 1.5 nm (blue dotted line on Figure III-9 (b)), the extracted dead layer thickness is reduced down to 0.05 nm and  $M_s$  is estimated around 1175 emu.cm<sup>-3</sup>. Those values are more consistent with the

previous results and the expected behavior for such a storage layer. It seems however that the validity of the dead layer model could be questioned here.

### III-1.4 Nature of the two MgO barriers

In the beginning of this study, we chose two different oxidation conditions for the MgO barriers. The first barrier was done by natural oxidation with our standard high pressure static conditions (HP = 150 mbar, 10s) and using the following thicknesses of Mg: Mg<sub>0.9</sub>/Ox/Mg<sub>0.5</sub>. The top one was also realized by natural oxidation but with the low pressure dynamic conditions (LP = 3.10<sup>-2</sup> mbar, 100 sccm, 360s) and thinner Mg layers: Mg<sub>0.6</sub>/Ox/Mg<sub>0.5</sub>. This choice is particularly relevant if one does not want to lose too much TMR by introducing a second resistive MgO layer on top of the stack. Indeed, we know our HP barriers exhibit a RA value around 50 Ωμm<sup>2</sup>, while the LP ones give a value of the order of 10 Ωμm<sup>2</sup>. This difference allows keeping a reasonable TMR signal.

Note that even though the two barriers are nominally identical, their RA products can be different. Some studies have indeed shown that the resulting TMR of a junction capped with MgO can be equivalent to the one of a standard Ta-capped junction as the environment of the MgO barriers (buffer and seed layers) changes the structure of the MgO, making the top one less resistive [\[Sat-13\]](#).

It could seem interesting to check the effect on perpendicular anisotropy of changing the nature of the MgO barriers. To that aim, three magnetic tunnel junctions were prepared, with varying oxidation conditions for the two barriers: either the high pressure (HP) or low pressure (LP) ones. The total top FeCoB thickness is chosen close to the perpendicular to planar anisotropy transition to have more sensitivity. A thin Ta insertion of 0.3 nm is included in the top FeCoB layer in that case so that we have the following stack for the storage layer: FeCoB<sub>1.5</sub>/Ta<sub>0.3</sub>/FeCoB<sub>1.5</sub>. Magnetic cycles measured by VSM are shown in Figure III-10.

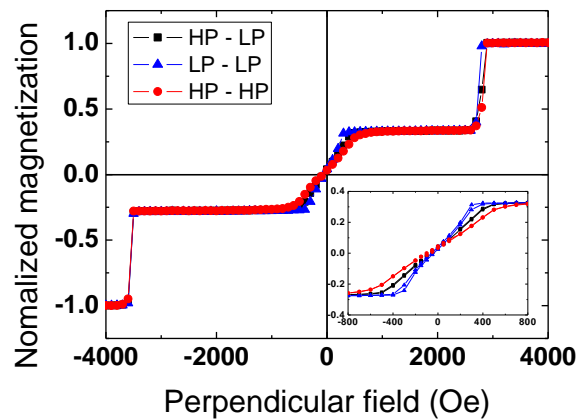


Figure III-10: Magnetic cycles measured by VSM with perpendicular applied field for junctions having a bottom SAF reference and a MgO capping. A Ta 0.3 nm layer is inserted in the FeCoB layer. Oxidation conditions of the two MgO barriers are varied: LP and HP stand for low and high pressure, respectively.

From these magnetic loops, it seems that modifying the oxidation conditions does not impact a lot the perpendicular anisotropy. There are slight changes in the saturation field that goes from 800 Oe for two HP barriers to 400 Oe for two LP ones. The asymmetric system (HP-LP) gives an intermediate value of 600 Oe. It appears then that to some extent the low pressure conditions improve perpendicular anisotropy but not in a significant way. Besides, in the vicinity of the critical thickness, the magnetic behavior is extremely sensitive to the deposited thickness so we cannot exclude here the possibility of small thickness variations.

In the case where these junctions would be used for STT-MRAM applications, one should favor the low pressure conditions as low RA values are necessary for writing with reasonable current densities. Even though this configuration will lead to a decrease in the resulting TMR signal, a compromise is required. The difference in RA will still be large enough to ensure a functional device.

## III-2. Development of magnetic tunnel junctions with a top reference

With the aim of developing double junctions with two reference layers, it seemed necessary to investigate the feasibility of top references in our deposition tool.

### III-2.1 Metallic synthetic antiferromagnetic layers

As seen in Chapter II, our standard bottom SAF layer is composed of Co/Pt multilayers and is deposited on top of a 5 nm Pt buffer layer. This buffer has been shown to be crucial to ensure good anisotropy properties to the multilayers. In the case of a top reference layer, a thick buffer cannot be used because a strong coupling needs to be kept between the FeCoB layer and the adjacent multilayers.

In order to start with simplified structures, purely metallic SAF without any FeCoB or oxide barriers have been investigated. Two types of multilayers were deposited:  $\text{Ta}_3/(\text{Co}_{0.5}/\text{Pt}_{0.25})_3/\text{Co}_{0.5}/\text{Ru}_{0.9}/(\text{Co}_{0.5}/\text{Pt}_{0.25})_5/\text{Co}_{0.5}/\text{Pt}_2$  and  $\text{Ta}_3/(\text{Co}_{0.3}/\text{Pd}_{1.2})_3/\text{Co}_{0.3}/\text{Ru}_{0.9}/(\text{Co}_{0.3}/\text{Pd}_{1.2})_5/\text{Co}_{0.3}/\text{Pd}_2$ . The stacks are made as mirrors of the standard bottom reference, with a number of repeats that is larger in the top multilayer. Figure III-11 shows the magnetic loops obtained by VSM.

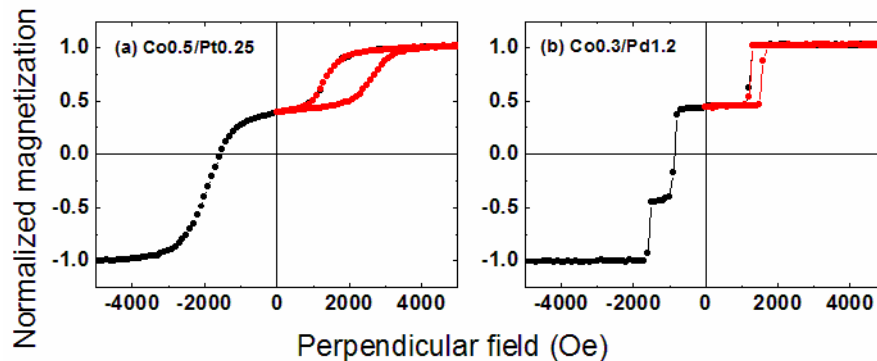


Figure III-11: Magnetic cycles measured by VSM with perpendicular applied field for SAF composed of (a)  $\text{Ta}_3/(\text{Co}_{0.5}/\text{Pt}_{0.25})_3/\text{Co}_{0.5}/\text{Ru}_{0.9}/(\text{Co}_{0.5}/\text{Pt}_{0.25})_5/\text{Co}_{0.5}/\text{Pt}_2$  and (b)  $\text{Ta}_3/(\text{Co}_{0.3}/\text{Pd}_{1.2})_3/\text{Co}_{0.3}/\text{Ru}_{0.9}/(\text{Co}_{0.3}/\text{Pd}_{1.2})_5/\text{Co}_{0.3}/\text{Pd}_2$ . Minor loops are included in red.

As already observed for a bottom SAF with a 0.25 nm thick buffer (Figure II-21 (a) in Chapter II), the anisotropy of the Co/Pt SAF in Figure III-11 (a) is strongly reduced. Transitions of the two parts of the SAF are not abrupt contrary to the case of Co/Pd multilayers in Figure III-11 (b). In that last case, three transitions appear in the magnetic loop, which is representative of system with strong RKKY coupling

energy. In terms of anisotropy properties, it seems then preferable to favor the Co/Pd multilayers in the stack of the top SAF references.

### III-2.2 Optimization of single junctions with SAF top references

To realize full junction with a top reference, a stack with Co/Pd top multilayers and a bottom FeCoB storage layer was deposited: Ta<sub>3</sub>/FeCoB<sub>1.2</sub>/MgO/FeCoB<sub>1.2</sub>/Ta<sub>0.2</sub>/(Co<sub>0.3</sub>/Pd<sub>1.2</sub>)<sub>4</sub>/Co<sub>0.3</sub>/Ru<sub>0.9</sub>/(Co<sub>0.3</sub>Pd<sub>1.2</sub>)<sub>8</sub>/Co<sub>0.3</sub>/Pd<sub>2</sub>. Numbers of repeats in the SAF have been optimized to obtain a ratio of magnetizations equal to 1.2 in order to limit stray fields in 100 nm pillars, as explained in Chapter II [Ban-10]. A layer of 1.2 nm of FeCoB is introduced in the bottom part of the SAF and separated from the multilayer by a thin Ta spacer in order to guaranty a good TMR signal. The junctions are annealed at our standard temperature of 300 °C and this will be the case for all the samples presented in the following. By analogy to the work done on the bottom SAF structure, we can schematically represent this type of junction as M'<sub>3</sub>/MgO/M'<sub>2</sub>/Ru/M'<sub>1</sub>. Its magnetic loop, plotted in Figure III-12, shows that coming from positive field saturation, the reversals of M'<sub>3</sub> and M'<sub>2</sub> are not distinct whereas the transition of M'<sub>1</sub> is clearly identifiable at a large negative field of -1840 Oe. However once the bottom part of the SAF M'<sub>2</sub> is fully saturated at a negative field larger than -500 Oe, a minor loop can be performed on the bottom free layer between ± 200 Oe and the transition M'<sub>3</sub> is recovered (see red loop in Figure III-12).

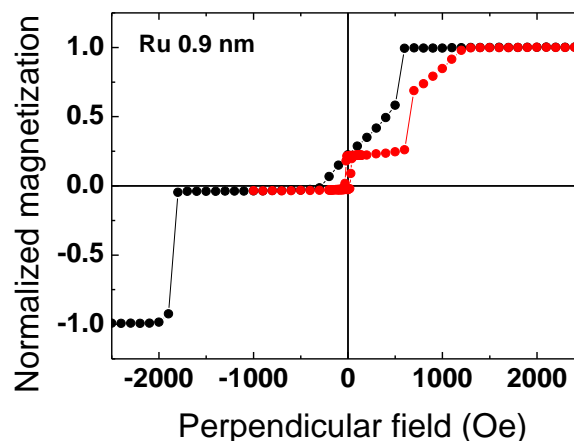


Figure III-12: Magnetic cycle measured by VSM with perpendicular applied field for a junction with top Co/Pd SAF reference, a Ru spacer of 0.9 nm and a bottom free layer of 1.2 nm of FeCoB. A minor loop is performed by saturating the system in a negative field of -1000 Oe and increasing it towards positive field saturation (red dots).

As the parallel and antiparallel states can be reached by a proper field treatment, this type of magnetic stack is functional and could be used in a device. However, it complicates the procedure as a saturation of the SAF in two steps is required. This is why we will try to further optimize the magnetic properties.

To see if the stability of the SAF could be enhanced, the RKKY coupling in the top SAF has been studied as a function of Ru thickness, similarly to what had been done in Chapter II for the bottom SAF. The rest of the stack is similar to the one of the junction in Figure III-12: Ta<sub>3</sub>/FeCoB<sub>1.2</sub>/MgO/FeCoB<sub>1.2</sub>/Ta<sub>0.2</sub>/(Co<sub>0.3</sub>/Pd<sub>1.2</sub>)<sub>4</sub>/Co<sub>0.3</sub>/Ru<sub>x</sub>/(Co<sub>0.3</sub>Pd<sub>1.2</sub>)<sub>8</sub>/Co<sub>0.3</sub>/Pd<sub>2</sub>. As can be observed in Figure III-13, similarly to the case of the bottom Co/Pt SAF (Figure II-16 in Chapter II), the classical oscillatory behavior is achieved with a largest amplitude around a Ru thickness of 0.45 nm, followed by a peak at 0.9-0.95 nm. The amplitude of the coupling field is however much reduced in the case of the Co/Pd SAF: at the second maximum,  $H_{\text{SAF}}$  reaches only -600 Oe instead of more than -3000 Oe in the bottom Co/Pt SAF. Moreover, the difference in amplitude between the two peaks is smaller in the top SAF (a factor 1.3 instead of 2 in the previous case).

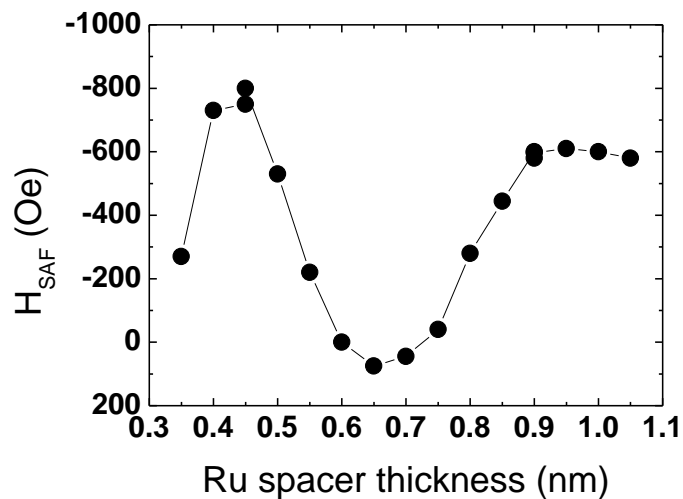


Figure III-13: RKKY coupling field as a function of Ru thickness for junctions with a Co/Pd SAF top reference.

An example of the magnetic loop obtained for a sample at the first maximum of RKKY coupling (0.45 nm) is given in Figure III-14. Even though the coupling strength is slightly larger than the one of the junction with a 0.9 nm thick spacer (Figure III-12), it is still not large enough to allow separating out the transitions of  $M'_2$  and  $M'_3$  at the first descending branch. We will then keep the same strategy as in the bottom Co/Pt SAF and opt for a thickness of 0.9 nm for the Ru layer, as this maximum still gives a larger range of stability in terms of spacer thickness (less sensitive to deposition-dependent thickness fluctuations).

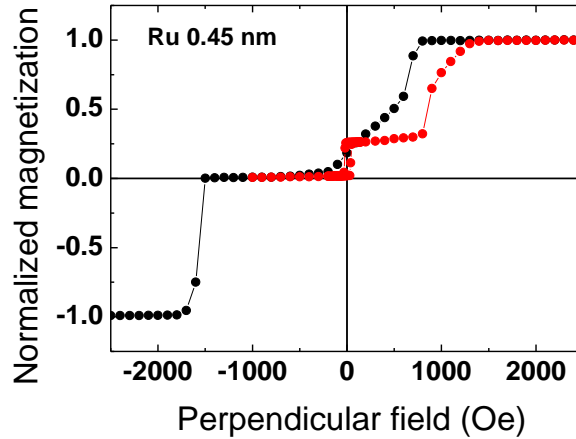


Figure III-14: Magnetic cycle measured by VSM with perpendicular applied field for a junction with top Co/Pd SAF reference, a Ru spacer of 0.45 nm and a bottom free layer of 1.2 nm of FeCoB. A minor loop is performed by saturating the system in a negative field of -1000 Oe and increasing it towards positive field saturation (red dots).

As varying the thickness of Ru spacer does not allow separating out the transitions of  $M'_2$  and  $M'_3$ , we investigated the effect of changing the thickness of the top FeCoB layer that is coupled to the Co/Pd multilayers. From Figure III-15 (a), it appears that, if the FeCoB layer is thin enough (0.6 nm), two separate transitions can be obtained without any special field treatment. As this thickness increases, both  $M'_2$  and  $M'_3$  start switching together at positive fields and thick FeCoB introduces slopes in the magnetic signal (Figure III-15 (c)). It could then seem interesting to choose thin FeCoB layers as they induce a good separation of the magnetic transitions thanks to a larger antiparallel plateau.

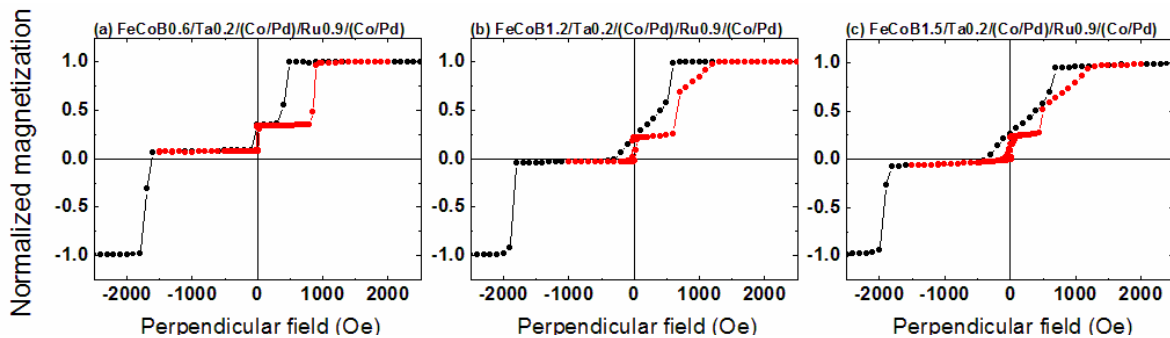


Figure III-15: Magnetic cycles measured by VSM with perpendicular applied field for junctions having varying thickness of FeCoB in the top SAF reference, Ta<sub>3</sub>/FeCoB<sub>1.2</sub>/MgO/FeCoB<sub>x</sub>/Ta<sub>0.2</sub>/(Co<sub>0.3</sub>/Pd<sub>1.2</sub>)<sub>4</sub>/Co<sub>0.3</sub>/Ru<sub>x</sub>/(Co<sub>0.3</sub>/Pd<sub>1.2</sub>)<sub>8</sub>/Co<sub>0.3</sub>/Pd<sub>2</sub>. (a) x=0.6 nm (b) x=1.2 nm (c) x=1.5 nm.

Using the full series of magnetic tunnel junctions with varying thicknesses of FeCoB in the top reference, we can plot the variation of the ratio  $M'_2/M'_1$  as a function of the FeCoB thickness (Figure III-16).

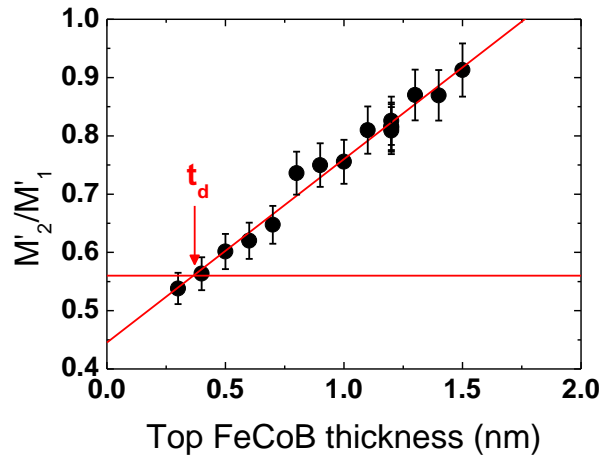


Figure III-16: Magnetization ratio  $M'_2/M'_1$  as a function of top FeCoB thickness. The horizontal line corresponds to the ratio  $M'_2/M'_1$  for zero FeCoB thickness, that is to say  $5/9$ .

Knowing that  $\frac{M'_{i2}}{M'_{i1}} = \frac{(t_{FeCoB} - t_d)M_{sFeCoB} + 5t_{Co}M_{sCo}}{9M_{sCo}}$  and assuming there is no magnetic dead layer in the Co/Pd multilayers, a magnetic dead layer of 0.36 nm is found in the top FeCoB layer, at the intercept between the linear fit and the line representing the ratio  $M'_2/M'_1$  without FeCoB, that is  $5/9$ . Taking  $M_{sCo} = 1200 \text{ emu.cm}^{-3}$ , as for the Co/Pt multilayers (see Chapter II), the slope gives a saturation magnetization  $M_{sFeCoB} = 1020 \text{ emu.cm}^{-3}$ .

The separation of the transitions of  $M'_2$  and  $M'_3$  appears to be only maintained in junctions with top FeCoB thickness thinner than 0.6 nm. Taking into account the magnetic dead layer calculated above, this leads to effective thicknesses of FeCoB smaller than 0.24 nm. Knowing, from the previous Chapter, that effective thicknesses larger than 0.6 nm are necessary to preserve high TMR signal, it seems impossible to get functional devices using such thin FeCoB layers in the top SAF reference.

Another way to adjust the anisotropy of the top Co/Pd reference is to adapt the Co thickness in the Co/Pd multilayers. Figure III-17 shows the magnetic loops of four samples with increasing Co thickness: Ta<sub>3</sub>/FeCoB<sub>1.2</sub>/MgO/FeCoB<sub>1.2</sub>/Ta<sub>0.2</sub>/(Co<sub>x</sub>/Pd<sub>1.2</sub>)<sub>4</sub>/Co<sub>x</sub>/Ru<sub>0.9</sub>/(Co<sub>x</sub>Pd<sub>1.2</sub>)<sub>8</sub>/Co<sub>x</sub>/Pd<sub>2</sub>. The top FeCoB thickness is fixed at 1.2 nm to ensure a sufficiently high TMR. For Co layers as thin as 0.2 nm (Figure III-17 (a)), it is not possible to distinguish the transitions of  $M'_2$  and  $M'_3$  as both layers switch together. The perpendicular anisotropy is quite low for this sample, probably because of weakly magnetized layers. As the Co thickness increases, the anisotropy is reinforced and for a value of 0.4 nm the SAF stability is finally large enough to allow separating the transition of the free layer  $M'_3$  from those of the SAF (Figure III-17 (c)). As the Co thickness is further increased, perpendicular anisotropy starts to decrease as can be deduced from the tilted transitions and the loss of remanence in

$M'_2$  in the case of 0.45 nm thick Co layers in Figure III-17 (d). A good compromise seems then to choose a thickness of 0.4 nm in the Co/Pd multilayers.

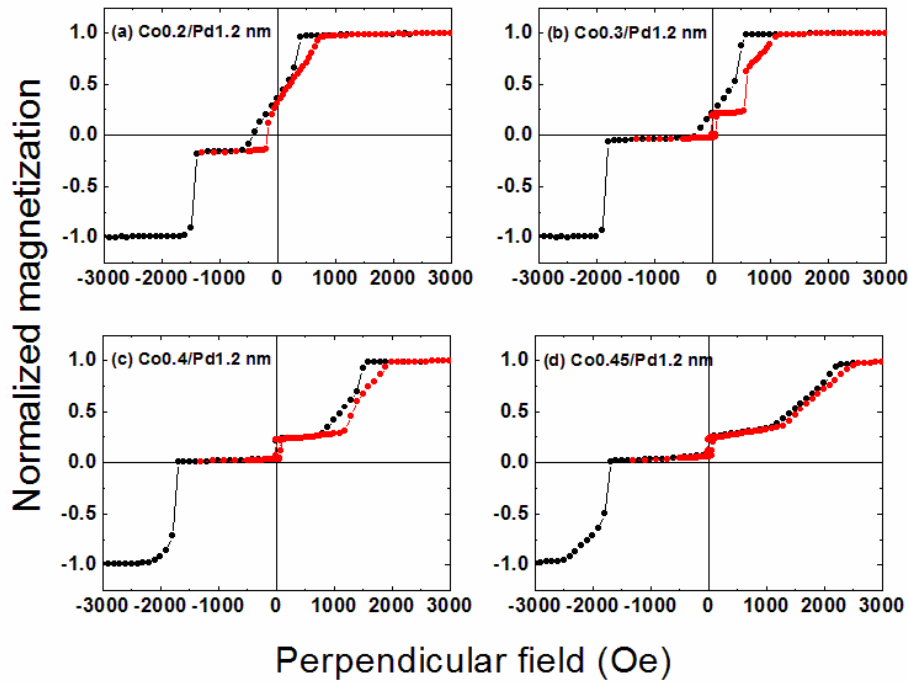


Figure III-17: Magnetic cycles measured by VSM with perpendicular applied field for samples with varying thickness of Co in the top Co/Pd SAF reference. (a) 0.2 nm (b) 0.3 nm (c) 0.4 nm (d) 0.45 nm.

Similarly to what had been done for the bottom SAF reference layer, we checked the optimal Ta insertion to use in order to structurally decouple the Co/Pd multilayers from the FeCoB layer. The stack of the junctions is the following: Ta<sub>3</sub>/FeCoB<sub>1.2</sub>/MgO/FeCoB<sub>1.2</sub>/Ta<sub>x</sub>Ta<sub>a</sub>/ (Co<sub>0.3</sub>/Pd<sub>1.2</sub>)<sub>4</sub>/Co<sub>0.3</sub>/Ru<sub>0.9</sub>/(Co<sub>0.3</sub>/Pd<sub>1.2</sub>)<sub>8</sub>/Co<sub>0.3</sub>/Pd<sub>2</sub>, with thicknesses in nm. Note that at the time of this study, the Co thickness had not been optimized yet. The TMR as a function of Ta thickness is given in Figure III-18.

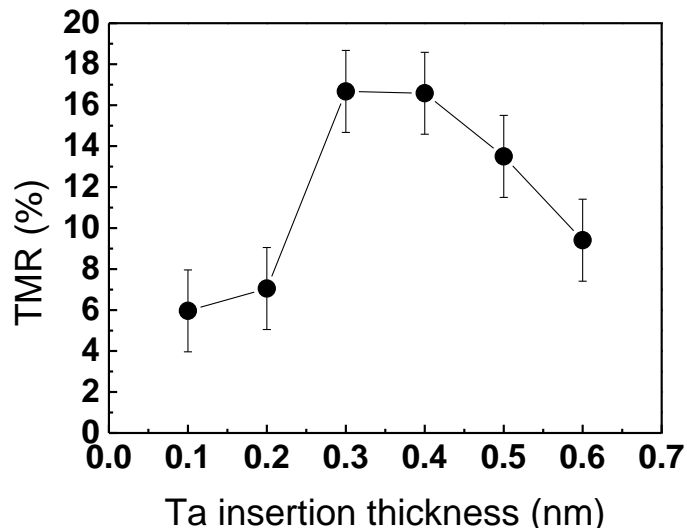


Figure III-18: TMR signal as a function of Ta insertion for samples with top SAF reference with Co/Pd multilayers.

Similarly to the previous results with Co/Pt multilayers, the TMR amplitude is rising upon increasing the Ta insertion thickness up to 0.3-0.4 nm. For thicker Ta spacers, the signal starts dropping. Interestingly, the same thickness of Ta insertion allows getting the maximum TMR in both kind of structures (bottom or top reference). It then seems that the order of deposition (CoFeB on Ta or Ta on CoFeB) does not modify the magnetic and transport behaviors of our samples.

We can observe that the TMR signal obtained with these top-referenced junctions is much smaller than the 70 to 100 % usually achieved with Co/Pt bottom referenced junctions. However, the same TMR values around 10-15 % have been obtained for inverted structures with bottom Co/Pd SAF reference layers. This effect seems then to be intrinsic to the nature of the material used in the multilayers or to deposition conditions in our sputtering tool.

### III-2.3 Thermal endurance of the junctions with a top reference

As was the case for the bottom SAF reference, a series of junctions with varying annealing temperature has been prepared with the following stack: Ta<sub>3</sub>/FeCoB<sub>1.2</sub>/MgO/FeCoB<sub>1.2</sub>/Ta<sub>0.2</sub>/ (Co<sub>0.3</sub>/Pd<sub>1.2</sub>)<sub>4</sub>/Co<sub>0.3</sub>/Ru<sub>0.9</sub>/(Co<sub>0.3</sub>/Pd<sub>1.2</sub>)<sub>8</sub>/Co<sub>0.3</sub>/Pd<sub>2</sub>. Unfortunately, at the time of this study, the stack was still not fully optimized, which means that the magnetic and transport properties will not be the ideal ones. Nevertheless, it allows us to check the qualitative behavior of this type of

junctions as a function of annealing temperature. In Figure III-19, we present the evolution of the TMR signal, measured by CIPT.

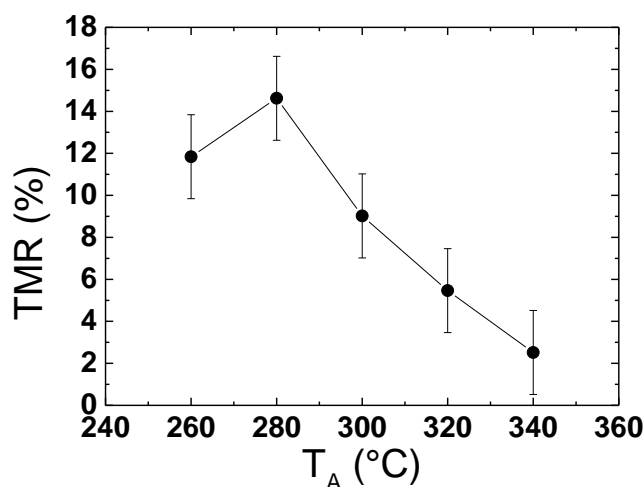


Figure III-19: Evolution of the TMR signal as a function of annealing temperature for magnetic tunnel junctions with a Co/Pd-based top reference layer.

Qualitatively, the same behavior is observed: a first increase of TMR due to the crystallization of the FeCoB appears until 280 °C, followed by a decrease at higher temperatures. Note that in the case of these junctions with top Co/Pd SAF reference, the decay of TMR happens at much smaller temperatures around 300 °C instead of more than 380 °C for the Co/Pt-based structures. They seem then less robust to the annealing step than our previous stacks. This had also been observed in a previous thesis done at Spintec [Ban-11]. It is however worth noting that due to the very small TMR signals measured in that case, it is relatively difficult to be absolutely confident in the trend observed here. Keeping the annealing temperature at its standard value of 300 °C should still be reasonable.

### III-2.4 Compatibility with the bottom SAF references

If one wants to build double junctions with perpendicular anisotropy having two reference layers and a storage layer in between, it is necessary to have distinct transition fields for all the magnetic layers. Figure III-20 allows visualizing that the junction we developed with top SAF reference provides a much reduced antiferromagnetic plateau compared to our standard Co/Pt bottom reference (between -1700 and 1200 Oe instead of -3500 and 2500 Oe). At first sight, both structures seem then usable in a full double junction as they should allow the stabilization of different magnetic configurations of the softest reference without perturbing the configuration of the hardest one. This is what we will try to show in the following part.

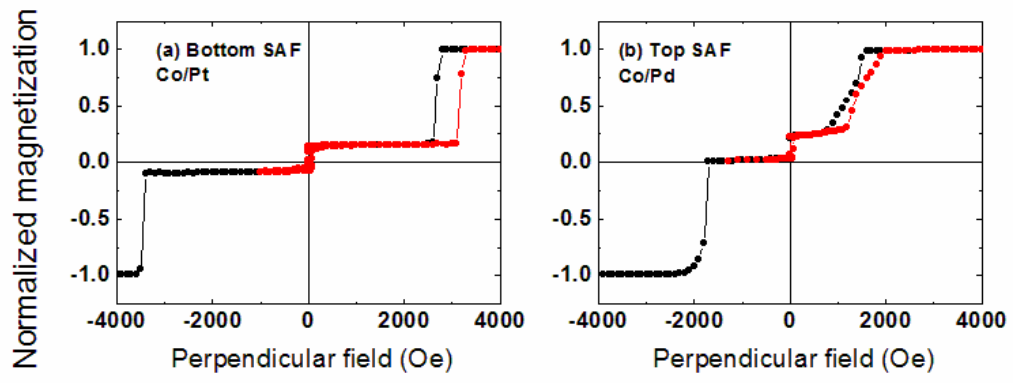


Figure III-20: Comparison of the magnetic loops of two junctions with (a) a bottom Co/Pt SAF reference (b) a top Co/Pd SAF reference.

### III-3. Double junctions with perpendicular anisotropy

#### III-3.1 Advantages of double junctions

More than ten years ago, interest started rising for systems with double barrier structures. Studies focused on magnetic tunnel junctions with planar anisotropy and it appeared that having two tunnel barriers presents various advantages.

It was shown in 2000 that such double structures enable reducing significantly the voltage bias dependence of TMR [Ino-00]. Indeed, it is well known that as the applied voltage on a junction increases, its TMR decreases and can lose a significant part of its value for voltages as low as 300-400 mV. Using double junctions is then particularly interesting for device applications as it allows enlarging the functioning range in terms of applied voltage.

More recently, double barrier junctions proved to be efficient candidates for STT switching. A study showed in 2007 that the intrinsic current density for switching could be reduced by a factor 2-3 for a structure with two barriers of different RA values and two pinned references oriented antiparallel [Dia-07]. But one can go much further with those structures and tune the STT efficiency. Indeed, in the case of a single ferromagnetic storage layer, if the two reference layers on both sides of the barriers have antiparallel magnetizations, the two spin transfer torques add up and allow reducing the critical current density for writing. On the contrary, when the references are parallel, the torques subtract and the STT efficiency is much reduced. It is then possible to alternate between a write mode and a read mode. The write mode with antiparallel references provides a low switching current. In the read mode, rather large voltages can be applied to retrieve the information without any risk of rewriting the memory element [Clé-14]. However, note that introducing a second barrier will increase the overall resistance so that it will be necessary to work with higher voltages if one wants to get the same current densities.

In this part, we propose to combine the advantages of double junctions with those of perpendicular anisotropy by creating perpendicular double junctions.

### III-3.2 Magnetic properties of perpendicular double magnetic tunnel junctions

As we have seen previously, adding a second MgO interface above the storage layer increases strongly its perpendicular anisotropy. Besides, junctions with top SAF references appeared to be functioning and compatible with the transition fields of our standard bottom SAF reference. It seems then natural to build a double junction in which the storage layer is a FeCoB layer sandwiched between a bottom Co/Pt-based SAF reference and a top Co/Pd-based SAF reference. Here are the stacks of the different blocks composing the double junction:

- SAF<sub>1</sub>=Ta<sub>3</sub>/Pt<sub>5</sub>/(Co<sub>0.5</sub>/Pt<sub>0.25</sub>)<sub>6</sub>/Co<sub>0.5</sub>/Ru<sub>0.9</sub>/(Co<sub>0.5</sub>/Pt<sub>0.25</sub>)<sub>3</sub>/Co<sub>0.5</sub>/Ta<sub>0.3</sub>/FeCoB<sub>1.2</sub>/MgO<sub>1.4</sub> (=M<sub>1</sub>/Ru/M<sub>2</sub>)
- Storage layer (SL)=FeCoB<sub>1.1</sub>/Ta<sub>0.3</sub>/FeCoB<sub>1.1</sub> (=M<sub>3</sub>)
- SAF<sub>2</sub>=MgO<sub>1.1</sub>/FeCoB<sub>1.2</sub>/Ta<sub>0.3</sub>/(Co<sub>0.4</sub>/Pd<sub>1.2</sub>)<sub>4</sub>/Co<sub>0.4</sub>/Ru<sub>0.9</sub>/(Co<sub>0.4</sub>/Pd<sub>1.2</sub>)<sub>8</sub>/Co<sub>0.4</sub>/Pd<sub>2</sub> (=M'<sub>2</sub>/Ru/M'<sub>1</sub>)

In that case, asymmetric tunnel barriers have been deposited. The bottom one is done under high pressure oxidation conditions and is 1.4 nm thick. It is expected to exhibit a larger RA than the top one which is done under low pressure oxidation conditions and is 1.1 nm thick.

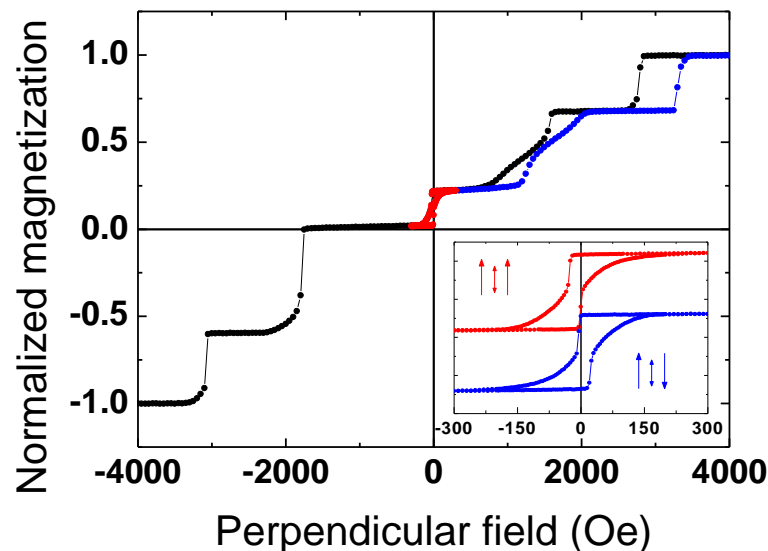


Figure III-21: Magnetic cycle measured by VSM with perpendicular field for a double junction with a FeCoB<sub>1.1</sub>/Ta<sub>0.3</sub>/FeCoB<sub>1.1</sub> storage layer. The inset shows minor loops performed on the free layer with either parallel (red) or antiparallel (blue) configuration of the reference layers.

Figure III-21 shows the magnetic loop obtained for such a double junction measured by VSM. As expected from the results of the individual junctions, the transition fields of all the five different magnetic layers are distinct. This means that different configurations of the references are achievable. Recalling that the junction stack can be schematically represented as  $M_1/\text{Ru}/M_2/\text{MgO}/M_3/\text{MgO}/M'_2/\text{Ru}/M'_1$ , Figure III-22 presents a schematic major loop to help visualizing the different magnetic transitions.

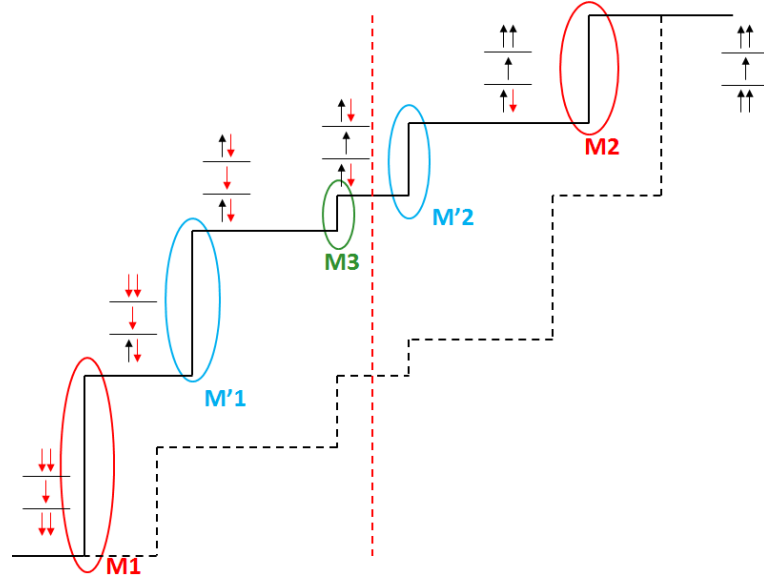


Figure III-22: Schematic representation of the major loop of a double junction. The black line corresponds to the descending branch coming from positive field saturation while the black dotted line shows the ascending branch. The red dotted line symbolizes  $H=0$ .

Coming from positive field saturation, the first transitions correspond to the reversals of the layers of the SAFs the closest to the MgO barriers: first, at larger fields, the top part of the bottom SAF  $M_2$  followed by the bottom part of the top SAF  $M'_2$ . At the center of the loop the switching of the storage layer  $M_3$  is visible. We represent it deliberately shifted towards negative fields to account for the commonly observed antiferromagnetic coupling through the MgO barrier. At negative fields, the hardest parts of the bottom and top SAF switch one after the other ( $M'_1$  followed by  $M_1$ ).

As shown in the inset of Figure III-21, minor loops can be performed on the storage layer with either parallel (red) or antiparallel (blue) configuration of the references. These two configurations are reached by applying a proper field treatment, as schematically represented in Figure III-23. Starting from positive field saturation and decreasing the field down to about -1000 Oe allows putting the references in parallel configuration (Figure III-23 (a)). The minor loop on the free layer is then done by increasing the field again towards positive values. At the same time, this treatment gives the minor loops on the bottom and top SAFs at larger fields. To set the references in an antiparallel configuration, the field has to be

decreased down to about -2500 Oe. It is then increased to switch back the magnetization of the bottom part of the top SAF  $M'_2$  and a minor loop can be performed on the free layer (Figure III-23 (b)).

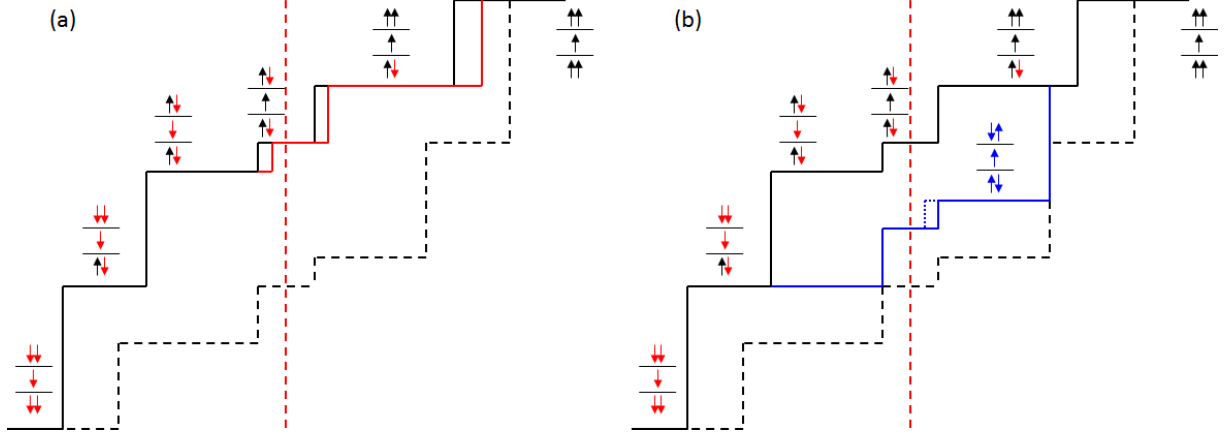


Figure III-23: Schematic representations of the field treatments needed to perform the minor loop on the free layer with (a) parallel or (b) antiparallel configuration of the references.

From these two minor loops, it is possible to extract the coupling fields acting on the free layer from both MgO barriers. Indeed, when the references are parallel the two coupling fields add whereas when they are antiparallel they subtract. In the case of the junction presented in Figure III-21, we found  $H_{cpl1}+H_{cpl2}=-16$  Oe and  $H_{cpl1}-H_{cpl2}=10$  Oe, where the indices 1 and 2 stand for the bottom and top barrier respectively. This translates into  $H_{cpl1}=-3$  Oe and  $H_{cpl2}=-13$  Oe. Both coupling are then weakly antiferromagnetic, with a larger one coming from the top MgO interface. This might be due to a larger roughness of the top MgO barrier than of the bottom one, probably because of different growth conditions.

### III-3.3 Transport properties of perpendicular double magnetic tunnel junctions

Depending on the relative orientations of the magnetizations in the reference layers, the resulting TMR of a double junction differs. If we call  $RA_1$  and  $TMR_1$  the parameters of the bottom MgO barrier and  $RA_2$  and  $TMR_2$  those of the top barrier the resulting TMR in the case of parallel or antiparallel references can be written as:

$$TMR_{tot/para} = \frac{RA_1 TMR_1 + RA_2 TMR_2}{RA_1 + RA_2} \text{ and } TMR_{tot/antipara} = \frac{RA_1 TMR_1 - RA_2 TMR_2}{RA_1 + RA_2 (1 + TMR_2)}$$

The expression of  $TMR_{tot/antipara}$  is correct in the case where  $RA_1TMR_1 > RA_2TMR_2$ . We chose this case as it is the most frequently encountered in our structures.

As we have seen in the magnetic loops of Figures III-21 and III-23, for switching between the antiparallel configuration of the references (which is necessary to enhance the STT efficiency) and the parallel one (that would ensure the stability of the stored information against read voltage), rather large magnetic fields are needed. In a device, applying these fields (if achievable) would lead to a loss of the written state of the memory dot.

One could then consider keeping the system in an antiparallel configuration of the references to benefit from the enhancement of the STT effect and still read the information in this configuration. This leads to some requirements on the two tunnel barriers. Indeed, as seen in the above expression, if one wants to have a resulting TMR with antiparallel references it is necessary to satisfy the condition  $RA_1TMR_1 > RA_2TMR_2$ , which is equivalent to having  $\Delta RA_1 > \Delta RA_2$ . This is commonly achieved by dissymmetrizing the barriers (changing the oxidation conditions for example).

In order to test the effect of the two barrier parameters on the transport properties of double magnetic tunnel junctions we deposited three stacks with varying MgO barriers. The junctions are composed of the same reference layers and storage layer as the junction shown in Figure III-21. Two types of barriers were deposited:

- LP = Mg0.6/Ox/Mg0.5 (low pressure conditions  $3.10^{-2}$  mbar, 100 sccm, 360 s)
- HP = Mg0.9/Ox/Mg0.5 (high pressure conditions 150 mbar, 10 s)

We then combine them so that we have either symmetric or asymmetric barriers in the stack. Transport properties were measured by CIPT in perpendicular mode, both with parallel or antiparallel configuration of the references. These configurations are obtained by applying the previously shown field treatments to the junctions, prior to the transport measurements. Results are given in Table III-1, where the first label corresponds to the bottom barrier and the second label to the top one.

Type of barriers	TMR <sub>para</sub> (%)	TMR <sub>antipara</sub> (%)
HP / LP	32	35
LP / LP	16	7
HP / HP	27	13

Table III-1: Values of the measured TMR by CIPT for double junctions with different types of oxidation conditions for the two tunnel barriers.

It appears that in the case of asymmetric barriers (HP/LP), the TMR values in parallel and antiparallel configurations are identical (within the error range of the measurement). This indicates that the  $\Delta RA$  of the top barrier done with low pressure conditions is negligible compared to the one of the bottom barrier. On the contrary,

with symmetric barriers (LP/LP or HP/HP), the TMR in the antiparallel configuration of the references is half the one obtained in the parallel configuration. Even though barriers are nominally identical, we notice that the TMR in the antiparallel configuration does not drop down to zero. This means that probably due to different growth conditions, the two barriers have distinct parameters which lead to a non-zero resulting TMR. This effect had already been observed in other studies [Sat-13].

One could however question the validity of the CIPT fit when two barriers are present. We then calculated the expected values of TMR in the double junctions, using the parameters measured in individual junctions with either bottom or top references (given in Table III-2). Values given here correspond to the standard mean values obtained for the different types of stack and barriers.

Type of barrier	Reference	RA ( $\Omega\mu\text{m}^2$ )	TMR (%)
HP	bottom	50	80
	top	50	15
LP	bottom	10	40
	top	10	10

Table III-2: Transport parameters measured on individual junctions by CIPT for two types of oxidation conditions (low pressure LP and high pressure HP).

Note that despite identical tunnel barriers, magnetic tunnel junctions with top Co/Pd reference always give smaller TMR signals, as was already observed previously.

Table III-3 presents the calculated values of TMR in double junctions with varying types of barrier, using the parameters of the individual barriers extracted from the measurements of single junctions. For the bottom barrier we take the parameters of the junctions with a bottom reference whereas for the top barrier we use those of the junctions with a top reference. We see that these results qualitatively agree with the CIPT measurements performed on full double junctions. Similarly, TMR signals in the parallel and antiparallel configurations of the references are almost identical in the case of asymmetric barriers while a rather large decrease is observed with the antiparallel configuration in the symmetric cases.

Type of barriers	TMR <sub>para</sub> (%)	TMR <sub>antipara</sub> (%)
HP / LP	68	64
LP / LP	10	6
HP / HP	48	30

Table III-3: Values of the calculated TMR by CIPT for double junctions with different types of oxidation conditions for the two tunnel barriers, using the parameters of single junctions given in Table III-2.

### **III-4. Conclusions**

We saw that replacing the Ta cap by an MgO one in our standard Co/Pt-based bottom referenced tunnel junctions enables improving significantly the perpendicular anisotropy of the storage layer. Indeed, in the case of a FeCoB/Ta<sub>0.3</sub>/FeCoB composite storage layer the effective critical thickness, at which we have the out-of-plane to in-plane reorientation of the magnetization, reaches 2.7 nm instead of 1.1 nm in the Ta-capped structures. The total interfacial anisotropy is also doubled (from about 1 to 2 erg.cm<sup>-2</sup>). This is a particularly interesting result that gives the possibility to improve the thermal stability of the memory dots.

We developed top reference layers made of Co/Pd multilayers. To obtain satisfying magnetic properties, several parameters have to be adjusted, in particular the magnetic thicknesses in the multilayers. These top references have been found to be compatible with the previously optimized Co/Pt bottom SAF references so that they could be integrated in a complete double structure.

We showed that a double magnetic tunnel junction with two MgO tunnel barriers and two SAF references can be prepared. As expected from the behavior of the different parts of the structure, a magnetically functional stack could be observed by VSM measurements.

### III-5. References

[Ban-10] S. Bandiera, R. C. Sousa, Y. Dahmane, C. Ducruet, C. Portemont, V. Baltz, S. Auffret, I. L. Prejbeanu, and B. Dieny, *Comparison between synthetic antiferromagnets and single hard layers as reference layer in perpendicular magnetic tunnel junctions*, [IEEE Magn. Lett.](#) **1**, 3000204 (2010).

[Ban-11] S. Bandiera, *Jonctions tunnel magnétiques à anisotropie perpendiculaire et écriture assistée thermiquement*, [PhD Thesis](#), Grenoble University (2011).

[Clé-14] P.-Y. Clément, C. Baraduc, M. Chshiev, B. Dieny, L. Vila, and C. Ducruet, *Double barrier magnetic tunnel junctions with write/read mode select layer*, Proceedings of the [6<sup>th</sup> IEEE International Memory Workshop \(IMW\)](#), Taipei (May 18-21, 2014).

[Cuc-15] L. Cuchet, B. Rodmacq, S. Auffret, R. C. Sousa, I. L. Prejbeanu, and B. Dieny, *Perpendicular magnetic tunnel junctions with double barrier and single or synthetic antiferromagnetic storage layer*, [J. Appl. Phys.](#) **117**, 233901 (2015).

[Dia-07] Z. Diao, A. Panchula, Y. Ding, M. Pakala, S. Wang, Z. Li, D. Apalkov, H. Nagai, A. Driskill-Smith, L-C. Wang, E. Chen, and Y. Huai, *Spin transfer switching in dual MgO magnetic tunnel junctions*, [Appl. Phys. Lett.](#) **90**, 132508 (2007).

[Ike-10] S. Ikeda, K. Miura, H. Yamamoto, K. Mizunuma, H. D. Gan, M. Endo, S. Kanai, J. Hayakawa, F. Matsukura, and H. Ohno, *A perpendicular-anisotropy CoFeB–MgO magnetic tunnel junction*, [Nature Mater.](#) **9**, 721-724 (2010).

[Ino-00] K. Inomata, Y. Saito, K. Nakajima, and M. Sagoi, *Double tunnel junctions for magnetic random access memory devices*, [J. Appl. Phys.](#) **87**, 6064-6066 (2000).

[Koz-10] X. Kozina, S. Ouardi, B. Balke, G. Stryganyuk, G. H. Fecher, C. Felser, S. Ikeda, H. Ohno and E. Ikenaga, *A nondestructive analysis of the B diffusion in Ta–CoFeB–MgO–CoFeB–Ta magnetic tunnel junctions by hard X-ray photoemission*, [Appl. Phys. Lett.](#) **96**, 072105 (2010).

[Kub-12] H. Kubota, S. Ishibashi, T. Saruya, T. Nozaki, A. Fukushima, K. Yakushiji, K. Ando, Y. Suzuki, and S. Yuasa, *Enhancement of perpendicular magnetic anisotropy in FeB free layers using a thin MgO cap layer*, [J. Appl. Phys.](#) **111**, 07C723 (2012).

[Liu-12] T. Liu, J. W. Cai, and Li Sun, *Large enhanced perpendicular magnetic anisotropy in CoFeB/MgO system with the typical Ta buffer replaced by an Hf layer*, [AIP Advances](#) **2**, 032151 (2012).

[Mon-02] S. Monso, B. Rodmacq, S. Auffret, G. Casali, F. Fettar, B. Gilles, B. Dieny and P. Boyer, *Crossover from in-plane to perpendicular anisotropy in Pt/CoFe/AlO<sub>x</sub> sandwiches as a function of Al oxidation: A very accurate control of the oxidation of tunnel barriers*, [Appl. Phys. Lett.](#) **80**, 4157-4159 (2002).

[Rod-09] B. Rodmacq, A. Manchon, C. Ducruet, S. Auffret, and B. Dieny, *Influence of thermal annealing on the perpendicular magnetic anisotropy of Pt/Co/AlO<sub>x</sub> trilayers*, [Phys. Rev. B](#) **79**, 024423 (2009).

[Sat-12] H. Sato, M. Yamanouchi, S. Ikeda, S. Fukami, F. Matsukura, and H. Ohno, *Perpendicular-anisotropy CoFeB-MgO magnetic tunnel junctions with a MgO/CoFeB/Ta/CoFeB/MgO recording structure*, [Appl. Phys. Lett.](#) **101**, 022414 (2012).

[Sat-13] H. Sato, M. Yamanouchi, S. Ikeda, S. Fukami, F. Matsukura, and H. Ohno, *MgO/CoFeB/Ta/CoFeB/MgO recording structure in magnetic tunnel junctions with perpendicular easy axis*, [IEEE Trans. Magn.](#) **49**, 4437-4440 (2013).



# CHAPTER IV

## Pt- and Pd-free synthetic antiferromagnetic structures

<b>IV-1. Variation of the coupling strength as a function of the nature and thickness of the insertion layer .....</b>	<b>130</b>
IV-1.1 Ta insertion.....	130
IV-1.2 Ru insertion.....	131
IV-1.3 Ta/Ru bilayer insertion .....	132
IV-1.4 Influence of Ta thickness on RKKY coupling.....	135
<b>IV-2. Magnetic properties of FeCoB-based SAF.....</b>	<b>137</b>
IV-2.1 Determination of the magnetic dead layer thicknesses.....	137
IV-2.2 Comparison between Ta/Ru and Ru spacers .....	139
IV-2.3 Modification of the magnetic compensation .....	140
<b>IV-3. Use of an FeCoB-based SAF in double junctions.....</b>	<b>143</b>
IV-3.1 Use as a SAF storage layer in a double junction with two SAF reference layers .....	144
IV-3.2 Use as a top reference in a double junction with single ferromagnetic storage layer .....	145
IV-3.3 Use as a SAF storage layer in a double junction with a bottom reference layer and a top soft control layer .....	146
<b>IV-4. FeCoB-based SAF as reference layers in single magnetic tunnel junctions .....</b>	<b>149</b>
IV-4.1 Use as a top reference.....	149
IV-4.2 Use as a bottom reference.....	150
<b>IV-5. Stability of the SAF configuration in small pillars .....</b>	<b>152</b>
<b>IV-6. Conclusions .....</b>	<b>154</b>
<b>IV-7. References .....</b>	<b>155</b>



As we have seen in Chapter I, the phenomenon of RKKY interactions was discovered relatively early in the 1950s. However, it is only for 25 years that practical applications have been developed in the field of spintronics. Indeed, being able to couple antiferromagnetically two magnetic layers is particularly interesting in the case of small devices for which stray field effects become extremely important.

In the case of perpendicular systems, the RKKY coupling has been mostly used in the reference layers made most of the time of Co/Pt or Co/Pd multilayers. If these materials are interesting for their large perpendicular anisotropy, they have the drawback of being difficult to etch. Besides they require a good control of the deposition tool as usual very thin layers of a few tens of nanometer are needed.

This is why we propose in this part to study synthetic antiferromagnetic structures made of two FeCoB layers separated by a spacer of different nature (Ta, Ru or Ta/Ru). We will first study the evolution of the magnetic properties of such systems as a function of the inserted layer. We will then see how we can tune these properties by playing on the nature of the spacer as well as on the magnetic compensation. We will show that such SAF layers can be used in different parts of double junctions with perpendicular anisotropy. Finally, using these structures as reference layers, we will be able to deposit Pt (Pd)-free single magnetic tunnel junctions [\[Cuc-16\]](#).

## **IV-1. Variation of the coupling strength as a function of the nature and thickness of the insertion layer**

As shown in 1991, the oscillatory behavior of magnetic coupling between two ferromagnetic layers separated by a metallic spacer is a common phenomenon observed with a wide range of spacer materials [Par-91]. The nature of the inserted layer however changes period, phase and strength of the coupling. In this part, we will study the antiferromagnetic coupling between two FeCoB layers as a function of spacer thickness for different types of insertion.

### **IV-1.1 Ta insertion**

In 2012, V. Sokalski *et al.* showed that an antiferromagnetic coupling can be obtained with two perpendicularly magnetized CoFeB layers separated by a Ta spacer [Sok-12]. This antiferromagnetic configuration of the magnetizations appears for Ta thicknesses larger than 0.6 nm but is rather weak: the antiferromagnetic plateau does not exceed 200-250 Oe, for magnetic thicknesses of 0.9 and 1.2 nm on both sides of the spacer. The case of thinner insertion layers has already been presented in Chapter III when introducing an MgO capping on top of the storage layer. With a 0.3 nm thick Ta insertion, the two FeCoB layers are strongly ferromagnetically coupled, probably thanks to direct coupling through pinholes.

We obtained results similar to those of the literature when inserting a Fe-rich FeCoB<sub>1.2</sub>/Ta<sub>0.8</sub>/FeCoB<sub>1.2</sub>/MgO composite storage layer in a MTJ stack comprising our standard Co/Pt-based bottom reference. The magnetic loop measured by VSM is presented in Figure IV-1.

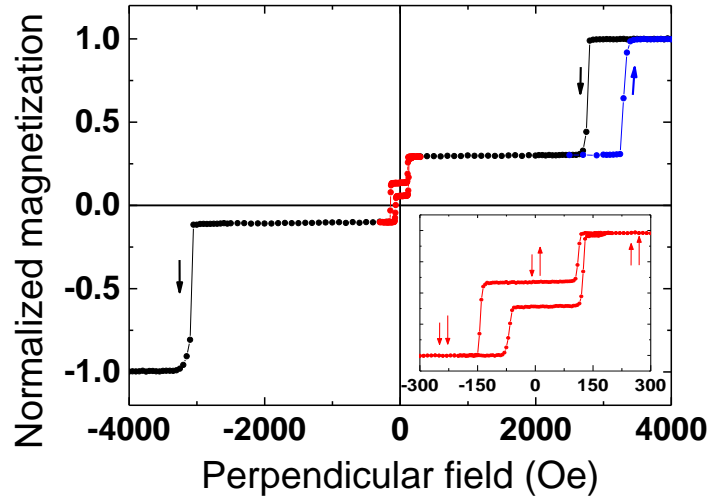


Figure IV-1: Magnetic loop measured by VSM with perpendicular applied field for a junction with bottom SAF reference and a top SAF storage layer made of FeCoB1.2/Ta0.8/FeCoB1.2/MgO.

As can be seen, the storage layer has indeed a typical SAF behavior with two transitions. The inset allows visualizing more precisely the loop performed on the free layer. After saturating the SAF in positive fields, the field is swept towards negative values down to a field of -300 Oe and is then increased again up to 300 Oe. This treatment gives the full loop of the SAF and shows that two antiparallel configurations of the FeCoB magnetizations are stable in zero field, making this SAF storage layer functional for memory applications. Note that as already pointed out, the stability of the antiferromagnetic plateau is rather limited (around 250 Oe in total in that case). We can see the transitions of the major loop performed on the SAF storage layer are also shifted due to the antiferromagnetic indirect coupling that exists through the MgO barrier.

### IV-1.2 Ru insertion

Knowing that the RKKY coupling is particularly strong with Ru and that good results were obtained with this spacer for the standard Co/Pt (Pd)-based SAF (see Chapters II and III), we decided to investigate the use of Ru with FeCoB layers. To that aim, a series of junctions with a bottom SAF reference and a top FeCoB1.3/Rux/FeCoB1.2/MgO composite storage layer was deposited, with varying Ru thickness. We recall that the standard bottom reference consists of: Ta<sub>3</sub>/Pt<sub>5</sub>/(Co<sub>0.5</sub>/Pt<sub>0.25</sub>)<sub>6</sub>/Co<sub>0.5</sub>/Ru<sub>0.9</sub>/(Co<sub>0.5</sub>/Pt<sub>0.25</sub>)<sub>3</sub>/Co<sub>0.5</sub>/Ta<sub>0.3</sub>/FeCoB1.2/MgO. For simplicity, it will be referred as SAF<sub>1</sub> in the following. It is included to account for the needs in terms of normalization, as explained previously. The FeCoB bilayer is made slightly dissymmetric as a larger magnetically dead layer is expected in the

bottom FeCoB (closest to the MgO barrier), by analogy with the results obtained with Ta in Chapter II.

Figure IV-2 shows the magnetic loops measured by VSM for six different Ru thicknesses. It appears that in the case of a Ru spacer, a three transitions type of behavior is observed (Figure II-14 (b), Chapter II). As explained previously, this is due to the coupling energy becoming stronger than the anisotropy one. Two reversible parts are visible at large fields on both sides of an abrupt transition at low field. Extracting the coupling field  $H_{SAF}$  is a bit complicated by the presence of the transitions of the bottom SAF at large fields, particularly in the case of large coupling strengths for Ru insertions of 0.5, 0.55 and 0.6 nm (see Figure IV-2 (a), (b), (c)). It can however already be seen that the coupling field is decreasing as the Ru thickness increases. However,  $H_{SAF}$  reaches values as large as -2500 Oe, which are much higher than the ones obtained with Ta.

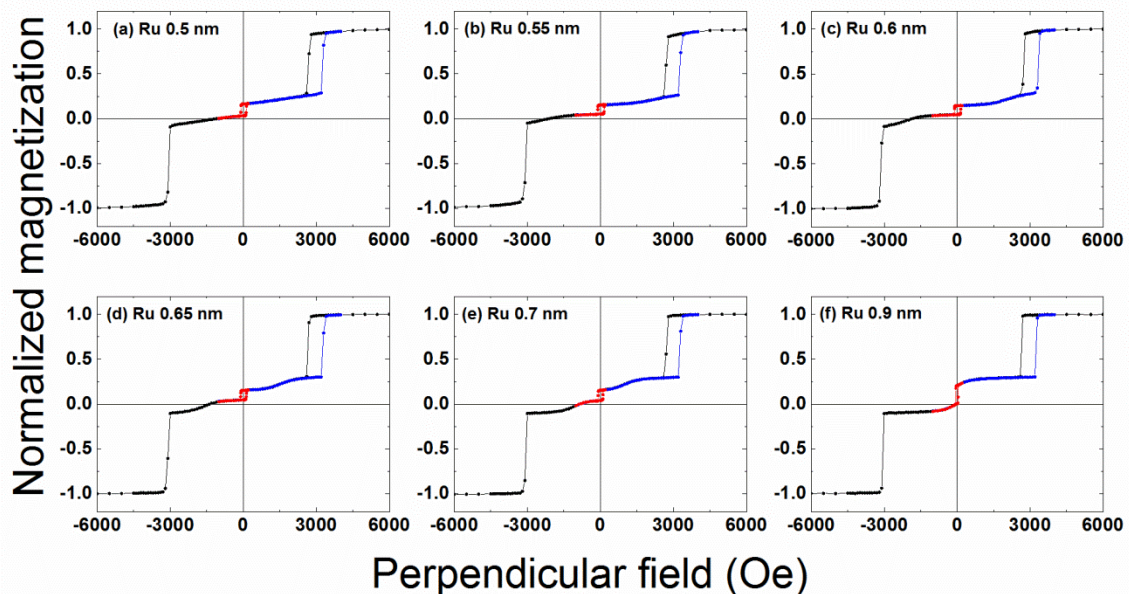


Figure IV-2: Magnetic loops measured by VSM with perpendicular applied field for samples with standard bottom SAF reference and a composite FeCoB<sub>1.3</sub>/Ru<sub>x</sub>/FeCoB<sub>1.2</sub> storage layer. Values of  $x$  are: (a) 0.5 (b) 0.55 (c) 0.6 (d) 0.65 (e) 0.7 (f) 0.9 nm.

### IV-1.3 Ta/Ru bilayer insertion

In Chapter II, we pointed out the important role of a Ta insertion in improving the TMR signal of our magnetic tunnel junctions. It is also known that the getter effect and the anisotropy are much lower with Ru than with Ta. Then, to try and combine the large RKKY coupling brought by Ru with the advantages of Ta, we changed the storage layer to FeCoB<sub>1.4</sub>/Ta<sub>0.2</sub>/Ru<sub>x</sub>/FeCoB<sub>1.1</sub>/MgO. We proceed similarly by depositing a series of junctions with varying spacer thickness. Some examples of the

magnetic cycles measured by VSM are given in Figure IV-3, with focus made on the storage layer cycle only.

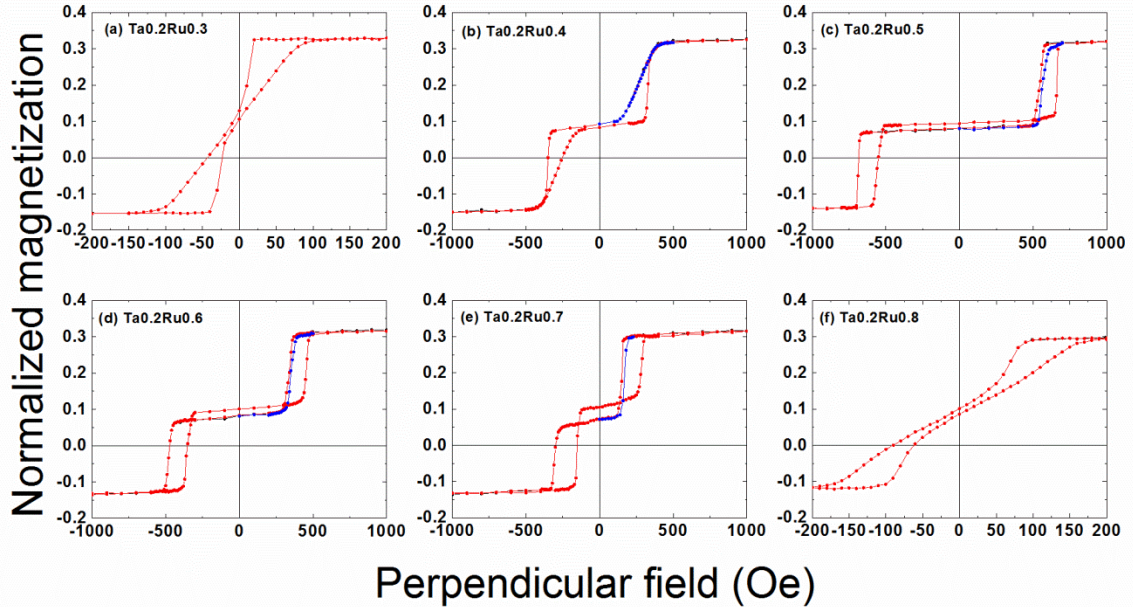


Figure IV-3: Magnetic loops measured by VSM with perpendicular applied field for samples with standard bottom SAF reference and a composite FeCoB<sub>1.4</sub>/Ta<sub>0.2</sub>Ru<sub>x</sub>/FeCoB<sub>1.1</sub> storage layer. Values of x are: (a) 0.3 (b) 0.4 (c) 0.5 (d) 0.6 (e) 0.7 (f) 0.8 nm. Only zooms on the storage layers are shown.

As the Ru thickness increases, we can see the coupling going from ferromagnetic to antiferromagnetic and back to ferromagnetic, which is typical of the oscillatory behavior of RKKY coupling. The antiferromagnetic coupling is maintained for Ru thicknesses between 0.4 and 0.7 nm and its strength depends on the spacer thickness. For very thin layers, the ferromagnetic coupling probably originates from direct coupling through pinholes. In the case of thick spacers, the ferromagnetic coupling might have a dipolar origin. As expected, the stability of the SAF is less than the one achieved with pure Ru. The perpendicular anisotropy is on the other hand higher as more abrupt transitions appear and the switching of the SAF happens in two steps instead of three.

When carefully looking at the loops of Figure IV-3, one notices that the levels of the antiparallel plateau vary as a function of Ru thickness. Between 0.4 and 0.5 nm of Ru, the levels even get inverted. This suggests that there is a change of total magnetization as the Ru spacer thickness varies. We can plot the amplitude of each transition (normalized to the amplitude of the bottom part of the SAF  $M_1$ ) as a function of insertion thickness. The SAF storage can be schematically represented as  $M_b$ /Ta<sub>0.2</sub>/Ru<sub>x</sub>/ $M_t$ . From the two distinct behaviors, as shown in Figure IV-4, we can attribute the constant transition to the bottom FeCoB magnetization  $M_b$  that does not see its interfaces change. On the contrary, the decreasing magnetization can be

associated to the top FeCoB magnetization  $M_t$ , which grows on a thicker and thicker Ru layer. This most probably translates into an increase in magnetic dead layer thickness. From this study, we can then infer that the first transition at positive field corresponds to the reversal of the bottom FeCoB layer  $M_b$  (in contact with the MgO barrier) and the second transition at negative field to the reversal of the top FeCoB layer  $M_t$  (in contact with the MgO capping layer).

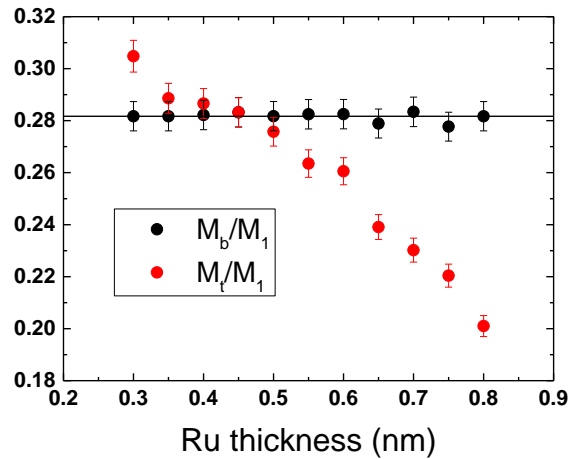


Figure IV-4: Normalized magnetizations  $M_b/M_1$  and  $M_t/M_1$  as a function of Ru thickness for junctions with bottom SAF reference and FeCoB1.4/Ta0.2/Rux/FeCoB1.1/MgO top storage layer.

To compare the Ta/Ru spacer with the Ru one, the values of the coupling field  $H_{SAF}$  have been extracted for both series of samples by carrying out minor loop measurements on the storage layer: after saturation at positive fields, the field is decreased down to 0 Oe and increased again to switch back the magnetization of the softest layer of the SAF. Note that in the case of ferromagnetic coupling, one cannot extract the value of the coupling field, so we arbitrarily set it at zero. The usual sign convention has been applied and negative values of field are taken to account for the antiferromagnetic nature of the coupling. The two plots of  $H_{SAF}$  as a function of Ru thickness are gathered in Figure IV-5.

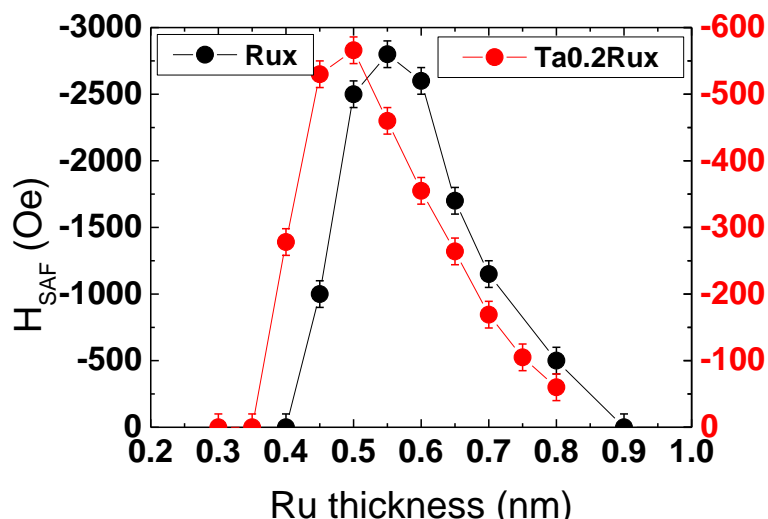


Figure IV-5: Evolution of the RKKY coupling field as a function of Ru thickness for Rux (black) and Ta<sub>0.2</sub>/Rux (red) spacers. Note the different scales for the field amplitude.

In both cases, the trend is really similar: the coupling field amplitude increases to reach a maximum around 0.5-0.6 nm of Ru and then monotonously decreases. We observe that the maximum that commonly appears around 0.9 nm in the Co/Pt SAFs is missing in that case. This might be due to the fact that the magnetic layers are alloys here instead of pure materials. Upon Ta insertion, the curve is slightly shifted towards smaller Ru thicknesses but by a value of 0.05 nm, smaller than the 0.2 nm of Ta insertion. This effect can be explained by the dependence in period, phase and amplitude of the RKKY coupling on the nature of the non-magnetic spacer [Par-91], as well as on the nature of the magnetic material [Pet-91]. Figure IV-5 allows noting especially that the maximum of amplitude of the coupling field is reduced by a factor of 5 when the Ru spacer is replaced by a Ta<sub>0.2</sub>/Ru one. This agrees with previous results indicating that the antiferromagnetic coupling is very weak with pure Ta. Even though the maximum coupling energies cannot be determined accurately due to the lack of information on saturation magnetization and magnetic dead layers with that kind of spacers, we can however estimate them to be roughly 0.30 erg.cm<sup>-2</sup> and 0.06 erg.cm<sup>-2</sup> for a Ru<sub>0.6</sub> and a Ta<sub>0.2</sub>Ru<sub>0.5</sub> spacer, respectively (using  $J_{\text{cpl}} = H_{\text{SAF}} M_s t$ , with  $M_s$  and  $t$  the saturation magnetization and thickness of the softest layer of the SAF).

#### IV-1.4 Influence of Ta thickness on RKKY coupling

To study more precisely the effect of Ta on the RKKY coupling, samples with varying thickness of Ta in the Ta/Ru spacer were prepared. In order to keep the maximum coupling amplitude, the Ru thickness is adjusted using a linear approximation between Ta<sub>0</sub> and Ta<sub>0.2</sub> nm. The width of the antiparallel plateau as a function of Ta thickness is plotted in Figure IV-6.

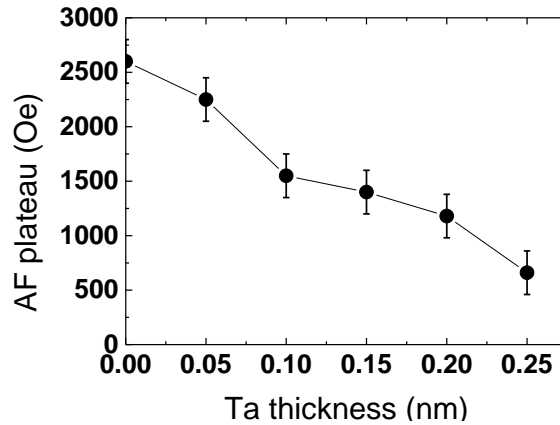


Figure IV-6: Variation of the width of the antiparallel plateau as a function of Ta insertion thickness for junctions made of SAF<sub>1</sub>/MgO/FeCoB<sub>1.4</sub>/Tax/Ruy/FeCoB<sub>1.1</sub>/MgO.  $y$  is adjusted to keep the maximum coupling amplitude.

A progressive decrease of the antiferromagnetic coupling strength is observed as the Ta thickness increases. The width of the antiparallel plateau goes from 2600 Oe without Ta insertion down to about 600 Oe for a Ta thickness of 0.25 nm. This agrees with our first result giving a stability range of only 250 Oe in the case of a pure Ta insertion of 0.8 nm.

## IV-2. Magnetic properties of FeCoB-based SAF

In this part, we will study in more details the magnetic properties of the FeCoB/(Ta)/Ru/FeCoB synthetic antiferromagnetic structures. We will in particular extract the magnetic dead layer thicknesses as well as examine the magnetic compensation of the stack.

### IV-2.1 Determination of the magnetic dead layer thicknesses

We present here the determination of the magnetic dead layer thickness in the bottom FeCoB layer for the SAF structure with a Ta<sub>0.2</sub>Ru<sub>0.5</sub> insertion. To that aim a series of junctions with the following composition has been prepared: SAF<sub>1</sub>/MgO/FeCoB<sub>x</sub>/Ta<sub>0.2</sub>/Ru<sub>0.5</sub>/FeCoB<sub>1.1</sub>/MgO/Pt<sub>2</sub>. As usual the bottom reference is used for normalization. The ratios  $M_b/M_1$  and  $M_t/M_1$  as a function of the nominal bottom FeCoB thickness are plotted in Figure IV-7.

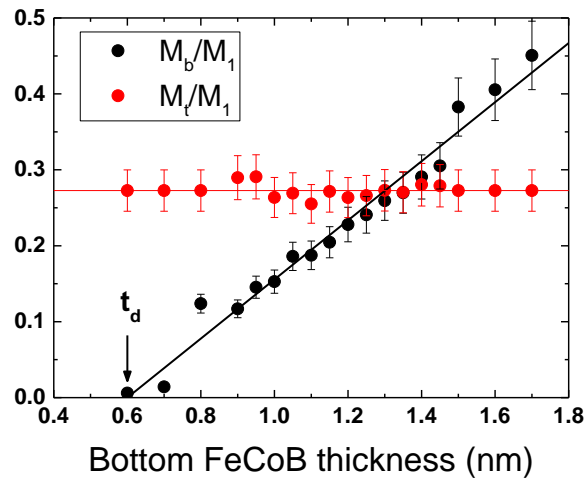


Figure IV-7: Normalized magnetizations  $M_b/M_1$  and  $M_t/M_1$  as functions of bottom FeCoB thickness for junctions consisting of SAF<sub>1</sub>/MgO/FeCoB<sub>x</sub>/Ta<sub>0.2</sub>/Ru<sub>0.5</sub>/FeCoB<sub>1.1</sub>/MgO.

The obtained trends are as expected: the magnetization of the top part  $M_t$  remains approximatively constant while the bottom magnetization  $M_b$  increases with FeCoB thickness. Note that for very thin FeCoB layers (<0.9 nm) it gets really difficult to extract the amplitude of the transition, as can be seen in the example of Figure IV-8 (a) that gives the magnetic loop of a junction with a FeCoB<sub>0.8</sub>/Ta<sub>0.2</sub>/Ru<sub>0.5</sub>/FeCoB<sub>1.1</sub> SAF storage layer. Thus, to calculate the value of  $M_b$ , we use the total amplitude of the SAF and assume  $M_t$  is equal to the mean value extracted from the other data points (horizontal red line on Figure IV-7). Similarly, for thicker FeCoB layers, when the magnetization starts to become planar, the

different contributions are also not so easy to distinguish, as illustrated in Figure IV-8 (b) for a FeCoB1.6/Ta0.2/Ru0.5/FeCoB1.1 storage layer. We then proceed the same way to extract the value of  $M_b$ . With this data treatment, there is a larger error for the estimated values at large and small thicknesses. Indeed, on the graph of Figure IV-7, we can clearly see that these points deviate from the linear fit. Using this fit, a magnetic dead layer thickness of about 0.6 nm is obtained as well as a saturation magnetization  $M_s=1630$  emu.cm<sup>-3</sup>. If we exclude the points corresponding to the three smaller and larger thicknesses, the slope of the linear fit is slightly reduced and gives a magnetic dead layer of about 0.5 nm and a saturation magnetization around 1390 emu.cm<sup>-3</sup>, which is closer to the value obtained previously in Chapter II for a standard Ta-capped FeCoB free layer.

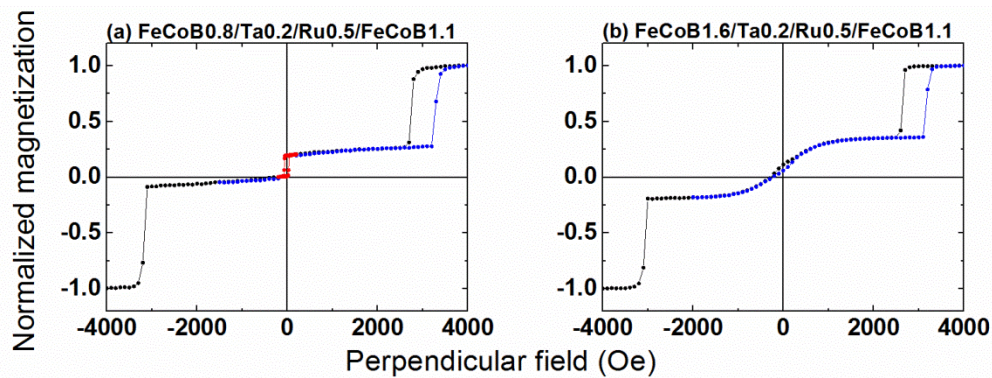


Figure IV-8: Magnetic loops measured by VSM with perpendicular applied field for samples with standard bottom SAF reference and a composite FeCoB<sub>x</sub>/Ta0.2/Ru0.5/FeCoB1.1 storage layer. Examples with (a) thin 0.8 nm and (b) thick 1.6 nm bottom FeCoB layers are shown.

This study as a function of thickness had also the advantage of confirming the assumption made previously that the first transition at positive fields corresponds indeed to the reversal of the bottom FeCoB layer, which is in contact with the tunnel barrier.

The magnetic dead layer of the top FeCoB layer may also be estimated from Figure IV-7, if one assumes that the saturation magnetization is the same in the two FeCoB layers. This hypothesis is probably not so accurate because, as we have seen in Chapter II, the value of  $M_s$  depends a lot on the nature of the other materials at the interfaces. This assumption enables however to get a crude estimation of the dead layer thickness. We see indeed that  $M_b=M_t$  for a bottom thickness of about 1.3 nm. Knowing that the nominal top FeCoB thickness is 1.1 nm, we estimate a magnetic dead layer thickness of 0.4 nm in the top FeCoB layer. This is in good qualitative agreement with our former results of Chapter II that gave larger magnetic dead layer thicknesses in the case of top FeCoB growing on MgO and capped with Ta, than in bottom FeCoB layers growing on Ta and capped with MgO.

### IV-2.2 Comparison between Ta/Ru and Ru spacers

To have an idea of the difference in magnetic behavior between a Ta/Ru and a pure Ru spacer, we compare directly the magnetic loops of two MTJs with the same nominal thickness of FeCoB in both parts of the SAF that is to say FeCoB<sub>1.4</sub>/spacer/FeCoB<sub>1.1</sub>. The loops are given in Figure IV-9, the bottom panel presenting zooms on the storage layer cycle.

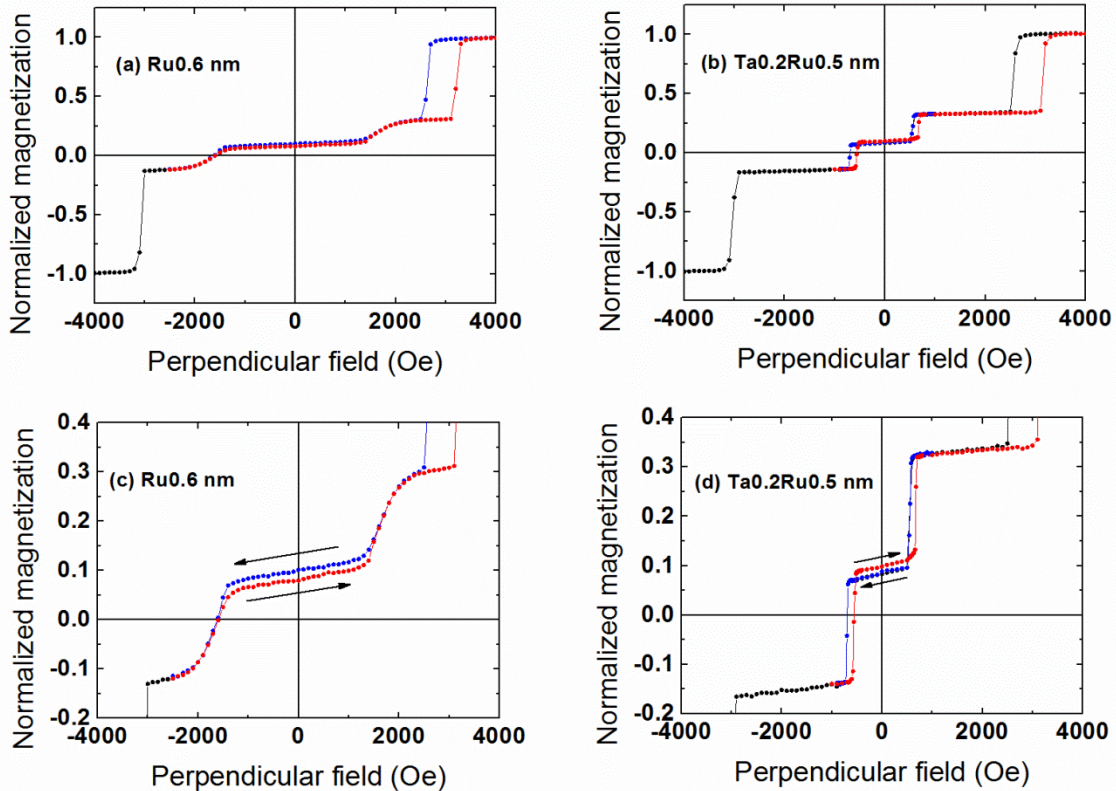


Figure IV-9: Magnetic cycles measured by VSM with perpendicular applied field for samples composed of SAF<sub>1</sub>/MgO/FeCoB<sub>1.4</sub>/spacer/FeCoB<sub>1.1</sub>/MgO/Pt<sub>2</sub>. The spacer is either Ru0.6 (a, c) or Ta0.2/Ru0.5 (b, d). Curves (c) and (d) are zooms of the top SAF.

As already pointed out in the previous part, the coupling strength is much larger with pure Ru as the stability of the antiparallel plateau ranges between  $\pm 1300$  Oe with Ru0.6 instead of  $\pm 600$  Oe for the Ta0.2Ru0.5 spacer.

The zooms of Figure IV-9 (c) and (d) show that changing the nature of the spacer results in a modification of the relative positions of the antiparallel plateau. The descending branch (in blue) of the loop is above the ascending one (in red) in the case of a Ru spacer whereas it is the opposite with the Ta/Ru bilayer spacer. The system is thus under-compensated in the first case and over-compensated in the other one. As the nominal thicknesses are identical, this is another indication that the magnetic dead layer varies as a function of the material at the interface. Normalizing the two

transitions by  $M_i$ ,  $M_t$  is found to remain constant while  $M_b$  decreases by about 15 % when the FeCoB/Ta interface is replaced by a FeCoB/Ru one. The magnetic dead layer thickness is then greater with a pure Ru spacer.

Assuming  $M_s$  is the same whatever the insertion layer (which is probably not so true, as explained earlier), we would find a magnetic dead layer thickness of about 0.7 nm in the bottom FeCoB layer in the case of a pure Ru spacer.

### IV-2.3 Modification of the magnetic compensation

In the previous series of samples with a Ta<sub>0.2</sub>Ru<sub>0.5</sub> spacer and a varying thickness of the bottom FeCoB layer, the stability of the SAF seemed to vary depending on the compensation state of the SAF. It was however not very easy to observe this phenomenon, probably because the coupling is rather weak with Ta/Ru insertions. This is why we carried out similar experiments with pure Ru-based tunnel junctions.

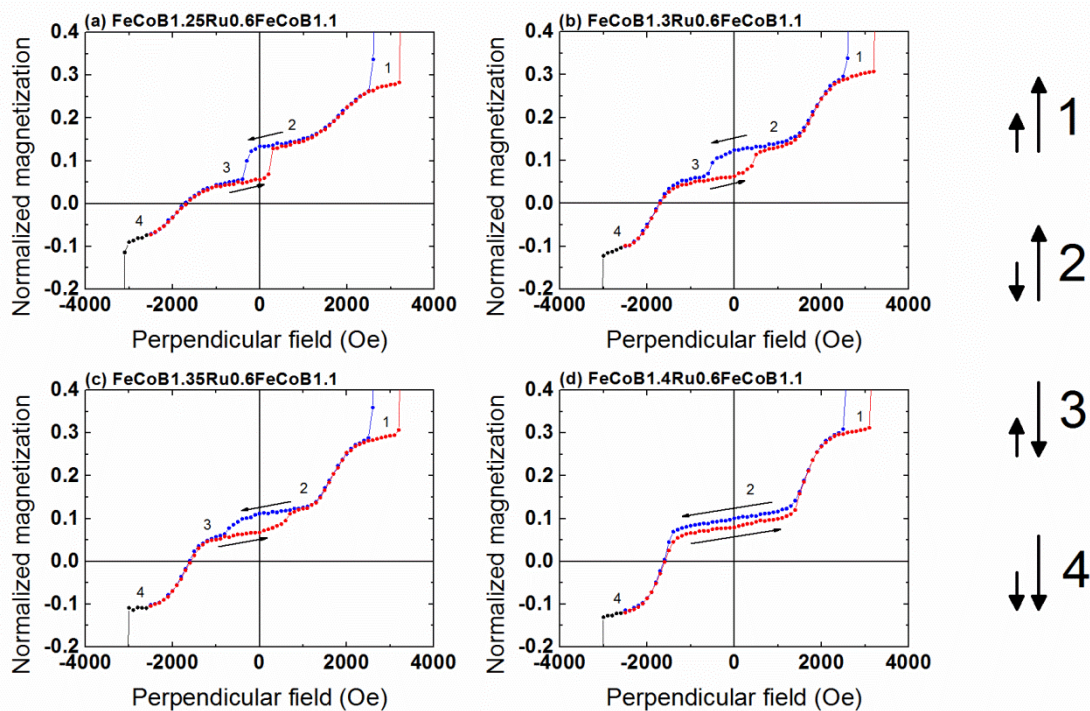


Figure IV-10: Magnetic cycles of SAF<sub>1</sub>/MgO/FeCoB<sub>x</sub>/Ru<sub>0.6</sub>/FeCoB<sub>1.1</sub>/MgO/Pt<sub>2</sub> structures measured by VSM with perpendicular applied field. 4 different thicknesses of bottom FeCoB are shown: (a) 1.25 (b) 1.3 (c) 1.35 and (d) 1.4 nm. The magnetic configurations labelled 1 to 4 on the graphs are schematically represented on the right.

Figure IV-10 shows the magnetic cycles of MTJs with a bottom reference SAF<sub>1</sub> and a SAF storage layer with a Ru<sub>0.6</sub> insertion and varying bottom FeCoB thickness. The stability of the structure strongly depends on the magnetic thicknesses and thus on

the magnetic compensation on both sides of the spacer. For the thinner layers, when the system is under-compensated, an additional transition appears corresponding to the reversal of the net magnetization of the SAF, still keeping an antiparallel alignment of the magnetizations (transition from configurations 2 to 3 in Figure IV-10).

Defining the RKKY energy through the Ru spacer as  $J_{Ru}$ ,  $H$  the applied field,  $K_{effb}$  the effective perpendicular anisotropy of the bottom FeCoB layer with magnetization  $M_b$  and effective thickness  $t_b$ , the additional transition appears when:

$$J_{Ru} > HM_b t_b + K_{effb} t_b$$

The fact that this additional transition is not clearly seen in the Ta/Ru systems probably originates from the much reduced RKKY coupling energy in these stacks compared to the RuO.6 SAFs.

This additional transition strongly reduces the stability range of the antiparallel plateau. It occurs at about -350 Oe in the case of the thinnest bottom FeCoB layer, as shown in Figure IV-10 (a). As the FeCoB thickness increases, we approach the magnetic compensation and the positions of the ascending and descending plateaus get progressively closer to one another. At the same time, the transition between configurations 2 and 3 shifts to larger fields and disappears around the magnetic compensation (see Figure IV-10 (d)). This comes from the fact that the torque exerted by the external field is inversely proportional to the net magnetization and becomes then less and less efficient as one reaches the magnetic compensation. This transition field  $H_{sw}$  can be qualitatively represented as:

$$H_{sw} = \frac{K_b t_b + K_t t_t}{M_t t_t - M_b t_b}$$

where  $K_{b,t}$ ,  $t_{b,t}$  and  $M_{b,t}$  are the anisotropy energy, effective magnetic thickness and saturation magnetization of the bottom and top FeCoB layers, respectively [Ber-97].

In Figure IV-11, we show the variation of this switching field as a function of the bottom FeCoB thickness. Using the above equation, we can make a fit (in red in the graph) that gives a compensation thickness of 1.44 nm for the bottom FeCoB layer at the divergence. Extracting any supplementary information from such a fit would require having a good knowledge of the saturation magnetizations and effective thicknesses. As was previously the case in the TaO.2RuO.5 system, such a compensation thickness indicates that the dead layer is larger in the bottom layer than in the top one.

The variation of the net magnetization (i.e. the difference between the two magnetic moments) of the SAF, normalized to  $M_1$ , as a function of bottom FeCoB thickness is also given in Figure IV-11. It corresponds to half the vertical opening of the low field magnetic cycle, as observed in Figure IV-10. As expected, the net magnetization decreases linearly with increasing FeCoB thickness. By extrapolating it

to zero, we find a compensation thickness for the bottom FeCoB layer of 1.46 nm, which is in very good agreement with the value of 1.44 nm determined previously.

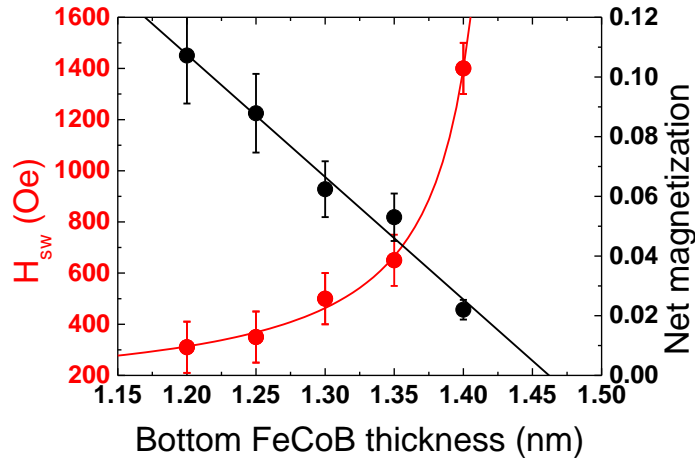


Figure IV-11: Switching field  $H_{sw}$  of the additional transition (in red) and net magnetization normalized to  $M_1$  (in black) as a function of the bottom FeCoB thickness for SAF<sub>1</sub>/MgO/FeCoB<sub>x</sub>/Ru<sub>0.6</sub>/FeCoB<sub>1.1</sub>/MgO/Pt<sub>2</sub> magnetic tunnel junctions.

If we assume the magnetic dead layer thickness of the top FeCoB layer to be identical in the Ta<sub>0.2</sub>Ru<sub>0.5</sub> and the Ru<sub>0.6</sub> systems (around 0.4 nm, as determined previously), we can estimate the magnetic dead layer of the bottom FeCoB, using a mean compensation thickness of 1.45 nm. We will in that case keep the hypothesis that the  $M_s$  value of FeCoB is the same in the whole stack. We then find a bottom magnetic dead layer thickness of about 0.75 nm, which leads to effective thicknesses of 0.7 nm in each FeCoB layer at the magnetic compensation. As seen in Chapter II, if the effective magnetic thicknesses are greater than 0.6 nm, the maximum TMR signal is guaranteed. This type of SAF should then be functional for device applications.

### IV-3. Use of an FeCoB-based SAF in double junctions

As we have seen in the previous parts, synthetic antiferromagnetic structures made of two FeCoB layers can be developed and their magnetic properties may be tuned by modifying the nature of the non-magnetic spacer or the magnetic compensation.

This type of SAF is particularly interesting for a use in double magnetic junctions with perpendicular anisotropy. Indeed, we presented in Chapter III the realization of double MTJs with a ferromagnetic storage layer in the middle of the stack [Cuc-15a]. In that type of stack, the most efficient configuration for STT switching is having antiparallel references. If the ferromagnetic storage layer is replaced by the newly developed FeCoB-based SAF, the STT efficiency will be in that case maximal if the references are oriented parallel. This is quite a good solution as the parallel configuration of the references might be favored due to dipolar coupling in patterned samples. Besides, having a SAF type of storage layer makes it more immune to the remaining stray fields. The two favorable configurations as a function of the type of storage layer are schematically represented in Figure IV-12.

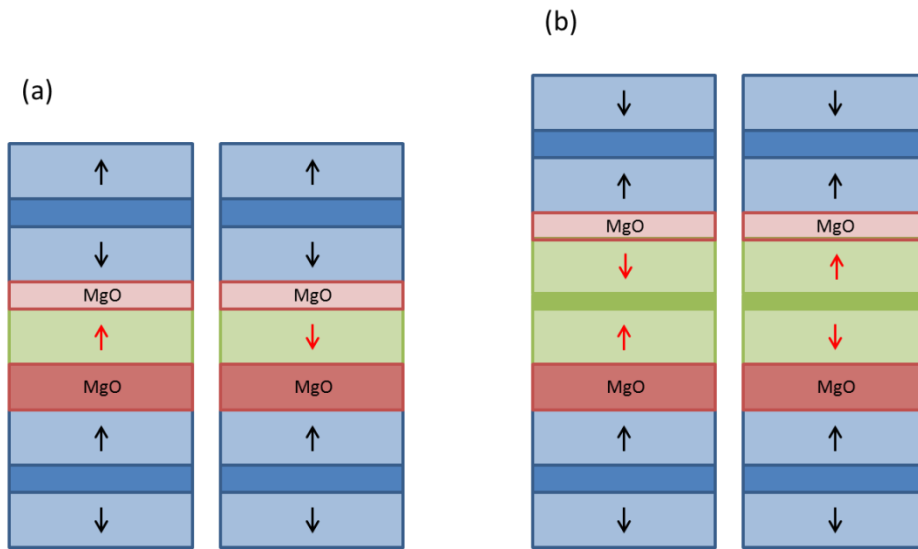


Figure IV-12: Schematic magnetic configurations optimizing STT efficiency in perpendicular double magnetic tunnel junctions: (a) antiparallel references and single ferromagnetic storage layer, (b) parallel references and synthetic antiferromagnetic storage layer.

The FeCoB-based SAF can be put at different positions in the structure and may have various functions as we will see in the following.

### IV-3.1 Use as a SAF storage layer in a double junction with two SAF reference layers

As explained above, the SAF can be put in the middle of the double junction stack presented in Chapter III instead of the single ferromagnetic layer. The stack then comprises three SAFs:

- Bottom reference SAF<sub>1</sub>: Ta<sub>3</sub>/Pt<sub>5</sub>/(Co<sub>0.5</sub>/Pt<sub>0.25</sub>)<sub>6</sub>/Co<sub>0.5</sub>/Ru<sub>0.9</sub>/(Co<sub>0.5</sub>/Pt<sub>0.25</sub>)<sub>3</sub>/Co<sub>0.5</sub>/Ta<sub>0.3</sub>/FeCoB<sub>1.2</sub>/MgO
- Storage layer SAF<sub>3</sub>: FeCoB/spacer/FeCoB
- Top reference SAF<sub>2</sub>: MgO/FeCoB<sub>1.2</sub>/Ta<sub>0.3</sub>/(Co<sub>0.4</sub>Pd<sub>1.2</sub>)<sub>4</sub>/Co<sub>0.4</sub>/Ru<sub>0.9</sub>/(Co<sub>0.4</sub>/Pd<sub>1.2</sub>)<sub>8</sub>/Co<sub>0.4</sub>/Pd<sub>2</sub>

Figure IV-13 shows an example of the magnetic loop obtained for a FeCoB<sub>1.2</sub>/Ta<sub>0.8</sub>/FeCoB<sub>1.2</sub> composite storage layer.

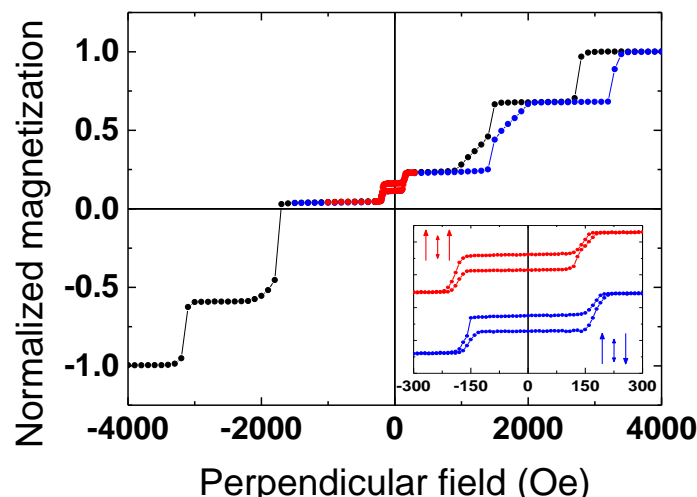


Figure IV-13: Magnetic cycle measured by VSM with perpendicular applied field for a double junction with SAF<sub>1</sub>/MgO/FeCoB<sub>1.2</sub>/Ta<sub>0.8</sub>/FeCoB<sub>1.2</sub>/MgO/SAF<sub>2</sub>. The inset shows minor loops recorded with either parallel (red) or antiparallel (blue) configuration of the reference layers.

As expected, six distinct transitions are visible in the magnetic loop and the central SAF storage layer can be switched without perturbing the two references. Similarly to what had been done in Figure III-21 for a single ferromagnetic storage layer, minor loops on the storage layer might be measured with either parallel references or antiparallel references. In the first case, the field has to be decreased down to about -1000 Oe, whereas in the other one it should reach -2500 Oe to switch the magnetization of the top reference layer. Using the shifts of the minor loops with regard to zero field, one also find here that the coupling energy through the bottom

barrier is three times smaller than through the top one ( $-1.10^{-3}$  instead of  $-3.10^{-3}$  erg.cm<sup>-2</sup>, respectively).

The advantage of such a structure, as explained previously, is that the storage layer would be particularly immune to remaining stray fields once patterned into small size devices. This idea was also used in some recent developments on single magnetic tunnel junctions. The storage layer was in that case composed of a CoFeB antiferromagnetically coupled to a Co/Pd multilayer [Yos-13, Yos-14]. In our double junctions, the parallel configuration of the references allows increasing the STT efficiency in the write phase. To perform the reading, one could want to put the references in an antiparallel configuration to increase the stability of the stored information against applied voltage. However, as was the case with the ferromagnetic storage layer, we cannot switch back with field the references in the antiparallel configuration without risking to rewrite the information of the memory bit. As previously, with that structure the best option is then to dissymmetrize the tunnel barriers and work with the parallel configuration of the reference layers at any time.

### IV-3.2 Use as a top reference in a double junction with single ferromagnetic storage layer

In the previous part, we have seen that rather large stabilities (above  $\pm 1000$  Oe) may be obtained with the FeCoB-based SAF structures. Knowing that the standard single ferromagnetic storage layers with MgO capping exhibit coercive fields of the order of 100 Oe (case of Ta insertion, see Chapter III), one can consider using the FeCoB/(Ta and/or Ru)/FeCoB SAF structures as top references in a double magnetic junction with perpendicular anisotropy. They would in that case replace the Co/Pd-based reference.

A junction has then been prepared with the following parts:

- Bottom reference SAF<sub>1</sub> (as in the previous part)
- Single ferromagnetic storage layer SL: FeCoB<sub>1.2</sub>/Ta<sub>0.3</sub>/FeCoB<sub>1.2</sub>
- Top reference SAF<sub>3</sub>: MgO/FeCoB<sub>1.4</sub>/Ru<sub>0.6</sub>/FeCoB<sub>1.1</sub>/MgO.

The magnetic cycle measured by VSM is shown in Figure IV-14. As expected, the reversal of the storage layer, in the middle of the loop, is fully distinct from the transitions of the two SAF references, the width of the smaller antiparallel plateau being about  $\pm 1300$  Oe. Similarly to the firstly presented double junction of Chapter III (see Figure III-21), the top reference can be put either parallel or antiparallel to the bottom reference. The antiparallel configuration remains here the one to maintain if one wants to maximize the STT efficiency. One should however note that in such a structure three MgO barriers are present. To have a functioning device, we

should then be careful of reducing the RA product of the top one if we do not want to get too large resistances.

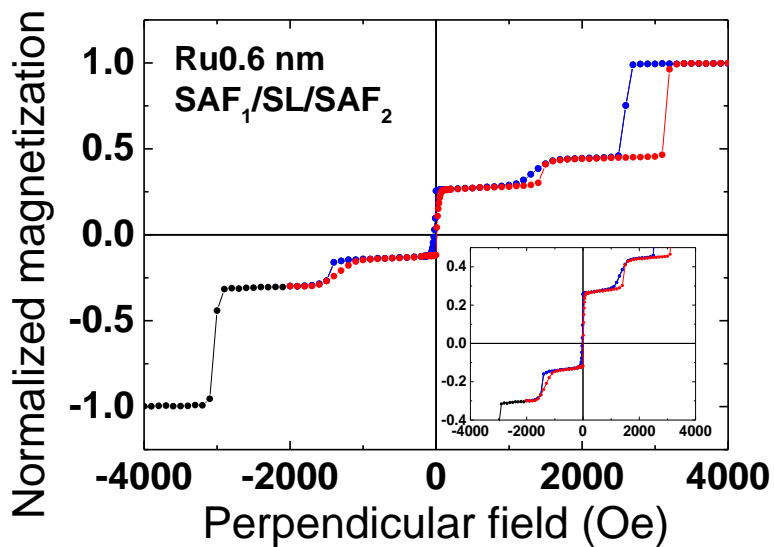


Figure IV-14: Magnetic loop measured by VSM with perpendicular applied field for a double junction having a SAF<sub>1</sub>/MgO/SL/MgO/SAF<sub>3</sub>/MgO structure.

### IV-3.3 Use as a SAF storage layer in a double junction with a bottom reference layer and a top soft control layer

Another solution could be using a SAF storage layer and a soft layer instead of the top reference. This type of structure has already been proposed for planar double magnetic tunnel junctions by P.-Y. Clément in Spintec [Clé-14]. The idea is that the top soft layer, also called control layer, can be switched by field without modifying the information stored in the SAF storage layer which is much harder. This makes it an even more efficient structure for STT applications. A schematic representation of the write and read modes with this stack is given in Figure IV-15.

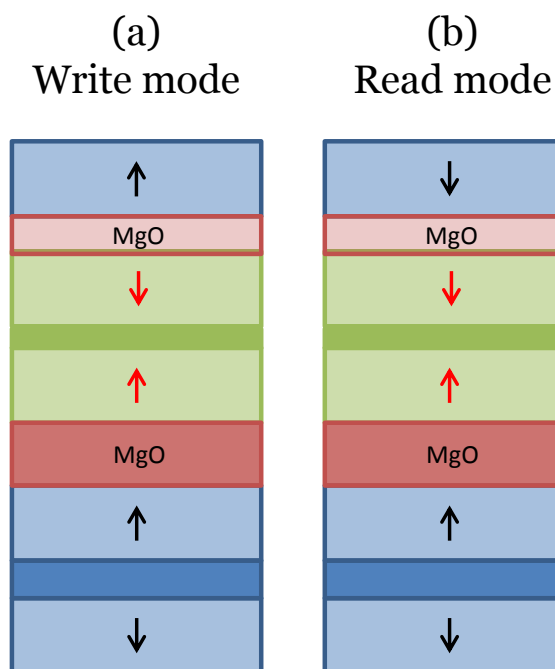


Figure IV-15: Schematic representation of the write (a) and read (b) modes in the case of double junctions with the following structure: SAF<sub>1</sub>/MgO/SAF<sub>3</sub>/MgO/SL, SL standing for the soft control layer.

A magnetic junction with this structure has been deposited. It comprises the following blocks:

- Bottom reference SAF<sub>1</sub> (as previously)
- Storage layer SAF<sub>3</sub>: FeCoB<sub>1.4</sub>/Ta<sub>0.2</sub>/Ru<sub>0.5</sub>/FeCoB<sub>1.1</sub>
- Top control layer SL: MgO/FeCoB<sub>1.4</sub>/Ta<sub>1</sub>/Pt<sub>2</sub>

We use in that case a Ta<sub>0.2</sub>Ru<sub>0.5</sub> insertion layer but pure Ta or pure Ru systems would work as well. To make the soft control layer, a standard single ferromagnetic FeCoB layer capped with Ta is chosen. It is identical to the storage layer of a single magnetic tunnel junction. Figure IV-16 presents the magnetic loop measured by VSM. We can distinguish the five different transitions, the reversal of the top control layer being contained in between those of the SAF storage layer, on the antiparallel plateau near zero field.

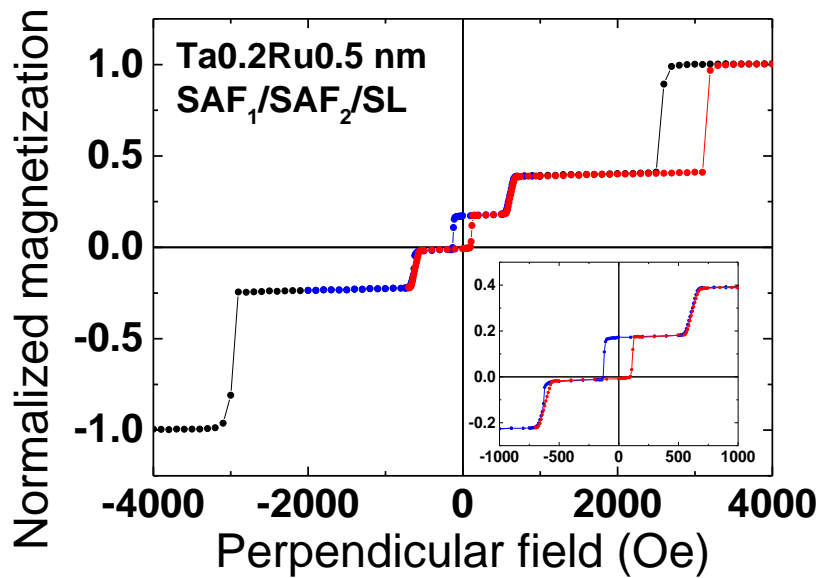


Figure IV-16: Magnetic loop measured by VSM with perpendicular applied field for a double junction having a SAF<sub>1</sub>/MgO/SAF<sub>3</sub>/MgO/SL structure.

As can be seen in the zoom between -1000 and 1000 Oe, the control layer can be switched by applying a small field of about 150 Oe, without changing the orientation of the magnetizations of the storage layer which reversals happen at larger field values (typically 700 Oe). We can also imagine other ways to switch the control layer like for example using a planar current in a stripe to induce domain wall propagation in a magnetic material or spin-orbit torque related effects at the interface with a heavy metal [Cub-14].

Note that it is however necessary to be able to stabilize the antiparallel configuration during writing, that is to say make the top control layer insensitive to STT. This may be done by introducing impurities with strong spin-orbit coupling that would lead to a larger Gilbert damping.

## IV-4. FeCoB-based SAF as reference layers in single magnetic tunnel junctions

Developing the FeCoB-based SAF structures, it appeared that the stability of such systems can be made notably large, in particular near the magnetic compensation. Antiparallel plateaus as wide as  $\pm 1300$  Oe may be achieved enabling these stacks to compete with the standard Co/Pt (Pd)-based SAF. The advantage of removing the multilayers is that not such a precise control of deposited thicknesses is needed anymore (typically 0.2-0.3 nm in the case of Pt). Besides, using noble metals such as Pt or Pd presents some drawbacks in terms of manufacturability. Indeed these materials are very difficult to etch by reactive ion etching techniques. If ion beam etching is still possible, this method is not really appropriate at the industry level for homogeneity reason and production of residues.

Moreover, using our FeCoB-based SAF as reference layers enables reducing drastically the thickness of the stack and then the amount of materials to etch. This is particularly interesting for the nanofabrication steps [Kar-14]. If this is already the case in the Ta/CoFeB/MgO/CoFeB/Ta junctions [Ike-10], such structures do not present a large difference of coercive fields between the reference and storage layers. Unless etching of the top electrode is stopped at the MgO barrier, stray fields from the reference layer may be too large and induce a loss of the dot magnetic bistability. This is why SAF structures in the reference are most of the time favored. This adds another advantage to the FeCoB/spacer/FeCoB structures: besides providing reduced magnetic thickness, they enable benefiting from a SAF configuration of the reference layer.

In this part, we propose to study the realization of single junctions including this new SAF structure as bottom or top reference. Note that the standard 2 nm thick Pt capping layer will be kept in the following developments. But tests with a Ru or a Ta capping layer above the top MgO layer revealed that the magnetic properties are very similar whatever the capping material. It should thus be possible to make entirely Pt-free magnetic tunnel junctions.

### IV-4.1 Use as a top reference

From previous Figure IV-14, the developed double junction already showed that using the FeCoB-based SAF as top reference, above a single ferromagnetic storage layer would be feasible. The zoom at small fields around  $\pm 4000$  Oe already gave a glimpse of what could be the magnetic cycle of the corresponding single junction.

We then prepared a magnetic tunnel junction made of Ta<sub>3</sub>/FeCoB<sub>1.2</sub>/MgO/FeCoB<sub>1.4</sub>/spacer/FeCoB<sub>1.1</sub>/MgO/Pt<sub>2</sub>. The spacer is either Ru<sub>0.6</sub> or Ta<sub>0.2</sub>Ru<sub>0.5</sub>.

Note that as the storage layer is now growing on Ta instead of MgO, we cannot make it as thick as in the storage layer of the double junction of Figure IV-14. Indeed, it does not benefit anymore from the supplemental anisotropy brought by the bottom MgO interface. The magnetic loops obtained for those two junctions are shown in Figure IV-17.

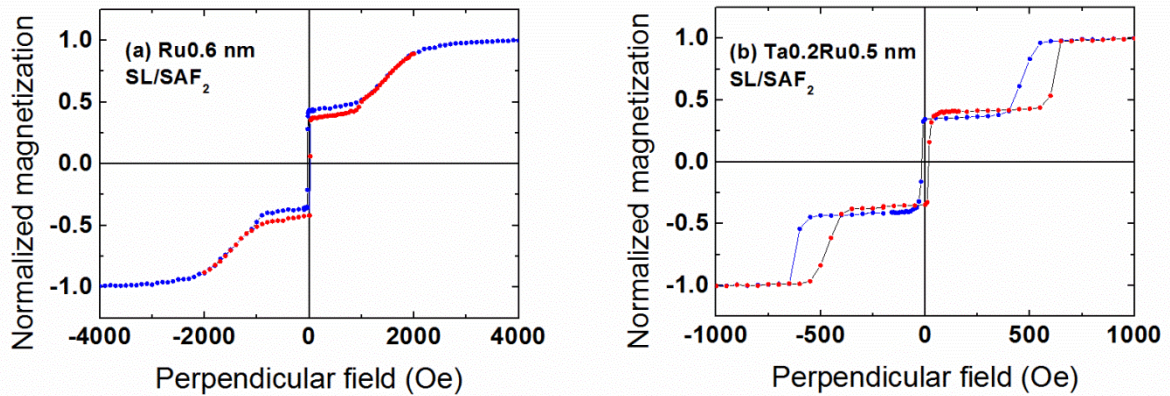


Figure IV-17: Magnetic cycles measured by VSM with perpendicular applied field for single junctions with a bottom storage layer SL = Ta<sub>3</sub>/FeCoB<sub>1.2</sub> and a top reference that is either (a) FeCoB<sub>1.4</sub>/Ru<sub>0.6</sub>/FeCoB<sub>1.1</sub>/MgO or (b) FeCoB<sub>1.4</sub>/Ta<sub>0.2</sub>/Ru<sub>0.5</sub>/FeCoB<sub>1.1</sub>/MgO.

As in the case of synthetic antiferromagnetic storage layers, almost the same stability ranges of the antiparallel plateau are found:  $\pm 1000$  Oe with a Ru<sub>0.6</sub> spacer and  $\pm 600$  Oe with a Ta<sub>0.2</sub>Ru<sub>0.5</sub> one. In both cases, functional magnetic tunnel junctions are obtained.

#### IV-4.2 Use as a bottom reference

Similarly, starting from the double junction developed in Figure IV-16, we prepared a single junction with a bottom FeCoB-SAF reference and a top single storage layer. The stack is the following: Ta<sub>3</sub>/FeCoB<sub>0.3</sub>/MgO/FeCoB<sub>1.4</sub>/spacer/FeCoB<sub>1.1</sub>/MgO/FeCoB<sub>1.4</sub>/Ta<sub>1</sub>/Pt<sub>2</sub>. As we are keeping the growth of the SAF on a MgO layer, a non-magnetic FeCoB underlayer, growing on Ta, is deposited so that the growth of the first MgO barrier is similar to the one obtained in double junctions or when the SAF is used as a top storage layer. The free layer is here our standard Ta-capped FeCoB layer.

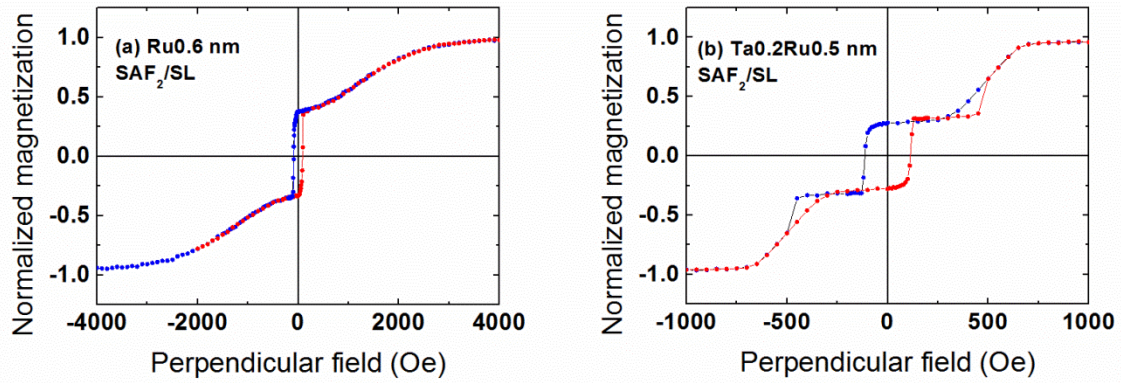


Figure IV-18: Magnetic cycles measured by VSM with perpendicular field for single junctions with a top storage layer SL=FeCoB1.4/Ta1 and a bottom reference that is either (a) MgO/FeCoB1.4/Ru0.6/FeCoB1.1 or (b) MgO/FeCoB1.4/Ta0.2/Ru0.5/FeCoB1.1.

Similarly to the top-referenced junctions developed above, two functional structures are realized. The perpendicular anisotropy seems however lower, with slightly more tilted transitions. The stability range of the SAF has also slightly decreased. This might be due to the difference in growth conditions, as the SAF is deposited on much thinner layers compared to the case of double MTJs.

## IV-5. Stability of the SAF configuration in small pillars

As we have seen, rather large antiparallel plateaus are obtained in the Pt-free SAFs, particularly when Ru spacers are used, with stabilities of about  $\pm 1300$  Oe. This is sufficient to make functional junctions at the macroscopic scale. However, one could question the stability of such structures in small size devices. Indeed, as the diameter of the nanopillar decreases, the stray fields become more and more important and tend to favor a parallel configuration of the magnetizations. As the coupling strength in our newly developed SAF structures is smaller than the one of the standard Co/Pt-based SAF references (with coupling fields around 3000 Oe or more), we wanted to check if the SAF behavior of the Pt-free structure could be maintained in small pillars.

To that aim, we deposited a SAF<sub>1</sub>/SAF<sub>2</sub> stack in which SAF<sub>1</sub> is the standard Co/Pt-based bottom SAF reference and SAF<sub>2</sub> is a Pt-free SAF with a Ru spacer. The exact stack of SAF<sub>2</sub> is the following: FeCoB1.2->1.5/Ru0.6/FeCoB1.1/MgO. The wedge on the bottom FeCoB layer was made to study the effect of the magnetic compensation in the SAF. Using the nanofabrication process that will be presented in details in the next Chapter, circular nanopillars of different diameters were patterned in the sample. The resistance as a function of applied field was then measured. We present in Figure IV-19, the R(H) loops obtained for 4 pillar sizes.

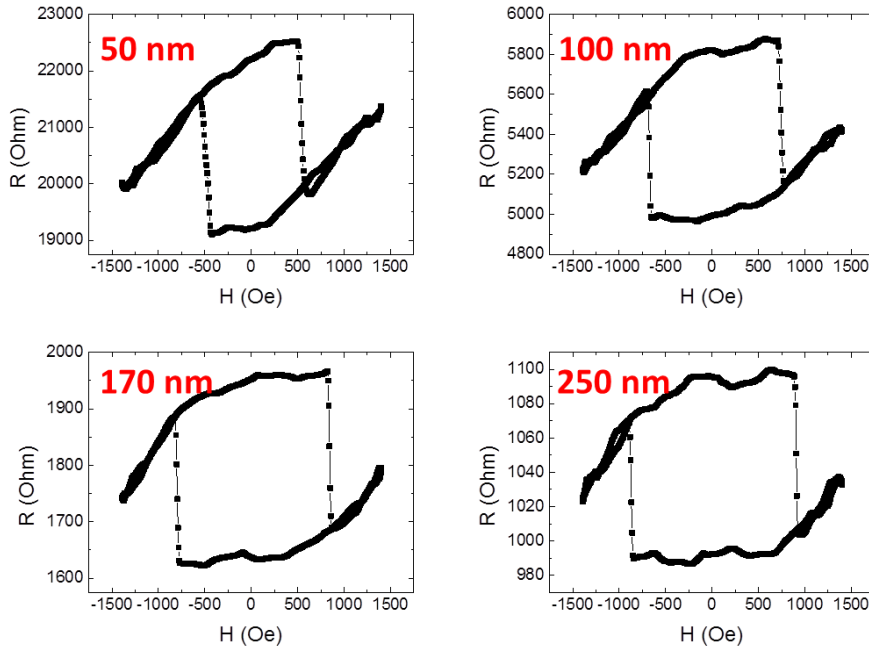


Figure IV-19: Resistance as a function of applied field for SAF<sub>1</sub>/SAF<sub>2</sub> structures patterned into circular nanopillars of different diameters.

It can be seen from these four graphs that the magnetic behavior of the SAF storage layer is very similar for all studied pillar sizes. The slopes that appear at

higher fields correspond to the reversible transitions that we also observe in the macroscopic loops (as seen in Figure IV-10 for example). Very large coercive fields are measured with this SAF storage layer, which should bring good thermal stability to the memory dots. We can however see an effect on the coercive field of the storage layer as a function of pillar diameter. In Figure IV-20, we gathered some data on different junctions measured on the sample.

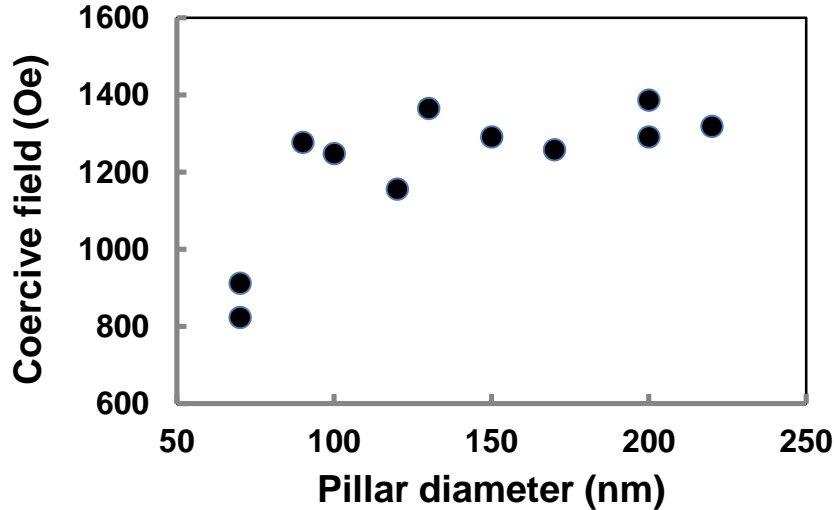


Figure IV-20: Coercive field of the storage layer as a function of pillar diameter for SAF<sub>1</sub>/SAF<sub>2</sub> junctions.

It appears that as the junction diameter is decreased, the coercive field decreases as well, a more abrupt reduction being observed as soon as the diameter gets below 100 nm. This is representative of the effect of stray fields which compete against the RKKY energy. However, it seems from these measurements that the SAF behavior is kept at least down to pillar diameters around 50 nm.

## IV-6. Conclusions

In this Chapter we have seen that we can create Synthetic AntiFerromagnetic layers with two FeCoB layers separated by a metallic spacer. Various spacer materials are functional and interesting results have been obtained with pure Ta, pure Ru or Ta/Ru bilayer insertions. As expected the coupling strength depends a lot on the nature of the spacer and it has been found to decrease continuously as the Ta content increases in the spacer for a constant total thickness. The properties of the SAF appear to be tunable, in particular by changing the magnetic compensation of the structure.

Such SAF layers can be used in double magnetic tunnel junctions and play different roles in the magnetic stack. Indeed we have shown that they can be used as SAF storage layers either in a double junction with top Co/Pd SAF reference layer or with a soft top control layer. The latter case is particularly interesting as the device could be switched from a write to a read mode, possibly enhancing considerably the STT performances. The FeCoB-based SAF structures can also more easily be used as top reference layer in the case of a double junction with a soft single storage layer in the middle of the two tunnel barriers.

Finally, we have seen that due to their good stability with antiferromagnetic plateaus as large as 500 to 1000 Oe, such SAF structures can be employed as top or bottom reference layers in single magnetic tunnel junctions. This result gives us the possibility to build Pt (Pd)-free structures which are particularly advantageous for practical applications.

Note that the stability of these SAF at small device sizes is however questionable. Indeed, if the (Co/Pt)-based SAF appeared to be stable in patterned samples, their stability in macroscopic samples is much higher (around 3000 Oe) than the one of the newly developed structures. We investigated the SAF behavior of the Pt-free systems at small sizes in a structure where they were used as storage layers. It seems from the magnetic characterization that the SAF is still functional at least down to sizes of 50 nm. Besides, some preliminary calculations considering the balance between the RKKY coupling energy and the dipolar energy show that these systems should be stable down to pillar diameters of about 30 nm. To further confirm this, samples are now in preparation to check the magnetic properties of such FeCoB-based as a function of pillar size, using arrays of pillars and a focused Kerr set-up.

## IV-7. References

[Ber-97] H. A. M. van der Berg, W. Clemens, G. Gieres, G. Rupp, M. Vieth, J. Wecker, and S. Zoll, *GMR angle detector with an artificial antiferromagnetic subsystem (AAF)*, [J. Magn. Magn. Mater.](#) **165**, 524-528 (1997).

[Clé-14] P.-Y. Clément, C. Baraduc, M. Chshiev, B. Dieny, L. Vila, and C. Ducruet, *Double barrier magnetic tunnel junctions with write/read mode select layer*, Proceedings of the [6<sup>th</sup> IEEE International Memory Workshop \(IMW\)](#), Taipei (May 18-21, 2014).

[Cub-14] M. Cubukcu, O. Boulle, M. Drouard, K. Garello, C. O. Avci, I. M. Miron, J. Langer, B. Ocker, P. Gambardella, and G. Gaudin, *Spin-orbit torque magnetization switching of a three-terminal perpendicular magnetic tunnel junction*, [Appl. Phys. Lett.](#) **104**, 042406 (2014).

[Cuc-15a] L. Cuchet, B. Rodmacq, S. Auffret, R. C. Sousa, I. L. Prejbeanu, and B. Dieny, *Perpendicular magnetic tunnel junctions with double barrier and single or synthetic antiferromagnetic storage layer*, [J. Appl. Phys.](#) **117**, 233901 (2015).

[Cuc-16] L. Cuchet, B. Rodmacq, S. Auffret, R. C. Sousa, I. L. Prejbeanu, and B. Dieny, *Perpendicular magnetic tunnel junctions with a synthetic storage or reference layer: A new route towards Pt- and Pd-free junctions*, to be published in *Sci. Rep.* (2016).

[Ike-10] S. Ikeda, K. Miura, H. Yamamoto, K. Mizunuma, H. D. Gan, M. Endo, S. Kanai, J. Hayakawa, F. Matsukura, and H. Ohno, *A perpendicular-anisotropy CoFeB–MgO magnetic tunnel junction*, [Nature Mater.](#) **9**, 721-724 (2010).

[Kar-14] G. S. Kar, W. Kim, T. Tahmasebi, J. Swerts, S. Mertens, N. Heylen, and T. Min, *Co/Ni based p-MTJ stack for sub-20nm high density stand alone and high performance embedded memory application*, Proceedings of the [Int. Electron Devices Meeting](#) (IEDM), San Francisco (Dec. 15-17, 2014).

[Par-91] S. S. P. Parkin, *Systematic variation of the strength and oscillation period of indirect magnetic exchange coupling through the 3d, 4d, and 5d transition metals*, [Phys. Rev. Lett.](#) **67**, 3598-3601 (1991).

[Pet-91] F. Petroff, A. Barthélémy, D. H. Mosca, D. K. Lottis, A. Fert, P. A. Schroeder, W. P. Pratt, R. Loloee and S. Lequien, *Oscillatory interlayer exchange and magnetoresistance in Fe/Cu multilayers*, [Phys. Rev. B](#) **44** 5355-5357 (1991).

[Sok-12] V. Sokalski, M. T. Moneck, E. Yang, and J. -G. Zhu, *Optimization of Ta thickness for perpendicular magnetic tunnel junction applications in the MgO-FeCoB-Ta system*, [Appl. Phys. Lett.](#) **101**, 072411 (2012).

[Yos-13] C. Yoshida, T. Takenaga, Y. Iba, Y. Yamazaki, H. Noshiro, K. Tsunoda, A.Hatada, M. Nakabayashi, A. Takahashi, M. Aoki, and T. Sugii, *Enhanced thermal stability in perpendicular top-pinned magnetic tunnel junction with synthetic antiferromagnetic free layers*, [IEEE Trans. Magn.](#) **49**, 4363 (2013).

[Yos-14] C. Yoshida, T. Takenaga, Y. Yamazaki, H. Uehara, H. Noshiro, K. Tsunoda, Y. Iba, A.Hatada, M. Nakabayashi, A. Takahashi, M. Aoki, and T. Sugii, *Reduction of offset field in top-pinned MTJ with synthetic antiferromagnetic free layer*, [IEEE Trans. Magn.](#) **50**, 3401804 (2014).

## CHAPTER V

# Electrical testing of patterned perpendicular magnetic tunnel junctions

<b>V-1. Nanofabrication process .....</b>	<b>160</b>
<b>V-2. Testing of standard magnetic tunnel junctions with a bottom SAF reference and a top Ta-capped FeCoB storage layer .....</b>	<b>166</b>
V-2.1 Field-pulse voltage diagrams.....	166
V-2.2 Coupling field as a function of pillar diameter.....	168
V-2.3 Critical current and anisotropy as a function of the storage layer thickness .....	169
V-2.4 Determination of the damping parameter $\alpha$ .....	171
V-2.5 Effect of the temperature.....	173
<b>V-3. Conclusions .....</b>	<b>175</b>
<b>V-4. References .....</b>	<b>176</b>



Mastering the properties of our magnetic tunnel junction at the macroscopic level is essential and as we have seen in the previous Chapters, if one wants to optimize the performances of the structures some compromises are necessary.

However, to make one step closer towards the MRAM applications, it is necessary to pattern the junctions into small nanopillars that will represent the memory dots of a future device. This is also the only way to test electrically the magnetic tunnel junctions and evaluate their performances regarding Spin Transfer Torque switching.

In a first part, we will recall the different steps of the nanofabrication process that we have performed in the clean room. This will be done by schematically representing the realization of a nanopillar thanks to a sequence involving several levels of mask.

In a second part, we will present the results of the electrical tests realized on our standard junctions with a bottom SAF reference and a Ta-capped storage layer.

## V-1. Nanofabrication process

In this part, we will schematically represent the different fabrication steps that enable us to get nanopillars, starting from the magnetic deposition on a Si wafer covered with a CuN buffer layer. This process is performed in the Plateforme Technologique Amont (PTA) of Grenoble and has been developed by Ricardo Sousa, Laurent Vila and Marie-Thérèse Delaye.

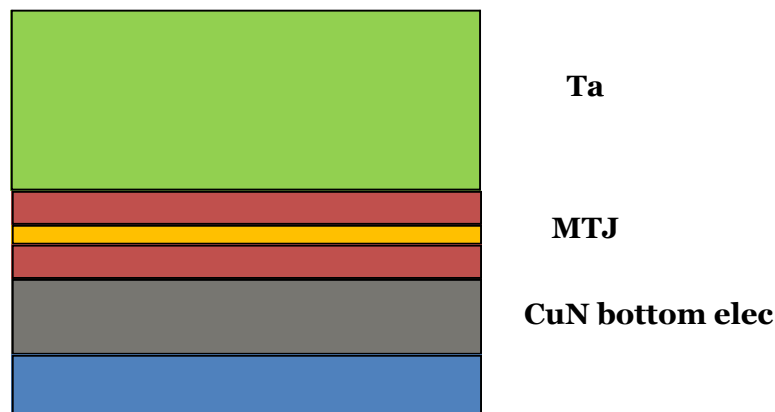


Figure V-1: Deposition of a 150 nm thick Ta hard mask on top of the magnetic tunnel junction.

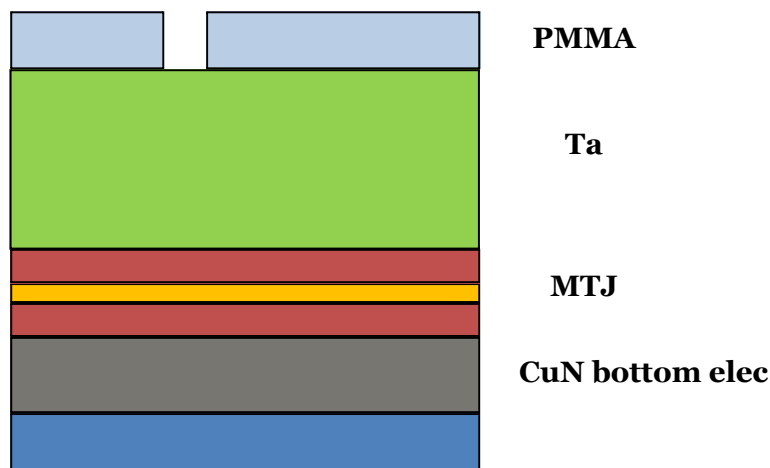


Figure V-2: Definition of the pillar sizes by electron beam lithography through a PMMA resist. Pillars diameters can vary between about 50 and 1000 nm. The resist is then developed.

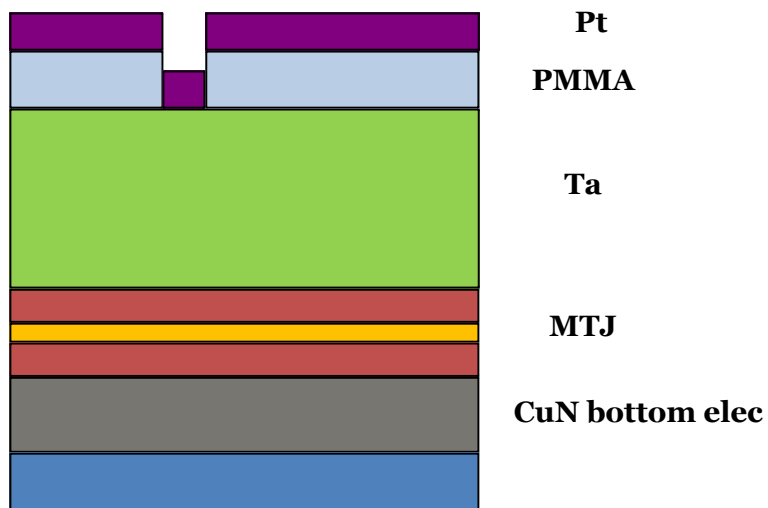


Figure V-3: Pt deposition by evaporation to protect the pillars.

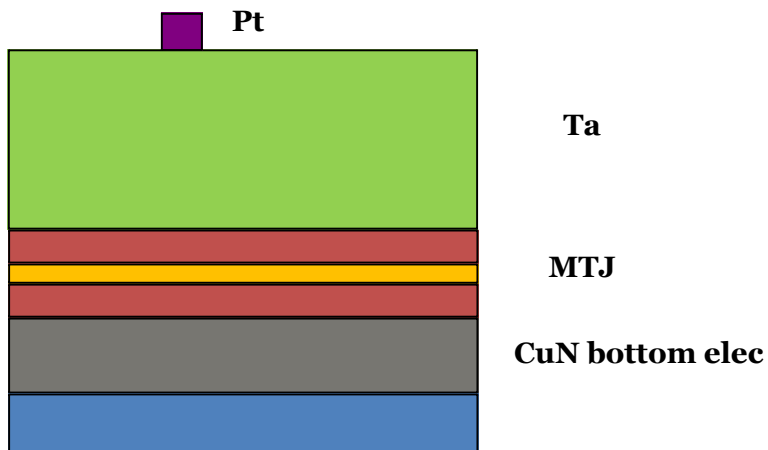


Figure V-4: Lift-off of the resist. The pillar is defined by the Pt deposition.

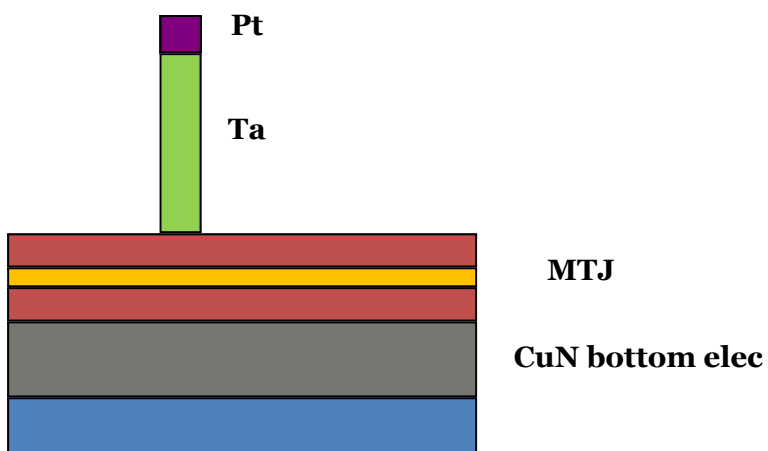


Figure V-5: Reactive ion etching of the Ta hard mask. The parts under the Pt are protected.

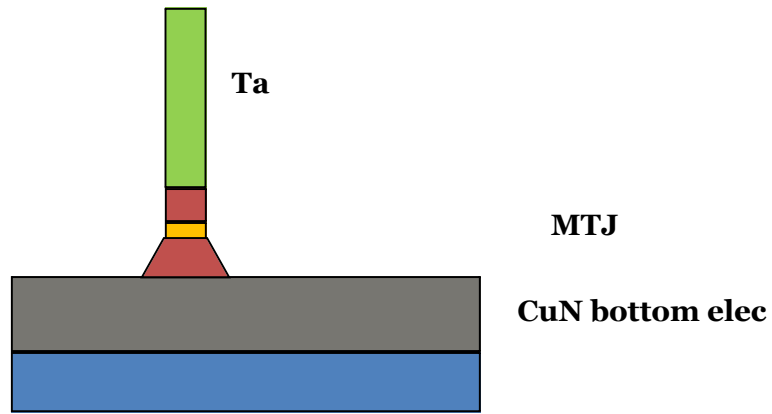


Figure V-6: Ion beam etching of the magnetic tunnel junction. Etching is performed with an angle of  $45^\circ$  which results in a conic base for the pillar.

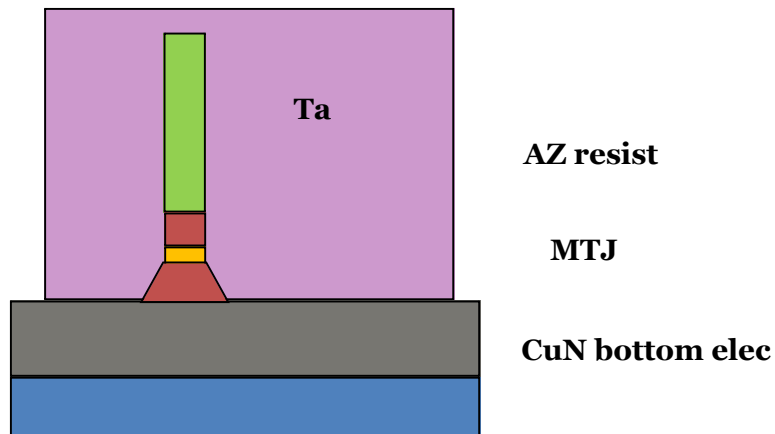


Figure V-7: Deposition of a positive resist (AZ) and optical lithography to define the bottom electrode.

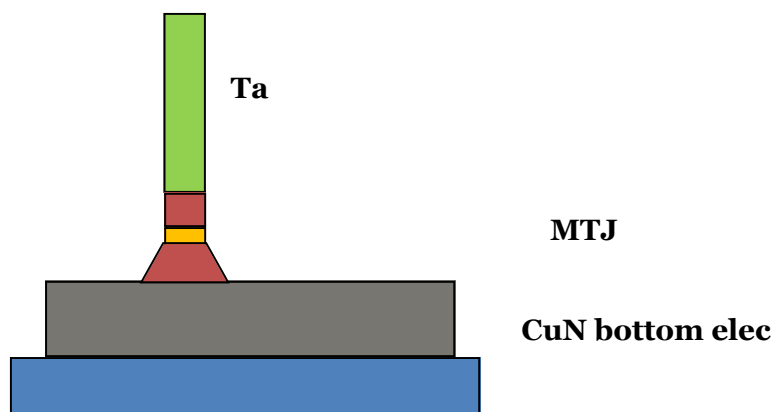


Figure V-8: Ion beam etching of the bottom electrode down to the substrate. The part protected by the resist is not etched. The resist is afterwards removed.

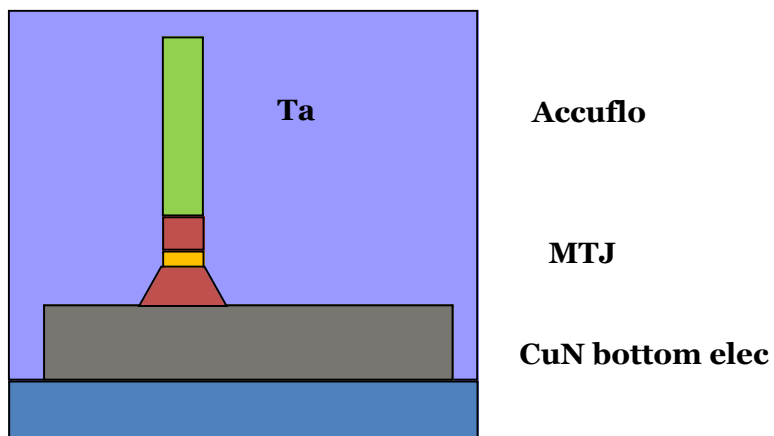


Figure V-9: Deposition of the planarizing polymer (Accuflo) which will isolate the bottom electrode from the top one.

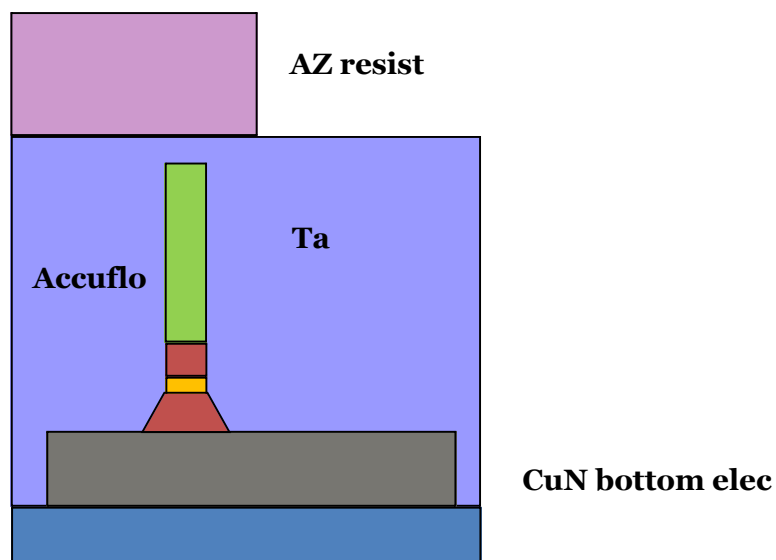


Figure V-10: Deposition of the positive AZ resist and optical lithography to define an insulating zone around the pillar.

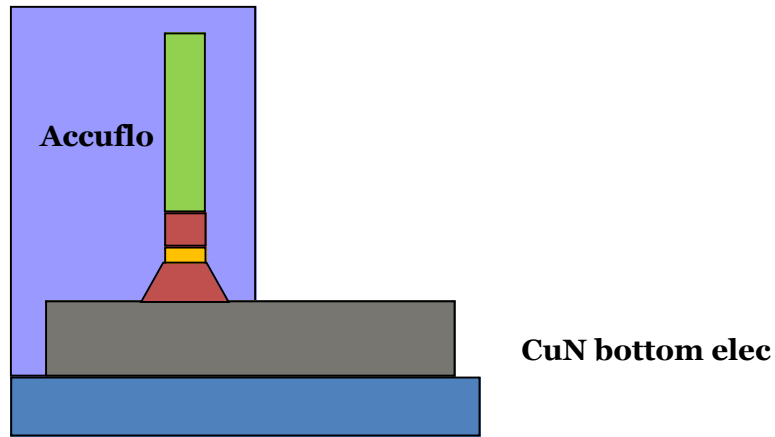


Figure V-11: Reactive ion etching of the Accuflo on the unprotected parts of the wafer. The resist is then removed.

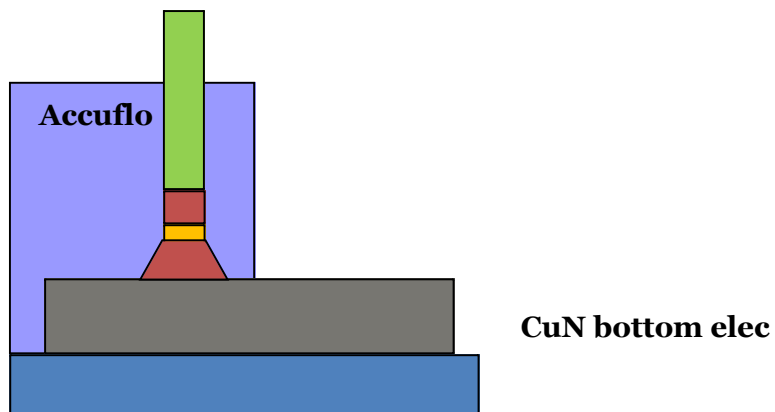


Figure V-12: Thinning down of the Accuflo to a thickness around 90-130 nm in order to free the top part of the Ta pillar.

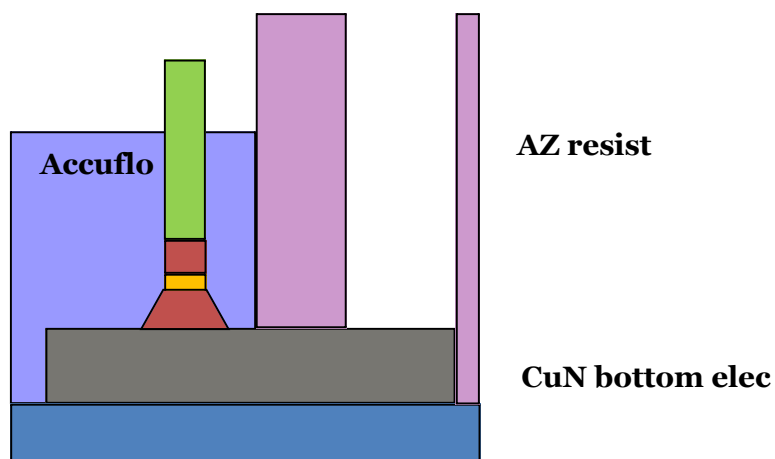


Figure V-13: Deposition of the positive AZ resist and optical lithography to define the top electrode. The resist is afterwards developed.

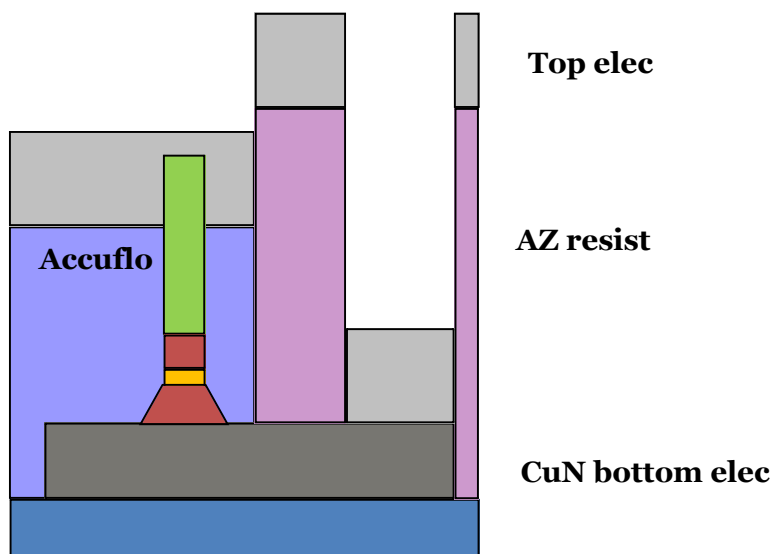


Figure V-14: Deposition of the Cr/Al metallic contacts by evaporation to create the top electrode.

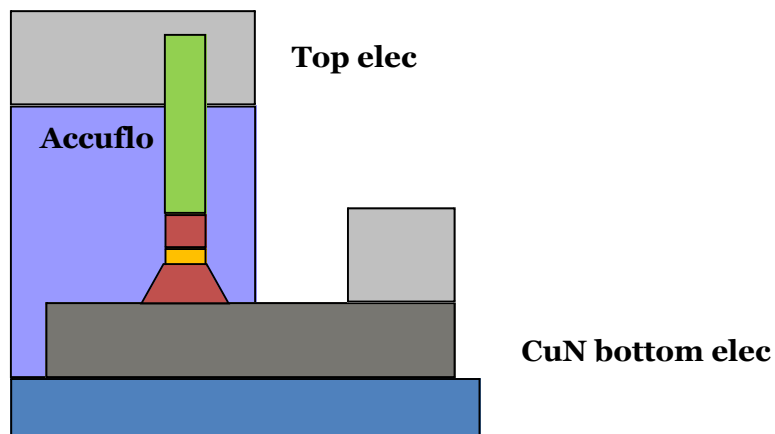


Figure V-15: Final lift-off of the resist.

## **V-2. Testing of standard magnetic tunnel junctions with a bottom SAF reference and a top Ta-capped FeCoB storage layer**

After the first materials optimizations performed on the standard junctions in Chapter II, we wanted to test their Spin Transfer Torque (STT) switching performances on patterned samples [Cuc-14]. A magnetic tunnel junction with a bottom Co/Pt-based SAF reference and a top FeCoB storage layer has been deposited on a 50 mm wafer covered with a CuN buffer layer. As seen in the previous part, this layer is used to make an electric contact on the bottom electrode.

The following stack has been chosen for the junction: Ta<sub>1</sub>/Pt<sub>5</sub>/(Co<sub>0.5</sub>/Pt<sub>0.4</sub>)<sub>5</sub>/Co<sub>0.5</sub>/Ru<sub>0.9</sub>/(Co<sub>0.5</sub>/Pt<sub>0.4</sub>)<sub>3</sub>/Co<sub>0.5</sub>/Ta<sub>0.3</sub>/CoFeB<sub>1.2</sub>/MgO/FeCoB<sub>1.0-1.4</sub>/Ta<sub>1</sub>/Pt<sub>2</sub>. We take advantage of the possibility to deposit thickness wedges in our deposition tool to vary the thickness of the storage wafer on the same wafer. This will enable keeping the same growth conditions and the same barrier for all the devices. We will be using nominal thicknesses in this Chapter but according to the results of Chapter II, a magnetic dead layer thickness of about 0.6 nm exists in this top storage layer. Note that the Pt thickness in the Co/Pt multilayers is 0.4 nm in that case instead of the optimized 0.25 nm, because at the time of the deposition this optimization has not yet been done. The structure is however functional, as we saw in Chapter II. Annealing was performed in our largest furnace with the standard procedure (250 °C for 1h30). The barrier is obtained with low pressure conditions and CIPT measurements on test samples deposited at the same time as the processed wafer gave a TMR signal of about 40 % and a RA value of 6 Ωμm<sup>2</sup>. On the patterned sample, maximum TMR was 36 % and the RA product is found slightly higher at 10 Ωμm<sup>2</sup>.

Using the method presented in the first part, the wafer was patterned into circular nanopillars with diameters ranging between 100 and 300 nm. The dot sizes given here correspond to the values defined in the electron beam lithography mask.

### **V-2.1 Field-pulse voltage diagrams**

To establish the magnetic field-pulse voltage state diagrams of one junction, 100 ns current pulses are applied at each point of the hysteresis loop, while measuring the resistance of the junction. The magnetic field is applied perpendicular to the plane of the magnetic layers. The hysteresis loops are recorded for different pulse amplitudes, applying consecutive pulses of the same polarity until switching occurs. A typical diagram obtained for a 100 nm pillar with a top FeCoB thickness estimated around 1.24 nm is presented in Figure V-16 (a).

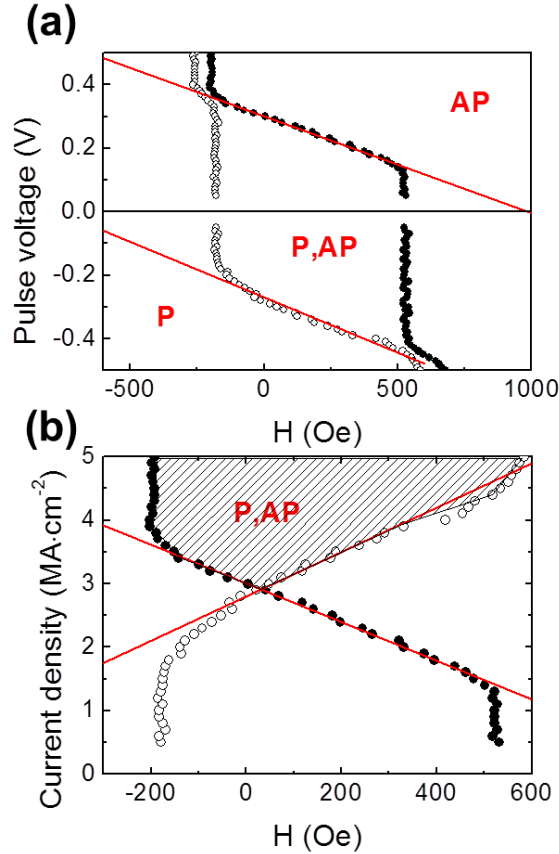


Figure V-16: (a) Field-pulse voltage diagram of a 100 nm pillar with a top FeCoB thickness of 1.24 nm. Parallel and antiparallel configurations of the magnetizations are represented as P and AP, respectively. (b) Current density as a function of applied field. The AP-P transition has been reversed to present the results in absolute values. Open circles = AP-P transition. Solid circles = P-AP transition.

The points at which switching occurs are represented with solid circles for the parallel to antiparallel (P-AP) switching and with open circles for the antiparallel to parallel (AP-P) case. At low pulse voltages amplitudes, the STT influence is negligible and the magnetization switches under the effect of the magnetic field, as soon as it overcomes the coercive field value. In our convention, positive voltage corresponds to electrons flowing from the storage layer to the reference layer. Therefore negative voltages favor the parallel state, while positive voltages favor the antiparallel state. On the field-pulse voltage diagram, these regions are separated by the bistable region, in which both parallel and antiparallel configurations are possible, depending on the previous field-voltage treatment. In the case of the junction presented in Figure V-16 (a), the coercive field is 350 Oe.

To determine the critical current density for the AP-P and the P-AP switching by STT, the data extracted from the phase diagram can be used. Using the value of RA measured on the patterned wafer, we can calculate the current density for each applied pulse amplitude as  $J = V/(R.A)$ . In Figure V-16 (b), both transition

boundaries are plotted as functions of magnetic field and absolute current density value. The minimum current density allowing both AP-P and P-AP transitions can be determined at the crossing between the two boundaries. At this field, switching between AP (P) and P (AP) states is possible with exactly the same current density. The origin of the switching current asymmetry observed in many STT writing data comes from the fact that the chosen offset field does not correspond to the boundary intersection field point. For this device, the lowest current density for AP (P) to P (AP) switching is found to be 2.9 MA.cm<sup>-2</sup> at a bias field of 33 Oe.

### V-2.2 Coupling field as a function of pillar diameter

One can also note in Figure V-16 that the bistable region is not centered on zero field. This is explained by the fact that at this pillar size, the magnetizations of the two parts of the bottom SAF reference do not allow a perfect compensation of the stray fields originating from the pillar edges. As we have seen previously, it is possible to reduce those stray fields by adjusting the magnetic thicknesses and numbers of repeats in the Co/Pt multilayers [Ban-10]. Note that however, this adjustment will only work for one pillar size. Similarly, if the thickness of the top free layer varies, the size at which compensation is obtained also changes (since for a given coupling energy, the coupling field is inversely proportional to the free layer thickness). This is shown in Figure V-17, where the coupling field  $H_{cpl}$  acting on the storage layer is plotted as a function of the pillar diameter for different thicknesses of the top FeCoB layer.

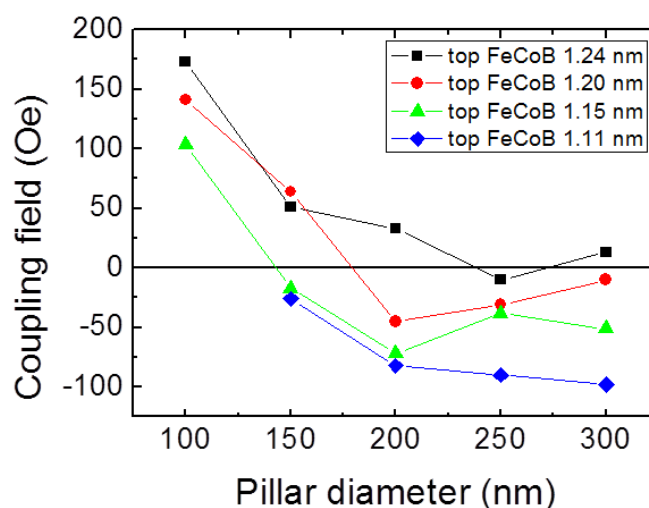


Figure V-17: Coupling field acting on the storage layer as a function of pillar diameter for different thicknesses of the top FeCoB layer.

Because of stronger stray fields at smaller junction sizes, the coupling field is found larger for the smallest dots of 100 nm. It then decreases as the dot size increases. One should notice that on macroscopic samples with the same stack, there exists an antiferromagnetic coupling through the MgO barrier that shifts the transition of the free layer. As explained in Chapter II, this coupling is mostly due to the existence of some roughness in the tunnel barrier [Mor-04, Nis-10]. This coupling amounts to about -50 to -100 Oe and should be subtracted to the  $H_{\text{cpl}}$  value to only estimate the effect of stray fields in the patterned pillar. From the graph of Figure V-17, it appears that for a diameter of 300 nm, we are very close to the behavior of a macroscopic sample. The effect of thickness appears clearly, particularly on the 300 nm pillars, where it can be seen that the coupling field increases in amplitude when the FeCoB layer gets thinner.

### **V-2.3 Critical current and anisotropy as a function of the storage layer thickness**

The critical current density for STT switching was measured as a function of free layer thickness with two different methods. The first one consists of using the phase diagrams measured with consecutive pulses of the same polarity, as shown in Figure V-16. In the second method, we apply current pulses of alternate polarity at each field point. This experiment is repeated 30 times until 100 % switching is obtained. In the case of consecutive pulses of the same polarity, a lower critical current is obtained because this way of measuring represents a low switching probability, similar to the measurements of critical currents with current ramps. The values extracted with alternate polarity pulses are more closely related to the actual memory operation, where a deterministic switching threshold is required. Results obtained with both methods are shown in Figure V-18 for 100 and 150 nm pillars as a function of FeCoB storage layer thickness.

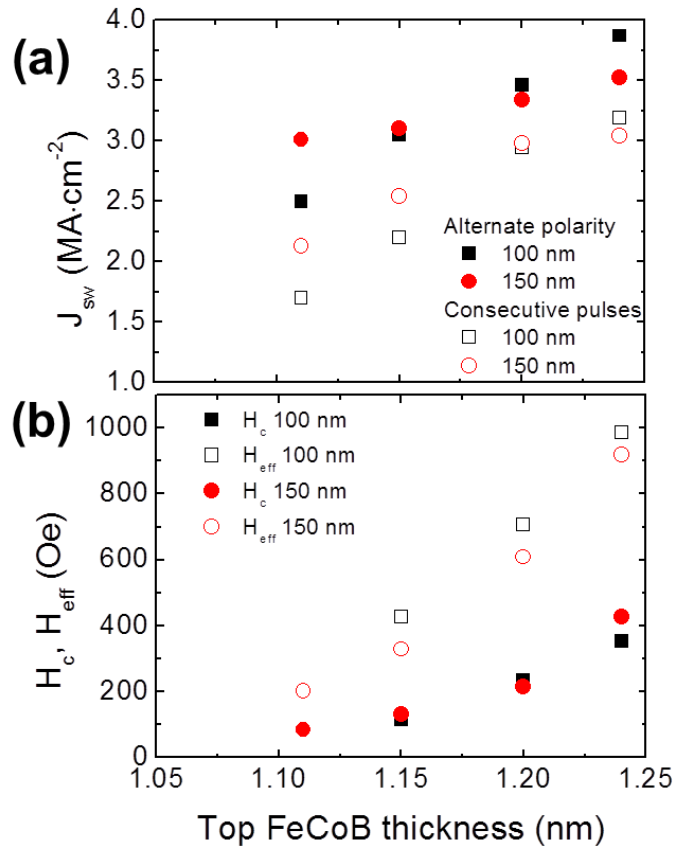


Figure V-18: (a) Critical current density  $J_{sw}$  for STT switching as a function of top FeCoB thickness. Results are shown for two pillar sizes, 100 nm (squares) and 150 nm (circles) and for the two measurement techniques, alternate polarity (solid symbols) and consecutive pulses (open symbols). (b) Coercive field  $H_c$  (solid symbols) and anisotropy field  $H_{eff}$  (open symbols) as a function of top FeCoB thickness.

In Figure V-18 (a), we observe an increase of the critical current density  $J_{sw}$  as the thickness of the storage layer increases. This is due to the fact that in this range of thicknesses, the effective perpendicular anisotropy energy  $K_{eff}$  is still increasing with thickness. This is what we observe in Figure V-18 (b) where we represent the coercive field  $H_c$  and the anisotropy field  $H_{eff}$  as a function of magnetic thickness. The values of  $H_{eff}$  are obtained from the phase diagrams by extrapolating the linear field-voltage dependence of the switching boundaries towards zero current. If this increase of perpendicular anisotropy with thickness seems counterintuitive, we recall, in Figure V-19, the data extracted on our macroscopic samples in Chapter II. It appears that in the small range of thicknesses we have on our patterned sample, we are still in the part of the curve where the anisotropy increases with thickness. Note that on this graph, we use effective magnetic thicknesses in which the 0.6 nm thick magnetic dead layer has been subtracted. From the data gathered in Figure V-18 (b), it seems that a slightly larger anisotropy is measured for 100 nm pillars compared to the 150 nm ones.

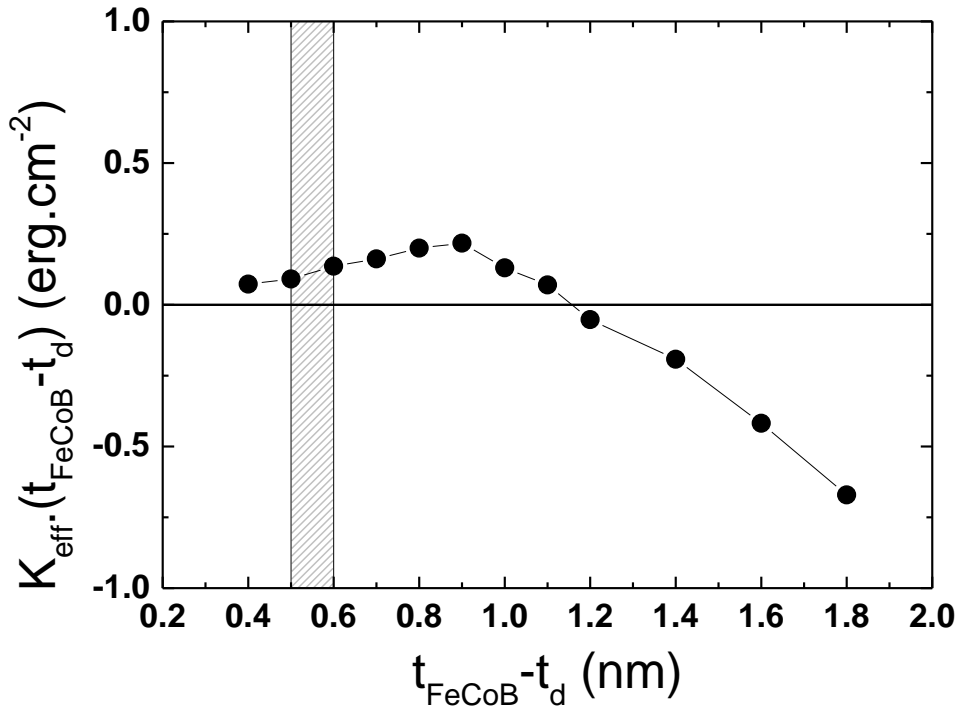


Figure V-19: Variation of the  $K_{\text{eff}} \cdot t$  product as a function of effective thickness for top FeCoB layers capped with Ta. The dashed region corresponds to the thickness range present on our patterned sample.

For junctions with 1.24 nm thick storage layer, the largest value of the average thermal stability  $\Delta$  was estimated to be around  $43 \pm 10$ . The stability of the AP state was found generally higher than that of the P state. The values were obtained from the standard Néel-Brown model for thermally activated reversal, by fitting the switching field distribution as a function of applied field. The switching field distribution was obtained from 100 successive hysteresis loop measurements under a constant sweep rate. This technique has been explained in more details in a recent publication [Tho-14].

#### V-2.4 Determination of the damping parameter $\alpha$

We know that the critical current density can be expressed this way [Man-09]:

$$J_{sw} = \frac{2e\alpha\mu_0 M_s t}{\hbar\eta} (H_{\text{eff}} + H_{\text{app}} + H_{\text{cpl}})$$

where  $\alpha$  is the Gilbert damping parameter,  $M_s$  the saturation magnetization of the storage layer,  $t$  its effective thickness,  $\eta$  the spin polarization,  $H_{\text{eff}}$  the anisotropy field,  $H_{\text{app}}$  the applied field and  $H_{\text{cpl}}$  the coupling field. As we have seen in Figure V-16 (a),

above a threshold voltage, a mostly linear relationship exists between the critical current density and the applied field. The slope  $\partial J_{sw}/\partial H$  corresponds to the prefactor in the above equation and depends on materials parameters: damping, spin polarization, thickness and magnetization. Deviations from the linear model can originate from a STT dependence on bias and dependence of spin polarization on the angle between the storage and reference layers.

From Figure V-16 (a), we extract a slope of  $-3 \text{ MA}\cdot\text{cm}^{-2}/\text{kOe}$  for the P-AP boundary and a slope of  $-3.5 \text{ MA}\cdot\text{cm}^{-2}/\text{kOe}$  for the AP-P boundary, in the case of the 100 nm pillar with a 1.24 nm thick storage layer. Similar state diagram measurements had given slopes of  $-18.2 \text{ MA}\cdot\text{cm}^{-2}/\text{kOe}$  (P-AP) and  $-13.8 \text{ MA}\cdot\text{cm}^{-2}/\text{kOe}$  (AP-P) in the case of Co/Ni perpendicular spin valves measured with dc bias current [Man-09]. The slope is reduced by a factor of 5 with our magnetic tunnel junctions, probably because the damping parameter is lower and the spin polarization higher in CoFeB/MgO systems.

We extracted the value of the P-AP slope as a function of FeCoB thickness for 150 nm pillars, as shown in Figure V-20. This slope is decreasing in amplitude linearly with increasing FeCoB thickness. We know that this slope can be expressed as:

$$\frac{\partial J}{\partial H} = -\frac{2e\alpha\mu_0 M_s t}{\hbar\eta}$$

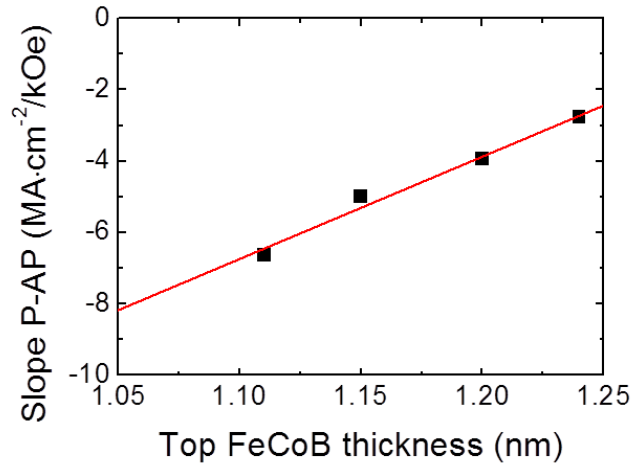


Figure V-20: Slope of the P-AP transition as a function of top FeCoB thickness for 150 nm pillars.

From the slope of Figure V-20 we can extract the damping parameter. Indeed, all the other materials parameters are known. From the study of Chapter II, we know that the saturation magnetization  $M_s$  is about  $1300 \text{ emu}\cdot\text{cm}^{-3}$ . The polarization  $\eta$  can be estimated around 0.3 using the following model:  $\eta = \sqrt{MR(MR + 2)}/(2(MR + 1))$  [Jul-75]. We thus find from the linear fit of Figure V-19 a damping parameter

$\alpha \sim 0.016 \pm 0.004$ , which is in good agreement with the values obtained by ferromagnetic resonance on similar samples [Dev-13].

### V-2.5 Effect of the temperature

Heat assisted MRAM have been found particularly interesting to reduce power consumption. Systems with perpendicular anisotropy were patented in Spintec [Die-08] and studied by S. Bandiera during his thesis [Ban-11]. In the case of perpendicular magnetic junctions, the idea is to heat the sample over a certain temperature above which there is a switching of the anisotropy from perpendicular to planar in the storage layer, configuration in which the spin transfer torque is maximal. As in standard STT writing, a spin-polarized current is applied. It will make the magnetization precess out-of-plane in one or the other direction, which will define the final orientation taken during the cooling phase.

With this concept in mind, we tested the effect of applying temperature on our patterned pillars. In Figure V-21, we present the variation of the coercive field  $H_c$  as a function of applied temperature for different thicknesses of the top FeCoB storage layer in the case of 100 nm pillars. The temperature is applied thanks to a heating chuck on which the wafer is installed and which temperature is controllable.

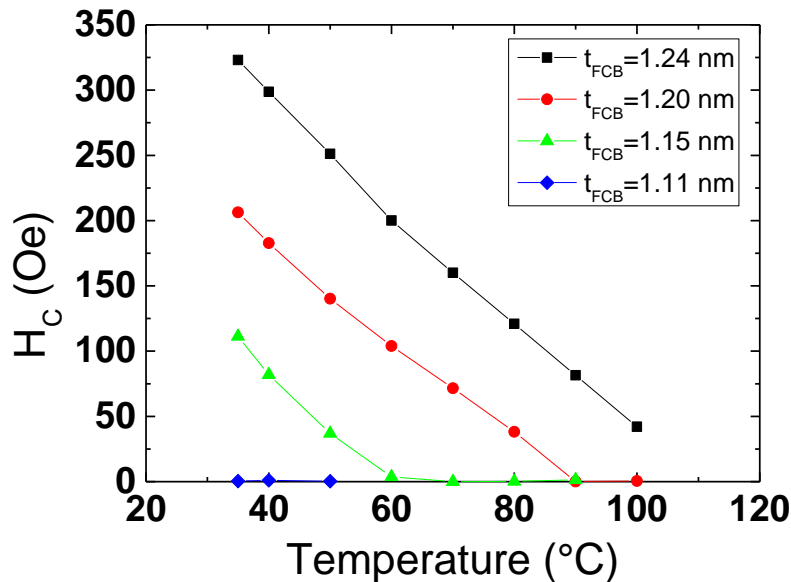


Figure V-21: Variation of the coercive field  $H_c$  as a function of the temperature for 100 nm pillars with varying thickness of the top FeCoB storage layer.

The general trend is a linear decrease of the coercive field with temperature. As already seen in Figure V-18 (b), the anisotropy and the coercive are getting larger as the thickness increases (in the range of studied thicknesses). The critical temperature at which the coercivity is lost is thus increasing with the thickness of the storage layer. In the case of very thin FeCoB layers, even at room temperature there is almost no coercive field as the perpendicular anisotropy is still low. For the 1.15 nm thick storage layer the critical temperature is found around 60 °C, it increases to 90 °C for 1.20 nm and we can extrapolate it around 110 °C for the thickest layer of 1.24 nm. A significant variation of this temperature is then observed in a relatively narrow range of magnetic thicknesses (0.13 nm only!). This can be explained by the large variation of anisotropy along the thickness wedge of the sample, as already seen in Figure V-18 (b).

### **V-3. Conclusions**

We have seen that thanks to a well-defined nanofabrication process it is possible to create small size pillars that allow electrical testing of the structures.

The performances of standard junctions with a bottom SAF reference and a top Ta-capped FeCoB storage layer were evaluated. Using a wedge configuration in our deposition tool, we were able to study some of the properties of our junctions as a function of storage layer thickness on the same wafer. Varying the pillar diameter also gave the possibility to see the effect of the dot size. Magnetic field vs pulse voltage phase diagrams could be established for individual junctions by applying consecutive pulses of the same polarity and measuring the resistance of the pillar. They enable to see that pure STT switching is possible and several parameters can be extracted from them. For example, in the case of a magnetic tunnel junction with a 1.24 nm thick FeCoB storage layer patterned in a 100 nm pillar a critical current of 2.9 MA.cm<sup>-2</sup> was measured as well as a coercive field of 350 Oe.

As the compensation of the SAF reference is not ideal for all pillar sizes, we could observe a coupling field on the storage layer that shifts its hysteresis loop. As expected, this coupling is increasing as the pillar diameter gets smaller. The effect of storage layer thickness is also visible and we could observe the increase of the coupling field as the thickness decreases. We saw as well that as the perpendicular anisotropy is still rising in the range of studied thicknesses, this translates into an increase of critical current density. From the phase diagrams, a linear relationship between current density and applied field is observed and we can use the extracted slope and its variation with magnetic thickness to extract the Gilbert damping parameter of our FeCoB storage layer (around 0.016).

Finally, the variation of the coercive field as a function of the temperature has been studied. It shows us how thermally assisted switching could be used in our perpendicularly magnetized systems, in which perpendicular anisotropy is lost or at least considerably reduced above a certain threshold temperature. It appears that, as the storage gets thicker, the temperature at which the anisotropy switches from perpendicular to planar increases. A large range of this critical temperature is obtained (between room temperature and 110 °C) while the FeCoB thickness only varies of a few tenths of nanometers.

## V-4. References

- [Ban-10] S. Bandiera, R. C. Sousa, Y. Dahmane, C. Ducruet, C. Portemont, V. Baltz, S. Auffret, I. L. Prejbeanu, and B. Dieny, *Comparison between synthetic antiferromagnets and single hard layers as reference layer in perpendicular magnetic tunnel junctions*, [IEEE Magn. Lett.](#) **1**, 3000204 (2010).
- [Ban-11] S. Bandiera, *Jonctions tunnel magnétiques à anisotropie perpendiculaire et écriture assistée thermiquement*, [PhD Thesis](#), Grenoble University (2011).
- [Cuc-14] L. Cuchet, R. C. Sousa, L. Vila, S. Auffret, B. Rodmacq, and B. Dieny, *Field dependence of spin transfer torque switching current in perpendicular magnetic tunnel junctions*, [IEEE Trans. Magn.](#) **50**, 4401404 (2014).
- [Dev-13] T. Devolder, P.-H. Ducrot, J.-P. Adam, I. Barisic, N. Vernier, Joo-Von Kim, B. Ockert, and D. Ravelosona, *Damping of  $Co_x Fe_{80-x}B_{20}$  ultrathin films with perpendicular magnetic anisotropy*, [Appl. Phys. Lett.](#) **102**, 022407 (2013).
- [Die-08] B. Dieny, *Heat-assisted magnetic write element*, Patent [WO2009136313 \(A1\)](#), May 6 2008.
- [Jul-75] M. Jullière, *Tunneling between ferromagnetic films*, [Phys. Lett.](#) **54A**, 225-226 (1975).
- [Man-09] S. Mangin, Y. Henry, D. Ravelosona, J. A. Katine, and E. E. Fullerton, *Reducing the critical current for spin-transfer switching of perpendicularly magnetized nanomagnets*, [Appl. Phys. Lett.](#) **94**, 012502 (2009).
- [Mor-04] J. Moritz, F. Garcia, J.-C. Toussaint, B. Dieny, and J.-P. Nozières, *Orange peel coupling in multilayers with perpendicular magnetic anisotropy: Application to (Co/Pt)-based exchange-biased spin valves*, [Europhys. Lett.](#) **65**, 123-129 (2004).
- [Nis-10] L. E. Nistor, B. Rodmacq, S. Auffret, A. Schuhl, M. Chshiev, and B. Dieny, *Oscillatory interlayer exchange coupling in MgO tunnel junctions with perpendicular magnetic anisotropy*, [Phys. Rev. B](#) **81**, 220407(R) (2010).
- [Tho-14] L. Thomas, G. Jan, J. Zhu, H. Liu, Y.-J. Lee, S. Le, R.-Y. Tong, K. Pi, Y.-J. Wang, D. Shen, R. He, J. Haq, J. Teng, V. Lam, K. Huang, T. Zhong, T. Torng, and P.-K. Wang, *Perpendicular spin transfer torque magnetic random access memories with high spin torque efficiency and thermal stability for embedded applications*, [J. Appl. Phys.](#) **115**, 172615 (2014).

# CONCLUSION

The aim of this thesis was to optimize the magnetic and transport properties of magnetic tunnel junctions with perpendicular anisotropy. This work was part of the current developments on such devices for Magnetic Random Access Memories. Indeed combined with Spin Transfer Torque (STT) switching [[Slo-96](#), [Ber-96](#)], this technology has been spotted as one of the most promising emerging type of non-volatile memories able to satisfy the requirements of the microelectronic industry in terms of scalability. However, building such structures is not straightforward and requires a good mastering of the deposited materials. Several parameters need to be optimized, in particular the materials thicknesses, if one wants to improve the performances of the devices both in terms of anisotropy and transport.

Perpendicular anisotropy, that is to say a preferred out-of-plane orientation of the magnetization, is a phenomenon that has been predicted for a long time and which has been proved to exhibit mostly interfacial origins [[Née-54](#)]. It was widely studied at first in the field of the Hard Disk Drive industry, in particular with the use of Pt (Pd)-based alloys that present strong spin-orbit coupling properties. Co/Pt multilayers appeared also interesting to create structures with large perpendicular anisotropy [[Joh-96](#)]. However, a great step forwards was made with the discovery of strong perpendicular anisotropy at the metal/oxide interface [[Mon-02](#)]. It enabled to consider the realization of perpendicular magnetic junctions as these structures are made of two magnetic layers separated by an insulating material.

Magnetic tunnel junctions are components that are at the origin of Tunnel MagnetoResistance (TMR), an effect that was discovered in 1975 [[Jul-75](#)] and that can be used to store the information. Indeed, depending on the relative orientations of the two magnetizations on both sides of the barrier, two resistance states are possible. It appeared from theoretical predictions [[But-01](#), [Mat-01](#)] that crystalline MgO barriers were a good choice of material to reach large TMR signals and this was confirmed experimentally in epitaxial systems [[Yua-04](#), [Par-04](#)]. Due to their advantages in terms of growth and crystallization, sputtered CoFeB alloys became favored rapidly [[Lee-07](#), [Yua-05](#), [Cho-07](#)] and could be also used in perpendicular magnetic tunnel junctions [[Ike-10](#)]. Studies also revealed that this type of junctions presents a lot of advantages in terms of STT applications compared to the planar systems (larger storage density, high thermal stability, lower current for switching). However to obtain this anisotropy, the choice of the buffer and capping layers has been found to be particularly important [[Wor-11](#), [Liu-12](#), [Nat-12](#), [Kub-12](#)].

We started from a standard structure comprising a Synthetic AntiFerromagnetic (SAF) reference layer made of Co/Pt multilayers and a top FeCoB free layer. In a SAF structure, the layers are coupled antiferromagnetically through a metallic spacer thanks to RKKY interactions [[Rud-54](#), [Kas-56](#), [Yos-57](#)] in order to reduce the stray

fields acting on the storage layer in small size devices [Ban-10]. The advantage of using Co/Pt multilayers in the reference is that they provide strong perpendicular anisotropy which makes them extremely stable. However, to obtain a large TMR signal, it is necessary to keep a CoFeB layer at the interface with the MgO barrier. It can be coupled to the Co/Pt multilayers but a thin Ta insertion is necessary to get the right bcc (001) orientation that guaranties good transport properties [Wor-11]. The advantage of using Ta is that its getter effect will have the ability to attract boron away from the interface with MgO which is beneficial to the TMR [Koz-10]. We studied the influence of the thickness of this insertion both on the magnetic and transport properties of the magnetic tunnel junctions [Cuc-13]. It appears that an optimal thickness around 0.3-0.4 nm allows keeping a strong magnetic coupling in the bottom reference, while improving the TMR signal of the junction thanks to the good crystallization of the CoFeB alloy.

The RKKY coupling strength in the SAF bottom reference was tested. As expected, the typical oscillatory behavior was obtained as a function of the Ru spacer thickness [Par-91]. It turns out that setting the Ru thickness at 0.9 nm allows benefiting from a strong antiferromagnetic coupling while being less sensitive to possible thickness variations as the peak is rather broad. The Co and Pt thicknesses in the multilayers as well as the Pt buffer layer play also an important role in the magnetic properties of the bottom SAF reference and have to be chosen carefully. Besides, knowing the characteristics of the bottom and top FeCoB electrodes is particularly interesting as it will allow knowing the working windows of the system. Thanks to series of samples with varying thicknesses of bottom and top FeCoB layers, the critical thicknesses, at the transition between perpendicular and planar anisotropy, could be extracted as well as the saturation magnetization and the magnetic dead layer thickness. This last parameter is necessary if one wants to evaluate the anisotropy of the magnetic layer through  $K_{\text{eff}} \cdot t$  vs  $t$  plots. From this treatment we could extract an interfacial anisotropy  $2K_s$  of the top free electrode around 1 erg.cm<sup>-2</sup>. Transport measurements by Current In-Plane Tunneling (CIPT) [Wor-03] on such structures showed that to get a maximum TMR signal, it is necessary to have effective magnetic thicknesses in the CoFeB electrodes that are larger than 0.6 nm [Cuc-14a].

Knowing that perpendicular anisotropy mostly arises at the metal/oxide interface, we replaced our standard Ta capping by a MgO one and it appeared that the effective critical thickness (taking into account the magnetic dead layer) is increased from 1.1 to 2.7 nm by using FeCoBx/Ta<sub>0.3</sub>/FeCoBx/MgO storage layers. This is accompanied by a doubling of the interfacial anisotropy constant that reaches about 2 erg.cm<sup>-2</sup> in the second case, which gives the ability to get a large thermal stability in these systems. That gives as well the possibility to work with thicker layers that should reduce the damping parameter. Note that a thin Ta insertion was used in the middle of the storage layer to keep its getter effect. Samples with a Ru insertion or without any insertion were also tested and appeared to be working as well. The type of MgO barrier can be varied in order to change its RA value. Indeed, a smaller RA should be used in the top MgO barrier if one wants to keep a reasonable resulting TMR. We

## Conclusion

found out that the nature of the barriers does not seem to influence a lot the perpendicular magnetic anisotropy of the storage layer.

From previous studies on planar structures, it appeared that the use of double junctions comprising two tunnel barriers and two polarizing layers is particularly interesting for STT applications [Dia-07, Clé-14]. Indeed, by adjusting the relative orientation of the reference layers, one can tune the STT efficiency to create a write mode with a low switching current and a read mode in which larger voltages can be applied without risking losing the stored information. We proposed then to add these advantageous properties to our perpendicular magnetic tunnel junctions [Cuc-15a]. To do so, a top Co/Pd reference was developed after several thicknesses optimizations. Note that as no Pd buffer layer can be used in these reversed structures, the perpendicular anisotropy is much reduced compared to our bottom Co/Pt reference. This is however a good point as it enables us to get distinct transitions in the two references and to build a functional system in which all magnetic layers can be switched independently. We have thus shown the realization of a double magnetic tunnel junction with perpendicular anisotropy made of a bottom Co/Pt-based SAF reference, a single ferromagnetic storage layer and a top Co/Pd-based SAF reference. By a correct field treatment, the storage layer can be switched with both parallel and antiparallel configurations of the references.

For practical applications, it would be interesting to work with SAF storage layers as they would be more immune to possible stray fields in small pillars. With that aim, we developed FeCoB-based structures with different spacer materials [Cuc-16]. It appears that if a Ru spacer gives the largest coupling strength, functioning systems can be built with Ta or Ta/Ru bilayers. Playing with the magnetic compensation of the FeCoB layers on both sides of the spacer allows enhancing the stability of the SAF. Such a structure can be used at different positions in a double magnetic junction, either as a reference or a SAF storage layer. It gives the possibility to imagine an even more efficient device in which the top reference layer would be replaced by a soft layer that could be switched by field between a write and read mode, without losing the information stored in the more stable SAF storage layer. This control layer will however have to be made immune to STT during the write phase.

These FeCoB-based SAF could be made particularly stable with antiferromagnetic plateaus that could reach  $\pm 1300$  Oe. They can thus advantageously replace our standard Co/Pt(Pd)-based SAF reference in single junctions. It gives the ability to a build Pt(Pd)-free system that would be a particularly efficient way to remove the thin noble materials multilayers that are difficult to etch by standard reactive ion etching techniques. The amount of materials involved is also reduced in that case.

After patterning into small pillars, the electrical properties of a standard junction with a Co/Pt-based SAF reference and a top Ta-capped FeCoB storage layer were evaluated [Cuc-14b]. Field vs pulse voltage diagrams were measured and critical current densities as low as  $2.9 \text{ MA.cm}^{-2}$  could be obtained. Thanks to the variation of the properties with magnetic thickness, the Gilbert damping parameter could be

estimated around 0.016, in good agreement with other studies [[Dev-13](#)]. The temperature dependence of the coercive field was also tested and proved to be related with the storage layer thickness as expected.

If these first electrical tests are encouraging, it would be interesting to test the performances of the MgO-capped structures as well as the double junctions. In that context, further work on the tunnel barriers might be necessary, in particular if we want to tune precisely the RA values of each barrier.

The FeCoB-based structures are particularly promising and could be tested for STT applications in various structures. However, the stability of the RKKY coupling in these structures at small dimensions is still to be confirmed. Preliminary results suggest that the SAF behavior can be maintained in pillars as small as 50 nm at least. This is a property that could be further tested by realizing arrays of pillars of different sizes and measuring their hysteresis loops with a focused Kerr set-up.

## References

[Ban-10] S. Bandiera, R. C. Sousa, Y. Dahmane, C. Ducruet, C. Portemont, V. Baltz, S. Auffret, I. L. Prejbeanu, and B. Dieny, *Comparison between synthetic antiferromagnets and single hard layers as reference layer in perpendicular magnetic tunnel junctions*, [IEEE Magn. Lett.](#) **1**, 3000204 (2010).

[Ber-96] L. Berger, *Emission of spin waves by a magnetic multilayer traversed by a current*, [Phys. Rev. B](#) **54**, 9353-9358 (1996).

[But-01] W. H. Butler, X.-G. Zhang, T. C. Schulthess, and J. M. MacLaren, *Spin-dependent tunneling conductance of Fe|MgO|Fe sandwiches*, [Phys. Rev. B](#) **63**, 092402 (2001).

[Cho-07] Y. S. Choi, K. Tsunekawa, Y. Nagamine, and D. Djayaprawira, *Transmission electron microscopy study on the polycrystalline CoFeBMgOCoFeB based magnetic tunnel junction showing a high tunneling magnetoresistance, predicted in single crystal magnetic tunnel junction*, [J. Appl. Phys.](#) **101**, 013907 (2007).

[Clé-14] P.-Y. Clément, C. Baraduc, M. Chshiev, B. Dieny, L. Vila, and C. Ducruet, *Double barrier magnetic tunnel junctions with write/read mode select layer*, Proceedings of the [6<sup>th</sup> IEEE International Memory Workshop \(IMW\)](#), Taipei (May 18-21, 2014).

[Cuc-13] L. Cuchet, B. Rodmacq, S. Auffret, R. C. Sousa, C. Ducruet, and B. Dieny, *Influence of a Ta spacer on the magnetic and transport properties of perpendicular magnetic tunnel junctions*, [Appl. Phys. Lett.](#) **103**, 052402 (2013).

[Cuc-14a] L. Cuchet, B. Rodmacq, S. Auffret, R. C. Sousa, and B. Dieny, *Influence of magnetic electrodes thicknesses on the transport properties of magnetic tunnel junctions with perpendicular anisotropy*, [Appl. Phys. Lett.](#) **105**, 052408 (2014).

[Cuc-14b] L. Cuchet, R. C. Sousa, L. Vila, S. Auffret, B. Rodmacq, and B. Dieny, *Field dependence of spin transfer torque switching current in perpendicular magnetic tunnel junctions*, [IEEE Trans. Magn.](#) **50**, 4401404 (2014).

[Cuc-15a] L. Cuchet, B. Rodmacq, S. Auffret, R. C. Sousa, I. L. Prejbeanu, and B. Dieny, *Perpendicular magnetic tunnel junctions with double barrier and single or synthetic antiferromagnetic storage layer*, [J. Appl. Phys.](#) **117**, 233901 (2015).

[Cuc-16] L. Cuchet, B. Rodmacq, S. Auffret, R. C. Sousa, I. L. Prejbeanu, and B. Dieny, *Perpendicular magnetic tunnel junctions with a synthetic storage or reference layer: A new route towards Pt- and Pd-free junctions*, to be published in *Sci. Rep.* (2016).

[Dev-13] T. Devolder, P.-H. Ducrot, J.-P. Adam, I. Barisic, N. Vernier, Joo-Von Kim, B. Ockert, and D. Ravelosona, *Damping of  $\text{Co}_x\text{Fe}_{80-x}\text{B}_{20}$  ultrathin films with perpendicular magnetic anisotropy*, [\*Appl. Phys. Lett.\* \*\*102\*\*, 022407 \(2013\)](#).

[Dia-07] Z. Diao, A. Panchula, Y. Ding, M. Pakala, S. Wang, Z. Li, D. Apalkov, H. Nagai, A. Driskill-Smith, L.-C. Wang, E. Chen, and Y. Huai, *Spin transfer switching in dual MgO magnetic tunnel junctions*, [\*Appl. Phys. Lett.\* \*\*90\*\*, 132508 \(2007\)](#).

[Ike-10] S. Ikeda, K. Miura, H. Yamamoto, K. Mizunuma, H. D. Gan, M. Endo, S. Kanai, J. Hayakawa, F. Matsukura, and H. Ohno, *A perpendicular-anisotropy CoFeB–MgO magnetic tunnel junction*, [\*Nature Mater.\* \*\*9\*\*, 721-724 \(2010\)](#).

[Joh-96] M. T. Johnson, P. J. H. Bloemen, F. J. A. den Broeder, and J. J. de Vries, *Magnetic anisotropy in metallic multilayers*, [\*Rep. Prog. Phys.\* \*\*59\*\*, 1409-1458 \(1996\)](#).

[Jul-75] M. Jullière, *Tunneling between ferromagnetic films*, [\*Phys. Lett.\* \*\*54A\*\*, 225-226 \(1975\)](#).

[Kas-56] T. Kasuya, *A theory of metallic ferro- and antiferromagnetism on Zener's model*, [\*Prog. Theor. Phys.\* \*\*16\*\*, 45-57 \(1956\)](#).

[Koz-10] X. Kozina, S. Ouardi, B. Balke, G. Stryganyuk, G. H. Fecher, C. Felser, S. Ikeda, H. Ohno, and E. Ikenaga, *A nondestructive analysis of the B diffusion in Ta–CoFeB–MgO–CoFeB–Ta magnetic tunnel junctions by hard X-ray photoemission*, [\*Appl. Phys. Lett.\* \*\*96\*\*, 072105 \(2010\)](#).

[Kub-12] H. Kubota, S. Ishibashi, T. Saruya, T. Nozaki, A. Fukushima, K. Yakushiji, K. Ando, Y. Suzuki, and S. Yuasa, *Enhancement of perpendicular magnetic anisotropy in FeB free layers using a thin MgO cap layer*, [\*J. Appl. Phys.\* \*\*111\*\*, 07C723 \(2012\)](#).

[Lee-07] Y. M. Lee, J. Hayakawa, S. Ikeda, F. Matsukura, and H. Ohno, *Effect of electrode composition on the tunnel magnetoresistance of pseudo-spin-valve magnetic tunnel junction with a MgO tunnel barrier*, [\*Appl. Phys. Lett.\* \*\*90\*\*, 212507 \(2007\)](#).

[Liu-12] T. Liu, J. W. Cai, and L. Sun, *Large enhanced perpendicular magnetic anisotropy in CoFeB/MgO system with the typical Ta buffer replaced by an Hf layer*, [\*AIP Advances\* \*\*2\*\*, 032151 \(2012\)](#).

[Mat-01] J. Mathon, and A. Umerski, *Theory of tunneling magnetoresistance of an epitaxial Fe/MgO/Fe(001) junction*, [\*Phys. Rev. B\* \*\*63\*\*, 220403\(R\) \(2001\)](#).

[Mon-02] S. Monso, B. Rodmacq, S. Auffret, G. Casali, F. Fettar, B. Gilles, B. Dieny, and P. Boyer, *Crossover from in-plane to perpendicular anisotropy in Pt/CoFe/AlO<sub>x</sub> sandwiches as a function of Al oxidation: A very accurate control of the oxidation of tunnel barriers*, [\*Appl. Phys. Lett.\* \*\*80\*\*, 4157-4159 \(2002\)](#).

## Conclusion

[Nat-12] A. Natarajarathinam, Z. R. Tadisina, T. Mewes, S. Watts, E. Chen, and S. Gupta, *Influence of capping layers on CoFeB anisotropy and damping*, [J. Appl. Phys.](#) **112**, 053909 (2012).

[Née-54] L. Néel, *Anisotropie magnétique superficielle et surstructures d'orientation*, [J. Phys. Radium](#) **15**, 225-239 (1954)

[Par-91] S. S. P. Parkin, *Systematic variation of the strength and oscillation period of indirect magnetic exchange coupling through the 3d, 4d, and 5d transition metals*, [Phys. Rev. Lett.](#) **67**, 3598 (1991).

[Par-04] S. S. P. Parkin, C. Kaiser, A. Panchula, P. M. Rice, B. Hughes, M. Samant, and S.-H. Yang, *Giant tunnelling magnetoresistance at room temperature with MgO (100) tunnel barriers*, [Nature Mater.](#) **3**, 862-867 (2004).

[Rud-54] M. A. Ruderman, and C. Kittel, *Indirect exchange coupling of nuclear magnetic moments by conduction electrons*, [Phys. Rev.](#) **96**, 99-102 (1954).

[Slo-96] J. C. Slonczewski, *Current-driven excitation of magnetic multilayers*, [J. Magn. Magn. Mater.](#) **159**, L1-L7 (1996).

[Wor-03] D. C. Worledge, and P. L. Trouilloud, *Magnetoresistance measurement of unpatterned magnetic tunnel junction wafers by current-in-plane tunneling*, [Appl. Phys. Lett.](#) **83**, 84-86 (2003).

[Wor-11] D. C. Worledge, G. Hu, D. W. Abraham, J. Z. Sun, P. L. Trouilloud, J. Nowak, S. Brown, M. C. Gaidis, E. J. O'Sullivan, and R. P. Robertazzi, *Spin torque switching of perpendicular Ta/CoFeB/MgO-based magnetic tunnel junctions*, [Appl. Phys. Lett.](#) **98**, 022501 (2011).

[Yos-57] K. Yosida, *Magnetic properties of Cu-Mn alloys*, [Phys. Rev.](#) **106**, 893-898 (1957).

[Yua-04] S. Yuasa, T. Nagahama, A. Fukushima, Y. Suzuki, and K. Ando, *Giant room-temperature magnetoresistance in single-crystal Fe/MgO/Fe magnetic tunnel junctions*, [Nature Mater.](#) **3**, 868-871 (2004).

[Yua-05] S. Yuasa, Y. Suzuki, T. Katayama, and K. Ando, *Characterization of growth and crystallization processes in CoFeB/MgO/CoFeB magnetic tunnel junction structure by reflective high-energy electron diffraction*, [Appl. Phys. Lett.](#) **87**, 242503 (2005).

# FRENCH SUMMARY

**Introduction.....185**  
**Chapitre I ..... 188**  
**Chapitre II..... 191**  
**Chapitre III .....193**  
**Chapitre IV.....195**  
**Chapitre V .....197**  
**Conclusion .....198**  
**Références ..... 202**

## **Introduction**

Depuis des millénaires, le stockage et la transmission de l'information ont joué un rôle très important dans la vie des Hommes. Après des années de transmission orale, l'apparition de l'écriture nous a permis de stocker une partie de l'information de façon beaucoup plus pérenne, sur un support externe tel qu'un livre. C'est cependant au cours du siècle passé que l'avènement de l'ère de l'électronique a vu la quantité d'informations stockées exploser.

Parallèlement, le magnétisme est un phénomène qui a toujours fasciné les Hommes. Il est relativement difficile de dater précisément la première utilisation du magnétisme mais certains documents semblent placer la découverte de la boussole au XI<sup>e</sup> siècle en Chine. Ce n'est cependant qu'à partir du XIX<sup>e</sup> siècle qu'une meilleure compréhension et maîtrise du magnétisme a été possible grâce aux nombreuses avancées faites dans le domaine de l'électromagnétisme.

Une des premières techniques de stockage de l'information sur un support magnétique fût la bande magnétique, créée en 1928. Les données y étaient stockées dans des particules d'oxyde de fer déposées dans un substrat flexible. Cette technologie permit d'enregistrer des données audio et vidéo mais fût également utilisée dans les premiers ordinateurs. Elle fût cependant rapidement remplacée dès les années 1950 par la technologie des disques durs qui permet une lecture beaucoup plus rapide de l'information. De nombreuses études ont été menées sur ces dispositifs, notamment afin d'augmenter les capacités de stockage. De nos jours, dans les disques durs, les densités de stockage peuvent atteindre plusieurs Tbit/in<sup>2</sup>.

Plus récemment, les découvertes en termes de transport de spin dans les matériaux ferromagnétiques ont donné naissance à une nouvelle discipline : la spintronique (ou électronique de spin). L'idée est de créer de nouvelles fonctionnalités en combinant le spin de l'électron au déplacement de sa charge tel qu'utilisé dans l'électronique traditionnelle. Ce domaine a été particulièrement dynamisé par la découverte de la MagnétoRésistance Géante (GMR) à la fin des années 1980 par A. Fert [\[Bai-88\]](#) et P. Grünberg [\[Bin-89\]](#), qui reçurent le prix Nobel de Physique en 2007 pour ces travaux. Ce phénomène a été rapidement mis en pratique de manière à améliorer les performances des têtes de lecture des disques durs [\[Die-91\]](#). Quelques années plus tard, un autre phénomène lié au transport de spin est apparu comme particulièrement prometteur pour les applications aux mémoires : la MagnétoRésistance Tunnel (TMR). Cet effet dépend de l'orientation relative des aimantations de deux couches magnétiques séparées par une couche isolante. Un tel empilement est appelé Jonction Tunnel Magnétique et constitue l'élément de base des mémoires magnétiques à accès aléatoire (Magnetic Random Access Memories, MRAM). Cette technologie fût ensuite encore améliorée par l'introduction de l'écriture par couple de transfert de spin (Spin Transfer Torque, STT), phénomène théorisé par J. C. Slonczewski [\[Slo-96\]](#) et L. Berger [\[Ber-96\]](#).

Comme prédit par la loi de Moore, le nombre de composants par puce électronique a augmenté de manière exponentielle aux cours des dernières décennies. Même si cette tendance commence à ralentir, il existe encore de nombreux développements vers la réduction des tailles des dispositifs. Sur cet aspect, les MRAM et tout particulièrement les STT-MRAM sont apparues comme des technologies significativement prometteuses parmi les mémoires non-volatiles émergentes. En effet, de même que les redox RRAM, elles ont été identifiées en 2010 par la commission de l'International Technology Roadmap for Semiconductors (ITRS, [Itr-10]) comme étant les technologies émergentes pouvant atteindre le nœud technologique 16 nm et même au-delà. D'autre part, la MRAM est aussi envisagée comme une possible mémoire universelle qui aurait la capacité de remplacer à la fois la DRAM (connue pour sa rapidité, sa faible consommation d'énergie, sa forte endurance et sa fiabilité) et la mémoire Flash avec sa capacité de stockage élevée et sa non-volatilité. Une comparaison des technologies Flash, FeRAM (pour Ferroelectric RAM, une autre mémoire émergente), MRAM et STT-MRAM est donnée dans le Tableau 1.

	Flash-NAND	FeRAM	MRAM	STT-MRAM
Capacité de stockage	> 1 Gb	> 10 Mb	16 Mb	1 Gb
Temps d'écriture	1 ms	10 ns	20 ns	3-10 ns
Temps de lecture	50 ns	45 ns	10 ns	10 ns
Energie d'écriture (pJ/bit)	> 0,01	0,03	70	0,1

Tableau 1 : Comparaison entre différentes technologies de mémoires non-volatiles [Hu-11].

C'est dans ce contexte que le laboratoire SPINTEC fût fondé en 2002, pour combiner des approches à la fois fondamentales et appliquées de la recherche en spintronique. Cette thèse a été réalisée au sein de l'équipe MRAM, avec l'idée de poursuivre les développements matériaux de jonctions tunnel magnétiques à anisotropie perpendiculaire. En effet, cette propriété, qui se caractérise par une orientation hors du plan de l'aimantation des couches magnétiques, est apparue particulièrement intéressante pour les applications pratiques. En comparaison des structures aimantées dans le plan, l'anisotropie perpendiculaire permet de réduire la taille des dispositifs, ce qui augmente la capacité de stockage. De plus, ce type d'anisotropie devrait apporter une plus grande stabilité thermique aux éléments mémoires, c'est-à-dire une plus grande stabilité de l'information face à l'agitation thermique. Enfin, il a été montré que l'efficacité de l'écriture par couple de transfert de spin est particulièrement bonne avec les systèmes à anisotropie perpendiculaire, ce qui permet de réduire significativement la consommation électrique des mémoires.

L'objectif de cette thèse est d'améliorer les propriétés magnétiques et de transport électrique de jonctions tunnel perpendiculaires, en ajustant soigneusement les différentes parties de l'empilement à la fonctionnalité visée. Cela est uniquement possible grâce à une bonne maîtrise de l'outil de dépôt et des différents matériaux utilisés. Dans le premier Chapitre, nous rappellerons l'origine de l'anisotropie magnétique perpendiculaire et les différents concepts qui ont accompagné les développements de la MRAM, en particulier dans le cas des systèmes perpendiculaires. Nous présenterons également les différentes procédures expérimentales que nous avons utilisées durant cette thèse, notamment pour la préparation des échantillons et leur caractérisation. Dans le deuxième Chapitre, nous verrons comment une jonction tunnel standard avec une référence inférieure à base de multicouches Co/Pt peut être optimisée en adaptant les épaisseurs des différentes couches constituant l'empilement. Nous montrerons que les propriétés magnétiques et les propriétés de transport sont liées et que certains compromis sont nécessaires. Le troisième Chapitre démontrera que des structures encore plus complexes peuvent être développées, comme des doubles jonctions tunnel magnétiques à anisotropie perpendiculaire dont les propriétés en termes de STT permettent d'imaginer des dispositifs encore plus performants. Nous commencerons par insérer une deuxième couche de MgO comme couverture et après avoir développé une couche de référence supérieure, nous montrerons la réalisation de doubles structures complètes. Dans le quatrième Chapitre, nous nous focaliserons sur le développement de couches antiferromagnétiques synthétiques à base de FeCoB comportant des inserts de différentes natures. Nous verrons que ces systèmes peuvent jouer différents rôles dans une double jonction mais peuvent également être rendus suffisamment stables pour servir de couche de référence dans une jonction sans Pt ni Pd. Finalement, le cinquième Chapitre expliquera le processus de nanofabrication et présentera les résultats de mesures électriques réalisées sur des nanopiliers à anisotropie perpendiculaire.

## Chapitre I

L'anisotropie magnétique perpendiculaire est un phénomène connu depuis de nombreuses années, notamment grâce aux avancées réalisées dans le domaine des disques durs. Cependant, l'intérêt accordé à cette propriété a considérablement augmenté au cours du développement des mémoires magnétiques à accès aléatoire (MRAM). L'objectif de ce premier Chapitre est de rappeler les origines de l'anisotropie perpendiculaire ainsi que les principales découvertes faites dans la spintronique. Un rapide état de l'art des développements de jonctions tunnel magnétiques permettra de mettre en évidence les compromis, notamment en termes de matériaux, nécessaires pour garantir une bonne fonctionnalité des dispositifs. Nous décrirons enfin les procédures expérimentales utilisées au cours de cette thèse pour l'élaboration et la caractérisation de nos échantillons.

L'anisotropie magnétique se caractérise par une orientation préférentielle de l'aimantation et comporte plusieurs contributions : l'anisotropie magnétocristalline, l'anisotropie magnétoélastique, l'anisotropie de forme et l'anisotropie d'interface. Un des effets prédominants dans l'anisotropie magnétique est le couplage spin-orbite qui lie le spin de l'électron à son mouvement orbital et qui est par conséquent particulièrement influencé par la structure cristalline du matériau. A mesure que les couches magnétiques deviennent de plus en plus minces, les contributions interfaciales prennent de plus en plus d'importance. Cet effet a été prédit dès 1954 [Née-54] et a été attribué à un changement des symétries aux interfaces. C'est pour cela que les systèmes multicouches à base de Co/Pt ou Co/Pd présentent de fortes anisotropies perpendiculaires : en plus de multiplier les interfaces, le Pt et le Pd possèdent de forts couplages spin-orbite [Joh-96]. Plus récemment, une autre forme d'anisotropie d'interface a été mise en évidence à l'interface entre les métaux magnétiques et les oxydes [Mon-02, Rod-03, Man-08]. Elle est du même ordre de grandeur que celle obtenue dans les systèmes Co/Pt et est extrêmement dépendante de l'état d'oxydation de l'interface [Yan-11].

L'anisotropie effective d'un système peut être définie par la formule suivante :

$$K_{eff} = -2\pi M_S^2 + K_V + \frac{2K_S}{t}$$

où  $2\pi M_S^2$  est l'énergie de champ démagnétisant,  $K_V$  la contribution volumique (anisotropies magnétocristalline et magnétoélastique),  $K_S$  la contribution surfacique et  $t$  l'épaisseur magnétique. Par convention,  $K_{eff}$  est positive si l'anisotropie est perpendiculaire et négative si elle est planaire.

Une des avancées majeures de la spintronique fût la découverte de la MagnétoRésistance Géante (GMR) par A. Fert [Bai-88] et P. Grünberg [Bin-89]. Cet effet est caractérisé par l'existence de deux états de résistance différents en fonction de l'orientation relative des aimantations de deux couches magnétiques séparées par un espaceur métallique. La MagnétoRésistance Tunnel (TMR) est un effet

relativement similaire qui apparaît dans le cas où l'espaceur métallique est remplacé par un oxyde [Jul-75], dans un empilement appelé jonction tunnel magnétique. Les premières jonctions développées étaient à anisotropie planaire et c'est seulement lorsque les barrières amorphes AlOx furent remplacées par des barrières cristallines MgO que les signaux de TMR augmentèrent significativement pour atteindre plusieurs centaines de pourcent (prévisions théoriques [But-01, Mat-01], mesures expérimentales dans des systèmes épitaxiés [Yua-04, Par-04]). La recherche s'est ensuite surtout focalisée sur les électrodes à base d'alliages de CoFeB qui peuvent être obtenues par pulvérisation cathodique, et ont la particularité d'être amorphes au moment du dépôt et de cristalliser pendant le recuit selon une texture bcc (001) ce qui garantit un bon effet tunnel [Yua-05, Cho-07].

Du fait de leurs propriétés avantageuses, notamment en termes de densité de stockage, différents groupes de recherche ont commencé à s'intéresser aux jonctions magnétiques à anisotropie perpendiculaire. Ainsi, en 2010, des jonctions perpendiculaires du type Ta/CoFeB/MgO/CoFeB/Ta ont pu être fabriquées sous forme de nanopiliers et ont donné de forts signaux de TMR d'environ 120 % [Ike-10]. Afin de durcir l'électrode de référence, des systèmes avec couche de référence antiferromagnétique synthétique (SAF) à base de multicouches Co/Pt couplées à une couche de CoFeB ont également été développées [Wor-11]. Il apparaît que dans ces empilements, les couches aux interfaces avec le CoFeB jouent un rôle très important dans l'anisotropie perpendiculaire, que ça soit la couche tampon [Liu-12, Sin-13, Liu-14] ou la couche de couverture [Nat-12, Kub-12, Yam-12].

Grâce aux théories développées par J. C. Slonczewski [Slo-96] et L. Berger [Ber-96], il est apparu que l'aimantation d'une couche magnétique peut être commutée grâce à un courant polarisé en spin : on parle de couple de transfert de spin (Spin Transfer Torque, STT). Cela a donné naissance à une nouvelle génération de mémoires MRAM pouvant être plus compactes. Pour ce type de mémoire, les systèmes perpendiculaires se révèlent être particulièrement compétitifs car ils permettent de réduire significativement les densités de courant nécessaires pour l'écriture [Wol-10, Yod-10, Hei-10]. D'autre part, du fait de leur forte constante d'anisotropie, ils présentent des stabilités thermiques élevées ce qui est bénéfique pour la rétention des données. Cependant, des compromis doivent être réalisés car le courant critique est proportionnel au facteur de stabilité thermique. Similairement, si de faibles épaisseurs magnétiques sont nécessaires pour assurer une forte anisotropie perpendiculaire, elles induisent également une augmentation du facteur d'amortissement de Gilbert, augmentant le courant d'écriture.

L'ensemble des échantillons réalisés pendant cette thèse a été déposé par pulvérisation cathodique dans un bâti de dépôt qui possède 12 cibles. Cela nous a permis de réaliser des empilements complexes avec un contrôle des épaisseurs jusqu'au dixième de nanomètre. D'autre part, la machine de dépôt est équipée d'une chambre de traitement permettant de réaliser les barrières tunnel par oxydation naturelle de Mg métallique. Différentes valeurs de produits résistance x aire (RA)

peuvent être obtenues en fonction des conditions d'oxydation choisies. Cet outil de dépôt nous donne également la possibilité de réaliser des gradients d'épaisseur sur un même échantillon en utilisant une configuration dite « off-axis ».

Les caractérisations magnétiques ont été principalement effectuées par magnétométrie VSM (Vibrating Sample Magnetometry). Cette technique permet de réaliser des mesures selon n'importe quelle direction de l'échantillon et donc de pouvoir en évaluer le champ d'anisotropie. Il faudra cependant faire attention au fait qu'il est très difficile d'obtenir des valeurs absolues d'aimantation avec cette technique. En effet, l'amplitude de l'aimantation dépend énormément de la position et de l'orientation de l'échantillon entre les bobines de détection. Pour obtenir la valeur de l'aimantation d'une couche, nous utiliserons donc une référence interne d'aimantation connue dans nos échantillons. D'autre part, nous avons pu observer une contribution importante des bords des échantillons lorsque ceux-ci ne sont pas protégés pendant le dépôt. Un signal parasite d'environ 5 % du signal total apparaît ainsi dans le cycle magnétique. A partir de cette observation, nous avons donc décidé de protéger soigneusement les bords des échantillons avant dépôt quand des mesures quantitatives précises étaient nécessaires. Une autre technique de caractérisation magnétique que nous avons employée est l'effet Hall extraordinaire. Il apparaît dans les matériaux magnétiques et est proportionnel à la composante perpendiculaire de l'aimantation. Cette méthode est donc particulièrement adaptée aux structures à anisotropie magnétique perpendiculaire. Cependant, cette technique de mesure ne fournit pas de valeur absolue de l'aimantation car la résistance mesurée dépend du coefficient d'effet Hall extraordinaire propre à chaque matériau et de la résistance des autres couches métalliques (en couverture par exemple).

Finalement, il a été possible de réaliser des mesures de transport grâce à un outil Capres de Crocus Technology, développé à partir de la technique « Current In-Plane Tunneling » (CIPT) mise au point en 2003 à IBM [[Wor-03](#)] et permet de caractériser les propriétés de la jonction (RA et TMR) sur des échantillons macroscopiques, sans avoir besoin de passer par le processus de nanofabrication. Cette technique réalise des mesures de résistance pour différents écartements de pointe ce qui permet de remonter aux paramètres de la barrière. Pour adapter les résistivités des électrodes inférieure et supérieure, nous travaillons avec des substrats de CuN et une couche de Ru est déposée sur l'échantillon après recuit.

## Chapitre II

Ce Chapitre présente le développement de jonctions simples avec couche de référence inférieure. Nous montrons comment il est possible d'optimiser à la fois les propriétés d'anisotropie et de transport dans ce type de structure.

Dans une première partie, nous avons étudié l'insert de Ta qui est introduit entre une multicouche Co/Pt et une couche de CoFeB qui forment l'électrode de référence. Le but de cet insert est de permettre d'obtenir une bonne texture de l'alliage de CoFeB ce qui ne serait pas possible si cette couche est directement déposée sur la multicouche Co/Pt [Wor-11]. Cependant, il faut être attentif à ce que cet insert soit suffisamment mince pour conserver un fort couplage magnétique entre les deux couches adjacentes. Pour optimiser cette épaisseur d'insert nous avons réalisé une série de jonctions à épaisseur de Ta variable. Il apparaît lors des mesures magnétiques que, pour l'épaisseur de CoFeB choisie, une composante planaire est visible dans le signal magnétique lorsque la couche de CoFeB se découple de la multicouche. Cela se produit à partir de 0,5 nm de Ta. Des mesures de transport ont permis de corréliser ses propriétés magnétiques à l'évolution du rapport de TMR. On observe ainsi une augmentation du signal de TMR avec l'épaisseur de Ta, suivie d'une chute brutale de ce signal lorsque le découplage magnétique apparaît. Une épaisseur optimale de Ta est donc obtenue autour de 0,3 nm car elle permet une amélioration de la texture cristalline du CoFeB tout en maintenant un fort couplage magnétique dans toute la structure.

Dans une deuxième partie, nous avons optimisé la structure SAF de l'électrode inférieure. Ce type de structure se compose de deux couches magnétiques couplées de manière antiferromagnétique à travers un espaceur métallique [Par-91]. Cela permet de réduire fortement les champs rayonnés sur la couche de stockage dans les dispositifs de petite taille. Il faut cependant adapter le rapport des aimantations à la taille de pilier visée [Ban-10]. Nous avons utilisé dans notre électrode des multicouches Co/Pt couplées à travers un espaceur de Ru. L'épaisseur de Ru a été fixée à 0,9 nm après avoir étudié la variation du couplage avec l'épaisseur d'espaceur. Les meilleures propriétés magnétiques en terme de couplage et d'anisotropie ont été obtenues pour des épaisseurs de 0,5 nm de Co et 0,25 nm de Pt dans les multicouches, ainsi qu'avec une épaisseur de couche tampon de Pt de 5 nm. Nous avons ensuite optimisé la température de recuit de ce type de jonction. Il apparaît qu'à 300°C à la fois de bonnes propriétés d'anisotropie et un fort signal de TMR autour de 100 % sont garantis. Il faut noter que les propriétés de transport sont maintenues jusqu'à environ 380°C.

Enfin, les épaisseurs magnétiques de CoFeB dans les électrodes inférieure et supérieure ont été étudiées. Grâce à des séries de jonctions à épaisseurs magnétiques variables, nous avons pu estimer les épaisseurs critiques à partir desquelles l'anisotropie perpendiculaire ne peut plus être maintenue. On obtient 1,6 nm et 1,7 nm dans l'électrode inférieure et supérieure, respectivement. Nous avons ensuite

déterminé les aimantations à saturation et les épaisseurs de couches magnétiquement mortes qui se forment aux interfaces. Pour la couche de CoFeB inférieure, nous obtenons  $M_{s\text{CoFeB}}=600 \text{ emu.cm}^{-3}$  et  $t_d=0,3 \text{ nm}$  et pour la couche de FeCoB supérieure  $M_{s\text{FeCoB}}=1300 \text{ emu.cm}^{-3}$  et  $t_d=0,6 \text{ nm}$ . Cette forte différence peut s'expliquer par la différence d'épaisseur de Ta aux interfaces : en effet la couche de CoFeB inférieure croît sur un insert de Ta mince alors que la couche supérieure est couverte par une couche de Ta épaisse de 1 nm. Nous avons ensuite évalué les propriétés de transport de nos jonctions en fonction des épaisseurs magnétiques. Dans les deux cas nous obtenons le même comportement : une augmentation du signal de TMR puis une stabilisation à sa valeur maximale autour de 90 % dès que les épaisseurs effectives dépassent 0,6 nm (tant qu'il est encore possible de saturer complètement le système en perpendiculaire avec le champ maximal de l'outil de mesure). Il apparaît donc que les jonctions perpendiculaires possèdent des gammes de fonctionnement en épaisseur plus réduites que les systèmes planaires. Les épaisseurs magnétiques effectives doivent en effet être comprises entre 0,6 nm et l'épaisseur critique si l'on veut obtenir bonnes propriétés d'anisotropie, et donc un fort signal de TMR.

## **Chapitre III**

L'objectif de ce Chapitre est de montrer comment il est possible d'aller vers des structures plus complexes à double barrière permettant d'améliorer significativement les performances des dispositifs, notamment l'efficacité de l'écriture par STT.

Comme nous l'avons vu dans le premier Chapitre, une très forte anisotropie perpendiculaire apparaît aux interfaces métal/oxyde. Nous avons donc voulu étudier dans un premier temps l'effet de remplacer la couche de couverture traditionnelle de Ta par une deuxième couche de MgO. Pour cela une série de jonctions avec épaisseur de couche de stockage supérieure variable a été déposée. Dans ce cas, un mince insert de 0,3 nm de Ta est inclus dans l'électrode de FeCoB de manière à conserver l'effet bénéfique du Ta sur les propriétés de transport. Nous avons ainsi observé que l'épaisseur critique est fortement augmentée et atteint 3 nm en épaisseur nominale. La couche morte a été estimée à 0,3 nm et des mesures d'anisotropie ont permis de constater que l'anisotropie d'interface est doublée avec la couverture MgO par rapport à la couverture Ta ( $2K_s=2,2 \text{ erg.cm}^{-2}$  contre 1,1). Il semble donc que l'interface avec Ta apporte très peu d'anisotropie perpendiculaire. Ces systèmes avec couverture MgO apparaissent donc prometteurs pour augmenter la stabilité thermique (à épaisseur constante) et permettent également de travailler avec des épaisseurs plus importantes à anisotropie perpendiculaire, ce qui devrait permettre de diminuer le facteur d'amortissement  $\alpha$ .

Afin de réaliser des doubles jonctions complètes avec une référence supérieure, nous avons travaillé sur le développement de structures de référence SAF supérieures. Il est rapidement apparu que du fait de l'absence de couche tampon dans ces structures inverses, il était difficile d'obtenir de bonnes propriétés d'anisotropie avec des multicouches Co/Pt. Nous avons donc développé des multicouches Co/Pd et après plusieurs étapes d'optimisation, il a été possible d'obtenir une couche de référence supérieure avec une bonne anisotropie perpendiculaire et présentant des champs de transition distincts de ceux de la référence inférieure en multicouches Co/Pt.

Enfin, nous avons pu réaliser des doubles jonctions à anisotropie perpendiculaire avec une couche stockage comprise entre deux références. L'idée est de combiner les avantages de l'anisotropie à ceux des structures à double barrière tels qu'ils ont pu être observés dans les systèmes planaires. Il est en effet possible de moduler l'efficacité de l'effet STT dans ce type de structure. Dans le cas d'une couche de stockage simple, lorsque les références sont en configuration antiparallèle, les couples de transfert de spin en provenance des deux références s'ajoutent ce qui permet de réduire le courant critique. Au contraire, si les références sont en configuration parallèle, les couples se soustraient, ce qui réduit l'efficacité du STT. Cela donne donc la possibilité de basculer entre un mode écriture à forte efficacité du STT et un mode lecture dans lequel on peut appliquer de fortes tensions pour lire rapidement

l'information, sans risquer de réécrire la mémoire. L'une des premières réalisations pratiques de double jonction perpendiculaire se composait d'une couche de stockage simple encadrée par les deux références SAF précédemment développées ( $\text{SAF}_1/\text{CL}/\text{SAF}_2$ ). La mesure du cycle magnétique au VSM de ce type de jonction nous a permis de constater, qu'avec des traitements en champ, il est possible de réaliser un cycle mineur sur la couche libre à la fois en configuration parallèle ou antiparallèle des références. Cependant de forts champs doivent être appliqués pour inverser la référence la plus douce, ce qui entraîne une perte de l'information stockée si l'on souhaite passer d'un mode écriture à un mode lecture. Une solution pour utiliser ce type de dispositif consiste à maintenir la configuration antiparallèle tout le temps, de manière à permettre la réduction du courant critique. Cela nécessite cependant de dissymétriser les barrières afin de conserver un signal de TMR résultant. Cela peut se faire en modifiant les conditions d'oxydation par exemple. Quelques mesures de transport ont été réalisées par la méthode CIPT sur ce type de structure avec plusieurs types de barrière. Si qualitativement les résultats sont conformes avec les prédictions, la validité des données extraites par l'outil de mesure pour ces structures à double barrière reste discutable.

## Chapitre IV

Comme nous l'avons vu précédemment, l'utilisation de couches de référence SAF est particulièrement intéressante pour réduire les champs rayonnés dans les dispositifs de petite taille. Les multicouches Co/Pt ou Co/Pd utilisées dans de telles structures ont l'avantage d'apporter de fortes anisotropies perpendiculaires et de constituer des références stables à fort champ de couplage. Cependant, il est nécessaire d'avoir un bon contrôle des épaisseurs déposées car les couches ne font généralement que quelques dixièmes de nanomètre dans ces structures. D'autre part, les matériaux nobles comme le Pt et le Pd coûtent relativement cher et sont difficiles à graver par gravure ionique réactive ce qui limite l'industrialisation de tels dispositifs. C'est pourquoi dans ce Chapitre nous avons voulu développer des structures SAF à fort champ de couplage sans utiliser de Pt (ou Pd).

Il a ainsi été observé que deux couches de CoFeB peuvent être couplées de manière antiferromagnétique à travers un espaceur de Ta d'épaisseur supérieure à 0,6 nm [Sok-12]. Cependant, avec ces inserts Ta, les champs de couplage obtenus sont plutôt faibles : nous avons mesuré un plateau antiparallèle de  $\pm 150$  Oe avec une structure FeCoB<sub>1,2</sub>/Ta<sub>0,8</sub>/FeCoB<sub>1,2</sub>. Cela est insuffisant pour servir de couche de référence dans une jonction tunnel. En revanche, de plus forts couplages peuvent être observés avec des inserts Ru ou Ta/Ru. Ainsi, des largeurs de plateau de  $\pm 1300$  Oe et  $\pm 700$  Oe peuvent être obtenues avec des inserts de Ru de 0,6 nm ou de Ta<sub>0,2</sub>/Ru<sub>0,5</sub> nm, respectivement. Il apparaît que la force du couplage diminue linéairement avec l'augmentation de la proportion de Ta dans l'insert.

Nous avons ensuite étudié plus précisément le comportement magnétique de ces structures. Nous avons pu constater que la position relative des plateaux sur les branches aller et retour des cycles magnétiques est inversée entre les inserts Ru et Ta/Ru. Cela signifie que la couche morte présente dans le FeCoB dépend des éléments présents aux interfaces. Nous en déduisons une plus grande épaisseur de couche morte dans la couche inférieure pour les structures avec insert de Ru pur. D'autre part, dans les structures avec ce type d'insert, la compensation magnétique du SAF joue un rôle important dans le comportement magnétique observé. En effet, comme l'énergie de couplage devient dominante, une troisième transition correspondant au retournement de l'aimantation nette du SAF apparaît et réduit fortement la stabilité de la référence. Cependant, plus on se rapproche de la compensation magnétique, plus cette transition se décale vers les champs forts, pour disparaître au moment où le SAF est compensé.

Après avoir développé des structures SAF sans Pt avec des champs de couplage plus ou moins importants, nous avons cherché à les introduire dans des doubles jonctions à anisotropie perpendiculaire. Nous pouvons ainsi utiliser les structures FeCoB<sub>1,2</sub>/Ta<sub>0,8</sub>/FeCoB<sub>1,2</sub> à faibles champs de couplage comme couche de stockage SAF dans une double jonction de la forme SAF<sub>1</sub>/SAF<sub>3</sub>/SAF<sub>2</sub>. Dans ce cas, nous conservons les références développées au Chapitre précédent. Dans un deuxième

temps, nous avons vu que nous pouvons remplacer la référence supérieure en Co/Pd par l'une des nouvelles structures SAF dans un empilement du type SAF<sub>1</sub>/CL/SAF<sub>2</sub>. Cependant, comme pour la première structure de double jonction introduite au Chapitre III, il est impossible de basculer entre les modes écriture et lecture sans appliquer de forts champs magnétiques. C'est pourquoi une nouvelle structure a été introduite en partant de l'idée d'une couche douce de contrôle développée dans la thèse de P.-Y. Clément [\[Clé-14\]](#). Il s'agit de remplacer la couche de référence supérieure par une couche douce qui pourra être retournée indépendamment par déplacement de parois de domaines ou utilisation de couples de spin-orbite. Il faudra cependant être attentif à ce que cette couche reste insensible au STT pendant la phase d'écriture.

Finalement, dans la dernière partie de ce Chapitre, nous avons pu vérifier la faisabilité de jonctions simples sans Pt et Pd en utilisant les structures SAF à base de FeCoB comme couche de référence inférieure ou supérieure. Dans le cas où ces SAFs servent de référence inférieure, les propriétés d'anisotropie sont légèrement moins bonnes, mais dans les deux types d'empilement des jonctions fonctionnelles ont pu être obtenues.

## Chapitre V

Ce Chapitre présente les résultats des mesures électriques effectuées sur des nanopiliers de différentes tailles.

Dans une première partie, le processus de nanofabrication est présenté. Après avoir effectué le dépôt magnétique et l'avoir caractérisé, un masque dur de 150 nm de Ta est déposé sur la plaque. Une première étape de lithographie électronique permet de définir la forme et la taille des piliers. Puis grâce à plusieurs étapes de lithographie optique et de gravure, les contacts sur les électrodes inférieure et supérieure peuvent être réalisés.

Les premiers tests électriques ont été faits sur la jonction optimisée au Chapitre I, qui se compose d'une électrode de référence SAF à base de multicouches Co/Pt et d'une électrode de stockage supérieure. Nous avons réalisé un gradient d'épaisseur sur la couche de stockage qui varie entre 1 et 1,4 nm sur la plaque de 50 mm de diamètre. Après nanofabrication, un signal maximal de TMR autour de 36% est mesuré et un RA d'environ  $10 \Omega\mu\text{m}^2$ . Des piliers circulaires de diamètre compris entre 100 et 300 nm ont été définis sur cet échantillon. Grâce à l'application d'impulsions de courant de 100 ns pour différentes valeurs de champ magnétique, il a été possible de tracer des diagrammes de phase champ-tension. Nous en avons déduit des densités de courant raisonnables pour l'écriture par STT autour de  $3 \text{ MA}\cdot\text{cm}^{-2}$  et un facteur de stabilité thermique  $\Delta$  d'environ 43. Ces mesures nous ont également permis d'observer la variation du champ de couplage dipolaire en fonction de la taille de pilier. Nous obtenons une forte augmentation de ce champ à mesure que la dimension du plot est réduite. En utilisant la dépendance en champ du courant critique ( $J_{sw} = \frac{2e\alpha\mu_0 M_s t}{\hbar\eta} (H_{eff} + H_{app} + H_{cpl})$ ) et la variation d'épaisseur de la couche libre, nous avons estimé le paramètre d'amortissement de Gilbert  $\alpha$  autour de 0,016. Nous avons également étudié l'influence de la température sur le champ coercitif de la couche de stockage. Il apparaît que  $H_c$  diminue linéairement quand la température augmente. Nous constatons que, lorsque l'épaisseur passe de 1,1 à 1,24 nm, la température à laquelle le champ coercitif devient nul augmente de 20 à presque 110 °C. Cela vient du fait que l'anisotropie perpendiculaire augmente avec l'épaisseur magnétique dans la gamme d'épaisseurs étudiée.

## Conclusion

Le but de cette thèse était d'optimiser les propriétés magnétiques et de transport de jonctions tunnel magnétiques à anisotropie perpendiculaire. Ce travail s'inscrit dans les développements actuels de ces dispositifs pour les mémoires magnétiques à accès aléatoire (MRAM). En effet, combinée à l'écriture par couple de transfert de spin (STT) [Slo-96, Ber-96], cette technologie a été repérée comme l'une des mémoires non-volatiles émergentes les plus prometteuses, capable de satisfaire les critères de l'industrie de la microélectronique en termes de réduction des tailles de dispositifs. Cependant, créer de telles structures n'est pas si simple et nécessite une très bonne maîtrise des matériaux déposés. De nombreux paramètres doivent être optimisés, notamment les épaisseurs des différents matériaux, si l'on veut améliorer les performances des dispositifs à la fois en termes d'anisotropie et de transport.

L'anisotropie magnétique perpendiculaire, c'est-à-dire l'orientation préférentielle de l'aimantation dans la direction hors-plan, est un phénomène qui fût prédit relativement tôt et dont les origines sont essentiellement interfaciales [Née-54]. Cet effet a été largement étudié dans un premier temps pour les applications aux disques durs, notamment dans les alliages à base de Pt ou Pd qui présentent de forts couplages spin-orbite. Les multicouches Co/Pt sont également apparues intéressantes pour créer des structures à forte anisotropie perpendiculaire [Joh-96]. Cependant, une grande avancée fût réalisée avec la découverte d'une anisotropie perpendiculaire élevée aux interfaces métal/oxyde [Mon-02]. Cela permet d'envisager la réalisation de jonctions tunnel magnétiques perpendiculaires car ces structures possèdent une barrière isolante séparant les deux électrodes magnétiques.

Les jonctions tunnel magnétiques sont des composants à la base de la MagnétoRésistance Tunnel (TMR), un effet qui fût découvert en 1975 [Jul-75] et qui peut être utilisé pour stocker de l'information. En effet, en fonction de l'orientation relative des aimantations de part et d'autre de la barrière, deux états de résistance peuvent être mesurés. De premières prédictions théoriques [But-01, Mat-01] montrèrent qu'une barrière tunnel cristalline de MgO se révélait être un bon choix de matériau pour obtenir de forts signaux de TMR, ce qui fût rapidement confirmé expérimentalement [Yua-04, Par-04]. Grâce à leurs avantages en termes de croissance et de cristallisation, les alliages de CoFeB obtenus par pulvérisation cathodique furent rapidement favorisés [Lee-07, Yua-05, Cho-07] et purent être utilisés pour obtenir des jonctions à anisotropie perpendiculaire [Ike-10]. D'autres études révélèrent également que ce type de jonctions magnétiques présentait de nombreux avantages pour les applications STT en comparaison avec les systèmes planaires (grande capacité de stockage, forte stabilité thermique, courant critique d'écriture plus faible). Cependant, pour obtenir cette anisotropie, le choix des couches tampon et de couverture est particulièrement crucial [Wor-11, Liu-12, Nat-12, Kub-12].

Nous sommes partis d'une structure standard comprenant une référence inférieure antiferromagnétique synthétique (SAF) à base de multicouches Co/Pt et d'une couche libre supérieure en FeCoB. Dans une structure SAF, les couches magnétiques sont couplées antiferromagnétiquement à travers un espaceur métallique, grâce aux interactions RKKY [Rud-54, Kas-56, Yos-57], de façon à réduire les champs rayonnés agissant sur la couche de stockage dans le cas de dispositifs de petite taille [Ban-10]. L'avantage d'utiliser des multicouches Co/Pt dans la référence est qu'elles apportent une forte anisotropie perpendiculaire ce qui rend la couche de référence très stable. Cependant, pour obtenir un fort signal de TMR, il est nécessaire de conserver une couche de CoFeB à l'interface avec la barrière MgO. Cette couche est couplée aux multicouches adjacentes mais à travers un mince insert de Ta permettant d'obtenir la bonne structure bcc (001) au moment de la cristallisation. Cela garantit de bonnes propriétés de transport à la structure [Wor-11]. Le tantale a l'avantage de présenter un fort effet « getter » et ainsi d'attirer une partie du bore loin de l'interface avec la barrière oxyde ce qui est bénéfique pour la TMR [Koz-10]. Nous avons étudié l'influence de l'épaisseur de cet insert à la fois sur les propriétés magnétiques et de transport de jonctions tunnel perpendiculaires [Cuc-13]. Il apparaît qu'une épaisseur optimale d'environ 0,3-0,4 nm permet de garder un fort couplage magnétique dans la référence inférieure tout en améliorant significativement le signal de TMR de la jonction grâce à la bonne cristallisation de l'alliage de CoFeB.

La force du couplage RKKY dans la structure SAF inférieure a été testée. Comme attendu, le comportement oscillatoire typique en fonction de l'épaisseur de l'espaceur de Ru est obtenu [Par-91]. Il apparaît que choisir une épaisseur de Ru autour de 0,9 nm permet de bénéficier d'un fort couplage antiferromagnétique tout en étant relativement peu sensible aux possibles fluctuations d'épaisseurs car le pic est relativement large autour de cette épaisseur nominale. Les épaisseurs de Co et de Pt dans les multicouches, ainsi que de la couche tampon de Pt jouent un rôle primordial dans les propriétés magnétiques de la structure SAF et doivent donc être choisies avec précaution. D'autre part, il est particulièrement important de connaître les caractéristiques des électrodes inférieures et supérieures pour savoir quelles sont les fenêtres de fonctionnement de nos systèmes. Grâce à des séries d'échantillons dont les épaisseurs de FeCoB inférieur ou supérieur ont été variées, les épaisseurs critiques (pour lesquelles on a une réorientation de l'aimantation de perpendiculaire à planaire), les aimantations à saturation et les couches magnétiquement mortes ont pu être extraites. Ce dernier paramètre est nécessaire si l'on veut évaluer l'anisotropie de la couche magnétique grâce à des courbes  $K_{\text{eff.t}}=f(t)$ . Avec ce traitement, nous avons pu extraire une anisotropie d'interface  $2K_s$  d'environ  $1 \text{ erg.cm}^{-2}$  dans la couche libre de FeCoB supérieure. Des mesures de transport par la méthode CIPT (Current In-Plane Tunneling) [Wor-03] sur ces structures ont montré qu'un signal maximal de TMR est obtenu à partir du moment où les épaisseurs magnétiques effectives des électrodes de CoFeB sont supérieures à 0,6 nm [Cuc-14a].

Sachant que l'anisotropie perpendiculaire provient essentiellement de l'interface métal/oxyde, nous avons remplacé la couverture standard de Ta par une seconde

couche de MgO. Nous avons ainsi observé une augmentation de l'épaisseur critique effective (en prenant en compte la couche morte) de 1,1 à 2,7 nm avec les couches de stockage FeCoBx/Ta<sub>0,3</sub>/FeCoBx/MgO. Cela s'accompagne d'une forte augmentation de l'anisotropie d'interface, qui atteint environ 2 erg.cm<sup>-2</sup> ce qui devrait apporter une forte stabilité thermique aux nanopiliers. De plus, cette forte anisotropie donne la possibilité de travailler avec des épaisseurs magnétiques plus élevées qui devraient permettre de réduire le facteur d'amortissement. Une fine couche de Ta est insérée dans la couche de stockage de manière à conserver son effet « getter ». Des échantillons avec un insert Ru ou sans insert ont été testés et fonctionnent également. Le mode de réalisation de la couverture MgO peut être modifié afin de changer la valeur de son produit RA. En effet, un faible RA doit être employé pour la barrière supérieure si l'on veut conserver une valeur raisonnable de TMR résultante. Il est apparu que la nature des barrières MgO ne semble pas influencer énormément les propriétés d'anisotropie de la couche de stockage.

D'après des études réalisées sur des structures à anisotropie planaire, il est apparu que l'utilisation de doubles jonctions comportant deux barrières tunnel et deux polariseurs est particulièrement attractive pour les applications STT [[Dia-07](#), [Clé-14](#)]. En effet, en ajustant l'orientation relative des couches de référence, il est possible de moduler l'efficacité du couple de transfert de spin pour créer un mode écriture avec un faible courant critique et un mode lecture dans lequel de fortes tensions peuvent être appliquées sans risquer de perdre l'information stockée dans le point mémoire. Nous avons donc proposé de combiner ces propriétés avantageuses à celles de l'anisotropie perpendiculaire [[Cuc-15a](#)]. Pour cela, une couche de référence supérieure à base de multicouches Co/Pd a été développée après plusieurs optimisations d'épaisseurs. Il faut noter que comme on ne peut pas utiliser de couche tampon épaisse de Pd dans ces structures inversées, l'anisotropie perpendiculaire est bien plus faible comparée aux systèmes inférieurs en Co/Pt. C'est cependant une bonne chose car cela nous permet d'obtenir des champs de transition distincts dans les deux références et de construire un système fonctionnel dans lequel toutes les aimantations des couches magnétiques peuvent être basculées indépendamment. Nous avons donc pu montrer la réalisation d'une double jonction à anisotropie perpendiculaire composée d'une référence inférieure SAF à base de multicouches Co/Pt, une couche de stockage simple et une référence supérieure SAF à base de multicouches Co/Pd. Grâce à différents traitements en champ, la couche de stockage peut être renversée à la fois en configuration parallèle ou antiparallèle des références.

Pour les applications pratiques, il peut être intéressant de travailler avec des couches de stockage de type antiferromagnétique synthétique, car elles seraient moins sensibles aux possibles champs rayonnés dans les piliers de petite taille. Dans ce but, nous avons développé des structures SAF à base de FeCoB possédant différents types d'espaceur [[Cuc-16](#)]. Même si l'espaceur de Ru donne la plus grande force de couplage, des systèmes fonctionnels peuvent également être obtenus avec du Ta ou des bicouches Ta/Ru. En jouant sur la compensation magnétique des couches de FeCoB de part et d'autre de l'espaceur, il est possible d'augmenter la stabilité de la

structure SAF. Elle peut ensuite être placée à différentes positions dans une double jonction, soit comme couche de référence soit comme couche de stockage SAF. Cela permet d'imaginer des dispositifs encore plus performants, dans lesquels la référence supérieure est remplacée par une couche magnétique douce dont l'aimantation pourrait être basculée par champ entre un mode écriture et un mode lecture, sans risquer de perdre l'information stockée dans la couche de stockage SAF, plus stable. Cette couche douce, dite de contrôle, doit cependant être rendue insensible au STT durant la phase d'écriture.

Durant leur développement, il est apparu que ces structures SAF à base de FeCoB pouvaient être particulièrement stables avec des plateaux antiferromagnétiques atteignant  $\pm 1300$  Oe. Elles peuvent donc avantageusement remplacer nos références SAF standard à base de Co/Pt (Pd) dans des jonctions magnétiques simples. Cela permet de créer des systèmes sans Pt ou Pd qui ne contiennent aucune multicouche à base de métaux nobles, difficiles à graver avec les techniques standard de gravure ionique réactive. De plus dans ce cas, la quantité de matériaux impliqués dans l'empilement magnétique est beaucoup plus réduite.

Après avoir réalisé l'ensemble des étapes de nanofabrication, les propriétés électriques d'une jonction standard avec référence SAF inférieure et couche libre supérieure avec une couverture Ta ont été évaluées [Cuc-14b]. Des diagrammes de phase champ magnétique-impulsion de tension ont été mesurés et des densités de courant critique aussi faibles que  $2,9 \text{ MA.cm}^{-2}$  ont pu être obtenues. Grâce à la variation des propriétés en fonction de l'épaisseur magnétique, le paramètre d'amortissement de Gilbert est estimé autour de 0,016, ce qui est en bon accord avec les résultats obtenus dans d'autres groupes [Dev-13]. La dépendance en température du champ coercitif de la couche de stockage a également été testée. Elle est fortement liée à l'épaisseur magnétique, comme attendu.

Ces premiers tests électriques sont encourageants mais il serait d'autant plus intéressant de pouvoir tester les performances des structures avec couverture MgO et des doubles jonctions perpendiculaires. Dans ce contexte, d'autres travaux sur les barrières tunnel seront probablement nécessaires, notamment afin de pouvoir moduler précisément le produit RA de chaque barrière.

Les structures SAF à base de FeCoB sont particulièrement prometteuses et pourraient être testées pour les applications STT dans de nombreuses structures. Cependant, la stabilité du couplage RKKY dans des piliers de petite taille devra être confirmée. Les premiers résultats préliminaires semblent indiquer un maintien des propriétés du SAF jusqu'à des tailles d'au moins 50 nm. Cela pourrait être vérifié plus précisément en réalisant des réseaux de plots de différentes tailles et en mesurant leurs cycles d'hystérésis par effet Kerr focalisé.

## Références

[Bai-88] M. N. Baibich, J.-M. Broto, A. Fert, F. Nguyen Van Dau, F. Petroff, P. Etienne, G. Creuzet, A. Friederich, and J. Chazelas, *Giant magnetoresistance of (001)Fe/(001)Cr magnetic superlattices*, [Phys. Rev. Lett.](#) **61**, 2472-2475 (1988).

[Ban-10] S. Bandiera, R. C. Sousa, Y. Dahmane, C. Ducruet, C. Portemont, V. Baltz, S. Auffret, I. L. Prejbeanu, and B. Dieny, *Comparison between synthetic antiferromagnets and single hard layers as reference layer in perpendicular magnetic tunnel junctions*, [IEEE Magn. Lett.](#) **1**, 3000204 (2010).

[Ber-96] L. Berger, *Emission of spin waves by a magnetic multilayer traversed by a current*, [Phys. Rev. B](#) **54**, 9353-9358 (1996).

[Bin-89] G. Binasch, P. Grünberg, F. Saurenbach, and W. Zinn, *Enhanced magnetoresistance in layered magnetic structures with antiferromagnetic interlayer exchange*, [Phys. Rev. B](#) **39**, 4828-4830 (1989).

[But-01] W. H. Butler, X.-G. Zhang, T. C. Schulthess, and J. M. MacLaren, *Spin-dependent tunneling conductance of Fe|MgO|Fe sandwiches*, [Phys. Rev. B](#) **63**, 092402 (2001).

[Cho-07] Y. S. Choi, K. Tsunekawa, Y. Nagamine, and D. Djayaprawira, *Transmission electron microscopy study on the polycrystalline CoFeBMgOCoFeB based magnetic tunnel junction showing a high tunneling magnetoresistance, predicted in single crystal magnetic tunnel junction*, [J. Appl. Phys.](#) **101**, 013907 (2007).

[Clé-14] P.-Y. Clément, C. Baraduc, M. Chshiev, B. Dieny, L. Vila, and C. Ducruet, *Double barrier magnetic tunnel junctions with write/read mode select layer*, Proceedings of the [6<sup>th</sup> IEEE International Memory Workshop \(IMW\)](#), Taipei (May 18-21, 2014).

[Cuc-13] L. Cuchet, B. Rodmacq, S. Auffret, R. C. Sousa, C. Ducruet, and B. Dieny, *Influence of a Ta spacer on the magnetic and transport properties of perpendicular magnetic tunnel junctions*, [Appl. Phys. Lett.](#) **103**, 052402 (2013).

[Cuc-14a] L. Cuchet, B. Rodmacq, S. Auffret, R. C. Sousa, and B. Dieny, *Influence of magnetic electrodes thicknesses on the transport properties of magnetic tunnel junctions with perpendicular anisotropy*, [Appl. Phys. Lett.](#) **105**, 052408 (2014).

[Cuc-14b] L. Cuchet, R. C. Sousa, L. Vila, S. Auffret, B. Rodmacq, and B. Dieny, *Field dependence of spin transfer torque switching current in perpendicular magnetic tunnel junctions*, [IEEE Trans. Magn.](#) **50**, 4401404 (2014).

[Cuc-15a] L. Cuchet, B. Rodmacq, S. Auffret, R. C. Sousa, I. L. Prejbeanu, and B. Dieny, *Perpendicular magnetic tunnel junctions with double barrier and single or synthetic antiferromagnetic storage layer*, [J. Appl. Phys.](#) **117**, 233901 (2015).

[Cuc-16] L. Cuchet, B. Rodmacq, S. Auffret, R. C. Sousa, I. L. Prejbeanu, and B. Dieny, *Perpendicular magnetic tunnel junctions with a synthetic storage or reference layer: A new route towards Pt- and Pd-free junctions*, à paraître dans Sci. Rep. (2016).

[Dev-13] T. Devolder, P.-H. Ducrot, J.-P. Adam, I. Barisic, N. Vernier, Joo-Von Kim, B. Ockert, and D. Ravelosona, *Damping of  $Co_x Fe_{80-x} B_{20}$  ultrathin films with perpendicular magnetic anisotropy*, [Appl. Phys. Lett.](#) **102**, 022407 (2013).

[Dia-07] Z. Diao, A. Panchula, Y. Ding, M. Pakala, S. Wang, Z. Li, D. Apalkov, H. Nagai, A. Driskill-Smith, L.-C. Wang, E. Chen, and Y. Huai, *Spin transfer switching in dual MgO magnetic tunnel junctions*, [Appl. Phys. Lett.](#) **90**, 132508 (2007).

[Die-91] B. Dieny, V. S. Speriosu, S. S. P. Parkin, B. A. Gurney, D. R. Wilhoit, and D. Mauri, *Giant magnetoresistive effect in soft ferromagnetic multilayers*, [Phys. Rev. B](#) **43**, 1297-1300 (1991).

[Hei-10] O. G. Heinonen, and D. V. Dimitrov, *Switching-current reduction in perpendicular anisotropy spin torque magnetic tunnel junctions*, [J. Appl. Phys.](#) **108**, 014305 (2010).

[Hu-11] J.-M. Hu, Z. Li, L.-Q. Chen, and C.-W. Nan, *High-density magnetoresistive random access memory operating at ultralow voltage at room temperature*, [Nat. Commun.](#) **2**, 553 (2011).

[Ike-10] S. Ikeda, K. Miura, H. Yamamoto, K. Mizunuma, H. D. Gan, M. Endo, S. Kanai, J. Hayakawa, F. Matsukura, and H. Ohno, *A perpendicular-anisotropy CoFeB–MgO magnetic tunnel junction*, [Nature Mater.](#) **9**, 721-724 (2010).

[Itr-10]  
[http://www.itrs.net/Links/2010ITRS/2010Update/ToPost/ERD\\_ERM\\_2010FINAL\\_ReportMemory\\_Assessment\\_ITRS.pdf](http://www.itrs.net/Links/2010ITRS/2010Update/ToPost/ERD_ERM_2010FINAL_ReportMemory_Assessment_ITRS.pdf)

[Joh-96] M. T. Johnson, P. J. H. Bloemen, F. J. A. den Broeder, and J. J. de Vries, *Magnetic anisotropy in metallic multilayers*, [Rep. Prog. Phys.](#) **59**, 1409-1458 (1996).

[Jul-75] M. Jullière, *Tunneling between ferromagnetic films*, [Phys. Lett.](#) **54A**, 225-226 (1975).

[Kas-56] T. Kasuya, *A theory of metallic ferro- and antiferromagnetism on Zener's model*, [Prog. Theor. Phys.](#) **16**, 45-57 (1956).

[Koz-10] X. Kozina, S. Ouardi, B. Balke, G. Stryganyuk, G. H. Fecher, C. Felser, S. Ikeda, H. Ohno and E. Ikenaga, *A nondestructive analysis of the B diffusion in Ta–*

*CoFeB–MgO–CoFeB–Ta magnetic tunnel junctions by hard X-ray photoemission*, [Appl. Phys. Lett.](#) **96**, 072105 (2010).

[Kub-12] H. Kubota, S. Ishibashi, T. Saruya, T. Nozaki, A. Fukushima, K. Yakushiji, K. Ando, Y. Suzuki, and S. Yuasa, *Enhancement of perpendicular magnetic anisotropy in FeB free layers using a thin MgO cap layer*, [J. Appl. Phys.](#) **111**, 07C723 (2012).

[Lee-07] Y. M. Lee, J. Hayakawa, S. Ikeda, F. Matsukura, and H. Ohno, *Effect of electrode composition on the tunnel magnetoresistance of pseudo-spin-valve magnetic tunnel junction with a MgO tunnel barrier*, [Appl. Phys. Lett.](#) **90**, 212507 (2007).

[Liu-12] T. Liu, J. W. Cai, and L. Sun, *Large enhanced perpendicular magnetic anisotropy in CoFeB/MgO system with the typical Ta buffer replaced by an Hf layer*, [AIP Advances](#) **2**, 032151 (2012).

[Liu-14] T. Liu, Y. Zhang, J. W. Cai, and H. Y. Pan, *Thermally robust Mo/CoFeB/MgO trilayers with strong perpendicular magnetic anisotropy*, [Sci. Rep.](#) **4**, 5895 (2014).

[Man-08] A. Manchon, C. Ducruet, L. Lombard, S. Auffret, B. Rodmacq, B. Dieny, S. Pizzini, J. Vogel, V. Uhlír, M. Hochstrasser, and G. Panaccione, *Analysis of oxygen-induced anisotropy crossover in Pt/Co/MO<sub>x</sub> trilayers*, [J. Appl. Phys.](#) **104**, 043914 (2008).

[Mat-01] J. Mathon, and A. Umerski, *Theory of tunneling magnetoresistance of an epitaxial Fe/MgO/Fe(001) junction*, [Phys. Rev. B](#) **63**, 220403(R) (2001).

[Mon-02] S. Monso, B. Rodmacq, S. Auffret, G. Casali, F. Fetta, B. Gilles, B. Dieny, and P. Boyer, *Crossover from in-plane to perpendicular anisotropy in Pt/CoFe/AlO<sub>x</sub> sandwiches as a function of Al oxidation: A very accurate control of the oxidation of tunnel barriers*, [Appl. Phys. Lett.](#) **80**, 4157-4159 (2002).

[Nat-12] A. Natarajarathinam, Z. R. Tadisina, T. Mewes, S. Watts, E. Chen, and S. Gupta, *Influence of capping layers on CoFeB anisotropy and damping*, [J. Appl. Phys.](#) **112**, 053909 (2012).

[Née-54] L. Néel, *Anisotropie magnétique superficielle et surstructures d'orientation*, [J. Phys. Radium](#) **15**, 225-239 (1954).

[Par-04] S. S. P. Parkin, C. Kaiser, A. Panchula, P. M. Rice, B. Hughes, M. Samant, and S.-H. Yang, *Giant tunnelling magnetoresistance at room temperature with MgO (100) tunnel barriers*, [Nature Mater.](#) **3**, 862-867 (2004).

[Par-91] S. S. P. Parkin, *Systematic variation of the strength and oscillation period of indirect magnetic exchange coupling through the 3d, 4d, and 5d transition metals*, [Phys. Rev. Lett.](#) **67**, 3598 (1991).

[Rod-03] B. Rodmacq, S. Auffret, B. Dieny, S. Monso, and P. Boyer, *Crossovers from in-plane to perpendicular anisotropy in magnetic tunnel junctions as a function of the barrier degree of oxidation*, [J. Appl. Phys.](#) **93**, 7513-7515 (2003).

[Rud-54] M. A. Ruderman, and C. Kittel, *Indirect exchange coupling of nuclear magnetic moments by conduction electrons*, [Phys. Rev.](#) **96**, 99-102 (1954).

[Sin-13] J. Sinha, M. Hayashi, A. J. Kellock, S. Fukami, M. Yamanouchi, H. Sato, S. Ikeda, S. Mitani, S. -H. Yang, S. S. P. Parkin, and H. Ohno, *Enhanced interface perpendicular magnetic anisotropy in Ta|CoFeB|MgO using nitrogen doped Ta underlayers*, [Appl. Phys. Lett.](#) **102**, 242405 (2013).

[Slo-96] J. C. Slonczewski, *Current-driven excitation of magnetic multilayers*, [J. Magn. Magn. Mater.](#) **159**, L1-L7 (1996).

[Sok-12] V. Sokalski, M. T. Moneck, E. Yang, and J. -G. Zhu, *Optimization of Ta thickness for perpendicular magnetic tunnel junction applications in the MgO-FeCoB-Ta system*, [Appl. Phys. Lett.](#) **101**, 072411 (2012).

[Wol-10] S. A. Wolf, J. Lu, M. R. Stan, E. Chen, and D. M. Treger, *The promise of nanomagnetism and spintronics for future logic and universal memory*, [Proc. IEEE](#) **98**, 2155-2168 (2010).

[Wor-03] D. C. Worledge, and P. L. Trouilloud, *Magnetoresistance measurement of unpatterned magnetic tunnel junction wafers by current-in-plane tunneling*, [Appl. Phys. Lett.](#) **83**, 84-86 (2003).

[Wor-11] D. C. Worledge, G. Hu, D. W. Abraham, J. Z. Sun, P. L. Trouilloud, J. Nowak, S. Brown, M. C. Gaidis, E. J. O'Sullivan, and R. P. Robertazzi, *Spin torque switching of perpendicular Ta/CoFeB/MgO-based magnetic tunnel junctions*, [Appl. Phys. Lett.](#) **98**, 022501 (2011).

[Yam-12] H. Yamamoto, J. Hayakawa, K. Miura, K. Ito, H. Matsuoka, S. Ikeda, and H. Ohno, *Dependence of magnetic anisotropy in  $Co_{20}Fe_{60}B_{20}$  free layers on capping layers in MgO-based magnetic tunnel junctions with in-plane easy axis*, [Appl. Phys. Expr.](#) **5**, 053002 (2012).

[Yan-11] H. X. Yang, M. Chshiev, B. Dieny, J. H. Lee, A. Manchon, and K. H. Shin, *First-principles investigation of the very large perpendicular magnetic anisotropy at Fe/MgO and Co/MgO interfaces*, [Phys. Rev. B](#) **84**, 054401 (2011).

[Yod-10] H. Yoda, T. Kishi, T. Nagase, M. Yoshikawa, K. Nishiyama, E. Kitagawa, T. Daibou, M. Amano, N. Shimomura, S. Takahashi, T. Kai, M. Nakayama, H. Aikawa, S. Ikegawa, M. Nagamine, J. Ozeki, S. Mizukami, M. Oogane, Y. Ando, S. Yuasa, K. Yakushiji, H. Kubota, Y. Suzuki, Y. Nakatani, T. Miyazaki, and K. Ando, *High efficient spin transfer torque writing on perpendicular magnetic tunnel junctions for high density MRAMs*, [Curr. Appl. Phys.](#) **10**, e87-e89 (2010).

[Yos-57] K. Yosida, *Magnetic properties of Cu-Mn alloys*, [Phys. Rev.](#) **106**, 893-898 (1957).

[Yua-04] S. Yuasa, T. Nagahama, A. Fukushima, Y. Suzuki, and K. Ando, *Giant room-temperature magnetoresistance in single-crystal Fe/MgO/Fe magnetic tunnel junctions*, [Nature Mater.](#) **3**, 868-871 (2004).

[Yua-05] S. Yuasa, Y. Suzuki, T. Katayama, and K. Ando, *Characterization of growth and crystallization processes in CoFeB/MgO/CoFeB magnetic tunnel junction structure by reflective high-energy electron diffraction*, [Appl. Phys. Lett.](#) **87**, 242503 (2005).

## ABSTRACT

Due to their advantageous properties in terms of data retention, storage density and critical current density for Spin Transfer Torque (STT) switching, the magnetic tunnel junctions with perpendicular anisotropy have become predominant in the developments for MRAM applications. The aim of this thesis is to improve the anisotropy and transport properties of such structures and to realize even more complex stacks such as perpendicular double junctions. Studies on the magnetic properties and Tunnel MagnetoResistance (TMR) measurements showed that to optimize the performances of the junctions, all the thicknesses of the different layers constituting the stack have to be adapted. To guaranty both a large TMR as well a strong perpendicular anisotropy, compromises are most of the time needed. Studies as a function of magnetic thickness enabled to extract the saturation magnetization, the critical thickness and the magnetic dead layer thickness both in the bottom reference and the top storage layer in structures capped with Ta. This type of junction could be tested electrically after patterning the sample into nanopillars. Knowing that perpendicular anisotropy mostly arises at the metal/oxide interface, the Ta capping layer was replaced by a MgO one, leading to a huge increase in the anisotropy of the free layer. A second top reference was then added on such a stack to create functional perpendicular double junctions. CoFeB/insertion/CoFeB synthetic antiferromagnetic storage layers could be developed and were proved to be stable enough to replace the standard Co/Pt-based reference layers.

**Keywords:** Spintronics, Magnetic Tunnel Junctions, MRAM, Perpendicular Magnetic Anisotropy, Double junctions, Spin Transfer Torque

## RESUME

Du fait de leurs propriétés avantageuses en termes de rétention des données, densité de stockage et faible courant critique pour l'écriture par courant polarisé en spin (STT), les jonctions tunnel magnétiques à anisotropie perpendiculaire sont devenues prédominantes dans les études sur les applications aux mémoires magnétiques MRAM. Les travaux de cette thèse s'inscrivent dans ce contexte avec pour but l'amélioration des propriétés de transport et d'anisotropie de telles structures ainsi que la réalisation d'empilements encore plus complexes tels que des doubles jonctions perpendiculaires. Grâce à l'étude des propriétés magnétiques et des mesures de MagnétoRésistance Tunnel (TMR), il apparaît que pour optimiser les performances des jonctions tunnel, l'ensemble des épaisseurs des couches composant l'empilement doit être adapté. Des compromis sont souvent nécessaires pour obtenir à la fois une forte anisotropie perpendiculaire et des signaux de TMR élevés. Des études en fonction des épaisseurs magnétiques ont permis de déterminer les aimantations à saturation, épaisseurs critiques et couches mortes dans les couches de référence et de stockage de jonctions standard avec électrode libre supérieure et couverture Ta. Ce type de jonction a pu être nano-fabriqué sous forme de piliers circulaires afin de tester l'écriture par STT. Sachant que l'anisotropie perpendiculaire provient essentiellement de l'interface métal/oxyde, la couverture Ta a été ensuite remplacée par une deuxième couche de MgO, permettant d'améliorer significativement l'anisotropie de la couche libre. En introduisant une seconde référence au-dessus de cette jonction, des doubles jonctions perpendiculaires fonctionnelles ont pu être fabriquées. Des couches de stockage antiferromagnétiques synthétiques de la forme CoFeB/insert/CoFeB ont pu être développées et apparaissent suffisamment stables pour pouvoir remplacer les traditionnelles références à base de multicouches Co/Pt.

**Mots-clés :** Electronique de Spin, Jonctions Tunnel Magnétiques, MRAM, Anisotropie Magnétique Perpendiculaire, Double jonctions, Couple de Transfert de Spin